TECHNICAL UNIVERSITY OF CRETE

School of Production Engineering & Management

DOCTORAL THESIS

Macroscopic Traffic Flow Modelling in the Presence of Vehicle Automation and Communication Systems

---

Kallirroi PORFYRI

A dissertation submitted in partial fulfillment of the requirements for the degree of Doctor of Philosophy (Ph.D.)

in the

Dynamic Systems & Simulation Laboratory,
School of Production Engineering &Management

Supervisor: Prof. I.K. Nikolos

Chania, July 2019

The present thesis is approved by the following jury:

Advisory Committee:

Dr. Ioannis K. Nikolos (Supervisor)
Professor, School of Production Engineering and Management,
Technical University of Crete, Chania, Greece

Dr. Markos Papageorgiou (Member of Advisory Committee)

Professor, School of Production Engineering and Management,
Technical University of Crete, Chania, Greece

Dr. Anargiros Delis (Member of Advisory Committee)
Associate Professor, School of Production Engineering and Management,
Technical University of Crete, Chania, Greece

Thesis Committee:

Dr. Ioannis Papamichail
Associate Professor, School of Production Engineering and Management,
Technical University of Crete, Chania, Greece

Dr. Nikolaos Bekiaris-Liberis
Assistant Professor, School of Electrical and Computer Engineering, Technical University of Crete, Chania, Greece

Dr. George Arampatzis
Assistant Professor, School of Production Engineering and Management,
Technical University of Crete, Chania, Greece

Dr. Claudio Roncoli
Assistant Professor, Department of Built Environment,
Aalto University, Espoo, Finland

Technical University of Crete

School of Production Engineering & Management

Abstract

Ph.D. Thesis

Macroscopic Traffic Flow Modelling in the Presence of Vehicle Automation and Communication Systems

by Kallirroi PORFYRI

Over the past few years most of the countries are facing the consequences of the ever-increasing number of vehicles, which lead to a continuous increase of congestion phenomena, resulting in significant increases in travel times, fuel consumption, and emissions, as well as reduced traffic safety. Conventional approaches for solving the problem of traffic congestion by expanding the existing infrastructure and operational improvements - such as auxiliary lanes, additional alternate routes and interchange modifications - remain practically infeasible, mainly due to economic and environmental reasons. Instead, comprehensive traffic control strategies can be defined to mitigate the problem of persisting traffic jams. However, the employment of efficient real-time traffic control measures entails the availability of reliable and robust traffic flow models that may be used to develop and validate the proposed control strategies. In this context, an effective calibration and validation process appears to be mandatory to ensure the credibility of traffic flow models in performing real-world simulations and optimization scenarios.

Concurrently, engineers are seeking for solutions to improve the road network efficiency and capacity by means of Intelligent Transportation Systems (ITS). Specifically, during the last decade, an enormous continuing interdisciplinary effort is performed by the automobile industry, as well as by various research institutions around the world, to plan, develop, test, and start deploying a variety of Vehicle Automation and Communication Systems (VACS) that are expected to bring radical changes in the way the traffic flow will be controlled and optimized within the next decades. VACS, such as Adaptive Cruise Control (ACC) and Cooperative Adaptive Cruise Control (CACC) systems, have been initially developed based on new commuting alternatives for drivers and passengers, with particular emphasis given on improving comfort, convenience, and safety, as well as reducing traffic congestion.

This thesis, which is composed of two parts, is an early attempt towards this direction. More specifically, the first part deals with the advancement of traffic flow models, with emphasis on macroscopic ones. In particular, within this thesis the well-known continuous second-order macroscopic gas-kinetic-based traffic model (GKT model) was validated, regarding the representation of traffic conditions at congested freeway areas. The model was calibrated and validated by employing an optimization methodology based on a parallel, metamodel-assisted Differential Evolution (DE) algorithm (synchronous and asynchronous) and using real traffic data from two different motorway networks; a motorway stretch in the

U.K., where severe traffic congestion is created due to high on-ramp flows during the morning peak periods, and a freeway stretch in Greece, where recurrent congestion is triggered by a saturated off-ramp during the morning peak hours. Moreover, a multi-lane approach of the GKT model is evaluated using real traffic data from the aforementioned network in the U.K. Subsequently, by implementing the same optimization scheme, the GKT model was compared with the most popular discrete time-space macroscopic traffic flow model, namely the METANET model, in terms of the representation of traffic flow conditions at the motorway stretch in the U.K.

The GKT second-order traffic flow model, presented in the first part of this dissertation, provides the methodical prerequisites for the second part of the dissertation, where a novel concept of two alternative models for the macroscopic simulation of ACC and CACC traffic is discussed. This approach is based on the introduction of a relaxation term in the momentum equation of the GKT model that satisfies the time/space-gap principle of ACC and CACC systems. In this thesis both linear and nonlinear stability analyses are performed, to derive the stability threshold of the aforementioned models, and additionally study the influence of the equipped vehicles on the traffic flow stabilization, with respect to both small and large perturbations around the equilibrium state.

Περίληψη

Τα τελευταία χρόνια, πολλές βιομηχανικές χώρες αντιμετωπίζουν τις συνέπειες του συνεχώς αυξανόμενου αριθμού των οχημάτων, γεγονός που οδηγεί σε συνεχή αύξηση των φαινομένων συμφόρησης. Αυτά έχουν ως αποτέλεσμα τη σημαντική αύξηση των χρόνων ταξιδιού, την κατανάλωση καυσίμων, τις εκπομπές καυσαερίων, καθώς και τη μείωση της κυκλοφοριακής ασφάλειας. Οι συμβατικές μέθοδοι για την επίλυση του προβλήματος της κυκλοφοριακής συμφόρησης, με επέκταση των υπαρχουσών υποδομών και λειτουργικές βελτιώσεις, όπως οι βοηθητικές λωρίδες, οι πρόσθετες εναλλακτικές διαδρομές και οι τροποποιήσεις των μεταφορών, παραμένουν πρακτικά ανέφικτες, κυρίως λόγω οικονομικών και περιβαλλοντικών λόγων. Αντίθετα, μπορεί να χρησιμοποιηθεί εναλλακτικά μια ολοκληρωμένη στρατηγική ελέγχου της κυκλοφορίας, προκειμένου να μετριαστεί το πρόβλημα των συνεχών κυκλοφοριακών συμφορήσεων. Ωστόσο, η εφαρμογή αποδοτικών μέτρων ελέγχου της κυκλοφορίας σε πραγματικό χρόνο συνεπάγεται την ύπαρξη αξιόπιστων και εύρωστων μοντέλων κυκλοφοριακής ροής, τα οποία μπορούν να χρησιμοποιηθούν για την ανάπτυξη και την επικύρωση των προτεινόμενων στρατηγικών ελέγχου. Στο πλαίσιο αυτό, μια αποτελεσματική διαδικασία βαθμονόμησης και επικύρωσης φαίνεται να είναι αναγκαία για να εξασφαλιστεί η αξιοπιστία των μοντέλων κυκλοφοριακής ροής κατά την εκτέλεση πραγματικών προσομοιώσεων και σεναρίων βελτιστοποίησης.

Ταυτόχρονα, επιστήμονες και μηχανικοί στις μέρες μας αναζητούν λύσεις για τη βελτίωση της αποτελεσματικότητας και της χωρητικότητας των οδικών δικτύων, μέσω των Συστημάτων Ευφυών Μεταφορών. Συγκεκριμένα, κατά τη διάρκεια της τελευταίας δεκαετίας, πραγματοποιήθηκαν τεράστιες συνεχιζόμενες διεπιστημονικές προσπάθειες από τον κλάδο της αυτοκινητοβιομηχανίας, καθώς και από πολυάριθμα ερευνητικά ιδρύματα σε όλον τον κόσμο για το σχεδιασμό, την ανάπτυξη, τη δοκιμή και τη χρησιμοποίηση ποικίλων συστημάτων αυτοματισμού και επικοινωνίας οχημάτων, τα οποία αναμένεται να φέρουν ριζικές αλλαγές στον τρόπο ελέγχου και βελτιστοποίησης της κυκλοφοριακής ροής στις επόμενες δεκαετίες. Τα συστήματα αυτά, όπως τα συστήματα Adaptive Cruise Control (ACC) και Cooperative Adaptive Cruise Control (CACC), αναπτύχθηκαν αρχικά βάση νέων εναλλακτικών μετακίνησης για τους οδηγούς και τους επιβάτες, με ιδιαίτερη έμφαση στη βελτίωση της άνεσης, της ευκολίας και της ασφάλειας, καθώς και στη μείωση της κυκλοφοριακής συμφόρησης.

Η εργασία αυτή, η οποία αποτελείται από δύο κύρια μέρη, είναι μία πρώτη προσπάθεια προς αυτή την κατεύθυνση. Πιο συγκεκριμένα, το πρώτο μέρος ασχολείται με την εξέλιξη των μοντέλων κυκλοφοριακής ροής, με έμφαση στα μακροσκοπικά μοντέλα. Στα πλαίσια της παρούσας διατριβής, το γνωστό συνεχές 2ης τάξης μοντέλο κυκλοφοριακής ροής gas-kinetic-based traffic model (GKT) αξιολογήθηκε σχετικά με την ικανότητά του να αναπαριστά τις κυκλοφοριακές συνθήκες σε περιοχές αυτοκινητόδρομων υπό κυκλοφοριακή συμφόρηση. Το μοντέλο βαθμονομήθηκε και επικυρώθηκε με τη χρήση μιας μεθόδου βελτιστοποίησης βασισμένη σε παράλληλο Διαφορικό Εξελικτικό αλγόριθμο (Differential Evolution (DE) algorithm), χρησιμοποιώντας πραγματικά δεδομένα κίνησης από δύο διαφορετικά δίκτυα αυτοκινητοδρόμων: από ένα τμήμα αυτοκινητοδρόμου στο Ηνωμένο Βασίλειο, όπου εμφανίζεται σοβαρή κυκλοφοριακή συμφόρηση εξαιτίας των υψηλών ροών στη ράμπα εισόδου κατά τις πρωινές ώρες αιχμής, καθώς και από ένα τμήμα αυτοκινητοδρόμου στην Ελλάδα, όπου επαναλαμβανόμενη συμφόρηση προκαλείται από μία ράμπα εξόδου, επίσης κατά τις πρωινές ώρες αιχμής. Επιπλέον, η προσέγγιση πολλαπλών λωρίδων του μοντέλου GKT αξιολογήθηκε με τη χρήση πραγματικών δεδομένων κίνησης από το προαναφερθέν δίκτυο στο Ηνωμένο Βασίλειο. Στη συνέχεια, εφαρμόζοντας τον ίδιο αλγόριθμο βελτιστοποίησης, το GKT μοντέλο συγκρίθηκε με το πιο δημοφιλές διακριτό

μακροσκοπικό μοντέλο, το METANET, σχετικά με την ικανότητά τους να αναπαραστήσουν τις συνθήκες κυκλοφοριακής ροής στο τμήμα του αυτοκινητόδρομου στο Ηνωμένο Βασίλειο.

Το 2ης τάξης GKT μοντέλο κυκλοφορικής ροής, όπως θα παρουσιαστεί στο πρώτο μέρος, παρέχει τα μεθοδολογικά προαπαιτούμενα για το δεύτερο μέρος της διατριβής, όπου παρατίθενται δύο νέα μοντέλα μακροσκοπικής προσομοίωσης για ACC και CACC οχήματα. Συγκεκριμένα, η νέα προσέγγιση βασίζεται στην εισαγωγή ενός όρου χαλάρωσης στην εξίσωση της ορμής του GKT μοντέλου, ο οποίος ικανοποιεί την αρχή του χρονικού/χωρικού κενού (time/space-gap) των ACC και CACC οχημάτων. Επιπρόσθετα, στη διατριβή αυτή εξετάζεται τόσο η γραμμική όσο και η μη γραμμική ανάλυση ευαισθησίας, προκειμένου να προκύψει το όριο ευστάθειας των νέων μοντέλων, τα οποία είναι ικανά να προσομοιώνουν τη συμπεριφορά των ACC και CACC οχημάτων στη κυκλοφοριακή ροή, καθώς επίσης και να μελετηθεί η επιρροή αυτών των εξοπλισμένων οχημάτων στη σταθεροποίηση της κυκλοφοριακής ροής, όσον αφορά τόσο μικρές όσο και μεγάλες διαταραχές γύρω από την κατάσταση ισορροπίας.

Acknowledgements

It's my pleasant duty to express my sincere regards and grateful obligation to those who have been very helpful during the completion of my research work.

First and foremost, I would like to express my deep sense of gratitude to my supervisor Professor Ioannis K. Nikolos, for his valuable expertise, guidance and supervision. I am immensely indebted for his inspiration, encouragement, kindness and ethics, which he showed during the entire period of my research.

I would like also to thank Associate Professor Anargiros I. Delis for his constant support and valuable guidance as co-advisor. I greatly appreciate his extraordinary generosity in sharing his knowledge and his ability for teamwork. Moreover, I would like to thank Professor Markos Papageorgiou for having supervised this work and for providing perfect working conditions and a stimulating environment. It has been an exciting and challenging time to work in his research group and for allowing me being member of the wide research community of Traffic Flow Modelling and Control.

The completion of this thesis is also owed to my beloved husband, Giorgos Strofylas, for his scientific and psychological contribution during all these years. And, albeit impossible to express in one sentence, I deeply thank him for all his love, the sleepless nights he has spent and his support in the moments when there was no one to answer my queries; this thesis is dedicated to him. I would also like to thank my family for being always next to me; I would like to express my gratitude to my parents Nikos and Panagiota and my brother John, for their support and confidence in me.

Finally, I would like to thank the research colleagues of TRAMAN21, a European Research Council (ERC) project under the European Union's Seventh Framework Programme (FP/20072013) / ERC Grant Agreement n. 321132. Funding from TRAMAN21 is also gratefully acknowledged.

Contents

List of Figures

List of Tables

List of Abbreviations

Abbreviation/Term	Definition
ACC	**A**daptive **C**ruise **C**ontrol
ANN	**A**rtificial **N**eural **N**etwork
AR	**A**w–**R**ascle
ARZ	**A**w–**R**ascle–**Z**hang
CA	**C**ellular **A**utomata
CACC	**C**ooperative **A**daptive **C**ruise **C**ontrol
cEA	**C**ellular **E**volutionary **A**lgorithm
CEM	**C**ross **E**ntropy **M**ethod
CFL	**C**ourant-**F**riedrichs-**L**ewy
CTH	**C**onstant **T**ime **H**eadway
CTM	**C**ell-**T**ransmission **M**odel
DE	**D**ifferential **E**volution
dEA	**D**istributed (island) **E**volutionary **A**lgorithm
EA	**E**volutionary **A**lgorithm
FD	**F**undamental **D**iagram
GEH	**G**eoffrey **E**. **H**aver
GKT	**G**as-**k**inetic-based **T**raffic
IDM	**I**ntelligent **D**river **M**odel
ITS	**I**ntelligent **T**ransportation **S**ystems
KK	**K**erner–**K**onhäuser
LWR	**L**ighthill-**W**hitham-**R**ichards
MAE	**M**ean **A**bsolute **E**rror
MANE	**M**ean **A**bsolute **N**ormalized **E**rror
ME	**M**ean **E**rror
MLP	**M**ulti-**l**ayer **P**erceptron
MNE	**M**ean **N**ormalized **E**rror
MPI	**M**essage **P**assing **I**nterface
OVM	**O**ptimal **V**elocity **M**odel
PEA	**P**arallel **E**volutionary **A**lgorithms
PDE	**P**artial **D**ifferential **E**quation
PW	**P**ayne–**W**hitham
RBF	**R**adial **B**asis **F**unction
RBFN	**R**adial **B**asis **F**unctions **N**etwork
RMA	**R**emote **M**emory **A**ccess
RMSE	**R**oot **M**ean **S**quare **E**rror
RMSNE	**R**oot **M**ean **S**quare **N**ormalized **E**rror
SE	**S**quared **E**rror
VACS	**V**ehicle **A**utomation and **C**ommunication **S**ystems
VMS	**V**ariable **M**essage **S**igns
WENO	**W**eighted **E**ssentially **N**on-**O**scillatory

To my family. . .

Chapter 1: Introduction

A rapid growth of vehicular traffic flow modelling has taken place over the last decades, the main reason being the need for efficient usage of existing traffic infrastructures and for the optimal design of new ones. The rising financial and, especially, environmental costs of persisting traffic jams, as well as their impact on the quality of life, put additional pressure towards the development of novel traffic flow simulation tools. Moreover, during the last decade, there has been an enormous continuing interdisciplinary effort, made by the automobile industry as well as by numerous research institutions around the world, to plan, develop, test and start deploying a variety of VACS that are expected to revolutionize the features and capabilities of individual vehicles within the next decades.

Towards this direction, in this thesis two second-order macroscopic traffic flow models, able to simulate the impact of ACC and CACC vehicles on traffic flow dynamics, are presented and analysed in order to study their qualitative properties by deriving proper stability conditions with respect to both small and large perturbations. For the development of these models, the existing second-order macroscopic GKT model was implemented as the basis model. Moreover, a novel numerical approach was applied for the numerical approximation of the GKT model, along with its multi-lane extension. Additionally, the numerical simulation approach was combined with an optimization procedure to enable the automatic estimation of the most crucial parameters of the model; specifically, a parallel, metamodel-assisted Differential Evolution (DE) algorithm was employed for the calibration of the GKT model (and its extensions).

In the following Sections 1.1 and 1.2, the motivation and the objectives of this work are presented. Section 1.3 provides an outline of the thesis structure and an overview of the remaining chapters. Finally, this first chapter will be completed by giving a list of the related publications (Section 1.4).

1.1 Motivation

The need for robust, realistic, and time-efficient modelling tools, for evaluating different traffic systems and ITS technologies, has increased remarkably in recent years. Traffic flow models can now be employed for the planning and assessment of road infrastructures, traffic surveillance and monitoring, incident detection, as well as for the development and testing of traffic control strategies and other operational tools (Kotsialos & Papageorgiou, 2001). Currently, several commercial traffic simulation models are available, and even more mathematical models have been developed by researchers all over the world (Van Wageningen-Kessels, 2013). However, several questions are raised about the level of proximity of these models to reality and its representation. In this context, an effective calibration and validation process is deemed mandatory for any simulation model, so as to ensure its credibility and validity in performing real-world simulations, by capturing realistic distribution for all possible traffic conditions (Henclewood *et al.*, 2017). However, the calibration and validation, especially of second-order macroscopic traffic flow models, constitutes a difficult task, as the assignment of appropriate values to the unknown model parameters is a challenging problem, because of the highly non-linear nature of the model

equations. As a matter of fact, relatively few calibration results for such macroscopic traffic flow models have been reported so far (Ngoduy & Maher, 2012). Hence, this thesis aims to commence a promising calibration process for establishing accurate and robust traffic flow simulations.

Over the past few decades, as the volume of transport has grown significantly, in contrast to the construction of transportation infrastructure, traffic congestion has become remarkably worse and more widespread in many countries (Papageorgiou *et al.*, 2003). Concurrently, many efforts have been made aiming to investigate the formation and diffusion of traffic flow instabilities; it is well known that even small perturbations resulting from the response of drivers to a stimulus can lead to the formation of congestion and traffic jams. In many occasions these emergent traffic jams could become a serious problem rather than a small inconvenience, deteriorating the overall traffic performance, increasing fuel consumption, increasing air pollution, as well as leading to severe infrastructure underutilization (Jiang *et al.*, 2017). Moreover, such traffic jams are usually associated with traffic flow instabilities, including stop-and-go driving conditions, which, under congested states, can grow and travel against traffic direction (Ngoduy, 2012a). The application of new technologies in the field of VACS, is expected to provide additional tools for the remedy of the aforementioned traffic flow problems, reducing the adverse impacts of traffic flow instabilities through the selection of suitable operating parameters.

1.2 Objectives and Approach

The aim of the present research is twofold. Firstly, it attempts to describe the development and implementation of a calibration and evaluation methodology, which is based on an optimization procedure, utilizing a parallel (synchronous or asynchronous), metamodel-assisted DE algorithm. The proposed methodology is applied for the calibration of the second-order macroscopic GKT model, as well as for the calibration of an extended version of the model, able to deal with multi-lane traffic. The model was numerically approximated by an accurate and robust high-resolution Finite-Volume (FV) relaxation scheme, where the nonlinear equations were first transformed to a semi-linear diagonalizable problem, with linear characteristic variables and stiff source terms, and then discretized using a higher-order weighted essentially non-oscillatory (WENO) scheme. For the evaluation of the proposed optimization procedure, this was employed for the calibration of the numerically discretized GKT model's parameters, using real traffic data from two different motorway networks; a motorway stretch in the U.K., where severe traffic congestion is created due to high on-ramp flows during the morning peak periods, and a freeway stretch in Greece, where recurrent congestion is triggered by a saturated off-ramp during the morning peak hours. For further increasing the computational efficiency of the utilized DE algorithm (on top of its parallelization), it was combined with two Artificial Neural Networks (ANNs), a multi-layer perceptron (MLP) and a radial basis functions network (RBFN), which serve as surrogate models and accelerate the convergence of the optimization procedure. Moreover, the proposed procedure was used to calibrate the well-known macroscopic second-order METANET model, for the aforementioned motorway stretch in the U.K., and compare the corresponding results to those of the recently developed second-order traffic flow model. Finally, both GKT and METANET models are validated against different traffic flow

conditions (than those used for their calibration), and compared regarding their accuracy in representing the prevailing traffic conditions.

The second objective of this dissertation refers to the investigation of the qualitative properties of the developed ACC and CACC models and the derivation of proper stability conditions, with respect to both small and large perturbations around the equilibrium state. To this end, the linear stability method is first applied, which refers to linear Taylor approximations, used throughout the analysis, in order to study the influences that small introduced perturbations induce to the macroscopic characteristics of ACC and CACC traffic flow. Linear stability analysis is a widely established approach to estimate the stability performance of the systems controlling the traffic flow, as it provides a valuable insight into the general behaviour and performance of the system (Ngoduy, 2012a). Furthermore, a non-linear stability analysis of the proposed macroscopic models for ACC and CACC traffic is performed, as it allows for a more accurate examination of the global stability conditions, under which a large perturbation travels against the traffic flow. Thus, a nonlinear stability criterion is derived, using a wavefront expansion method under large perturbations, which enables the investigation of the shock wave propagation properties of the developed ACC and CACC macroscopic model. Moreover, numerical simulation is additionally conducted to validate the derived non-linear stability conditions for the developed ACC model.

Specifically, considering similar studies available in the literature, the following contributions are introduced in this dissertation:

- The development of a computational procedure, based on a parallel (synchronous or asynchronous), metamodel-assisted DE algorithm, for solving the constrained continuous multi-extremal optimization problem of traffic flow model calibration. The proposed procedure is evaluated with respect to its efficiency, accuracy, and robustness for the automated calibration of different second-order traffic flow models.

- The implementation of the proposed computational procedure for the calibration of the numerically approximated single-lane GKT model via a high-resolution finite volume relaxation scheme. Additionally, the validation of the model takes place to assess its accuracy in the reproduction of congestion created at freeways close to on/off-ramps.

- The implementation and testing of the proposed computational procedure for the calibration of the multi-lane extension of the GKT model, which includes a large number of calibration parameters, with the specific hi-order discretization scheme. The ability of the proposed computational procedure to calibrate a large number of parameters is demonstrated, while the robustness of the calibration procedure is confirmed through the validation of the model in different traffic flow conditions.

- The evaluation and comparison of the synchronous and asynchronous versions of the developed parallel, metamodel-assisted DE algorithm (in the test problem of the GKT traffic flow model calibration), in order to demonstrate which one of them is best suited for the problem at hand, in terms of computational efficiency and quality of the optimal solution.

- The application of the proposed computational procedure for the calibration of an alternative traffic flow model, namely the METANET, and the comparison of the produced calibration and validation results with those produced for the GKT second-order traffic flow model.

- The linear stability analysis and the derivation of the corresponding stability conditions for the ACC/CACC extensions of the GKT model, to investigate the effects of the incorporated ACC and CACC characteristics on the stabilization of the traffic flow, under small perturbations around the equilibrium state.

- The nonlinear stability analysis and the derivation of the corresponding stability conditions for the ACC/CACC extensions of the GKT model, to investigate the effects of the incorporated ACC and CACC characteristics on the stabilization of the traffic flow, under large perturbations around the equilibrium state.

- The investigation of the theoretical findings of the previous linear and nonlinear stability analyses, using appropriate numerical simulations.

1.3 Thesis Outline

The thesis consists of two major parts, organized in a series of self-contained chapters. In Part I, the computational methodology, developed for the calibration and validation of macroscopic traffic flow models, will be presented. Part II, contains the linear and nonlinear stability analysis of the ACC/CACC extensions of the GKT second-order macroscopic traffic flow model and the numerical investigation of the findings of the corresponding analyses.

This first chapter introduces the reader to the importance of the topic being studied and presents the motivation and the objectives of this thesis. The structure of the rest of the thesis is as follows: Chapter 2 presents some prerequisite notions and a state-of-the-art of traffic flow modelling, with emphasis on macroscopic traffic flow models. Chapter 3 presents a full description of the major elements composing the proposed numerical optimization procedure and presents the numerically approximated GKT model via a high-resolution finite volume relaxation scheme; this is later employed and evaluated, regarding the representation of traffic conditions at congested freeway on/off-ramps areas. A brief description of the well-known METANET model, which is compared with the GKT model, regarding the proposed optimization scheme, is also included. Chapter 4 contains the calibration and validation results of the proposed optimization method, including qualitative and quantitative comparisons of the obtained results for the GKT model, using real traffic data for two particular freeway stretches, as well as for the METANET model. In Chapters 5 and 6 the two macroscopic approaches reflecting ACC and CACC traffic dynamics in the GKT model are analysed; a linear and a nonlinear method are utilized to analytically derive the influencing conditions to the stability of traffic flow based on the developed models. Numerical study to qualitatively support the analytical findings is also involved. Finally, Chapter 7 contains some conclusions and information on ongoing and future work.

1.4 Publications Related to this Work

The research findings of this dissertation have contributed to the following publications:

Journal Publications

1. Strofylas G.A., Porfyri, K.N., Nikolos, I.K., Delis, A.I., Papageorgiou, M. (2018), "Using Synchronous and Asynchronous Parallel Differential Evolution for Calibrating a Second-order Traffic Flow Model", Advances in Engineering Software, 125, pp. 1-18.
2. Porfyri, K.N., Nikolos, I.K., Delis, A.I., Papageorgiou, M., "Calibration and validation of the GKT and METANET second-order traffic flow models using a metamodel-assisted parallel Differential Evolution algorithm", (under preparation).
3. Porfyri, K.N., Nikolos, I.K., Delis, A.I., Papageorgiou, M., "Stability Analysis of a Macroscopic Traffic Flow Model with Adaptive and Cooperative Adaptive Cruise Control Systems", (under preparation).

Publications in Conference Proceedings

1. Ntousakis, I.A., Porfyri, K., Nikolos, I.K., Papageorgiou, M., "Assessing the impact of a cooperative merging system on highway traffic using a microscopic flow simulator", Proceedings of the ASME 2014 International Mechanical Engineering Conference & Exposition, IMECE2014, Nov. 14-20, Montreal, Quebec, Canada, Paper No. IMECE2014-39850.
2. Porfyri, K.N., Nikolos, I.K., Delis, A.I., Papageorgiou, M. (2015), "Stability analysis of a macroscopic traffic flow model for adaptive cruise control systems", Proceedings of the ASME 2015 International Mechanical Engineering Conference & Exposition, IMECE2015, Nov. 13-19, Houston, Texas, USA, Paper No. IMECE2015-50977.
3. Porfyri, K.N., Nikolos, I.K, Delis, A.I., Papageorgiou, M. (2016), "Nonlinear stability analysis of a macroscopic traffic flow model for Adaptive Cruise Control systems", Proceedings of the ASME 2016 International Mechanical Engineering Conference & Exposition, IMECE2016, Nov. 11-17, Phoenix, Arizona, USA, Paper No. IMECE2016-66470.
4. Porfyri, K.N., Nikolos, I.K., Delis, A.I., Papageorgiou, M. (2016), "Calibration of a second-order traffic flow model using a metamodel-assisted Differential Evolution algorithm", Proceedings of the International IEEE Conference on Intelligent Transportation Systems (ITSC 2016), Rio de Janeiro, Brazil, November 1-4.
5. Porfyri, K.N., Delis, A.I., Nikolos, I.K., Papageorgiou, M. (2017), "Calibration and validation of a macroscopic multi-lane traffic flow model using a differential evolution algorithm", in Proceedings of the 96th Annual Meeting of the Transportation Research Board (TRB), Washington, D.C., January 8-12 (17-01340).
6. Strofylas G.A., Porfyri, K.N., Nikolos, I.K., Delis, A.I., Papageorgiou, M. (2017), "Calibrating a Traffic Flow Model with Parallel Differential Evolution", Proceedings of the Fifth International Conference on Parallel, Distributed, Grid and Cloud Computing for Engineering, P. Ivanyi, B.H.V. Topping and G. Varady (Editors), Civil-Comp Press, Stirlingshire, Scotland, 2017.

Part I

Macroscopic Traffic Flow Models Calibration and Validation

Chapter 2: State-of-the-art of Vehicular Traffic Flow Modelling

2.1 Introduction

Vehicular traffic flow modelling is rapidly growing, mainly due to the rising need for more efficient usage of existing traffic infrastructures and for the optimal design of new ones. The constantly increasing economic and environmental cost of traffic congestion and its influence on the quality of life, put additional pressure on the development of novel and accurate traffic simulation models. Such traffic flow models may be used for traffic surveillance and monitoring, as well as for the development and testing of traffic control strategies and other operational tools (Kotsialos & Papageorgiou, 2001). Thus, to effectively manage and control traffic flow in order to improve mobility, appropriate traffic models have been developed to simulate and forecast traffic flow states; for the time being, at least 100 traffic flow models have been studied, which are broadly classified into microscopic, mesoscopic and macroscopic ones (Wagner, 2010). The objective of this chapter is to present an overview of the most important developments in traffic flow modelling at two fundamentals levels: the microscopic and the macroscopic one (including the successful gas kinetic approaches), focusing on the most popular macroscopic traffic flow models.

In general, traffic simulation models can be roughly divided according to the level of detail they provide. Specifically, microscopic traffic flow models capture traffic dynamics through highly detailed representations of individual vehicles. Moreover, the use of microscopic models is widely spread among researchers and engineers due to their properties, such as their versatility, the included visual interfaces and the visualization of the actual vehicle movement, their ability to model different vehicle and driver characteristics, and the use of actual road geometries. Microscopic simulation models are often used in evaluating congested intersections (Messer, 1998), weaving sections (Stewart *et al.*, 1996), freeway bottlenecks (Halkias *et al.*, 2007), merging and lane changing (Hidas, 2002), among others. On the other hand, macroscopic approaches capture traffic dynamics in lesser detail, by using aggregated relationships and variables, such as flow, density, and mean speed. It is worth noting that macroscopic models describe traffic flow as a continuum flow and are derived in proportion to continuum models for compressible fluid. The application of macroscopic simulation models is addressed at large-scale networks (Kotsialos *et al.*, 2002; Carlson *et al.*, 2010) or real time traffic control in order to reduce congestion and improve mobility (Hegyi et al., 2005a, 2005b; Lu et al., 2010). Finally, the mesoscopic models use a medium level of detail, combining the accuracy of the microscopic and the computational efficiency of the macroscopic approaches into a hybrid model. The most successful among these are based on the gas-kinetic model, which is used to derive the macroscopic models based on the method of moments (Helbing, 1997a; Hoogendoorn, 1999).

The decision on which scale of models, i.e. microscopic or macroscopic (including the gas kinetic models) is the correct one to formulate traffic flow problems, has troubled many traffic engineers over the last decades. From the state-of-the-art review, the substantial advantages and disadvantages of the two different categories of traffic flow models are briefly resumed below. Primarily, microscopic models require a large number of parameters

compared to macroscopic models, which frequently are not easy to observe and measure. So, in general, microscopic models deemed more demanding than macroscopic ones, requiring greater effort for the calibration and validation procedures. Moreover, despite their significant improvement over the last years, disadvantages still exist. For example, unnatural lane changing and car merging in on-ramps has been observed, which asks for more attention by the research teams involved in their development (Hueper *et al.*, 2009; Van Wageningen-Kessels, 2013).

On the other hand, the lower complexity of macroscopic models makes them more suitable for studying large-scale problems. Furthermore, some of the main advantages of the macroscopic models are their numerical efficiency (compared to microscopic ones), their good agreement with empirical data, their suitability for analytical investigations, the simple treatment of inflows (contrary to microscopic models), and the allowance to simulate multi-lane flows by effective one-lane models. Nevertheless, the microscopic simulation models' attribute to recognize in detail the behavior of each vehicle, enables more accurate estimation of individual vehicles' response under realistic traffic conditions, such as the congestion propagation and dissipation (Van Wageningen-Kessels, 2013).

The rest of this chapter is structured as follows: Section 2.2 presents an overview of the most important developments of microscopic traffic flow models. Section 2.3 discusses the evolution of macroscopic traffic flow models over the last few decades. Section 2.4 introduces the reader to calibration process of traffic flow models.

2.2 Microscopic Traffic Flow Models

Microscopic traffic flow models are used to describe the motion of each individual level and they were primarily developed in the '50s, after the pioneering works on car-following theory by Reuschel, 1950 and Pipes, 1953, see Figure 2.1. In general, microscopic models can be distinguished in the following two major categories:

- *Continuous Space and Time Models* use ordinary or delay-differential equations and, consequently, the variables vary continuously in space and time. One of the most prominent examples of this approach is the car-following models that are based on the assumption that drivers follow their leader and adjust their behavior according to the conditions in front (Treiber & Kesting, 2013).

- *Discrete Time and Discrete Space - Cellular Automata (CA) Models* describe traffic dynamics in a completely discrete way by using (generally small) integers; where space is subdivided into cells and time into time steps (Figure 2.1). The first CA model has been proposed in (Cremer & Ludwig, 1986).

In microscopic traffic flow models, vehicles are numbered to indicate their order: n denotes the vehicle under consideration (subject vehicle), $n-1$ denotes its leader, $n+1$ its follower etc. The behavior of each individual vehicle is modeled in terms of the position of the front of the vehicle x_n, velocity $v_n = \frac{dx_n}{dt}$ and acceleration $a_n = \frac{dv_n}{dt} = \frac{dx_n{}^2}{dt^2}$ (Van Wageningen-Kessels, 2013). In the remainder of this section, some examples of models for each of the above categories will be discussed, providing some insight into mechanisms of different microscopic modelling approaches.

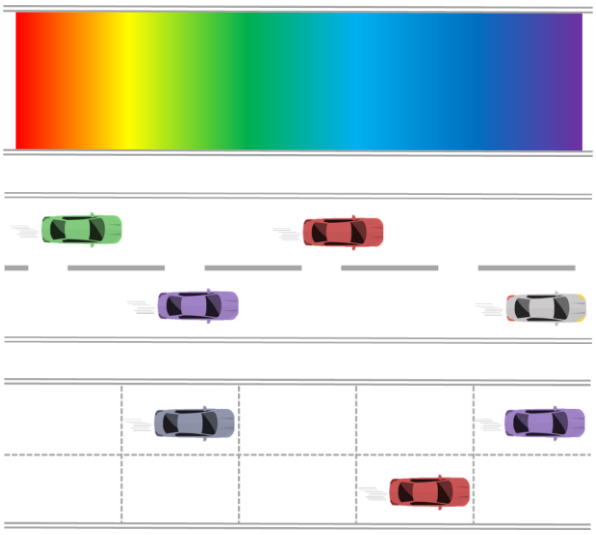

FIGURE 2.1: *Illustration of different traffic modelling approaches: A snapshot of a road section at time* t_o *is either characterized by macroscopic traffic flow quantities, such as average velocity* $u(x, t_o)$*, traffic density* $\rho(x, t_o)$ *or flow* $q(x, t_o)$*, or, microscopically, by the positions* $x_a(t_o)$ *of single driver-vehicle units* a*. For CA, the road is divided into cells, which can be either empty or occupied by one vehicle maximum.*

2.2.1 Car-following models

Several theories have been proposed in the literature since the '50s to model car-following behavior that can be further divided into safe-distance models, stimulus response models and action point models.

Safe-distance models

Safe-distance or collision avoidance models try to simply describe the dynamics of the following vehicle in relation to the leading one, by adapting their velocity to maintain a safe distance to avoid collision. In this respect, a very simple model is Pipes' rule (Pipes, 1953), according to which the position of the leader is expressed as a function of its follower formulated by

$$x_{n-1} = x_n + \mathrm{S} + \mathrm{T}v_n + l_{n-1} \tag{2.1}$$

with S being the distance between the two successive vehicles at standstill, T the minimum time headway and l_{n-1} the length of the leading vehicle; $\mathrm{T}v_n$ is interpreted by Pipes as the "legal distance" between the two vehicles.

A similar approach was proposed by Forbes *et al.*, 1958, while Kometani & Sasaki, 1961, tried to improve the traffic dynamic theory of Pipes by deriving a new car-following model based on the basic Newtonian equations of motion. More specifically, it was assumed that the driver seeks to maintain a safe following distance behind the leading vehicle, even if the predecessor were to act "unpredictably" (e.g., slows-down abruptly). Furthermore, they replaced the distance between the two successive vehicles at standstill, S, in Pipes' model with

a velocity-dependent term and introduced reaction time τ (time delay). Through their study, they established the basic concept of the collision avoidance model in car-following situations. The mathematical formulation of the model is given as:

$$\Delta x(t-\tau) = \alpha v_{n-1}^2(t-T) + \beta_1 v_n^2(t) + \beta v_n + b_0\,, \tag{2.2}$$

where Δx is the relative distance between vehicle n and $n-1$, τ is the reaction time and α, β_1, β and b_0 are constants to be calibrated.

The next major development of safe-distance models was made by Gipps, 1981, who configured the reaction of the following vehicle based on the supposition that each driver sets limitations to their desired braking and acceleration rates. These limitations allow the model to estimate a safe speed for the following vehicle in order that it can come to a safe stop if the preceding vehicle stops abruptly. Gipps' model has the following form:

$$v_n(t+\tau) = min\left\{ v_n(t) + 2.5a_{max}\tau\left(1-\frac{v_n(t)}{v_{max}}\right)\sqrt{0.25-\frac{v_n(t)}{v_{max}}}\,, \right. \tag{2.3}$$
$$\left. a_{min}\tau + \sqrt{a_{min}^2\tau^2 - a_{min}\left(2\left(x_{n-1}(t)-x_n(t)-s_{jam}\right) - v_n(t)\tau - \frac{v_{n-1}(t)^2}{b}\right)}\right\},$$

where a_{max} denotes the maximum acceleration, a_{min} the maximum deceleration (minimum deceleration), v_{max} the desired (maximum) velocity, τ the reaction time and s_{jam} the jam spacing (front-to-front, or equivalently rear-to-rear, distance between two vehicles at standstill). Another simple safe-distance model with delay was proposed by Newell, 1961 and a second one a few years later by Newell, 2002.

Stimulus-response models

The second class of car-following models involves a stimulus–response notion, based on the supposition that the drivers of the following vehicle attempt to adapt to the behavior of the vehicle ahead. This car-following procedure is based on the following principle

$$Response(t+\tau) = \text{Sensitivity} \times \text{Stimulus}(t)\,, \tag{2.4}$$

and can be interpreted as that the following vehicle's driver's action (response) is proportional to the magnitude of the stimulus created by the leading vehicles' behavior; the response is the acceleration or deceleration of the following vehicle, delayed by an overall reaction time τ.

A well-known application of stimulus-response models in traffic analysis is the car-following approach by Chandler *et al.*, 1958, which is based on the intuitive hypothesis that the driver's response (acceleration or deceleration) is proportional to the relative speed between the leader and the follower, as shown below

$$a_n(t+\tau) = \gamma\left(v_{n-1}(t) - v_n(t)\right)\,, \tag{2.5}$$

or equivalently

$$a_n(t) = \gamma\left(v_{n-1}(t-\tau) - v_n(t-\tau)\right)\,, \tag{2.6}$$

where γ denotes the driver's sensitivity; the receding rate $v_{n-1}(t-\tau) - v_n(t-\tau)$ is considered as the stimulus, the acceleration $a_n(t)$ as the response, hence the name stimulus-response

model. The stimulus-response concept was also used in the car-following model by Herman *et al.*, 1959 and Helly, 1961. Moreover, Gazis *et al.*, 1961 proposed the following expression for driver's sensitivity γ, consolidating the now famous GHR-model (named after the authors Gazis, Herman, & Rothery)

$$\gamma = c\frac{\left(v_{n-1}(t)\right)^{c_1}}{\left(x_{n-1}(t-\tau)-x_n(t-\tau)\right)^{c_2}}, \tag{2.7}$$

where c is a sensitivity parameter and c_1 and c_2 are parameters used to fit the model to the data.

More recently, a new model called Optimal Velocity Model (OVM) was developed by Bando *et al.*, 1995, introducing an optimal velocity function that allows the following vehicle to adjust its speed towards the optimal one, which is a function of the headway. The governing equations are as follows

$$a_n(t) = k\left(v_{opt}\left(\Delta x_n(t)\right) - v_n(t)\right), \tag{2.8}$$

$$v_{opt}(\Delta x) = v_{max}(tanh(s-c_1)+c_2), \tag{2.9}$$

with k the sensitivity parameter, Δx_n the spacing with respect to the leader ($\Delta x_n = x_{n-1} - x_n$) and c_1 and c_2 the parameters of the optimal velocity function $v_{opt}(\Delta x)$ such that $tanh\left(s_{jam}-c_1\right)+c_2 = 0$. Bando *et al.*, 1998 extended their model by introducing the explicit delay time τ in order to construct realistic models of traffic flow: in the right-hand side of equation (2.8) t is replaced by $t-\tau$.

Finally, the Intelligent Driver Model (IDM) by Treiber *et al.*, 2000 is one of the most popular stimulus-response models that have emerged over the last years. The IDM model was developed to better reproduce the various traffic situations realized by the following continuous acceleration function

$$a = a_{max} = \left(1 - \left(\frac{v}{v_{max}}\right)^{\delta} - \left(\frac{s^*(v,\Delta v)}{s}\right)^2\right), \tag{2.10}$$

where a_{max} denotes the maximum acceleration, v_{max} the maximum velocity, δ the acceleration exponent and $s^*(v,\ \Delta v)$ the desired space gap function. According to equation (2.10) the acceleration in the IDM model consists of two parts, one comparing the current velocity v to the maximum (desired) velocity v_{max}, and another comparing the current distance s to the desired distance s^*, given by Treiber & Kesting, 2013

$$s^*(v,\Delta v) = s_{jam} + max\left(0, Tv + \frac{v\,\Delta v}{2\sqrt{a_{max}a_{min}}}\right), \tag{2.11}$$

with a_{min} denoting the minimum acceleration, s_{jam} the jam spacing and T the minimum time headway.

Action point models

The third class of car-following models consists of action point or psycho-spacing models, first introduced by Wiedemann, 1974. In general, the psycho-spacing car-following models follow thresholds where a driver makes a change in their behavior at an action point.

The basic behavioral rules of such so-called action point models are:

- At large spacings, the behavior of the following vehicle is not influenced by that of other vehicles.

- At small spacings, the behavior of the following vehicle is only influenced by that of other vehicles if changes in relative velocity and headway are large enough to be perceived.

2.2.2 Cellular Automata (CA) Models

To conclude this section, a special class of discrete microsimulation models is discussed; the well-known CA models, with the approach by Nagel & Schreckenberg, 1992, being the most famous one. In the cellular automata models, the space is split into homogeneous cells of equal length, and time is divided into time steps of equal duration. These cells can be either empty or occupied by one vehicle at maximum, while each vehicle has an integral velocity with values ranging from zero to v_{max}, see Figure 2.1.

One update of the system consists of the following consecutive steps, which are performed in parallel for all the vehicles

- *Acceleration*: If the vehicle has a smaller velocity than its maximum, v_{max}, then accelerates: $\tilde{v} \rightarrow min(\tilde{v}+1, \tilde{v}_{max})$.

- *Deceleration*: If the headway to the preceding vehicle is too small, then the vehicle will decelerate: $\tilde{v} \rightarrow min(\tilde{v}, \tilde{s}_{jam}-1)$.

- *Dawdling*: Given a probability π, the velocity of a vehicle decreases spontaneously: $\tilde{v} \rightarrow max(\tilde{v}-1, 0)$ with probability π.

- *Moving*: $\tilde{x} \rightarrow \tilde{x}+\tilde{v}$,

where $\tilde{v}$ is the normalized vehicle velocity in number of cells per time step, $\tilde{v}_{max}$ the normalized maximum velocity, $\tilde{s}_{jam}$ the normalized jam spacing in number of cells, $\tilde{x}$ the cell number and π the deceleration probability.

2.3 Macroscopic Traffic Flow Models

Macroscopic traffic flow models, which describe traffic behavior in terms of aggregated traffic flow variables, can be classified into first-, second-, or higher-order models in the sense of the

number of partial differential equations they involve, see Figure 2.1. First-order models, originally developed by the pioneers Lighthill–Whitham–Richards, 1956 (LWR model), (Lighthill & Whitham, 1955; Richards, 1956) adopt the mass conservation equation and the fundamental diagram to describe the evolution of traffic density. However, although the approaches of this class are simple, reproducing qualitatively a number of real traffic phenomena, such as the formation of shock waves, they suffer from several limitations and they have proved to be inadequate for describing complicated traffic flow dynamics. More specifically, these models do not allow for fluctuations of velocity around the so-called equilibrium fundamental diagram and they have limited capability to replicate certain real dynamic phenomena observed on freeways, such as the hysteresis, the capacity drop and relaxation, the stop-and-go waves at bottlenecks, as well as the spontaneous congestion or platoon diffusion. To overcome the shortcomings of the LWR-type models a lot of research has been devoted to develop second- or higher-order macroscopic models, which incorporate (at least) the momentum equation, in addition to the continuity one, to describe the evolution of flow/speed dynamics. Although such models, with the Payne model (Payne, 1971) being one of the most popular among them, have the potential to capture the aforementioned non-linear wave phenomena with higher accuracy, when compared to real-time traffic data, they use an increased number of parameters to describe the aggregate infrastructure-vehicle-driver behaviors.

In this section, an elaborate description of the most popular models of the two major branches of macroscopic models is presented, namely first-order models (Section 2.3.2) and higher-order models (Section 2.3.3). Furthermore, in Section 2.3.1 the conservation equation that governs all macroscopic traffic flow models is discussed.

2.3.1 Conservation Equation of Macroscopic Traffic Flow Models

All macroscopic traffic flow models are governed by one fundamental equation that is based on the conservation of vehicles on the road. Assuming that the vehicles are moving from left to right, the conservation of vehicles equation, also known as the continuity equation, can be written as (Gerlough & Huber, 1976; Kühne & Michalopoulos, 1997):

$$\frac{\partial \rho(x,t)}{\partial t} + \frac{\partial q(x,t)}{\partial x} = 0\,, \tag{2.12}$$

where x $[km]$ denotes the spatial coordinate in the direction of traffic flow, t $[h]$ is the time, ρ $[veh/km]$ is the density and q $[veh/h]$ denotes the flow. This equation formally represents the assumption that between two counting stations in a motorway section without entrances and exits, the traffic flow is always conserved; in other words, vehicles are not created or destroyed. This equation is complemented by the fundamental relationship

$$q(x,t) = \rho(x,t)v(x,t) \tag{2.13}$$

with v $[km/h]$ being the mean speed. However, equations (2.12) and (2.13) constitute a system of two independent equations and three unknown variables. Consequently, to solve this system an additional equation or an assumption is needed, which by extension can lead to various types of continuum traffic flow models. For example, the equation which is based on the assumption that flow is a function of density ($q = q(\rho)$) or equivalently that speed is also a function of density ($v = v(\rho)$) leads to the first-order macroscopic traffic flow models, while

the high-order continuous models are supplemented by momentum equations. In the ensuing of this section, several model specifications are reviewed.

2.3.2 First-order Models

Lighthill and Whitham (Lighthill & Whitham, 1955) and, independently, Richards (Richards, 1956) have taken the first major step towards the development of the most popular first-order model so far, commonly referred to as the LWR model. The LWR model employs the conservation equation (2.12) and is supplemented by the fundamental equation of traffic flow (equation (2.13)) and the following relationship between the mean speed and the traffic density under equilibrium conditions (known as the fundamental diagram):

$$v(x,t) = V^e[\rho(x,t)]\,. \tag{2.14}$$

Hence, the non-linear first-order partial differential equation that results by substituting equation (2.13) and (2.14) into conservation equation (2.12) has the following form:

$$\frac{\partial \rho(x,t)}{\partial t} + \frac{\partial(\rho(x,t)V^e[\rho(x,t)])}{\partial x} = 0\,. \tag{2.15}$$

Because of its simplicity, the LWR model has received a lot of attention and critique. The main drawback of the model lies on the fact that vehicles are assumed to attain their desired speed (represented by the fundamental diagram) instantaneously after a change in the traffic state, implying infinite acceleration and deceleration. However, as pointed out by Liu *et al.*, 1998, since the speed in this model is determined by the equilibrium speed–density relationship (equation (2.14)), no fluctuations of velocity around the equilibrium fundamental diagram are allowed. Thus, the model is not suitable for the description of non-equilibrium traffic flow dynamics occurring at on-ramp areas, lane-drop areas, or stop-and-go traffic, having as well other unrealistic consequences, such as the lack of hysteresis effects or traffic instabilities. Another deficiency of the LWR model is that the shift from the free flow regime to the congestion one always takes place at the same density and without a decline in the capacity; therefore, the use of the LWR model for designing traffic control strategies is restricted (Papageorgiou, 1998). Several researchers tried to address the above model limitations by variants of the LWR model (see, e.g., Newell, 1965; Daganzo *et al.*, 1997; Lebacque, 2002; Leclercq, 2007).

2.3.3 Higher-order Models

Second-order or higher-order traffic flow models incorporate one (or more) Partial Differential Equation(s) (PDE(s)), in addition to the continuity one (equation (2.12)), to describe the evolution of flow/speed dynamics. In this section, the most pioneering approaches of high-order traffic flow models are presented.

The Payne-Witham (PW) model (1974)

The Payne–Whitham (PW) model, proposed independently in (Payne, 1971) and in (Whitham, 1974), is one of the first non-equilibrium traffic flow models derived from a simple stimulus-

response car-following model by means of Taylor's expansion. Its acceleration equation (momentum equation) has the following form

$$\frac{\partial(\rho u)}{\partial t} + \frac{\partial\left(\rho u^2 + P(\rho)\right)}{\partial x} = \rho\left(\frac{V^e(\rho) - u}{\tau}\right), \tag{2.16}$$

where $P(\rho)$ is the pressure like term of flow, given as $P(\rho) = c_0^2\rho$ with c_0 the anticipation parameter that reflects how the drivers react to traffic density. Further, the model includes a relaxation term that keeps speed concentration in equilibrium (the drivers tend to adapt their speed to the equilibrium speed-density relation $V^e(\rho)$), with $V^e(\rho)$ being the equilibrium speed described by the fundamental relation and τ being a speed relaxation time.

Although the PW model improved the deficiencies of the LWR model, allowing fluctuations of speed around the equilibrium values and taking into account the vehicles' acceleration capabilities and the drivers' reaction time, it has received much critique as it seems to fail in some fundamental properties of traffic flows (Del Castillo *et al.*, 1994; Daganzo, 1995a). The main drawback of the model that Daganzo (Daganzo, 1995a) has been concerned about, is that the anisotropic nature of traffic is not preserved, implying that vehicles do not only react to the downstream traffic conditions but also on upstream traffic conditions. Moreover, the PW model allows slower vehicles to be affected by the faster ones and there can also be cases (e.g. tail of congested regions) of negative speeds and flows.

Over the years, a number of extensions-modifications of the momentum equation of the PW model have been proposed, in order to improve the models' deficiencies. In particular, writing the momentum equation (2.16) in its most general form

$$\underbrace{\frac{\partial u}{\partial t} + u\frac{\partial u}{\partial x}}_{acceleration} = \underbrace{\frac{V^e(\rho) - u}{\tau}}_{relaxation} - \underbrace{\frac{1}{\rho}\frac{\partial P}{\partial x}}_{anticipation} \tag{2.17}$$

and using different settings for the traffic pressure P, the relaxation time τ and the equilibrium speed-density relation $V^e(\rho)$, the following macroscopic traffic flow models arise:

- **Phillips' model** (Phillips, 1979) is obtained using a density dependent relaxation time $\tau = \tau(\rho)$ and approximating the traffic pressure using $P(\rho) = \rho\theta(\rho)$, with $\theta(\rho)$ being the velocity variance; this is estimated as $\theta(\rho) = \theta_0(1 - \rho/\rho_{max})$ with ρ_{max} being the maximum traffic density.

- **Papageorgiou's model** (Papageorgiou *et al.*, 1990) is derived for $P(\rho) = -V^e(\rho)/2\tau$ and constant relaxation time τ. Moreover, additional terms were introduced in order to consider merging and lane-changing phenomena, namely the $-\delta vr/\rho$ and the $-\varphi\Delta\lambda\rho u^2/\rho_{cr}$ term; δ and φ, being model parameters, r is the incoming on-ramp flow, $\Delta\lambda$ are the number of lanes being dropped and ρ_{cr} is the critical density.

- **Kerner–Konhäuser (KK) model** (Kerner & Konhäuser, 1993, 1994) is obtained using $P(\rho) = \rho\theta(\rho) - \eta\frac{\partial u}{\partial x}$, with $\theta(\rho) = \theta_0$ being a positive constant and $\eta = \eta_0$ a viscosity coefficient.

- **Zhang's model** (Zhang, 1998) is derived for $P(\rho) = \frac{1}{3}\rho^3 V^{e\prime 2}(\rho)$ with $V^{e\prime}(\rho) = \frac{dV^e(\rho)}{d\rho}$. This approach ensures that traffic disturbances are always propagated against the traffic stream.

Treiber et al. model (1999)

A recent contribution to the field of macroscopic flow models is made by (Treiber *et al.*, 1999). The authors proposed a model based on gas-kinetic principles, the well-known GKT model that was derived from a microscopic model of vehicles' dynamics. The resulting speed equation is given as

$$\frac{\partial u}{\partial t} + u\frac{\partial u}{\partial x} = \rho\left(\frac{V^e(\rho, u, \rho_\alpha, u_\alpha) - u}{\tau}\right) - \frac{1}{\rho}\frac{\partial P}{\partial x}. \tag{2.18}$$

In the GKT model, the "traffic pressure" P is given by $P = \rho\theta = \rho A(\rho)u^2$, with $\rho A(\rho)$ a density-dependent function, while the equilibrium velocity, towards which the average velocity relaxes in the real traffic state, is defined as

$$V^e(\rho, u, \rho_\alpha, u_\alpha) = u_{max}\left[1 - \frac{\theta + \theta_\alpha}{2A\rho_{max}}\left(\frac{\rho_\alpha T}{1 - \rho_\alpha/\rho_{max}}\right)^2 B(\Delta u)\right], \tag{2.19}$$

where u_{max} is the maximum desired speed, T is the desired time-gap, ρ_{max} is the maximum density, ρ_α and u_α are the density and velocity, respectively, at an advanced "interaction point" and B is the Boltzmann factor. In contrast to other macroscopic models, equation (2.19) depends not only on the local (ρ, u) but also on the non-local traffic state (ρ_α, u_α), thus introducing non-locality. The non-locality has smoothing properties similar to those of a viscosity term, but its effect is forwardly directed and, therefore, more realistic. A detailed description of the GKT models' equations is provided in Chapter 3.

The Aw–Rascle (AR) model and the Aw–Rascle–Zhang (ARZ) model (2000)

In order to remove the defects of the PW and its derivative models, Aw and Rascle (Aw & Rascle, 2000) proposed the involvement of the total derivative of the pressure-like terms in the momentum equation (without relaxation term) that reads as

$$\frac{\partial\big(u + P(\rho)\big)}{\partial t} + u\frac{\partial\big(u + P(\rho)\big)}{\partial x} = 0\,, \tag{2.20}$$

where now the pressure term $P(\rho)$ is a smooth and increasing function of density, given as $P(\rho) = \rho^\gamma, \gamma > 0$.

A model similar to the AR model was proposed in (Zhang, 2002), the so-called Aw–Rascle–Zhang (ARZ) model; the momentum equation that describes speed dynamics is derived from a car-following model and is given as

$$\frac{\partial y}{\partial t} + \frac{\partial P(\rho)}{\partial x} = 0\,, \tag{2.21}$$

where $y = \rho u - \rho V^e(\rho)$ and $P(\rho) = \rho u\big(u - V^e(\rho)\big) = uy$. The variance y in this case can be considered to be the difference between the actual flow ($q = \rho u$) and equilibrium flow ($q^e = \rho V^e$).

2.3.4 Discretization of Continuum Macroscopic Models

All macroscopic traffic flow models presented so far (in Sections 2.3.2 and 2.3.3), are based on conservation of the traffic flow. Mathematically, each of these models originally consist a hyperbolic system of PDEs that describes the time-evolution of traffic density, speed and flow. These partial differential equations cannot be solved analytically; thus, appropriate numerical schemes must be applied before being used in a computer simulation. In general, time is divided into discrete time steps while, depending on the model, also space or other continuous variables are discretized. Subsequently, numerical methods are applied to approximate solutions for conservation laws (approximate the new traffic state at each time step), resulting in a discrete traffic flow model. From an engineering application approach, the ultimate space-time discretized models should be as plain as possible and have nice analytical attributes (e.g. have a precise state-space form, perform continuous and differentiable functions), which would permit simple, as well as transparent computation codes, convenient discretization intervals, brief computation times, as well as direct application of dynamic mathematical methods (e.g. Kalman filtering, optimization, optimal control) (Papageorgiou, 1998; Kotsialos & Papageorgiou, 2001).

To date, several discrete traffic flow models have been derived from continuum ones. Examples are the numerical solutions to the LWR model, namely, the Cell-Transmission Model (CTM) by Daganzo, 1994, 1995b and the discretized approach by Lebacque, 1996, who applied the Godunov-scheme. Moreover, the FREFLO model by Payne, 1979, which is a discretized version of the second order Payne model and the METANET model by Messmer & Papageorgiou, 1990, which is a discretized and enhanced variation of the Payne model, are among the most popular simulation tools. The models of Van Maarseveen, 1982, Kotsialos *et al.*, 1999, Lyrintzis *et al.*, 1994, and Liu *et al.*, 1998, are also some examples of discrete Payne-type models.

2.4 Calibration of Traffic Flow Models

No matter which approach is used, the microscopic or macroscopic one, accurate modelling of traffic flow requires three types of data: model inputs, model parameters and observed outputs. Model inputs involve the demand-side data, for which a traffic simulation is performed. Model parameters involve different types of supply-side parameters used in the traffic simulation, depending on the level of complexity in modelling. This is true for both microscopic and macroscopic models, since they all contain some set of parameters in their structure, whose values represent the particular road network's traffic flow features. The output data observed in the real-world is required in order to compare model outputs and evaluate the accuracy of the models. Macroscopic models call for a relatively small number of parameters, compared to microscopic ones, which results in significantly less demanding and computationally expensive, but by no means trivial, calibration and validation processes and, therefore, in a more versatile model development for real-world applications.

Within this thesis the discrete second-order model METANET and the numerically solved second-order gas-kinetic-based traffic GKT model are tested, validated and compared with respect to their accuracy in the reproduction of congestion created at freeways close to on/off-ramps, using real traffic data from two freeway stretches located in U.K. and Greece. Moreover, the recently developed multi-lane GKT model is validated using real traffic data from a three-lane freeway stretch in the U.K. Both METANET and GKT models are among the most widely used macroscopic traffic flow models and have been utilized by several research groups in order to handle various traffic engineering tasks, such as simulation, optimization, estimation and optimal freeway traffic control. Chapter 3 includes a detailed description of the utilized macroscopic traffic flow models and the calibration procedure, while the calibration and validation results are presented in Chapter 4.

Chapter 3: Calibration of Macroscopic Traffic Flow Models

3.1 Introduction

The rapidly expanding traffic and transportation applications call for efficient and accurate traffic flow models, for assessing their potential impact on environment and community decision-making. As such, accurate traffic flow models are a prerequisite for a number of important tasks in the field of traffic management, including transportation planning, traffic simulation, traffic surveillance and monitoring, incident detection, assessment and planning of road infrastructures, control strategy design as well as the evaluation of transport energy consumption. Currently, several commercial traffic simulation software packages are available, and even more mathematical models have been proposed by research centers and groups all over the world. However, several questions are raised about the level of proximity of these models to reality and its representation. Hence, to ensure the credibility and validity of any model in performing real-world simulations and optimization scenarios, providing simultaneously reliable and reproducible results, the implementation of a calibration and validation procedure is mandatory.

Despite the increasing popularity of macroscopic traffic simulation models, relatively few studies in the literature have addressed, or actually conducted, calibration and validation of such models against real traffic data; most of the research done to date has focused on model and software development. However, as indicated by Papageorgiou, 1998 and Ni *et al.*, 2004, model validation is the ultimate criterion for assessing the extent to which existing or new macroscopic traffic flow models replicate real traffic phenomena, and consequently the usefulness of their development and implementation is a valuable tool for the efficient simulation and optimization of traffic flow for specific transportation infrastructures.

Regarding the calibration of first-order macroscopic traffic flow models, the Fundamental Diagram (FD), which represents a direct mapping from density to traffic flow, plays a vital role. The FD calibration procedure mainly concerns the estimation of the FD parameters of the relevant discrete road sections in order to maximize the model's descriptive power to represent traffic flow characteristics. The most widely deployed model of this order is the CTM by Daganzo, 1994 and detailed calibration methodologies can be found in Muñoz *et al.*, 2004, 2006. Moreover, a comparative study of the first-order CTM and the second-order METANET (Messmer & Papageorgiou, 1990) for a freeway in Greece, based on the deterministic Nelder-Mead algorithm (see, e.g., Nelder & Mead, 1965; Lagarias *et al.*, 1998) has been recently presented by Spiliopoulou *et al.*, 2014.

Within the vast literature of second-order macroscopic traffic flow models, researchers have come up with different employed algorithms to calibrate and validate them against real traffic data. Extensive validation studies of METANET for the modelling of the Paris ring road and the large scale motorway networks around Amsterdam are reported by Papageorgiou *et al.*, 1990, and Kotsialos *et al.*, 1998, 2002, respectively, where the deterministic complex algorithm of Box (Box, 1965) was used for the calibration procedure. The Box algorithm was also used to calibrate the improved Payne's model (Cremer & Papageorgiou, 1981; Sanwal *et al.*, 1996), as well as a proposed macroscopic traffic simulation model (of the so-called ''node

model'' type) by Monamy *et al.*, 2012. An extension of the Nelder–Mead optimization technique was described by Ngoduy *et al.*, 2004, in order to determine the parameters of the considered macroscopic model equations for various numerical schemes. Moreover, the gas-kinetic traffic flow model (Treiber *et al.*, 1999) was validated by Ngoduy & Maher, 2012, on a 5 km section of a motorway in the U.K., using a generic Monte Carlo technique, namely the Cross Entropy Method (CEM) (Boer *et al.*, 2005). A number of derivative free optimization algorithms are evaluated and compared in Spiliopoulou *et al.*, 2015, for the parameter estimation problem of METANET model with respect to the robustness of the proposed model, the required computation time, and the optimum cost function time. A parameter identification algorithm for the METANET model, with a limited number of loop detectors, is discussed by Frejo *et al.*, 2012; the algorithm was tested with real traffic data from a highway in California with satisfactory results. The METANET validation of a U.K. motorway is also described by Poole & Kotsialos, 2012, where the calibration problem was solved by means of a genetic algorithm with a least-squares method.

At this point, it is worth mentioning that there are several works in the literature concerning the development of online calibration methods for macroscopic traffic flow models, where a random walk is introduced to the model parameters, resulting to augmented traffic flow variables and the model parameters being estimated (see, e.g., Wang & Papageorgiou, 2005; Wang *et al.*, 2006; Luspay *et al.*, 2010; Ngoduy, 2011); although such applications have been extensively used for real-time traffic state estimation problems, they are beyond the scope of this thesis. Moreover, despite the fact that this work is devoted to the calibration and validation of macroscopic traffic flow models, it is important to highlight that a great deal of studies have been undertaken by several researchers dedicated to optimization methods for the calibration of microscopic traffic models (Brockfeld *et al.*, 2005; Hoogendoorn & Ossen, 2005; Lee & Ozbay, 2009; Hoogendoorn & Hoogendoorn, 2010).

This thesis puts forward an optimization scheme, based on a parallel, synchronous or asynchronous metamodel-assisted DE algorithm (Storn & Price, 1995, 1997; Price *et al.*, 2005), to determine the optimal parameters of the second-order macroscopic GKT model (Treiber *et al.*, 1999; Helbing *et al.*, 2001; Treiber & Kesting, 2013). This optimization algorithm is used to minimize the relative error between the model prediction and the observed real data. Such a calibration process presents a quite complex problem, since it takes the form of minimizing a cost function with numerous local minima, which traditional gradient-based algorithms usually fail to avoid.

Among the various search and optimization techniques, Evolutionary Algorithms (EAs) have emerged over the past few years as an essential and versatile tool of dealing with demanding high-dimensional real-world optimization problems. EAs are capable of handling non-differentiable, nonlinear and multimodal cost functions, based on the principles of natural selection and evolution. From a population of candidate solutions, each individual is evaluated on the basis of its fitness function, and the best one is selected to proceed to the next generation and evolve through a certain process. However, despite the important contribution of EAs in solving complicated problems, they suffer from a significant drawback; a considerable number of evaluations is needed, which usually calls for significantly increased computation time. In order to overcome this barrier, the use of surrogate models (metamodels), in conjunction with parallel processing, appears to be an efficient approach.

The population-based searching mechanism of EAs makes them eminently suitable for parallelism. In the vast literature, different Parallel Evolutionary Algorithms (PEAs) can be found (Luque & Alba, 2011; Alba *et al.*, 2013) aiming not only to improve the efficiency, but

also to enhance the arithmetic performance, if structured populations are adopted. The different types of parallel EAs can be mainly divided in two categories; panmictic EAs and structured ones (Cantu-Paz, 1999; Alba & Tomassini, 2002). Combinations of the aforementioned categories have been reported in the literature, resulting in hybrid models, such as hierarchical hybrids (Hu & Goodman, 2002; Jong *et al.*, 2004; Oliveira *et al.*, 2004; Acampora *et al.*, 2011). In panmictic EAs, a global parallelization model is usually followed, which utilizes a unique population of candidate solutions, while the selection operation is applied to all members of the population. The whole procedure is tailored by a central processor, which distributes the members of the population to different processors in order to be evaluated in parallel, while the selection step is performed only by the central one sequentially. This model is usually combined with a Master-Slave architecture. Synchronous and asynchronous parallel implementations of panmictic PEAs have been proposed in the literature (Alba & Troya, 1999, 2001). Since synchronous parallel EAs waste a lot of idle time waiting for completion of the longest fitness evaluation, asynchronous evolutions approaches seem like a mandatory step towards computational-time-savings. In general, asynchronous parallel implementations of EAs generate a new solution without waiting for the evaluations of other solutions, unlike the conventional synchronous approaches, which should wait for all evaluations to be completed before continuing with the next generation (Scott & De Jong, 2015a, 2015b).

In general, PEAs mostly use structured populations, following either the island (dEAs) or the cellular model (cEAs) (Cantu-Paz, 1999; Llorà & Garrell, 2001; Li & Kirley, 2002; Alba & Dorronsoro, 2005; Tomassini, 2005). For the parallel implementation, the population is divided into subpopulations called demes, and each one evolves separately on its assigned processor. In dEAs each subpopulation is comprised by many individuals, while in cEAs the subpopulation corresponds to a single individual. The demes exchange individuals with some migration frequency, to ensure the propagation of good solutions. In a dEA the subpopulations are loosely connected to each other, whereas in cEAs every individual can interact only with its neighbours. When implementing the island model, only a small number of subpopulations is used, in opposition to cEAs, where the number of subpopulations is equal to the population size (Cantu-Paz, 1999; Alba & Tomassini, 2002). Hybrid PEAs implementations utilize the multi-population dEA model along with the fine grained cEA model, resulting in better convergence behavior (Hu & Goodman, 2002; Jong *et al.*, 2004; Oliveira *et al.*, 2004; Acampora *et al.*, 2011).

In this thesis, a parallel DE algorithm has been developed, based on the panmictic approach, by using a unique population that is distributed among the processors with a Master-Slave architecture. Separate executable programs perform the evaluation of each individual in the population, while the required data exchange and communication between the processors are achieved by using MPI (Message Passing Interface) library functions. Furthermore, the utilization of two ANNs as surrogate models within the DE algorithm enhances its performance by substituting the computationally time-consuming exact evaluations of the fitness function with low-cost approximations.

The structure of the present chapter is as follows: In Section 3.2 the numerically approximated GKT model (along with its multi-lane extension) via a high-resolution finite volume relaxation scheme, as well as a brief description of the METANET model, are presented. In Section 3.2.3 a full description of the major elements composing the proposed numerical optimization scheme is outlined.

3.2 Selected Macroscopic Traffic Flow Models

3.2.1 GKT Model

In this section, we recall some basic definitions and the differential equations governing the GKT model, according to Treiber *et al.*, 1999, Helbing *et al.*, 2001, Treiber & Kesting, 2013 and Delis *et al.*, 2014, 2015a. Let $\rho(x,t)$, hereafter ρ for short, denoting the traffic density (number of vehicles occupying at unit length), which accounts at location x and time instant t, $u(x,t)$, hereafter u for short, denoting the average speed, while by definition $q = \rho u$ denotes the traffic flow rate (number of vehicles per unit of time). The GKT model can be written in conservation form (balance law) form with source terms, namely the r_{rmp} and h_{rmp} ones, representing traffic flow from on-ramps (or to off-ramps), as well as a traffic relaxation term, with V_e^* being the equilibrium speed as

$$\partial_t \rho + \partial_x(\rho u) = r_{rmp}\,, \tag{3.1}$$

$$\partial_t(\rho u) + \partial_x(\rho u^2 + \theta\rho) = \rho\left(\frac{V_e^*(\rho) - u}{\tau}\right) + h_{rmp}. \tag{3.2}$$

Following from Treiber & Kesting, 2013, the term r_{rmp} on the right-hand side of the continuity equation (3.1) denotes the effective source density that is only active within the merging (diverging) sections with length l_{rmp} and inflow $q_{rmp} > 0$ from (or outflow $q_{rmp} < 0$ to) the ramps, and is determined as

$$r_{rmp}(x,t) = \begin{cases} \dfrac{q_{rmp}(t)}{l_{rmp}} & if\ x\ inside\ the\ merging\ zone, \\ 0 & elsewere. \end{cases} \tag{3.3}$$

Further, the source term h_{rmp} in the momentum dynamics equation (3.2) describes changes in the macroscopic local speed, by assuming that on-ramp vehicles merge to the main road at speed $u_{rmp} <$ u. On the contrary, the drivers considered to leave the main road reduce their speed to u_{rmp} before they diverge to the off-ramp. Hence, this term can be written as

$$h_{rmp}(x,t) = \frac{q \cdot r_{rmp}}{\rho} + \frac{(u_{rmp} - u)|q_{rmp}|}{l_{rmp}}. \tag{3.4}$$

In equation (3.2), θ denotes the pressure-like term, computed as a density-dependent fraction $A(\rho)$ of the squared velocity $\theta = A(\rho)u^2$, where $A(\rho)$ is given by the Fermi function as

$$A(\rho) = A_0 + \delta A\left[1 + \tanh\left(\frac{\rho - \rho_{cr}}{\delta\rho}\right)\right], \tag{3.5}$$

where ρ_{cr} is the critical density, reflecting the boundary for the transition from the free flow to congested traffic state, with A_0 and $A_0 + 2\delta A$ the variance pre-factors between the aforementioned two states, while $\delta\rho$ is the width of the transition region. Typical parameter value ranges for A_0, δA, and $\delta\rho$, along with other typical used model parameters of the GKT model are specified by Treiber *et al.*, 1999, Helbing *et al.*, 2001, Treiber & Kesting, 2013 and Delis *et al.*, 2014, 2015a.

Another advantageous feature of this model is the involved traffic relaxation term that tends to keep the velocity concentration in equilibrium state, with $V_e^* = V_e^*(\rho, u, \rho_\alpha, u_\alpha)$ being the dynamic equilibrium speed, depending not only on the local (ρ, u) but also on the non-local traffic state (ρ_α, u_α). Thus, the dynamic equilibrium speed, towards which the average speed relaxes, is determined as

$$V_e^*(\rho) = u_{max}\left[1 - \frac{\theta + \theta_\alpha}{2A\rho_{max}}\left(\frac{\rho_\alpha T}{1 - \rho_\alpha/\rho_{max}}\right)^2 B(\delta u)\right]. \tag{3.6}$$

According to equation (3.6), the dynamic equilibrium speed is computed as the maximum desired speed, u_{max}, reduced by a braking non-local term, which reflects necessary deceleration maneuvers in traffic flow at the downstream interaction location $x_\alpha = x + \gamma(1/\rho_{max} + T \cdot u)$, with T being the average time-headway, ρ_{max} the maximum density and γ a scale factor. Finally, $B(\delta u)$ is a so-called Boltzmann interaction factor that contains the standard normal distribution and the Gaussian error function, given as

$$B(\delta u) = 2\left[\delta u \frac{e^{-\delta u^2/2}}{\sqrt{2\pi}} + (1 + \delta u^2)\int_{-\infty}^{\delta u} \frac{e^{-y^2/2}}{\sqrt{2\pi}} dy\right]. \tag{3.7}$$

The above monotonically increasing term describes the dependence of the braking interaction on the dimensionless velocity difference $\delta u = (u - u_a)/\sqrt{\theta + \theta_\alpha}$, taking into account the velocity and variance at the actual position x and the interaction point x_α, respectively.

The decisive difference between the GKT model and other macroscopic traffic flow models is its non-local character, which was derived by adopting realistic assumptions of driving behavior. Specifically, it turned out that the non-locality of the braking term in equation (3.6) has similar smoothing attributes as a diffusion or viscosity term, but its effect is more realistic, as it is forwardly directed, which means that vehicles react on density or velocity gradients in front of them. Moreover, in contrast to other macroscopic models, the steady-state (equilibrium) speed-density relation of GKT model, $V^e(\rho)$, is not explicitly given, but it rather results from the steady-state condition of homogeneous traffic.

3.2.1.1 The Multi-lane GKT Model

In the following, the recently developed by Delis *et al.*, 2015b, multi-lane GKT model is briefly presented. In general, continuous models that simulate multi-lane traffic flow dynamics, are based on a nonlinear system of conservation laws, with additional source/sink terms, in order to take into account lane-changes due to vehicle interactions, as well as spontaneous ones. Hence, assuming a highway with N lanes, which are numbered by $l = 1, 2, \dots, N$, the multi-lane GKT model can be written in vector form (for each lane, l), supplied with initial conditions, as follows

$$\begin{aligned} \partial_t \boldsymbol{u}_l + \partial_x \boldsymbol{f}(\boldsymbol{u}_l) &= \boldsymbol{s}(\boldsymbol{u}_l) + \boldsymbol{w}_l(\boldsymbol{u}_1, \dots, \boldsymbol{u}_N)\,, \\ \boldsymbol{u}_l(x, 0) &= \boldsymbol{u}_{l,0}(x)\,, \end{aligned} \tag{3.8}$$

where the functions $\boldsymbol{u}_l$, $\boldsymbol{f}(\boldsymbol{u}_l)$ and $\boldsymbol{s}(\boldsymbol{u}_l) \in \mathbb{R}^2$ with $\boldsymbol{u}_l = [u_l^1, u_l^2]^{\mathrm{T}} = [\rho_l, q_l]^{\mathrm{T}}$, $\boldsymbol{f}(\boldsymbol{u}_l) = [\rho_l u_l,\ \rho_l {u_l}^2 + \theta_l \rho_l]^{\mathrm{T}}$ and $\boldsymbol{s}(\boldsymbol{u}_l) = [r_{rmp,1}, (\rho_l V_{e,l}^* - \rho_l u_l)/\tau + h_{rmp,1}]^{\mathrm{T}}$. The variables ρ_l, u_l, and

q_l are the traffic density, the average speed of vehicles and the traffic flow rate at the l-th lane, for $l = 1, 2, \dots, N$, respectively. Herein, following the definition of the pressure-like term $\theta_l = A(\rho_l){u_l}^2$, the density-dependent variance factor $A(\rho_l)$ is given as:

$$A(\rho_l) = A_{0,l} + \delta A_l \left[1 + \tanh\left(\frac{\rho_l - \rho_{cr,l}}{\delta \rho_l}\right)\right]. \tag{3.9}$$

Furthermore, terms $r_{rmp,1}$ and $h_{rmp,1}$ reflect the impact of traffic flow from on-ramps (or to off-ramps) on the first lane and take non-zero values only for the corresponding lane. As in the case of the single-lane GKT model (see Section 3.2.1), the term $r_{rmp,1}$ denotes the effective source density that is only active within the merging sections with length l_{rmp} and inflow $q_{rmp,1} > 0$ from (or outflow $q_{rmp,1} < 0$ to) the ramps, determined as

$$r_{rmp,1}(x,t) = \begin{cases} \dfrac{q_{rmp,1}(t)}{l_{rmp}} & if\ x\ inside\ the\ merging\ zone, \\ 0 & elsewere, \end{cases} \tag{3.10}$$

while the term $h_{rmp,1}$ describes changes in the macroscopic local speed by assuming that on-ramp vehicles merge to the main road at speed $u_{rmp} <$ u. On the contrary, the drivers considering to leave the main road reduce their speed to u_{rmp} before they diverge to the off-ramp. Hence, for the multi-lane GKT model this term is expressed as

$$h_{rmp,1}(x,t) = \frac{q_1 \cdot r_{rmp,1}}{\rho_1} + \frac{(u_{rmp} - u_1)|q_{rmp,1}|}{l_{rmp}}. \tag{3.11}$$

The non-local and dynamic equilibrium speed, $V^*_{e,l}(\rho_l, u_l, \rho_{\alpha,l}, u_{\alpha,l})$, toward which the average speed relaxes, is determined as

$$V^*_{e,l} = u_{max,l}\left[1 - \frac{\theta_l + \theta_{\alpha,l}}{2A(\rho_{max,l})}\left(\frac{\rho_{\alpha,l}\ T_l}{1 - \rho_{\alpha,l}/\rho_{max,l}}\right)^2 B(\delta u_l)\right] \tag{3.12}$$

while the Boltzmann factor $B(\delta u_l)$, with $\delta u_l = (u_l - u_{a,l})/\sqrt{\theta_l + \theta_{\alpha,l}}$, takes the form

$$B(\delta u_l) = 2\left[\delta u_l \frac{e^{-\delta {u_l}^2/2}}{\sqrt{2\pi}} + (1 + \delta {u_l}^2)\int_{-\infty}^{\delta u_l} \frac{e^{-y^2/2}}{\sqrt{2\pi}} dy\right]. \tag{3.13}$$

Further, according to model equations (3.8) for the multi-lane traffic, the source term $\boldsymbol{w}_l(\boldsymbol{u}_1, \dots, \boldsymbol{u}_N) \in \mathbb{R}^2$ represents the sources and sinks due to lane-changing, resulting in a weakly coupled system of $2N$ equations. The components of the lane-changing terms are defined as

$$w_l^{1,2} = \left(\frac{1}{T^L_{l-1}} u^{1,2}_{l-1} - \frac{1}{T^R_l} u^{1,2}_l\right)(1 - \delta_{l,1}) + \left(\frac{1}{T^R_{l+1}} u^{1,2}_{l+1} - \frac{1}{T^L_l} u^{1,2}_l\right)(1 - \delta_{l,N}), \tag{3.14}$$

with $\frac{1}{T^L}$ and $\frac{1}{T^R}$ being the lane changing rates from lane l to left $l+1$ and right $l-1$, respectively, and $\delta_{i,j}$ the Kronecker delta. The lane changing rates are defined as

$$\frac{1}{T^L_l} = P_L(\rho_{l+1}) v(\rho_l) + S^L_l\,, \tag{3.15}$$

$$\frac{1}{T_l^R} = P_R(\rho_{l-1})\big(1 - P_L(\rho_{l+1})\big)v(\rho_l) + S_l^R \,,$$

where the terms $P_{R,L}(\rho_l)$ are the lane-changing probabilities in response to vehicle interactions and $v(\rho_l) = v_f(1-\rho_l)\rho_l^2$ are the interaction frequencies regarding deceleration and acceleration; for simplicity, considered that $P_R(\rho) = P_L(\rho)$. The shape of $P_{R,L}(\rho_l)$ depends on a characteristic density value (ρ_P), while that of $v(\rho_l)$ depends on the value of v_f, as depicted for example in Figure 3.1.

Further, we assume here that the spontaneous lane changes, which are not caused by vehicle interactions and described by the terms $S_l^{L,R}$, are formulated as

$$S_l^{L,R} = k_l^{L,R}\left(1 - \frac{\rho_{l\pm1}}{\rho_{max,l\pm1}}\right)^{\beta} \tag{3.16}$$

in which $k_l^{L,R}$ and β are spontaneous lane-changing parameters. For the spontaneous lane-changing terms in equation (3.16), the European-rule of primarily using the right lane at low densities is adopted (Shvetsov & Helbing, 1999; Ngoduy *et al.*, 2005). Calibration results have shown that spontaneous lane-changing mainly influences low-density regimes. Setting $\beta = 8$ in equation (3.18), a smooth correction pre-factor G_{Eu}, with $0 < G_{Eu}(\rho) < 1$, is used to account for the European traffic rule by modifying S_l^L as $S_l^L\, G_{Eu}$ and S_l^R as $S_l^R\, /G_{Eu}$ (Delis *et al.*, 2015b).

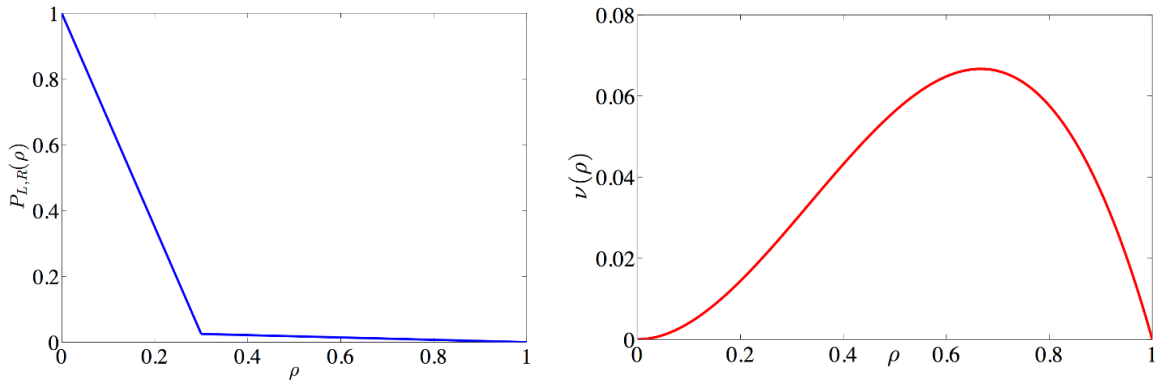

FIGURE 3.1: *(Left) Lane changing probability for* $\boldsymbol{\rho_{cr,l}=0.3\rho_{max,l}}$ *and* $\boldsymbol{\rho_P=0.025}$*. (Right) Lane changing frequency for normalized density, for* $\boldsymbol{v_f=0.4}$*.*

3.2.1.2 The Relaxation Approach for 1-D systems of conservations laws

For the numerical integration of system (3.1)-(3.2) or equivalent system (3.8), an accurate and robust high-resolution finite volume relaxation scheme was applied. This section, briefly describes the developed relaxation scheme and its numerical discretization.

Model equations (3.1)-(3.2) can be written in vector form, supplied with initial conditions, as

$$\begin{aligned} &\partial_t \boldsymbol{u} + \partial_x \boldsymbol{f}(\boldsymbol{u}) = \boldsymbol{s}(\boldsymbol{u}) \,, \\ &\boldsymbol{u}(x,0) = \boldsymbol{u}_0(x) \,, \end{aligned} \tag{3.17}$$

where the functions $\boldsymbol{u}$, $\boldsymbol{f}(\boldsymbol{u})$ and $\boldsymbol{s}(\boldsymbol{u}) \in \mathbb{R}^2$ with $\boldsymbol{u} = [\rho, q]^{\mathrm{T}}$, $\boldsymbol{f}(\boldsymbol{u}) = [\rho u,\ \rho u^2 + \theta\rho]^{\mathrm{T}}$ and $\boldsymbol{s}(\boldsymbol{u}) = [r_{rmp}, (\rho V_e^* - \rho u)/\tau + h_{rmp}]^{\mathrm{T}}$.

Systems in the form of (3.17) can be rewritten in quasi-linear form

$$\partial_t \boldsymbol{u} + \mathbf{J}(\boldsymbol{u})\partial_x \boldsymbol{u} = \boldsymbol{s}(\boldsymbol{u})\,, \tag{3.18}$$

in which $\mathbf{J}(\boldsymbol{u}) = \frac{\partial \boldsymbol{f}}{\partial \boldsymbol{u}}$ is the Jacobian matrix of the system. This Jacobian matrix has two distinct, real and positive eigenvalues, for all physically reasonable parameter sets, given as

$$\lambda_{1,2} = u + \frac{1}{2}\frac{\partial P}{\partial q} \pm \sqrt{\left(\frac{1}{2}\frac{\partial P}{\partial q}\right)^2 + \frac{q}{r}\frac{\partial P}{\partial q} + \frac{\partial P}{\partial \rho}}\,, \tag{3.19}$$

which denote that the model equations constitute a strictly hyperbolic set of partial differential equations.

In what follows, the class of relaxation models by Jin & Xin, 1995, which applied to various second-order macroscopic traffic flow models by Delis *et al.*, 2014, is briefly presented. Introducing the artificial variables $\boldsymbol{w}$, the corresponding to (3.17), relaxation system reads as

$$\begin{aligned} \partial_t \boldsymbol{u} + \partial_x \boldsymbol{w} &= \boldsymbol{s}(\boldsymbol{u})\,, \\ \partial_t \boldsymbol{w} + \boldsymbol{C}^2 \partial_x \boldsymbol{u} &= \frac{\boldsymbol{f}(\boldsymbol{u}) - \boldsymbol{w}}{\epsilon}\,. \end{aligned} \tag{3.20}$$

and the extra initial condition $\boldsymbol{w}(x,0) = \boldsymbol{w}_0(x) = \boldsymbol{f}\big(\boldsymbol{u}_0(x)\big)$, where the small parameter ϵ $(0 < \epsilon \ll 1)$, is the relaxation rate, and $\boldsymbol{C}^2 = diag\{c_1^2, c_2^2\}$ is a positive diagonal matrix. Applying the Chapman-Enskog expansion in system (3.20), the following approximation for $\boldsymbol{u}$ can be obtained,

$$\partial_t \boldsymbol{u} + \partial_x \boldsymbol{f}(\boldsymbol{u}) = \boldsymbol{s}(\boldsymbol{u}) + \epsilon\partial_x\left[\left(\frac{\partial \boldsymbol{f}(\boldsymbol{u})}{\partial \boldsymbol{u}}\right)\boldsymbol{s}(\boldsymbol{u})\right] + \epsilon\partial_x\left[\left(\boldsymbol{C}^2 - \left(\frac{\partial \boldsymbol{f}(\boldsymbol{u})}{\partial \boldsymbol{u}}\right)^2\right)\partial_x \boldsymbol{u}\right] + O(\epsilon)^2\,. \tag{3.21}$$

Equation (3.21) controls the first-order behavior of system (3.20), with the third term on the right-hand side being an $O(\epsilon)$ dominant dissipation term in the model with $\left(\boldsymbol{C}^2 - \left(\frac{\partial \boldsymbol{f}(\boldsymbol{u})}{\partial \boldsymbol{u}}\right)^2\right)$ being the diffusion-like coefficient matrix. Model (3.20) is well-posed only if the matrix is positive semi-definite for all $\boldsymbol{u}$. This requirement on the diffusion coefficient matrix is the well-known sub-characteristic condition (Jin & Xin, 1995)

$$\boldsymbol{C}^2 - \left(\frac{\partial \boldsymbol{f}(\boldsymbol{u})}{\partial \boldsymbol{u}}\right)^2 \geq 0, \quad \forall \boldsymbol{u}\,. \tag{3.22}$$

Condition (3.22) can always be satisfied by choosing sufficiently large values for the elements in $\boldsymbol{C}^2$, for $\boldsymbol{u}$ varying in a bounded domain. As such, the solution of the relaxation model (3.20) strongly converges to the unique entropy solution of the original conservation laws. In practice this can be equivalent to the choice

$$\lambda^2 \leq c^2, \text{ where } \lambda = \max_{1\leq i\leq 2}|\lambda_i| \text{ and } c = \min_{1\leq i\leq 2}|c_i|\,. \tag{3.23}$$

Now, system (3.20) can be easily diagonalized, leading to the following decoupled system of equations

$$\partial_t(\boldsymbol{w}+\boldsymbol{Cu})+\boldsymbol{C}\partial_x(\boldsymbol{w}+\boldsymbol{Cu})=\frac{\boldsymbol{f}(\boldsymbol{u})-\boldsymbol{w}}{\epsilon}+\boldsymbol{Cs}(\boldsymbol{u}); \tag{3.24}$$

$$\partial_t(\boldsymbol{w}-\boldsymbol{Cu})-\boldsymbol{C}\partial_x(\boldsymbol{w}-\boldsymbol{Cu})=\frac{\boldsymbol{f}(\boldsymbol{u})-\boldsymbol{w}}{\epsilon}-\boldsymbol{Cs}(\boldsymbol{u})\,. \tag{3.25}$$

The left-hand side of system (3.24)-(3.25) is linear with constant wave speeds. Its solution has the property that it propagates at finite speeds along linear characteristic curves $dx/dt=\pm\boldsymbol{C}$. From (3.24)-(3.25), and by setting $\boldsymbol{g}_{1,2}=\boldsymbol{w}\pm\boldsymbol{C}$, the following relations to the original variables of the relaxation system hold

$$\boldsymbol{u}=\tfrac{1}{2}\boldsymbol{C}^{-1}(\boldsymbol{g}_1-\boldsymbol{g}_2)\text{ and }\boldsymbol{w}=\tfrac{1}{2}(\boldsymbol{g}_1+\boldsymbol{g}_2)\,. \tag{3.26}$$

The structure of the linear characteristic field of the relaxation system constitutes a clear advantage compared to the original conservation laws for their numerical integration.

For the spatial discretization of (3.20) the finite volume approach is adopted. Let $x_i=i\Delta x$, $x_{i\pm\frac{1}{2}}=\left(i\pm\frac{1}{2}\right)\Delta x$, where Δx is a uniform spatial discretization step. The discrete cell average of $\boldsymbol{u}$ in the cell $I_i=\left[x_{i-\frac{1}{2}},x_{i+\frac{1}{2}}\right]$ at time t is defined as $\boldsymbol{u}_i(t)$ and the approximate value of $\boldsymbol{u}$ at $\left(x_{i+\frac{1}{2}},t\right)$ by $\boldsymbol{u}_{i+\frac{1}{2}}(t)$. The semi-discrete relaxation system is given as

$$\begin{aligned}\frac{\partial}{\partial t}(\boldsymbol{u}_i)+\frac{1}{\Delta x}\left(\boldsymbol{w}_{i+\frac{1}{2}}-\boldsymbol{w}_{i-\frac{1}{2}}\right)&=\boldsymbol{s}(\boldsymbol{u})_i\,,\\ \frac{\partial}{\partial t}(\boldsymbol{w}_i)+\frac{\boldsymbol{C}^2}{\Delta x}\left(\boldsymbol{u}_{i+\frac{1}{2}}-\boldsymbol{u}_{i-\frac{1}{2}}\right)&=-\frac{1}{\epsilon}(\boldsymbol{w}_i-\boldsymbol{f}(\boldsymbol{u})_i)\,.\end{aligned} \tag{3.27}$$

where $\boldsymbol{s}(\boldsymbol{u})_i$ and $\boldsymbol{f}(\boldsymbol{u})_i$ are discrete averages of the source term and flux function, respectively. To completely define the spatial discretization, we need to compute the flux values $\boldsymbol{u}_{i\pm\frac{1}{2}}$ and $\boldsymbol{w}_{i\pm\frac{1}{2}}$. As system (3.20) has linear characteristics and its characteristic speeds, $+c_k$ and $-c_k$, are constant, the construction of an upwind scheme is much simpler than developing such a scheme for the original nonlinear conservation laws. For example, the first-order upwind scheme (Jin & Xin, 1995; Delis *et al.*, 2014), applied to $\boldsymbol{g}_1$ and $\boldsymbol{g}_2$ gives $\boldsymbol{g}_{1_{i+\frac{1}{2}}}=\boldsymbol{g}_{1_i}$ and $\boldsymbol{g}_{2_{i+\frac{1}{2}}}=\boldsymbol{g}_{2_{i+1}}$.

In order to increase the spatial order of accuracy, a WENO-type interpolant approach is applied, where the approximate solution is reconstructed by using higher-order polynomials. By direct application of this reconstruction to the $k-$th components of the characteristic variables, $\boldsymbol{g}_{1,2}=\boldsymbol{w}\pm\boldsymbol{Cu}$, a non-oscillatory higher-order spatial discretization is obtained. The superiority of applying higher-order schemes, compared to low-order ones, in traffic flow simulations has been recently demonstrated by Delis *et al.*, 2014. By applying a fifth-order WENO reconstruction the discrete values of each component of $\boldsymbol{g}_{1_{i+\frac{1}{2}}}$ and $\boldsymbol{g}_{2_{i+\frac{1}{2}}}$, at a cell boundary $i+\frac{1}{2}$, are defined as left and right extrapolated values $\boldsymbol{g}^-_{1\,i+\frac{1}{2}}$ and $\boldsymbol{g}^+_{2\,i+\frac{1}{2}}$ i.e., $\boldsymbol{g}_{1_{i+\frac{1}{2}}}=\boldsymbol{g}^-_{1\,i+\frac{1}{2}}$ and $\boldsymbol{g}_{2_{i+\frac{1}{2}}}=\boldsymbol{g}^+_{2\,i+\frac{1}{2}}$. After the reconstructions have been performed to each component of the characteristic variables, the numerical fluxes for $\boldsymbol{u}_{i+\frac{1}{2}}$ and $\boldsymbol{w}_{i+\frac{1}{2}}$ are computed from (3.26). The face values at cell boundary $-\frac{1}{2}$ are computed in a similar manner.

The semi-discrete relaxation system (3.27) constitutes a system of autonomous ordinary differential equations with a stiff relaxation term. A time marching approach based on implicit-explicit (IMEX) Runge-Kutta (RK) splitting was considered, in order to avoid the time step restrictions imposed by an explicit solver due to stiffness. As such, the explicit RK scheme treats the non-stiff stage of the splitting, while a diagonally implicit RK scheme treats the stiff one. We note that even though an implicit scheme is used, either linear or nonlinear algebraic equations have to be solved due to the special structure of the relaxation system. The choice of the time marching step Δt^n is based only on a usual CFL (Courant-Friedrichs-Lewy) condition,

$$CFL = \max\left(\left(\max_{i,k} c_k^n\right)\frac{\Delta t^n}{\Delta x}, \frac{\Delta t^n}{\Delta x}\right) \leq \frac{1}{2}, \tag{3.28}$$

where the values of the relaxation constants c_k^n are re-computed at each time step based on the Jacobian eigenvalues so as to satisfy the sub-characteristic condition (3.22). A detailed description of the spatial and temporal discretization schemes, as well as the superiority and performance of the applied higher-order scheme, with respect to low-order ones, in traffic flow simulations has been demonstrated by Delis *et al.*, 2014.

3.2.2 METANET Model

Further in this thesis the single-lane GKT model (see Section 3.2.1) is validated and compared with the METANET model (Messmer & Papageorgiou, 1990) in terms of the representation of traffic flow conditions at congested freeway areas. The METANET model is the most commonly used macroscopic traffic flow model and has been utilized by several research groups to handle various traffic engineering tasks, such as simulation, optimization, estimation and optimal freeway traffic control. In what follows, a brief description of the METANET model is presented.

The METANET model is a discretized and enhanced variant of the Payne (PW) model. Within METANET, the freeway is divided into homogeneous, consecutively numbered sections i, with respective lengths L_i and number of lanes λ_i, as shown in Figure 3.2. Time is also discretized into uniform intervals of duration T, with a discrete time index $k = 0,1,2,\dots,K$ where K is the time horizon. The state variables for section i are the density $\rho_i(k)$ (in veh/km/lane) and the mean speed $u_i(k)$ (in km/h) at the time instant kT, which are calculated according to the following equations:

$$\rho_i(k+1) = \rho_i(k) + \frac{T}{L_i\lambda_i}[q_{i-1}(k) - q_i(k) + r_i(k) - s_i(k)], \tag{3.29}$$

$$u_i(k+1) = u_i(k) + \frac{T}{L_i}u_i(k)[u_{i-1}(k) - u_i(k)] + \frac{T}{\tau}[V^e[\rho_i(k)] - u_i(k)] - \frac{\nu T[\rho_{i+1}(k) - \rho_i(k)]}{\tau L_i[\rho_i(k) + \kappa]}, \tag{3.30}$$

where, q_i is the traffic flow exiting section i and entering section $i+1$, $r_i(k)$ is the traffic flow entering the freeway section i from an on-ramp and $s_i(k)$ is the traffic flow exiting the freeway section from an off-ramp, and equals to $s_i(k) = \beta_i(k)q_i(k)/[1-\beta_i(k)]$ where $\beta_i(k)$ is the

splitting ratio. Moreover, τ (a time constant), ν (an anticipation constant) and κ are model parameters, while function $V^e[\rho_i(k)]$ corresponds to the fundamental diagram, calculated using the following equation:

$$V^e[\rho_i(k)] = u_{f,i}\, exp\left[-\frac{1}{a_i}\left(\frac{\rho_i(k)}{\rho_{cr,i}}\right)^{a_i}\right], \tag{3.31}$$

where $u_{f,i}$ is the free flow speed, $\rho_{cr,i}$ is the critical density (for which the flow at section i is maximized) and a_i is a further model parameter for section i. Moreover, the mean speed calculated by the model is truncated if it is below a minimum value u_{min}. Papageorgiou *et al.*, 1990, proposed two additional terms for more accurate modelling of merging and lane-drop phenomena. In particular, the impact on mainstream speed due to an on-ramp merging flow is calculated by adding the term $-\delta T r_i(k) v_i(k)/L_i\lambda_i\,[\rho_i(k)+\kappa]$ at the right hand side of equation (3.30) for the merging section, where δ is a model parameter. This term is not used if there is a lane gain downstream of the on-ramp, i.e., if there is a lane dedicated for entering vehicles. In order to take into account the impact on speed due to intensive lane-changing at lane-drop areas, the term $-\varphi T \Delta\lambda \rho_i(k) v_i(k)^2 / L_i\lambda_i\,\rho_{cr,i}$, is added to equation (3.30) for the section immediately upstream of the lane drop, where φ is a model parameter and $\Delta\lambda$ is the number of dropped lanes.

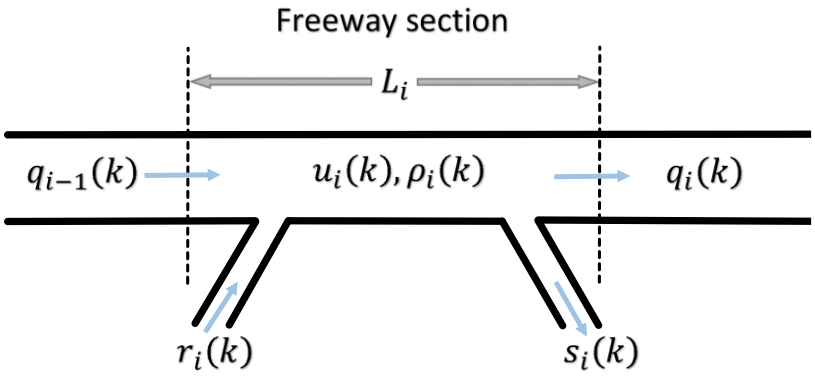

FIGURE 3.2: *Freeway discretization in the METANET model.*

At bifurcation locations (e.g. off-ramps), a downstream density $\rho_{i+1}(k)$ is needed in equation (3.30) for section i entering the bifurcation; this density reflects the upstream influence of the downstream traffic conditions. However, since we have at least two downstream sections at bifurcations, the following formula was proposed by Messmer & Papageorgiou, 1990, for usage

$$\rho_{i+1}(k) = \sum_{\mu\epsilon O_\iota} \rho_\mu{}^2(k) \Big/ \sum_{\mu\epsilon O_\iota} \rho_\mu(k)\,, \tag{3.32}$$

where $\rho_{i+1}(k)$ is the virtual density downstream of section i, which is used in equation (3.30), and $\rho_\mu(k)$ is the density of each section downstream of section i, O_ι being the set of existing sections. The quadratic average used in (3.32) accounts for the fact that congestion may spill back to a section i from any one of its downstream sections (e.g., in case of spillback from a saturated off-ramp), even if the rest downstream sections are not congested. Notice that equation (3.32) does not include any parameter to be calibrated. Finally, the flow $q_i(k)$ exiting section i and entering section $i+1$ is computed as

$$q_i(k) = u_i(k)\rho_i(k)\lambda_i[1-\beta_i(k)]\,. \tag{3.33}$$

3.2.3 The Differential Evolution Algorithm

Among the various search and optimization techniques, the development of EAs has become increasingly appealing over the last decade, as a flexible and robust tool, capable of addressing high-dimensional real-world optimization problems that have several local optima. They constitute a class of search methods with a remarkable balance between exploitation of the best solutions and exploration of the search space, as well as low sensitivity to local minima treatment. They combine elements of directed and stochastic search and, therefore, are more robust than directed search methods. Within the proposed numerical optimization scheme, a DE Algorithm is utilized. This is a versatile stochastic search method, introduced by Storn & Price, 1995, 1997, capable of handling non-differentiable, nonlinear and multimodal cost functions, providing superior convergence performance than other EAs (Storn & Price, 1995, 1997; Price *et al.*, 2005). Contrary to other EAs, the DE compares each new candidate member (offspring) of the population only against a single existing one (parent), which is its counterpart in the current population. The new parameter vector (offspring) results after applying mutation and crossover operators; specifically, this is a linear combination between a randomly selected member of the current population (chromosome) and a weighted difference between two other randomly chosen chromosomes.

Below, an analytical description of the basic elements composing a classic DE algorithm is presented. Given a cost function

$$f_{cost}(\boldsymbol{x}) = f_{cost}(x_1\,, x_2, \dots, x_n) \rightarrow min \tag{3.34}$$

where $\boldsymbol{x}$ denotes the vector containing the n design variables (number of genes) of the problem under consideration and $f_{cost}\,(\boldsymbol{x})$: $\mathbb{R}^n \rightarrow \mathbb{R}$ a real function. The optimization target is the minimization of the cost function f_{cost} by modulating the values of its design variables $(x_1\,, x_2, \dots, x_n)$, while each one of the design variables is bounded between an upper x_i^u and a lower x_i^l value. DE evolves a fixed size population of N_p individuals (chromosomes) for a finite number of generations G_{max}. The initialization of the first population $G = 0$ is established by randomly assigning values to the design variables within their given boundaries

$$\begin{gathered} x_{k,i}^0 = r \cdot \left(x_i^u - x_i^l\right) + \; x_i^l, \;\; i = 1, \dots, n, \qquad k = 1, \dots, N_p, \\ x_i^l \leq x_{k,i}^0 \leq x_i^u\,, \end{gathered} \tag{3.35}$$

where r denotes a random number generated with uniform probability within the range $[0, 1]$. After the evaluation of each individual's cost function, operators are applied to the population, simulating the according natural processes. The first operator applied is the mutation scheme, which generates a new chromosome (mutant), based on three randomly selected individuals (chromosomes) of the current generation G. The formation of the new parameter vector is realized by adding a weighted difference vector between the two members of the triad to the third one, the so-called "donor". Then, the uniform crossover scheme is applied; the mutant and the chromosome of the current population (parent) are subjected to a discrete recombination, which produces the final candidate solution

$$x_{k,i}^{\prime G+1} = \begin{cases} x_{C_k,i}^{G} + F\left(x_{A_k,i}^{G} - x_{B_k,i}^{G}\right) & if\ r \le C_r \quad or \quad i = i^* \ \forall\, i = 1, \dots, n \\ x_{k,i}^{G} & otherwise, \end{cases} \tag{3.36}$$

$$k = 1, \dots, N_p, i = 1, \dots, n$$
$$A_k \in [1, \dots, N_p\,], \qquad B_k \in [1, \dots, N_p\,], \qquad C_k \in [1, \dots, N_p\,], \qquad A_k \neq B_k \neq C_k$$
$$C_r \in [0,1], \qquad F \in [0, 1+], \qquad r \in [0,1]\,,$$

where $x_{C_k,i}^{G}$ are the elements of the "donor" vector (chromosome), G is the current generation and i^* is a randomly selected integer within $[1, n]$, chosen once for all members of the population. The random number r is seeded for every gene of each chromosome whereas the parameters F and C_r consider the mutation and crossover operations, respectively. Specifically, the scale factor F controls the diversification rate of the population, while the crossover probability C_r controls the fraction of design values that are inherited from the mutant. Moreover, the design variable, which corresponds to the randomly selected index, i^*, is taken from the mutant to ensure that the trial vector (offspring) does not duplicate the initial one (parent). Scaling vector differences ensures that trial vectors do not duplicate existing members in the population. Additionally, scaling can shift the focus of the search between local and global.

Subsequently, each member of the resulting intermediate population (offspring) is evaluated and competes against its counterpart in the current population (parent); the best-fitted individuals are the ones that will form the next generation. The DE selection scheme ensures the survival of the elitists and can be described as follows:

$$\boldsymbol{x}_k^{G+1} = \begin{cases} \boldsymbol{x}_k^{\prime G+1} & if\ f\left(\boldsymbol{x}_k^{\prime G+1}\right) \le f\left(\boldsymbol{x}_k^{G}\right), \\ \boldsymbol{x}_k^{G} & otherwise. \end{cases} \tag{3.37}$$

The process is successively repeated, providing populations with better-fitted individuals.

The DE selection scheme has a substantial difference compared to other EAs, owing to the fact that the offspring is not compared against all the members of the current population, but only against its parent, replacing it if it's better-fitted. This important characteristic allows for a relatively easy implementation of an asynchronous parallelization procedure, as it will be described in a following section. If each population member is assigned to a different processor (or core), this processor can proceed to the evaluation of a new individual, after completing the evaluation of its parent. Communication between the different processors is mainly required in order to perform the mutation operation. This does not necessitate the existence of a generation in the strict sense; a population comprising chromosomes belonging to different generations may be used instead. Additional communication with the master node is needed in the case of utilizing surrogate models, which are re-trained in each generation (which is the case in our implementation).

3.3 Macroscopic Traffic Flow Model Calibration

Macroscopic traffic simulation models are essential tools in modelling transport systems; one of the challenges faced by such a model is to respond to prevailing local conditions with the highest possible level of accuracy. In fact, the process of model calibration is a prerequisite for

any macroscopic model so as to ensure its credibility and reliability in performing real-world simulations, capturing realistic distribution of all possible traffic conditions of a freeway network and producing valid results. To do so, an optimization problem should be solved in order to mine the optimal design parameters of the model, which minimize the relative error between the model prediction and the observed data. However, such a calibration process is a challenging problem, since the equations of both the GKT and the METANET models (see Section 3.2.1 and 3.2.2) are highly nonlinear.

3.3.1 The Combined Use of Surrogate Models

In each DE generation, each trial vector (offspring) must first be evaluated (by computing its cost function using simulation software) and then compared with its parent, so as to select the better-fitted between them to pass on to the next generation. The computation of the offspring's cost function is (in most real-world applications) a time-consuming operation. The concept of utilizing surrogate models in this evaluation procedure is to replace the costly exact evaluations with fast inexact approximations, without sacrificing the robustness of the DE algorithm. These surrogate models are established using a data-driven approach, where only the input and output behavior of the simulation model of the cost function is taken into account, as to create a mechanism that mimics that behavior. Two types of Artificial Neural Networks (ANNs) are used as surrogate models; a Multi-Layer Perceptron (MLP) and a Radial Basis Function (RBF) ANN, respectively. A detailed description of their implementation within the DE optimizer can be found in (Nikolos, 2004, 2011, 2013), along with related references to available types of surrogate models and their combination with EAs. Each offspring is pre-evaluated, using the available surrogate models, in a fast screening procedure. If an offspring is pre-evaluated and found lower-fitted than its parent, then no further exact evaluation is taking place, and the current vector (parent) is transferred to the next generation, while the offspring is abandoned. In the opposite case, where the offspring is pre-evaluated as better-fitted than its parent, an exact (and costly) re-evaluation is performed after the pre-evaluation, along with a second comparison between the two vectors. If the offspring is found again better-fitted than its parent, then the offspring passes on to the next generation. Otherwise, its parent will pass on to the next generation and the offspring will be abandoned.

An additional small percentage ($5\% - 10\%$) of the candidate solutions are selected with uniform probability to be exactly evaluated, without taking into account their pre-evaluation by the utilized surrogate models, to further enhance the robustness of the procedure. Moreover, in the first two generations of the DE, all trial vectors are exactly evaluated (without using the surrogate models), so as to initialize the central database (pool) required for the training of the surrogate models. As it was previously described, only exactly-evaluated candidate solutions have the opportunity to pass on to the new generation. Consequently, in each generation the current population always comprises individuals that have been selected using exact evaluation. Therefore, one part of the comparison (the parent) in the pre-evaluation phase is always an exactly-evaluated vector, and this enhances the robustness of the procedure. It should be emphasized that the surrogate model predictions replace exact and costly evaluations only for the less-promising individuals. The pre-

evaluation phase is used to quickly reject them without spending valuable computational resources to exactly-evaluate them.

Each evaluated chromosome, along with its resulted fitness function value, is stored in the central database. The training and testing data sets are selected in each generation from the corresponding database, to be used by all available surrogate models. If NR is the length of the training set and NT is the length of the testing set (defined by the user in the beginning of the optimization procedure), the $NR + NT$ best members of the central database are deterministically selected. From this set, NR members are randomly selected (with uniform probability) to be utilized as the training set, while the rest NT are being used for testing. In this way the surrogate models, which are re-trained and re-tested in each generation, evolve with the population and use only the currently most-promising individuals for approximating the cost function.

The utilized surrogate models can be used either independently or as an ensemble. In the first case, a single surrogate is used throughout the whole optimization procedure. In the second case all surrogates are re-trained and re-tested in each generation (using the same training and testing data sets for all surrogates). Then, only the best one is used in the pre-evaluation phase of the trial vectors. The selected surrogate (different in each generation) is the one with the lower value of the testing error. The second procedure is usually preferred, since it is not known a-priori which surrogate is the best for a new cost function and for each region of the cost function, thus this automated procedure decides for the surrogate to be used in each generation. The re-training of all the available surrogates in each generation adds negligible cost, compared to the cost of the evaluations (Nikolos, 2004, 2011, 2013; Strofylas & Nikolos, 2015).

3.3.2 Parallel Implementation

Despite the important contribution of EAs in solving complicated problems, they tend to be excessively time-consuming, since they require a considerable number of evaluations. Thus, appropriate acceleration through parallel processing appears to be mandatory; this is supported by the fact that EAs are inherently parallel algorithms, as they deal with a population of different candidate solutions in each generation. The concept behind the developed parallelization strategy is to enable the cooperation of the DE with different simulation software in the form of executables. The required data transfer between the DE and the simulation software is succeeded with appropriate text files. The communication among the processors and the parallel implementation is achieved using MPI library functions. The proposed strategy appears to be quite efficient, regardless of the use of text files, considering that the computational time of data transfer is negligible compared to that of the evaluation step. Two different parallel implementations have been developed, a *synchronous* and an *asynchronous* one; their common characteristics will be described next, along with their differences.

For both parallel implementations, the population members are distributed a priori among the available processors; each processor is in charge of the evaluation of one individual. Next, a unique rank is assigned to each processor, while one of them is identified as the master node that keeps track of the whole procedure. This master node performs all the pre-process that is required prior to the beginning of the optimization procedure. This

includes the creation of a working folder for each processor where the executables comprising the evaluation step and their corresponding text files are replicated. Furthermore, the master node distributes all the necessary information concerning the DE algorithm to all other processors, i.e., the number of the design variables, their upper and lower bounds and control parameters for the DE algorithm. Actually, the parallel implementation is a hybrid master/slave one. There exists a master node, which performs the pre-process, as well as the auxiliary evaluations of the surrogate models. However, exchange of information, concerning the modification of the population, is allowed between the various processors through broadcasting (and not exclusively through the master node), as this is more computationally efficient. This hybrid master/slave model is tailor-made for a multi-core server application.

In the synchronous implementation (Figure 3.3), each generation is strictly defined and comprises a population of candidate solutions, which undergo the various DE operations simultaneously (in parallel). All the current members of the population belong to the same generation. In order to pass on to the next generation, all the individuals of the previous generation (parents) are first evaluated and then compared with their offspring individuals (using pre-evaluation with surrogates and then exact evaluation). More specifically, after the completion of the initialization step, the main procedure begins. Each processor is generating a random individual within the specified bounds for each gene of the chromosome and evaluates it. Next, the fitness values of the candidate solutions and their corresponding chromosomes are broadcasted to all processors, in order to update their databases with the new population members. Each processor evolves one chromosome separately, and the new resulting one (offspring) is stored in its corresponding working folder.

All the operations needed (mutation, crossover and selection) for the evolution process, are implemented after the evaluation step of each generation, on each node separately for its assigned chromosome. Nevertheless, the auxiliary evaluations of the surrogate models are performed only by the master node for all chromosomes. According to the prescribed approximate pre-evaluation procedure, a Boolean array is filled, indicating whether the new trial vector (offspring) is better-fitted than its parent and should hence be exactly evaluated. Subsequently, the selected candidates (only a part of the offspring auxiliary population) are exactly evaluated. For the rest their fitness function values and trial vectors are explicitly broadcasted by the master node to their corresponding processors for the consistency of the procedure. The optimization process is terminated when a prescribed number of generations is reached.

The prescribed algorithm implements a synchronous strategy of survivor selection to update the population members. During each generation loop, the evolutionary operations are imposed on each selected member of the population to produce an auxiliary population of (offspring) trial vectors. Once the calculations with the current population members finish at the end of each generation, the original population is updated instantaneously. This implies an implicit synchronization mechanism, ensuring that evolution operators are performed on all population members of the *current* generation. The utilized synchronization barrier causes processes to stop at the end of each offspring evaluation, waiting for all the remaining members of the auxiliary population to finish their own evaluations. This barrier results in a time overhead, if the evaluation processes have different time durations between the processors, thus allowing the slowest evaluation process to determine the speed of the computational procedure.

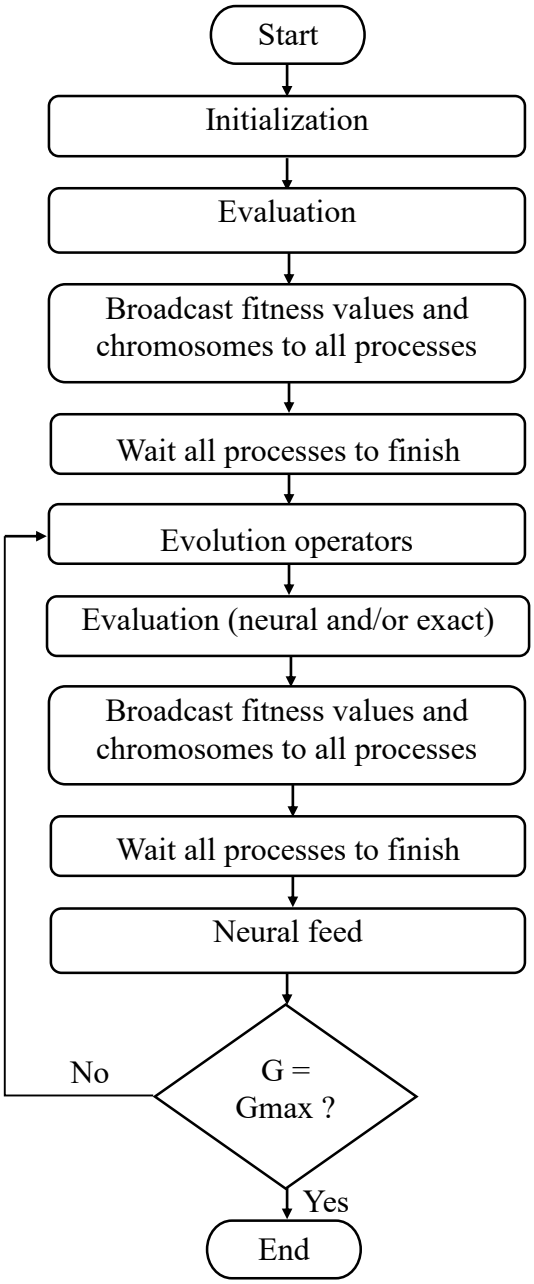

FIGURE 3.3: *Flowchart of the synchronous implementation of the parallel Differential Evolution algorithm.*

On the contrary, in an asynchronous implementation the generation is not strictly defined and the current population (at each time instant) can comprise individuals belonging to different generations. More specifically, each newly generated trial vector (offspring) can replace its parent (if better-fitted) and become a member of the current population, just after the completion of its evaluation process, without waiting for the completion of the evaluation phases of the rest members of the auxiliary population (Figure 3.4). Thus, individuals evolve independently, without strict central control or full coordination between generations.

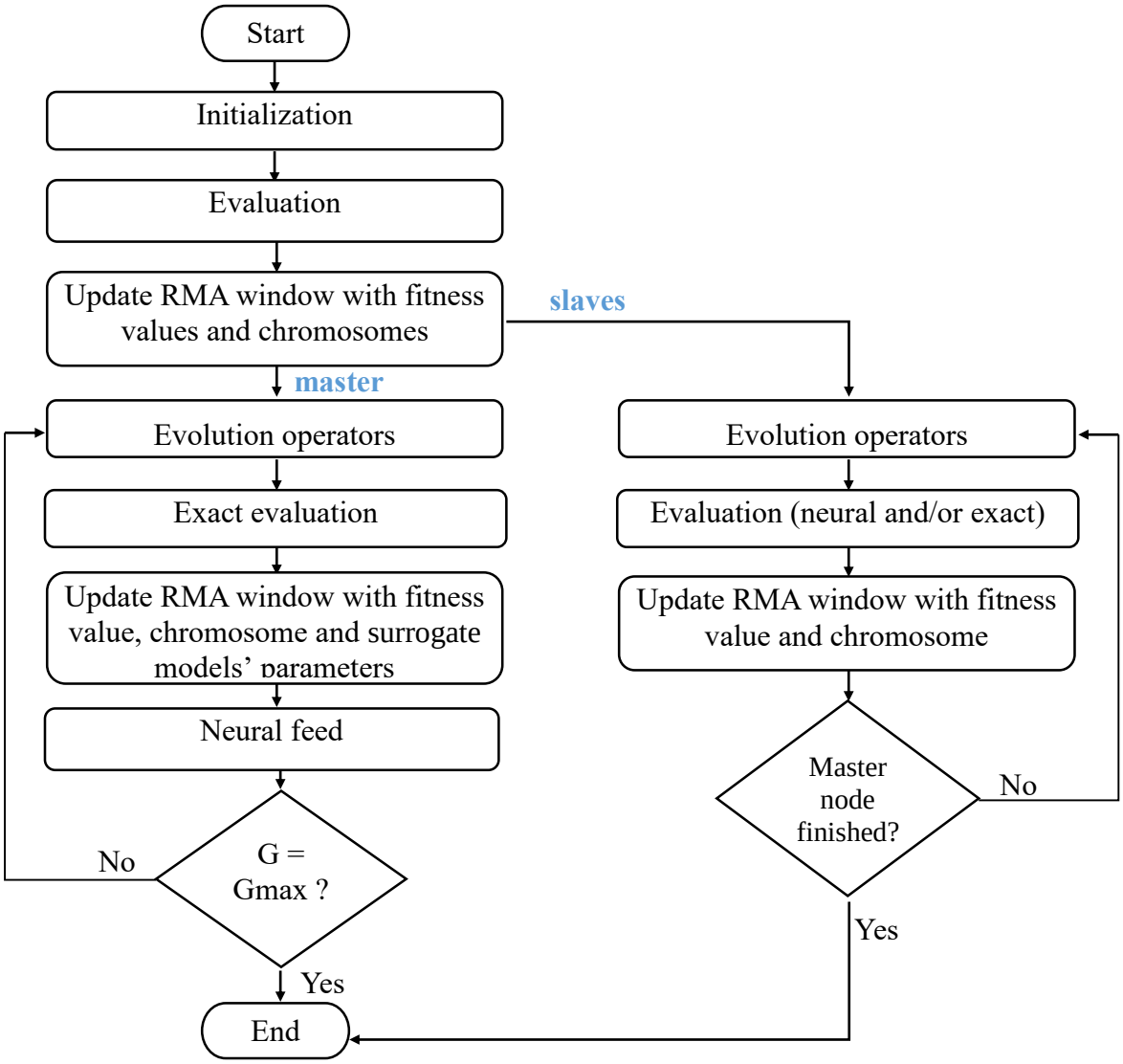

FIGURE 3.4: *Flowchart of the asynchronous implementation of the parallel Differential Evolution algorithm.*

Consequently, asynchronous update has the clear advantage that the improved solutions can contribute to the evolution immediately, without time-lags, and can speed up the convergence to become faster than the synchronous update. As the cycle over all the population members is removed, the concept of generations is obsolete in the asynchronous DE.

The choice of a triplet of randomly selected individuals for each population member, used in the mutation DE operator (equation (3.36)), is an issue which emerges as soon as we switch from a synchronous to an asynchronous update population mode. As the generation concept is no longer applicable, the random selection of three members of the current population (at the corresponding time instant) means that those individuals may not belong to the same generation. However, this has been proven to introduce no convergence problems to the asynchronous DE version. On the contrary, as the various individuals evolve independently to each other, with a faster convergence rate, the randomly chosen triplet is likely to have better characteristics, compared to the synchronous case.

The proposed asynchronous implementation of the DE algorithm uses non-blocking MPI communication operations. An asynchronous master-slave architecture has been

followed, i.e., the master process steers the evolution procedure, trains and tests the surrogate models, and collects/distributes data from all other processes. This is achieved by using Remote Memory Access (RMA) windows. To allow for remote memory access, the master node exposes contiguous regions of memory to the rest of the processes, which are called windows. MPI accomplishes this by a collective function called "MPI_Win_create". A process can get and set data to remote memory via "MPI_Get" and "MPI_Put". As MPI forbids concurrent access to the same memory location in the window, it is necessary to have a mechanism which ensures that access operations are completed before using the data. Thus, updates to the RMA windows by other processes are protected by the master node, using exclusive locks in case of a conflict. Non-conflicting accesses (such as read-only accesses or accumulate accesses) are protected by shared locks, both for local accesses and for RMA accesses.

Each slave node works independently, updating periodically only the fitness function value and its corresponding chromosome to the RMA windows. Each one of the slave nodes executes the same process in an infinite loop, checking first the receiving buffer to see if the termination message from the master node has arrived. Subsequently, it acquires all the updated data, essential for the calculations performed during a DE iteration. These include the fitness values of the candidate solutions and their corresponding chromosomes, as well as the parameters of the surrogate models through the RMA windows, in order to perform the evolution operators.

Due to the non-blocking communication, the processes never wait for one another. That is, they run completely asynchronously, and the slowest process does not slow down the others. This characteristic is essential, especially when using surrogate models, since the pre-evaluation of the trial vector is performed very fast. This means that, if the trial vector (offspring) is lower-fitted than the corresponding vector of the current population (parent), the processor won't have to wait for all other processors to finish the computations. Instead, it can proceed to the production of the next trial vector and its evaluation.

As it has been previously stated, in the asynchronous version of the parallel DE algorithm the concept of generation is no longer present. However, a definition for a "generation" number is needed for defining a frequency for the re-training and re-testing of the surrogate models, for interpreting the convergence history of the optimization run, and for comparison purposes. Thus, the generation number for the asynchronous parallel DE is defined as follows: the master node, which controls the DE procedure, is enforced to always exactly evaluate its corresponding chromosome. Therefore, the change between successive individuals for the master node defines a generation for this node, which is also used to define a "generation" for the whole population. This definition is rather connected to computation time intervals, than to a real generation concept. The exact evaluation time for each individual is roughly the same for all processes in a system comprising identical processors or cores (as the one used in this work). Therefore, the utilized definition of "generation" in the asynchronous DE case renders the comparisons between synchronous and asynchronous runs, with respect to the generation number, valid.

3.3.3 Fitness Function Formulation

As already mentioned, this thesis addresses the problem of calibrating the parameters of the second-order GKT and METANET models to best match the real-measured traffic data, by

means of the optimization scheme for the calibration and validation of macroscopic traffic flow models. In particular, this methodology attempts to minimize the discrepancy between model generated data and the measurements taken from the detectors (real data), in terms of a fitness function with appropriate specification of the parameters included in the model.

Within the literature there are many discrepancies error measures (goodness-of-fit measures) that can be used to evaluate the overall performance of simulation models by showing the differences between real and simulated data; some of the most common ones, along with their expressions, are presented below (Hollander & Liu, 2008; Ciuffo *et al.*, 2012).

- *Squared Error (SE)*

$$SE(x,y) = \sum_{i=1}^{N} (x_i - y_i)^2 \tag{3.38}$$

- *Mean Error (ME)*

$$ME(x,y) = \frac{1}{N} \sum_{i=1}^{N} (x_i - y_i) \tag{3.39}$$

- *Mean Normalized Error (MNE)*

$$MNE(x,y) = \frac{1}{N} \sum_{i=1}^{N} \frac{(x_i - y_i)}{y_i} \tag{3.40}$$

- *Mean Absolute Error (MAE)*

$$MAE(x,y) = \frac{1}{N} \sum_{i=1}^{N} |x_i - y_i| \tag{3.41}$$

- *Mean Absolute Normalized Error (MANE)*

$$MANE(x,y) = \frac{1}{N} \sum_{i=1}^{N} \frac{|x_i - y_i|}{y_i} \tag{3.42}$$

- *Root Mean Square Error (RMSE)*

$$RMSE(x,y) = \sqrt{\frac{1}{N} \sum_{i=1}^{N} (x_i - y_i)^2} \tag{3.43}$$

- *Root Mean Square Normalized Error (RMSNE)*

$$RMSE(x,y) = \sqrt{\frac{1}{N} \sum_{i=1}^{N} \left(\frac{x_i - y_i}{y_i}\right)^2} \tag{3.44}$$

where x_i and y_i represent, respectively, the averages of simulated predictions and the real measurements used in the calibration problem at space–time point i, while N is the total amount of all available data. The measures ME, MNE, MAE, MANE use the difference or the

absolute value of the difference between the real and simulated measurements, providing in this way equal weights to all errors. On the other hand, the measures that depend on squared difference (SE, RMSE and RMSNE) place a higher penalty on large errors, which are more appropriate, given that penalizing small errors is wrong for traffic modelling and may lead to an over-specified model, considering that minor fluctuations over the means are in the nature of traffic phenomena (Hollander & Liu, 2008).

Another measure that is widely accepted is the Geoffrey E. Havers' (GEH) statistic (Highway Agency, 1996), which is not evaluated over a series of traffic data, but over a single pair of real and predicted measurements. Hence, the index for each counting station is calculated as:

$$GEH_i(x,y) = \sqrt{\frac{2(x_i - y_i)^2}{x_i + y_i}} \tag{3.45}$$

Subsequently, an aggregated index is estimated by means of the following algorithm:

For $i = N$ *(number of counting stations)*
  If $GEH_i(x,y) \leq 5$, *then set* $GEH_i(x,y) = 1$
    Otherwise set $GEH_i(x,y) = 0$
  Endif;
End for;
Let $GEH(x,y) = \frac{1}{N}\sum_{i=1}^{N} GEH_i(x,y)$
If $GEH(x,y) \geq 85\%$ *then accept the model*
  Otherwise reject the model
Endif;

which can be interpreted as follows: if the deviation of the simulated values with respect to the observed measurements is smaller than 5% in at least 85% of the pairs (cases), then the two series of data show a good fit and the model is accepted.

Theil's inequality coefficient (Theil, 1961) is another normalized measure used to provide information on the relative error between real and simulated traffic measurements, smoothing out the impact of large errors. This measure is given by

$$U(x,y) = \frac{\sqrt{\frac{1}{N}\sum_{i=1}^{N}(x_i - y_i)^2}}{\sqrt{\frac{1}{N}\sum_{i=1}^{N} x_i{}^2} + \sqrt{\frac{1}{N}\sum_{i=1}^{N} y_i{}^2}} \tag{3.46}$$

in which U is bounded between 0 and 1 ($0 \leq U \leq 1$). $U = 0$ indicates a perfect fit between the real and simulated data, while $U = 1$ implies the worst possible fit.

Theil's indicator can be decomposed into three proportions: the bias (U^M), the variance (U^S) and the covariance (U^C) proportion, which are, respectively, defined as:

$$U^M = \frac{N(\bar{y} - \bar{x})^2}{\sum_{i=1}^{N}(y_i - x_i)^2}, \tag{3.47}$$

$$U^S = \frac{N(\sigma_y - \sigma_x)^2}{\sum_{i=1}^{N}(y_i - x_i)^2}, \tag{3.48}$$

$$U^C = \frac{2(1-r)\cdot N\cdot \sigma_x\sigma_y}{\sum_{i=1}^{N}(y_i - x_i)^2}, \tag{3.49}$$

where $\bar{x}$ and $\bar{y}$ are the means of real and simulated values, respectively, σ_x and σ_y are their standard deviations and r is the correlation coefficient. They satisfy the following relationship: $U^M + U^S + U^C = 1$. The proportion U^M is a measure of systematic error; $U^M = 0$ indicates a perfect fit, while high values close to 1 indicates an unacceptable bias. The variance proportion, U^S, measures how the distribution of simulated measurements diverge from that of the real traffic data; $U^S = 0$ indicates a perfect fit while $U^S = 1$ indicates the worst fit, since the simulated series has a significantly different variability. Finally, the proportion U^C measures the existence of unsystematic error and, consequently, it should take high values close to 1 for a good fit.

Detailed discussion over the choice of the various cost functions for the calibration problems of traffic flow models can be found in the studies proposed by Hollander & Liu, 2008, and Ciuffo *et al.*, 2012. Nevertheless, it is straightforward to apply the metamodel-assisted DE algorithm presented in Sections 3.2.3 and 3.3.1 for any of the above formulations of the cost functions in order to calibrate the selected macroscopic traffic flow models. In this thesis, however, we limit ourselves to the following cost functions (equations (3.50), (3.51) and (3.52)) and leave the test for other forms for a future research.

Specifically, the developed GKT model (Section 3.2.1) is fed with real traffic data to reproduce the complete traffic state of different scenarios, while for evaluating the resulting models' accuracy, three different cost functions have been tested, formulated in terms of discrete combinations of the speed, flow, and density values of real and simulated virtual detectors, within the simulated area. In particular, a combined total mean square normalized errors of the model estimated and real measured speed and flow is used first, specifically

$$f(\boldsymbol{x}) = \frac{1}{C}\sum_{k=1}^{K}\sum_{i=1}^{n}\left[(1-\mu)\left(1-\frac{u_{i,k}}{u_{i,k}^d}\right)^2 + \mu\left(1-\frac{q_{i,k}}{q_{i,k}^d}\right)^2\right], \tag{3.50}$$

where μ is a weighting factor equal to 0.5. Alternatively, by substituting flow with density in equation above, the cost function is reformulated as

$$f(\boldsymbol{x}) = \frac{1}{C}\sum_{k=1}^{K}\sum_{i=1}^{n}\left[(1-\mu)\left(1-\frac{u_{i,k}}{u_{i,k}^d}\right)^2 + \mu\left(1-\frac{\rho_{i,k}}{\rho_{i,k}^d}\right)^2\right]. \tag{3.51}$$

Moreover, by following the root mean square speed and density normalized errors the cost function is given as

$$f(\boldsymbol{x}) = \sqrt{\frac{1}{C}\sum_{k=1}^{K}\sum_{i=1}^{n}\left(\frac{u_{i,k}^d - u_{i,k}}{u_m^d}\right)^2}\sqrt{\frac{1}{C}\sum_{k=1}^{K}\sum_{i=1}^{n}\left(\frac{\rho_{i,k}^d - \rho_{i,k}}{\rho_m^d}\right)^2}, \tag{3.52}$$

where, $u_{i,k}$, $\rho_{i,k}$, and $q_{i,k}$ represent, respectively, the predicted mean speed, density and flow, computed at detector location k (K is the number of detectors that are available for calibration) and time instant i (n is the simulation time horizon) and $C = nK$; $u_{i,k}^d$, $\rho_{i,k}^d$ and $q_{i,k}^d$ represent, respectively, the observed mean speed, density and flow computed at location k and time instant i, while u_m^d and ρ_m^d denote the corresponding maximum values of the observed mean speed and density.

The calibration procedure commences with an initial random population of candidate solutions (chromosomes); every chromosome (calibrated model parameter vectors $\boldsymbol{x}$) is randomly initialized, within their predefined upper and lower bounds. A numerical simulation for the traffic flow situation is then carried out for each candidate chromosome, which is used along with the boundary input data, to produce a space-time distribution of flow and speed. Then, at each generation the cost function of each candidate chromosome is evaluated according to the pre-specified cost function, i.e. the discrepancy between the real-world traffic data and the simulated data; note that it is this step that suffers from significant computational resources, and calls for the use of surrogate models in order to decrease the computational effort of the optimization process. The assistance of these models lies in time-savings, due to avoiding the computationally intensive exact evaluations of each one of the candidate solutions, but using a trained neural network instead (Nikolos, 2013), as it was previously described. Subsequently, for each generation, the elitist reproduction scheme of the DE algorithm is implemented so as to evolve the newly generated population based on the mutation, crossover, and selection operators, aiming to the best parameter candidate vector, according to the proposed cost function. The whole procedure is terminated when a pre-described number of generations has been reached. The overall optimization scheme for the calibration of the considered macroscopic traffic flow models is described as a flow chart in Figure 3.5.

The following chapter contains the calibration and validation results of the single- and multi-lane GKT macroscopic traffic flow models, by employing the above optimization procedure. The same optimization procedure was also implemented for the calibration of the METANET macroscopic traffic flow model, followed by comparative results with the GKT one.

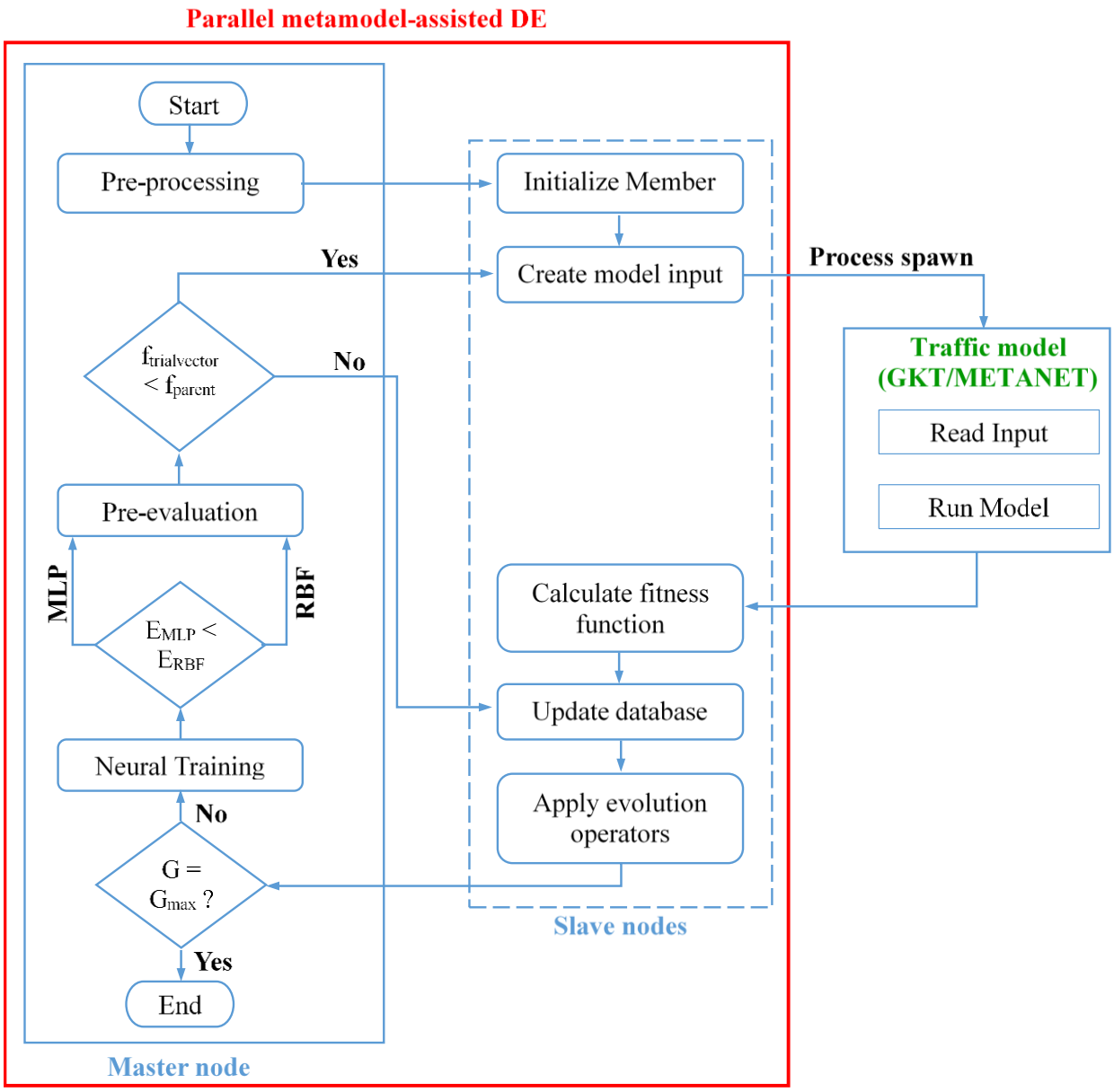

FIGURE 3.5: *Flowchart with the major steps of the optimization process.*

Chapter 4: Calibration and Validation Results

4.1 Introduction

The calibration process constitutes a crucial step for the successful development and application of any macroscopic traffic flow model in transportation planning and real traffic management. Indeed, the reliability and credibility of a model to reproduce different traffic flow conditions inside a freeway network with the best possible accuracy is of major importance. However, the estimation of proper parameter values used in the selected models (see Section 3.2) is a challenging task, because of the highly non-linear nature of the models equations in both its parameters and state variables. Furthermore, after the calibration procedure, the traffic flow models must be validated before their potential use. The validation procedure aims to ensure that the resulting traffic flow models reliably reflect the prevailing traffic flow characteristics of the investigated networks, thus they may sufficiently reproduce their typical traffic conditions.

This section continues with the evaluation of the proposed methodology against test cases using real traffic data from different motorway networks, considering the congestion created close to on/off-ramps during the morning peak periods. Section 4.2 presents the considered freeway stretches and the utilized real traffic data, Section 4.3 describes the calibration settings for both GKT and METANET models for the optimization procedure, while Section 4.4 displays the calibration and validation results for 4 different scenarios. Finally, Section 4.5 summarizes the results and conclusions of the calibration procedure.

4.2 Tests Networks and Real Traffic Data

The second-order macroscopic GKT traffic flow model described in Section 3.2.1 is applied to two different motorway networks in order to calibrate its parameters and validate its equations under recurrent traffic flow conditions. Moreover, a comparative study of the GKT and the METANET models (Section 3.2.2) for the considered motorway network in U.K., based on the previous described calibration methodology (see Section 3.2.3), is also presented.

4.2.1 The Motorway Network in U.K. and the Real Traffic Data

The first considered network is a stretch of the M56 motorway located in the areas of Cheshire and Greater Manchester, U.K. (with direction from Chester to Manchester), as shown in Figure 4.1. Specifically, the chosen network, sketched in Figure 4.2, is 9.45 km long and is composed by three lanes, including one off-ramp and a two-lane on-ramp, which, before merging into the mainstream, splits into two separate lanes.

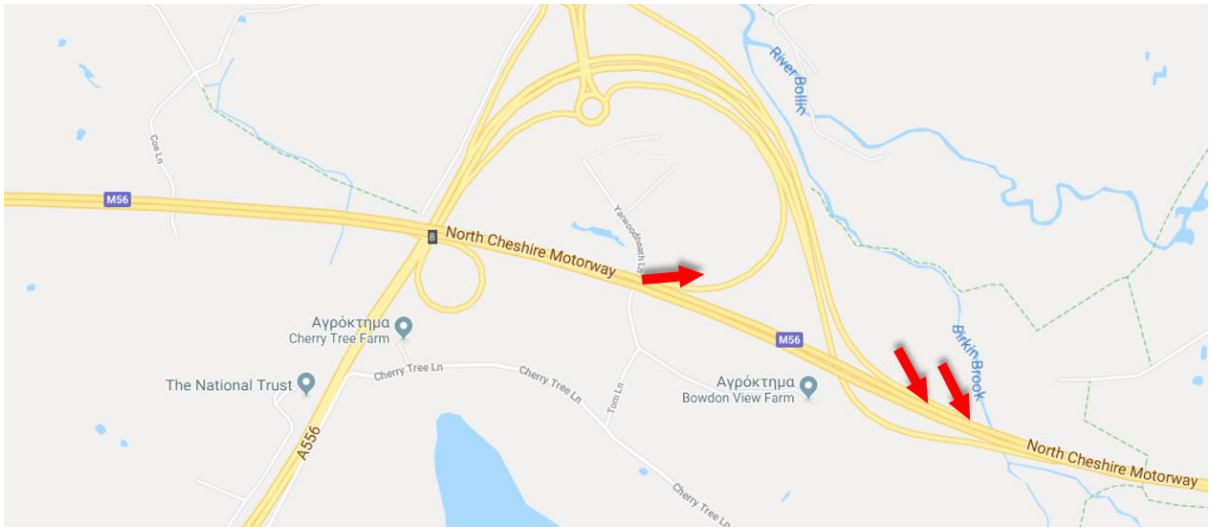

FIGURE 4.1: *U.K. freeway stretch.*

Real-time traffic data, provided by MIDAS database[1], is collected through 6 detector-stations (D-locations in Figure 4.2) that deliver measurements of flow and speed per lane with a time resolution of 60 s. Detectors are also installed on the ramps, measuring the corresponding incoming and outgoing traffic flows. Measured data corresponding to the stretch's boundaries were also available, and used as boundary conditions in the numerical model.

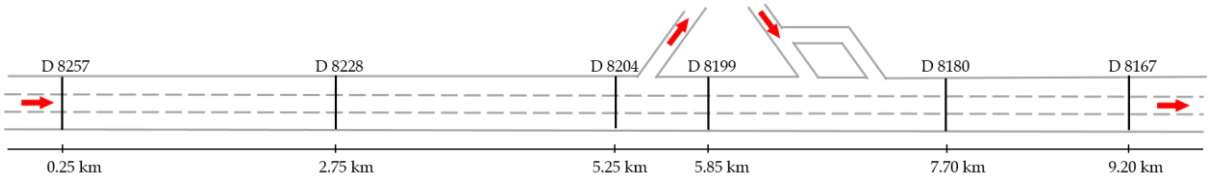

FIGURE 4.2: *A graphical representation of the U.K. freeway stretch considered.*

The quantitative real-time traffic data analysis regarding the considered test network showed that a major recurrent congestion is formed, originated from high on-ramp flows during a typical morning's rush hour (see Figure 4.3). Hence, it was decided to use the data of June 3rd 2014 for model calibration, taking into account the morning peak hours, specifically from 6: 30 a.m. to 9: 00 a.m.. Morning peak data of June 24th 2014 were reserved for model validation. In particular, based on the contour plots shown in Figure 4.4, for visual inspection of the space-time evolution of the real speed measurements for the 3rd and 24th of June 2014, it can be observed that traffic congestion is formed upstream of the second on-ramp between 7: 00– 8: 00 a.m. for both days; this strong congestion pattern spills back onto the freeway mainstream, producing an intensive high density area of several kilometers. It is worth noting that the dominant criterion for selecting these two days was that, during the morning hours 6: 30 a.m. to 9: 00 a.m. no incident and no sensor failure occurred at the examined test network, which could not be reproduced by the utilized or any other traffic flow models.

[1] Highways Agency, 2007. Motorway Incident Detection and Automatic Signaling (MIDAS) Design Standard. (No. 1st ed.). Bristol, UK.

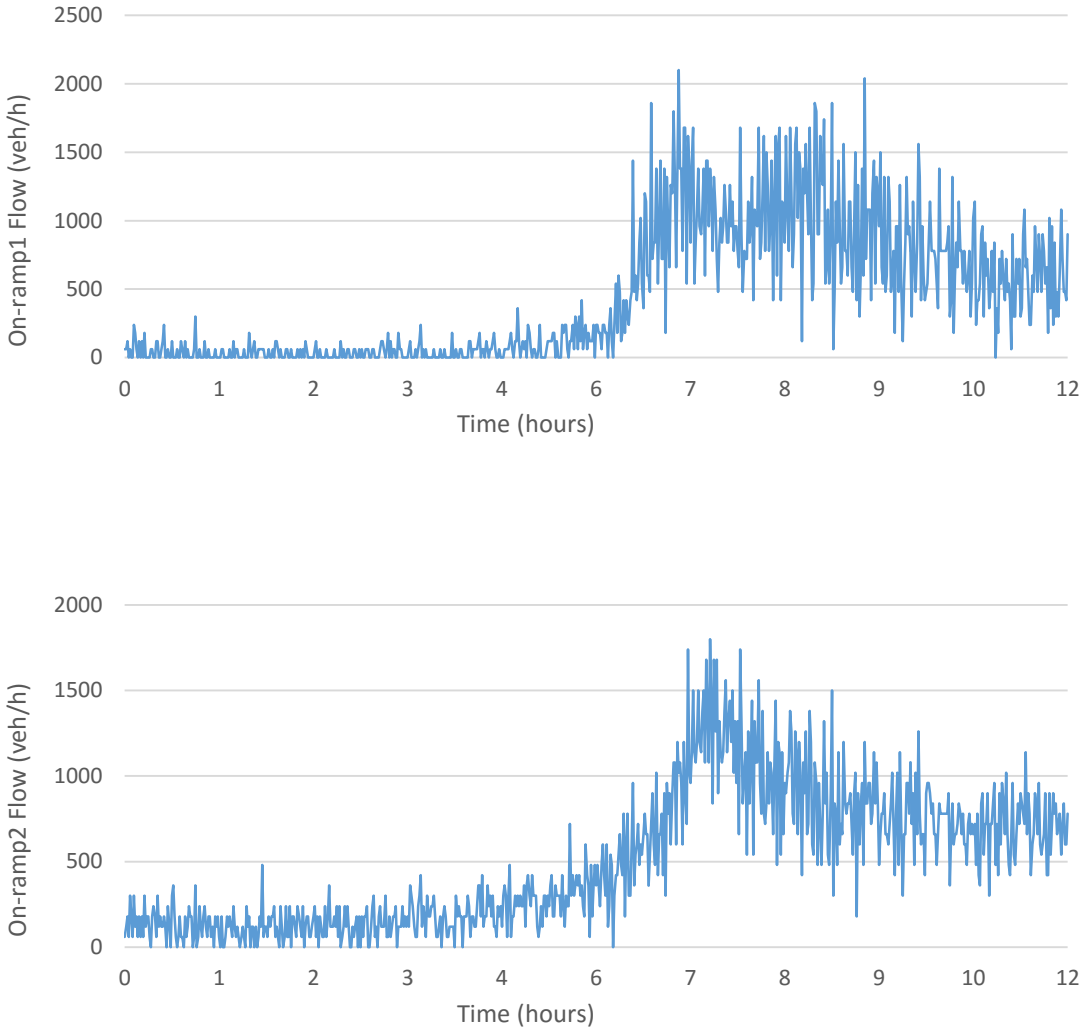

FIGURE 4.3: *Measured on-ramp flows of the U.K. freeway stretch for 3/6/2014.*

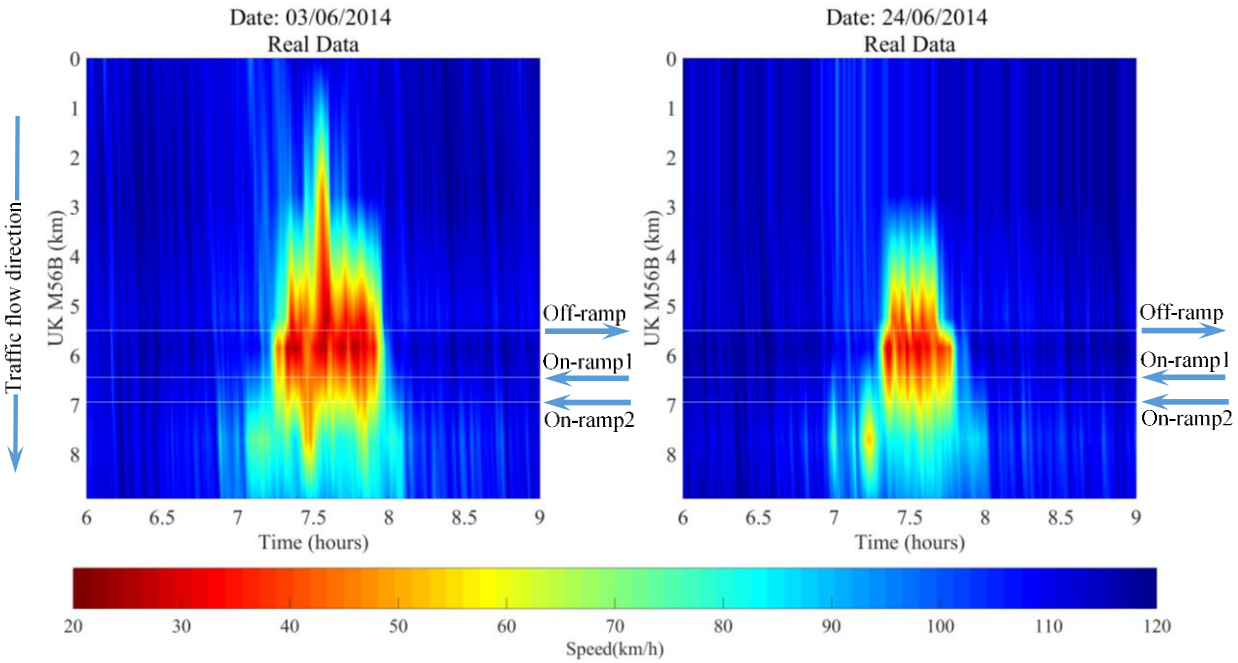

FIGURE 4.4: *Phase space speed dynamics at the U.K. freeway stretch for two different days.*

4.2.2 The Motorway Network in Greece and the Real Traffic Data

The second freeway stretch considered in this thesis is a part of Attiki Odos motorway in Athens, Greece. Specifically, it is an urban motorway characterized by a traffic pattern that is strongly dependent on the demand due to the commuters using the specific network. In Figure 4.5, an aerial map of the area is shown; the highlighted road is the considered stretch of Attiki Odos freeway, where the direction from the Airport to Elefsina will be considered (from East to West).

FIGURE 4.5: *Attiki odos freeway stretch.*

Specifically, the chosen network, as shown in Figure 4.6, is 6.2 km long (from 34th to 27.8th km) and is composed by three lanes, which widens to four lanes from 30.8th to 30.3rd km, including three on-ramps and three off-ramps, depicted by arrows in Figure 4.6. The locations of the available detector stations (13 in total) are also illustrated in Figure 4.6.

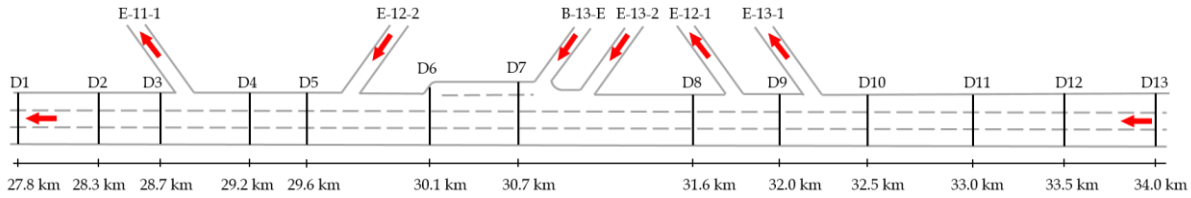

FIGURE 4.6: *A graphical representation of the considered Attiki Odos freeway stretch.*

The real traffic data were provided by the company ATTIKES DIADROMES S.A., which is responsible for the operation and maintenance of the motorway, as well as for traffic management and customer service. In particular, data were collected at the 13 detector-stations (Figure 4.6) that delivered measurements of flow and speed per lane with a time resolution of 20 s, for the time period May–June 2009. Detectors were also installed on the ramps, measuring the corresponding ingoing and outgoing traffic flows. Measured data corresponding to the stretch's boundaries were also available, and were used as boundary conditions in the numerical model.

A qualitative of real-time data analysis shows that, within this examined freeway stretch, a recurrent congestion is formed, originated from high exit flow off-ramp during a typical morning's rush hour. Hence, it was decided to take into account the morning rush hour, specifically from 6:00 a.m. to 12:00 p.m., and to use morning peak data of June 16th 2009 for model calibration, while corresponding data of June 23rd 2009 are reserved for model validation; in both days no incident and no sensor failure was reported at the test network. At this point, it is important to highlight that although recurrent congestion originated from an off-ramp area is a quite frequent case of traffic flow degradation, appearing mainly at freeways during the peak periods, it is not a trivial task to deal with, since it is difficult to control the freeway exit flow.

Based on the contour plots shown in Figure 4.7, the congestion creation area is formed upstream of the off-ramp E-11-1 during $8:00 - 10:00$ a.m. for both days. In particular, this major congestion originates at the 29th km and spills back onto the considered network, producing an intensive high density area up to the 33nd km. The main reason behind this major congestion created in the specific diverging area is a combination of the increased exit flow that the off-ramp E-11-1 receives and its limited capacity, along with an increase to the entering flow from upstream The traffic congestion lasts for a couple of hours, until it is dissolved thanks to the demand reduction at the end of the peak period. It is emphasized that on the selected two days there are no incidents nor sensor failures during the morning hours at the considered network.

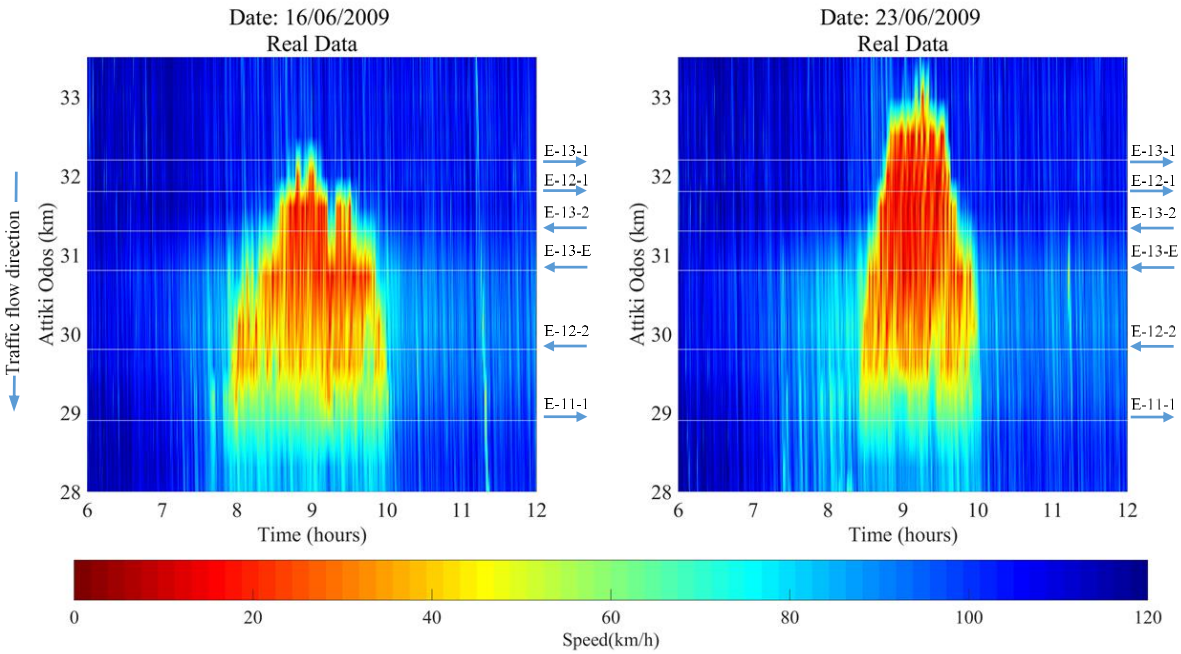

FIGURE 4.7: *Phase space speed dynamics at Attiki Odos freeway stretch for two different days.*

4.3 Calibration Settings

The main aim in this chapter is to assess the continuous second-order GKT model by implementing the automated calibration procedure, as presented in Section 3.2.3, in order to represent the traffic conditions of the specific freeway stretches (see Section 4.2) with the highest possible level of accuracy. Subsequently, the same optimization scheme is applied to the widely used discrete second-order METANET model as to compare these two selected traffic flow models. Hence, the optimization problem must be solved to mine the optimal design parameters of the models, which minimize the relative error between the model prediction and the observed data.

Herein, the parameter vector for the calibration of the single-lane GKT model consists of the maximum desired velocity u_{max}, the maximum density ρ_{max}, the critical density ρ_{cr}, the desired time gap T, the anticipation factor γ, the relaxation time τ, the variance pre-factor for free traffic A_0, the pre-factor δA and the transition width $\delta\rho$. Thus, the parameter vector $\boldsymbol{x}$ for the GKT model is $\boldsymbol{x} = [u_{max},\ \rho_{max},\ \rho_{cr}, T, \gamma,\ \tau,\ A_0,\ \delta A,\ \delta\rho]$. In the case of the automated calibration process for the multi-lane GKT model, the parameter vector to be calibrated consists of the following additional parameters: the frequency factor for lane changing, ν_f, the critical density for lane changing probability, ρ_P, the percentage of reducing speed at exiting/entering, (u_{rmp}/u_l), and the spontaneous lane-changing parameter, $k_l^{L,R}$. Specifically, for the examined three-lane freeway stretch in the U.K. (see Section 4.2.1) the parameter vector $\boldsymbol{x}$ takes the form $\boldsymbol{x} = [u_{max,l},\ \rho_{max,l},\ \rho_{cr,l}, T_l, \gamma_l,\ \tau_l,\ A_{0,l},\ \delta A_l,\ \delta\rho_l, (u_{rmp}/u_1), \nu_f, \rho_P, k_1^L, k_2^R, k_2^L, k_3^R\ ]$, $l = 1,2,3$, (ending up to 34 parameters/design variables in total).

Regarding the METANET model, the parameter vector $\boldsymbol{x}$ consists of the free flow speed u_f, the critical density ρ_{cr} and the parameters a, τ, ν and δ, which are common for all

the freeway sections. Moreover, the model includes two extra parameters, which are known from previous validation exercises to be of minor importance and are, therefore, given constant values, in order to reduce the dimension of the parameter vector. In particular, κ is set equal to 10 $veh/km/lane$ and u_f is set to 7 km/h. Thus, one single fundamental diagram is considered for all freeway sections in this model. Considering the above, the parameter vector for the METANET model is $\boldsymbol{x} = [\tau,\ \nu, \delta, u_f, \rho_{cr}, a]$.

Hence, for both traffic flow models the vector $\boldsymbol{x}$ includes the unknown models parameters that need to be defined for each model so as to minimize the discrepancy between the simulated and real traffic data by using an appropriate cost function, hereafter denoted by $f(\boldsymbol{x})$. The parameter estimation problem consists of finding the optimal vector of $\boldsymbol{x}$ subject to equations (3.1) and (3.2) in case of the GKT model or to model (3.8) in case of the multi-lane GKT model, and to equations (3.29) and (3.30) in case of the METANET model for all $\boldsymbol{x} \in \Omega$, where Ω defines a bounded admissible parameter space, determined on the basis of physical constraints. However, such a parameter estimation (model calibration) problem is particularly challenging, since it is formulated as a global optimization of a continuous multi-extrema cost function, see, e.g., Ngoduy & Maher, 2012, with numerous local minima, which traditional gradient-based optimization algorithms typically fail to avoid. To this end, we apply the parallel, metamodel-assisted Differential Evolution algorithm, as presented in Section 3.2.3, for optimizing the aforementioned complex continuous problem with multiple local minima (Nikolos, 2013; Strofylas & Nikolos, 2015).

The runs of the DE algorithm for the calibration of the GKT model have been performed on a DELL™ R815 PowerEdge™ server with four AMD Opteron™ 6380 sixteen-core processors at 2.50 GHz (64 cores in total), while the traffic simulations were performed using a desktop computer with 2.4 GHz CPU and 2.0 GB of RAM. The calibration procedure, including the traffic flow models and the optimization algorithm, has been programmed in FORTRAN.

4.4 Calibration and Validation Results for Different Test Cases

4.4.1 Calibration and Validation of the single-lane GKT Model Using the Parallel, Synchronous, Metamodel-Assisted DE Algorithm with Different Fitness Functions (U.K. network)

As mentioned before, the optimization problem addressed in this thesis consists of minimizing the deviation between the GKT model calculations and the real-measured traffic data. Hence, the first test case considers the employment of the parallel, synchronous, metamodel-assisted DE algorithm (see Section 3.2.3) for the calibration of the model using real traffic data from the motorway network in the U.K. (see Section 4.2.1); in this test case, a single-lane with the mean values of the flow quantities of the three-lane stretch is considered. More specifically, the numerically discretized GKT model was first calibrated to specify the optimal parameter values for the considered network, using the measured data for a specific day. Eventually, the GKT model was validated using data collected at the same freeway on a different day, to ensure that the model is able to reliably reproduce the traffic conditions of the examined site.

Initially, in order to evaluate the resulting model accuracy, the three different cost functions (equations (3.50), (3.51) and (3.52)), presented in Section 3.3.3, are tested. Briefly, a combined total mean square normalized error of the model estimated and real measured speed and flow was used first:

$$f(\boldsymbol{x}) = \frac{1}{C}\sum_{k=1}^{K}\sum_{i=1}^{n}\left[(1-\mu)\left(1-\frac{u_{i,k}}{u_{i,k}^{d}}\right)^{2} + \mu\left(1-\frac{q_{i,k}}{q_{i,k}^{d}}\right)^{2}\right]. \tag{4.1}$$

Next, by substituting flow with density in the equation above, the cost function is reformulated as

$$f(\boldsymbol{x}) = \frac{1}{C}\sum_{k=1}^{K}\sum_{i=1}^{n}\left[(1-\mu)\left(1-\frac{u_{i,k}}{u_{i,k}^{d}}\right)^{2} + \mu\left(1-\frac{\rho_{i,k}}{\rho_{i,k}^{d}}\right)^{2}\right]. \tag{4.2}$$

Finally, by utilizing the root mean square speed and density normalized errors, the third cost function that is tested is given as

$$f(\boldsymbol{x}) = \sqrt{\frac{1}{C}\sum_{k=1}^{K}\sum_{i=1}^{n}\left(\frac{u_{i,k}^{d}-u_{i,k}}{u_{m}^{d}}\right)^{2}}\sqrt{\frac{1}{C}\sum_{k=1}^{K}\sum_{i=1}^{n}\left(\frac{\rho_{i,k}^{d}-\rho_{i,k}}{\rho_{m}^{d}}\right)^{2}}. \tag{4.3}$$

4.4.1.1 Calibration Results

The calibration results were obtained using real traffic data from the 3rd of June, 2014 (see Section 4.2.1). The model parameters with their corresponding feasible bounds, conforming with those given in Treiber *et al.*, 1999, Helbing *et al.*, 2001, Treiber & Kesting, 2013, and Delis *et al.*, 2014, are presented in Table 4.1. The DE algorithm was employed with a population size equal to 50, whereas the maximum number of generations was set equal to 1100; the control parameters for the mutation and crossover operations were $F = 0.6$ and $C_r = 0.45$.

TABLE 4.1: *Admissible range of the parameter vector used for the GKT model calibration (U.K. network – as single lane).*

Model parameters	***Units***	***Bounds***
Desired free speed, u_{max},	km/h	[105, 135]
Maximum density, ρ_{max}	veh/km	[100, 200]
Critical density, ρ_{cr}	veh/km	[30, 60]
Desired time gap, T	s	[0.5, 2.5]
Anticipation factor, γ		[1, 2]
Relaxation time, τ	s	[10, 40]
Variance pre-factor for free traffic, A_0		[0.0025, 0.015]
Pre-factor, δA		[0.01, 0.03]
Transition width, $\delta\rho$	veh/km	[3.5, 20]

TABLE 4.2: *Cost function values and the resulted optimal parameter values for the calibration phase (U.K. network – as single lane).*

Model Parameters	u_{max} (km/h)	ρ_{max} (veh/km)	ρ_{cr}	T (s)	γ	τ (s)	A_0	δA	$\delta\rho$ (veh/km)	*Cost Function Value (%)*
Cost Function (4.1)	115	170	42	2	2	20	0.0025	0.015	10	**1.16**
Cost Function (4.2)	120	150	40	2.3	2	24	0.0025	0.019	11	**1.45**
Cost Function (4.3)	115	140	45	2.4	2	22	0.0025	0.027	12	**0.2**

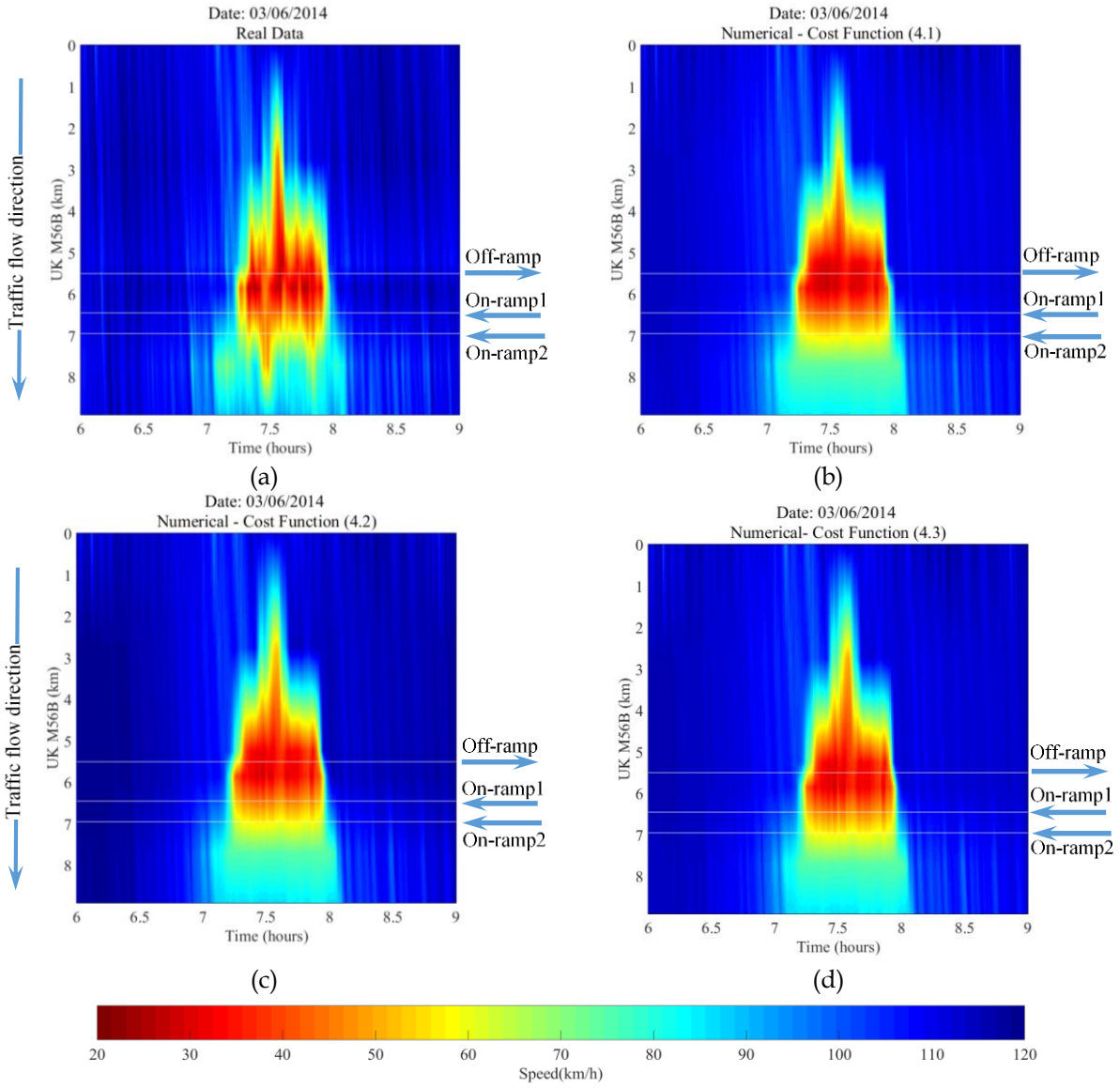

FIGURE 4.8: *(U.K. network – as single lane) Phase space speed dynamics for real measured speed (a) and the model predictions for the calibration date using: (b) cost function (4.1), (c) cost function (4.2), (d) cost function(4.3).*

The considered 9.45 km stretch was simulated for 3 morning peak hours (i.e. from 6:00 a.m. to 9:00 a.m.), whereas the space discretization was $\Delta x = 100$ m. The numerical scheme is stable under the usual CFL stability condition for explicit discretization schemes thus the CFL value was set equal to 0.5. The clock computational time for 1100 generations was 146.5 min. Table 4.2 contains the minimum value of the three alternative cost functions (which were obtained in three respective optimization runs for the same calibration problem), along with the resulted optimal parameters. Very good agreement with the measured data set and very similar optimal parameter vectors have been obtained with all three cost functions.

Figure 4.8 displays the space-time evolution of the speed reproduced by simulation compared to the observation for the calibration day, for the three alternative cost functions Figure 4.9 contains the DE convergence history of the best value of the three different cost functions in each generation. Finally, Figures 4.10-4.12 display the speed dynamics for all detector locations, produced using the optimal parameter values of the calibration procedure with the three different cost functions. It is clear that for all the examined cost functions the real traffic conditions are well reproduced by the calibrated model, capturing with sufficient accuracy when and where the traffic flow becomes congested, for the correct duration and extent, as observed in the real traffic data, regardless of which function was used.

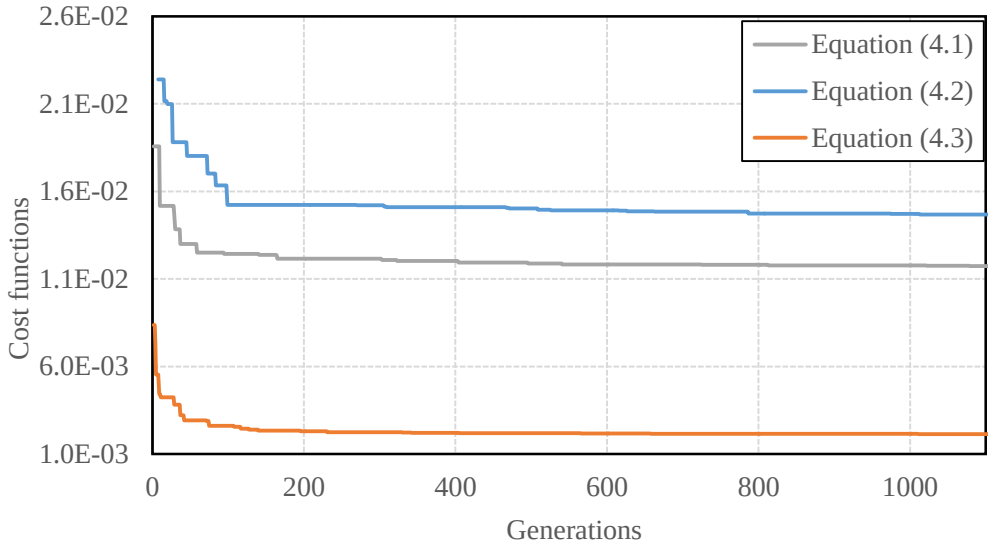

FIGURE 4.9: *(U.K. network – as single lane) The convergence history of the best solution of each generation of the DE algorithm as a function of the generation number for the three cost functions.*

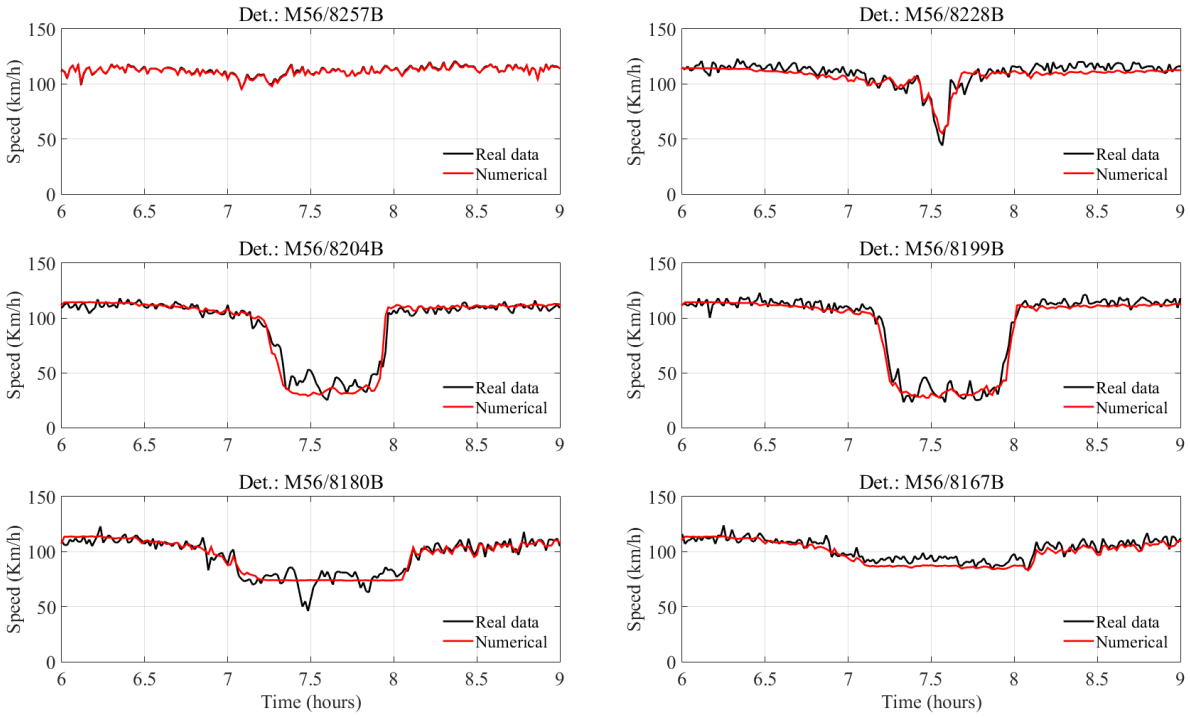

FIGURE 4.10: *(U.K. network – as single lane) Time-series of the real speed measurements (black) and the model prediction of speed (red) using cost function (4.1) at various detector locations for the* ***calibration day****.*

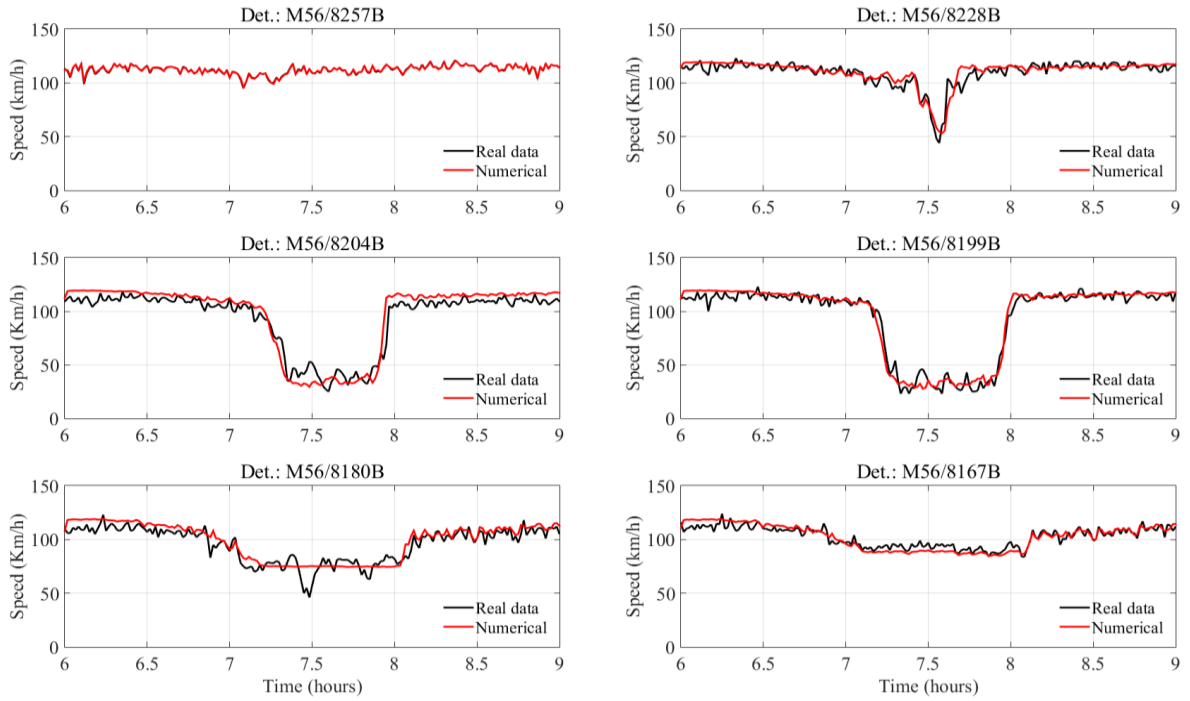

FIGURE 4.11: *(U.K. network – as single lane) Time-series of the real speed measurements (black) and the model prediction of speed (red) using cost function (4.2) at various detector locations for the* ***calibration day****.*

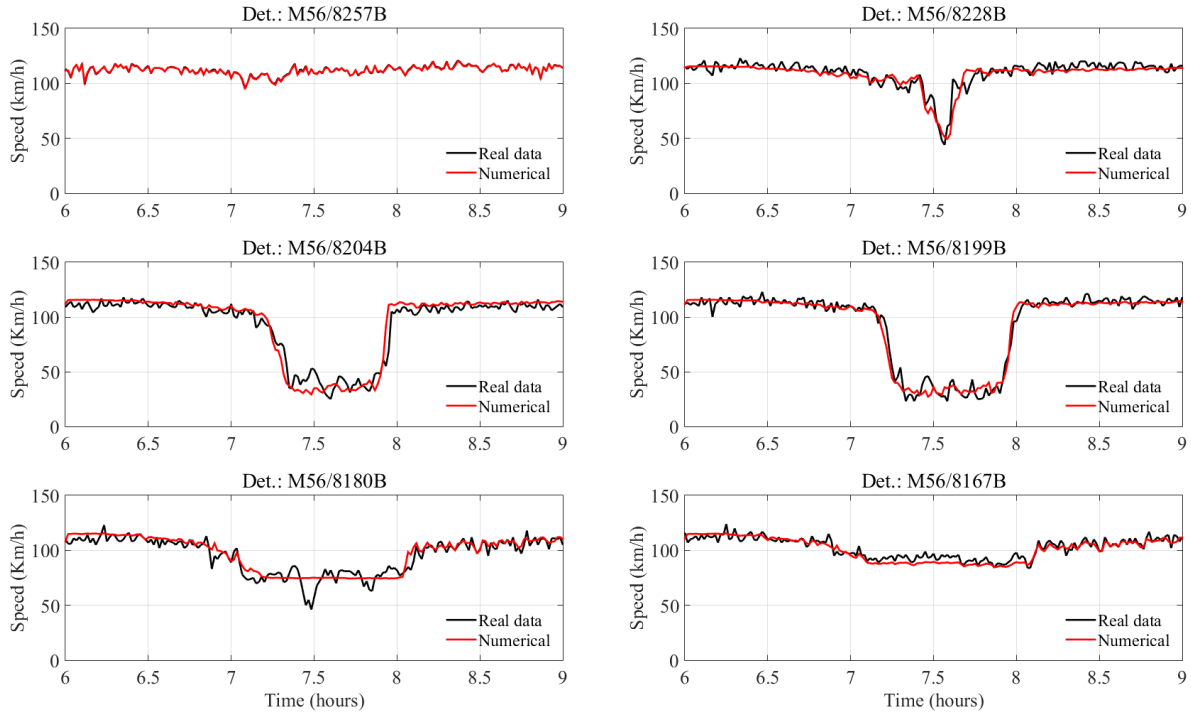

FIGURE 4.12: *(U.K. network – as single lane) Time-series of the real speed measurements (black) and the model prediction of speed (red) using cost function (4.3) at various detector locations for the* ***calibration day****.*

4.4.1.2 Validation Results

To test and assess the robustness of the GKT model the resulting, from the previous calibration procedure (Section 4.4.1.1), optimal parameters of the three proposed cost functions were applied to the same motorway stretch, but for a different day, the 24th of June, 2014. For the validation day, the recurrent congestion in the traffic flow behavior is similar to the one of the calibration day. The cost function values obtained for this validation procedure were 1.64% for equation (4.1), 4% for equation (4.2) and 4.8% for equation (4.3).

The validation results presented in Figures 4.13, 4.14, 4.15 and 4.16, are seen to capture with sufficient accuracy the real traffic flow conditions in the particular U.K. freeway stretch, for all the examined cost functions, although not at the exact same level of accuracy as the calibrated ones. In particular, the GKT model was able to reproduce the congestion extend as well as the average speed reduction but slightly overestimated its duration (starting later and finished later) at some locations. However, the overall comparison, also in terms of the three alternatives cost functions, is considered as satisfactory, given the complexity of the traffic flow phenomena.

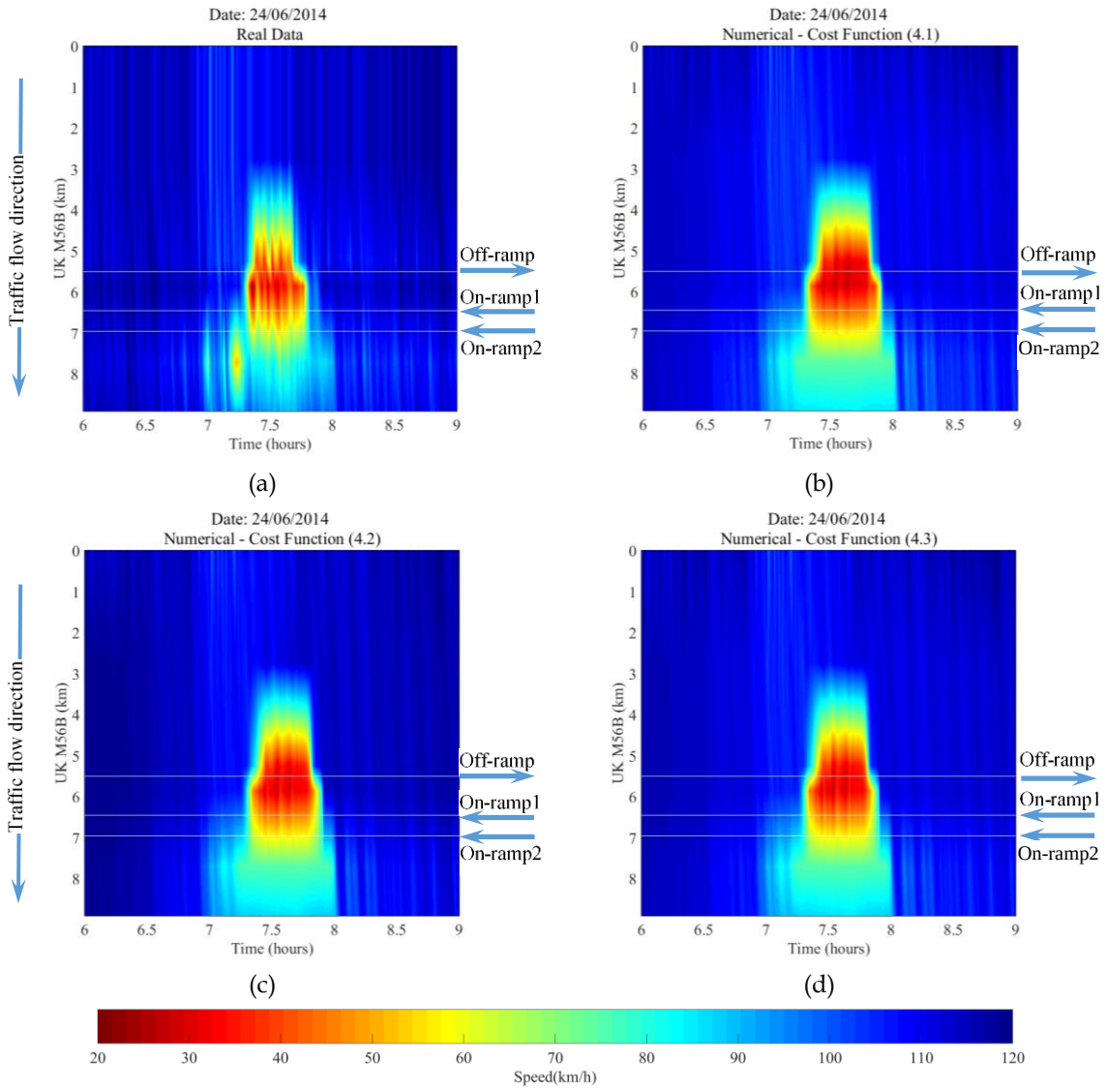

FIGURE 4.13: *(U.K. network – as single lane) Phase space speed dynamics for real measured speed (a) and the GKT model predictions for the validation date using: (b) cost function (4.1), (c) cost function (4.2), (d) cost function (4.3).*

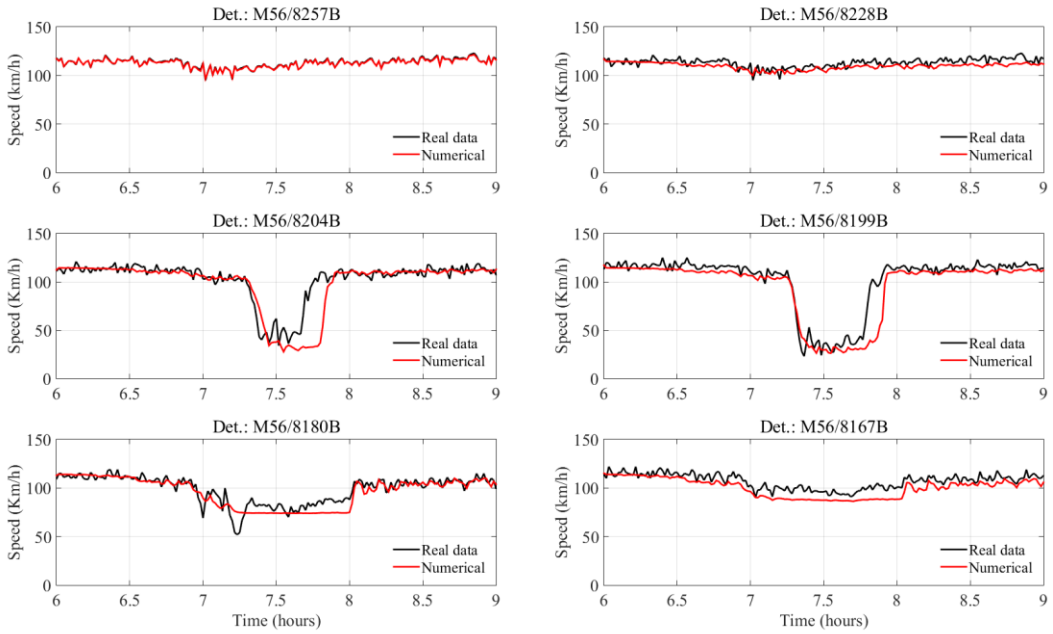

FIGURE 4.14: *(U.K. network – as single lane) Time-series of the real speed measurements (black) and the GKT model prediction of speed (red) using cost function (4.1) at various detector locations for the* ***validation day****.*

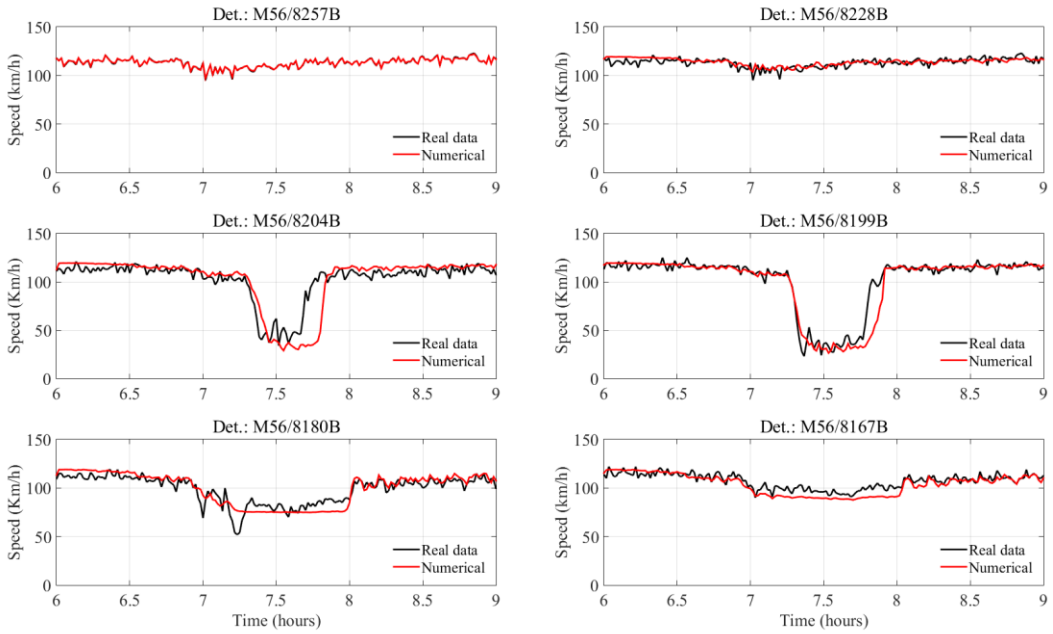

FIGURE 4.15: *(U.K. network – as single lane) Time-series of the real speed measurements (black) and the GKT model prediction of speed (red) using cost function (4.2) at various detector locations for the* ***validation day****.*

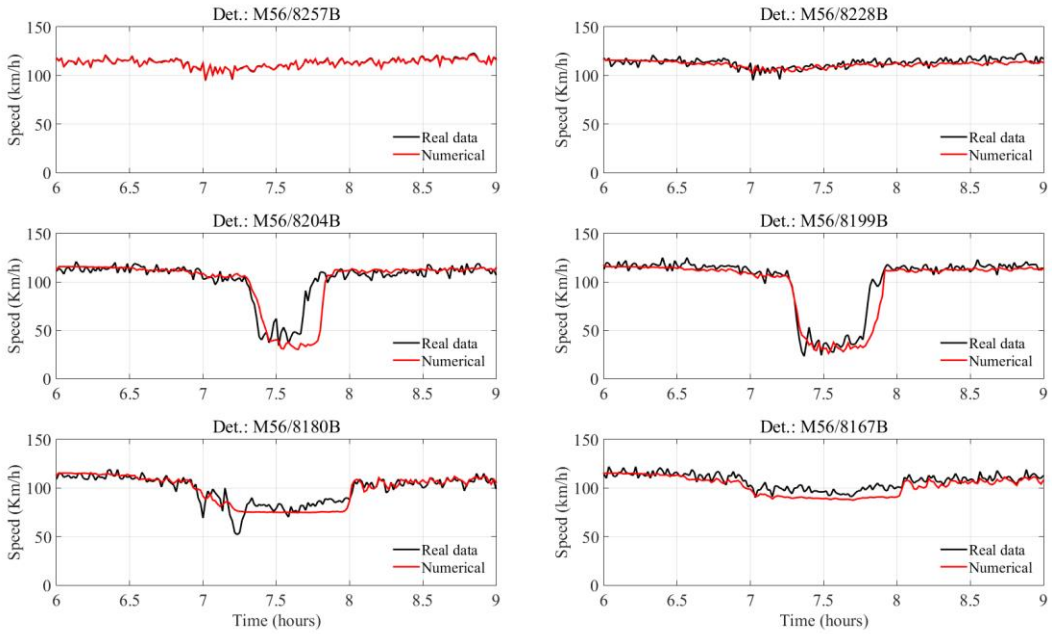

FIGURE 4.16: *(U.K. network – as single lane) Time-series of the real speed measurements (black) and the GKT model validation of speed (red) using cost function (4.3) at various detector locations for the* ***calibration day****.*

Based on the fact that a very good agreement with the measured data set and very similar optimal parameter vectors have been produced with all three cost functions, but cost function (4.1) had slightly better value for the validation procedure, the next test cases will be conducted only using this cost function.

4.4.2 Calibration and Validation of the Multi-Lane GKT Model Using the Parallel, Synchronous, Metamodel-Assisted DE Algorithm (U.K. network)

The second problem encountered, concerns the validation of the multi-lane GKT model (as presented in Section 3.2.1.1) with respect to its accuracy in the reproduction of the recurrent congestion originated from high on-ramp flows during the morning peak hours, using real traffic data from the three-lane freeway stretch in the U.K. (see Section 4.2.1). As described in Section 3.2.1.1, in the developed multi-lane GKT model, the lane-changing terms, simulating lane-changes due to vehicle interactions as well as spontaneous ones, are introduced as source and sink terms in the model equations; the model provides the ability to use different calibration parameters per lane. Hence, the numerically discretized multi-lane GKT model was first calibrated to specify the optimal parameter values for the considered network, using the measured data for a specific day. Again, to demonstrate the validity of the developed model to reliably reproduce the traffic conditions of the examined site, the optimal parameters resulting from the calibration procedure were applied to the same freeway on a different day.

Before we proceed, it is important to highlight that the selected cost function (4.1) is adapted in this case, in order to calibrate the complicated multi-lane GKT model that has a

relatively large number of (usually) counteracting calibration parameters. Therefore, the cost function (4.1) is reformulated as

$$f(\boldsymbol{x}) = \frac{1}{C}\sum_{l=1}^{N}\sum_{k=1}^{K}\sum_{i=1}^{n}\left[(1-\mu)\left(1-\frac{u_{l,i,k}}{u_{l,i,k}^{d}}\right)^{2}+\mu\left(1-\frac{q_{l,i,k}}{q_{l,i,k}^{d}}\right)^{2}\right]. \tag{4.4}$$

where, $u_{l,i,k}$, and $q_{l,i,k}$ represent the predicted mean speed and flow, respectively, computed for lane l, location k (K is the number of detectors that are available for calibration) and time instant i (n is the simulation time horizon); $u_{l,i,k}^{d}$ and $q_{l,i,k}^{d}$ represent, respectively, the observed mean speed and flow computed at lane l, location k and time instant i, while $C = N \cdot n \cdot K$, and μ is a weighting factor equal to 0.5.

4.4.2.1 Calibration Results

As in the previous test case, the real measurements per-lane used for the calibration process were collected on the M56 motorway in U.K. on the 3rd of June, 2014. The multi-lane GKT model parameters, along with their corresponding admissible bounds, being consistent with those given in Delis *et al.*, 2014, 2015b, are presented in Table 4.3. The DE algorithm was employed with a population size equal to 60, whereas the maximum number of generations was set equal to 1500; the control parameters for the mutation and crossover operations were $F = 0.6$ and $C_r = 0.45$.

TABLE 4.3: *(Multilane U.K. network) Admissible range of the parameter vector used for* ***the multi-lane*** *GKT model calibration.*

Model parameters	***Units***	***Bounds***
Desired free speed, $u_{max,l}$	km/h	[80, 140]
Maximum density, $\rho_{max,l}$	veh/km	[140, 160]
Critical density, $\rho_{cr,l}$	veh/km	[30, 60]
Desired time gap, T_l	s	[1, 2]
Anticipation factor, γ_l		[1, 1.5]
Relaxation time, τ_l	s	[20, 40]
Variance pre-factor for free traffic, $A_{0,l}$		[0.006, 0.01]
Pre-factor, δA_l		[0.008, 0.04]
Transition width, $\delta\rho_l$	veh/km	[3.5, 20]
Frequency factor for lane changing, ν_f		[0.1, 1]
Critical density for lane changing probability, ρ_P,		[0.02, 0.04]
Percentage of reducing speed at exiting/entering, (u_{rmp}/u_1)		[0.4, 0.9]
Spontaneous lane-changing factor, k_1^L	Events/sec/m	[0.001, 0.1]
Spontaneous lane-changing factor, k_2^R	Events/sec/m	[0.001, 0.04]
Spontaneous lane-changing factor, k_2^L	Events/sec/m	[0.001, 0.1]
Spontaneous lane-changing factor, k_3^R	Events/sec/m	[0.001, 0.04]

Again, the considered U.K. stretch (9.45 km length) was simulated for 2.5 morning peak hours (i.e. from 6: 30 a.m. to 9:00 a.m.), whereas the space discretization was $\Delta x = 100$ m and

the CFL value was set equal to 0.5, as in the first test case. The clock computational time for 1500 generations was 781.3 min.

Figure 4.17 displays the space-time evolution of the simulated speed, contrasted to the observations for the calibration day. Figure 4.18 contains the DE convergence history of the best value of the cost function (4.4) in each generation. Figure 4.19 depicts the measured and estimated speed dynamics for all detector locations around the congested area; as it can be observed, the real traffic conditions are well reproduced by the calibrated model, capturing with sufficient accuracy the onset of congestion with accurate timing and at the correct location, as observed in the real traffic data. The optimal model parameters and the minimum value of the cost function are given in Table 4.4.

TABLE 4.4: *(Multilane U.K. network) Cost function values and the resulted optimal parameter values for the calibration phase.*

Lanes	u_{max} $\frac{km}{h}$	ρ_{max} $\frac{veh}{km}$	ρ_{cr}	T (s)	γ	τ (s)	A_0	δA	$\delta\rho$ $\frac{veh}{km}$	v_f	ρ_P	$\left(\frac{u_{rmp}}{u_1}\right)$	k_1^L	k_2^R $\frac{Events}{sec \cdot lane}$	k_2^L	k_3^R
Lane1	96	140	30	1.4	1.5	28	0.009	0.01	20							
Lane2	118	142	59	2	1.5	23	0.0065	0.032	10	0.44	0.02	0.76	0.003	0.007	0.001	0.04
Lane3	128	140	60	2	1.5	21	0.0064	0.032	14							
Cost Function Value (%) : 2.9																

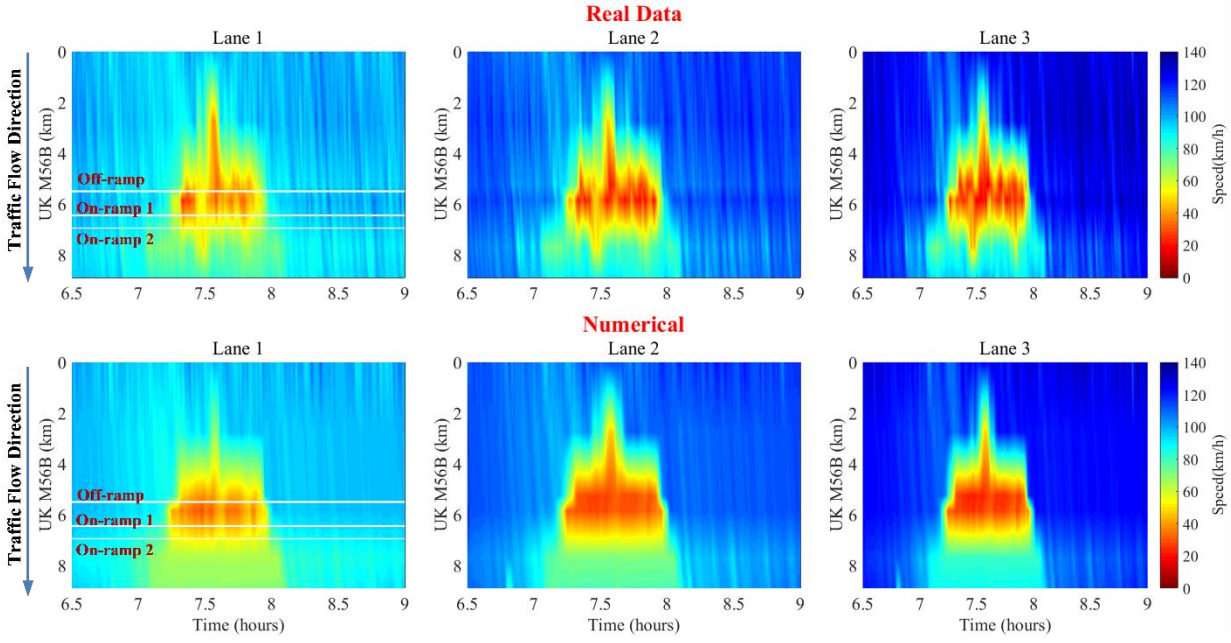

FIGURE 4.17*: (Multilane U.K. network) Lane phase space speed dynamics for real measured speed (upper) and the GKT model prediction (lower) for the* ***calibration date.***

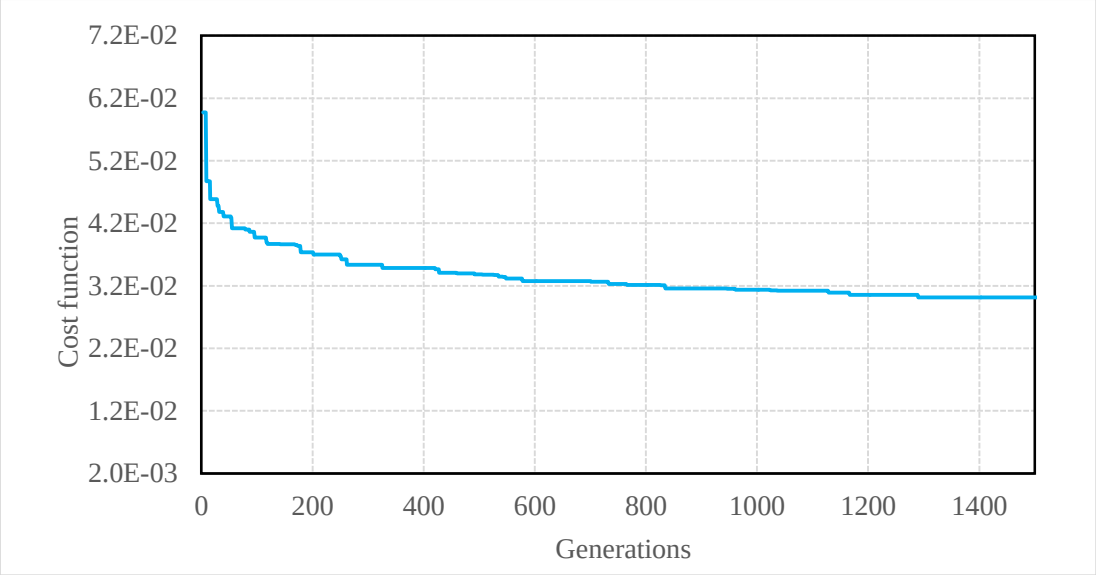

FIGURE 4.18: *(Multilane U.K. network) The convergence history of the best solution of each generation of the DE algorithm as a function of the generation number.*

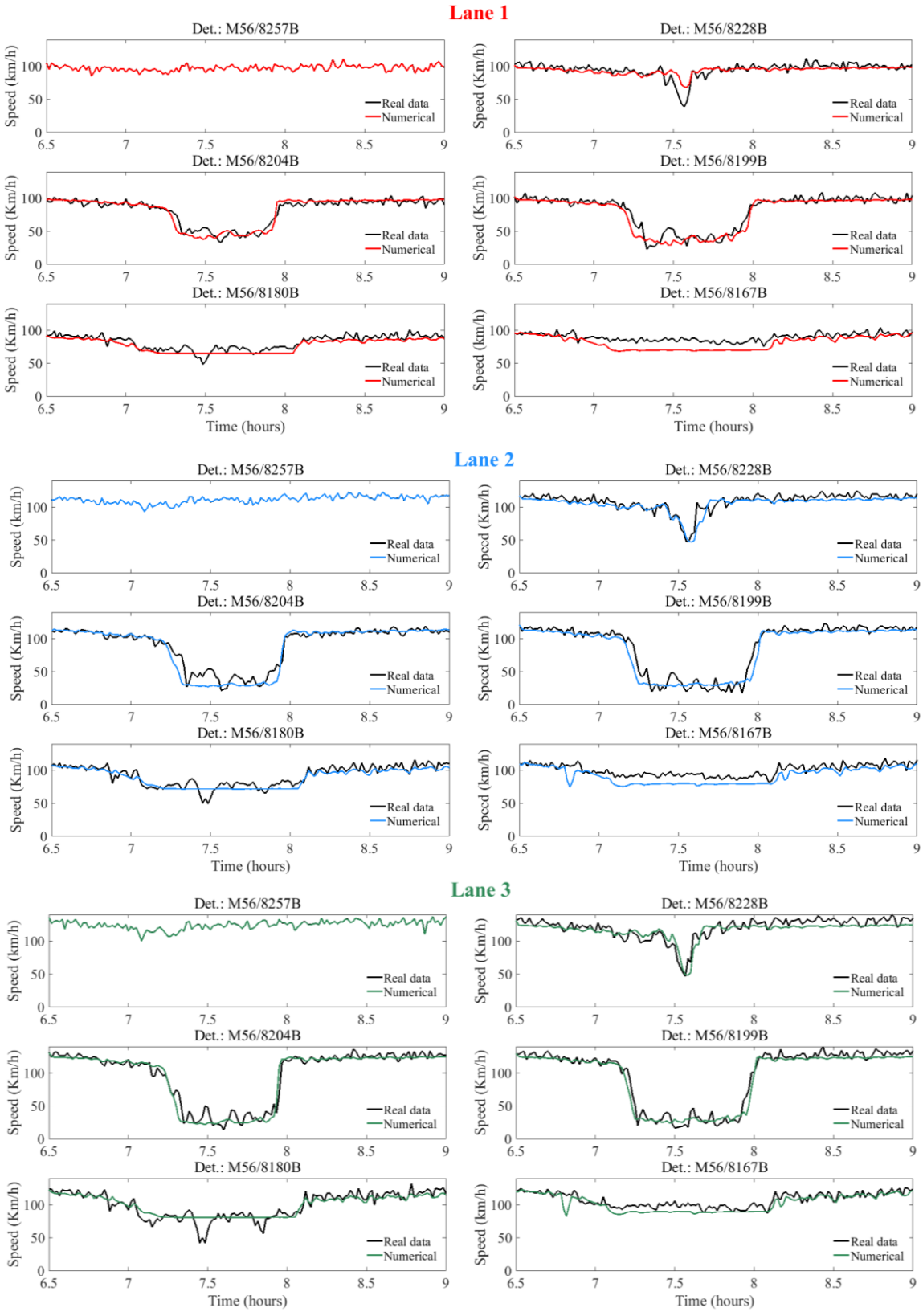

FIGURE 4.19: *(Multilane U.K. network) Time-series of the real speed measurements (black) and the GKT model prediction of speed at various detector locations for the* ***calibration day****.*

4.4.2.2 *Validation Results*

Again, to assess the robustness of the produced calibrated parameters, the resulting multi-lane GKT model was validated using real traffic data in the same freeway stretch on a different day, which is the 24th of June, 2014, using the optimal parameters of the previous calibration procedure (Section 4.4.2.1). The validation results presented in Figure 4.20 and Figure 4.21, are observed to capture with sufficient accuracy the real traffic flow conditions in the particular freeway stretch, although not at the exact same level of accuracy as the calibrated ones. The cost function value for this validation procedure was 5.4 %. From the simulation results it can be observed that, although the value of the cost function is low, the simulation is not able to fully replicate all the flow fluctuations inside the congested region. Nevertheless, the proposed model shows a good potential for simulating such traffic flow patterns in multi-lane highways.

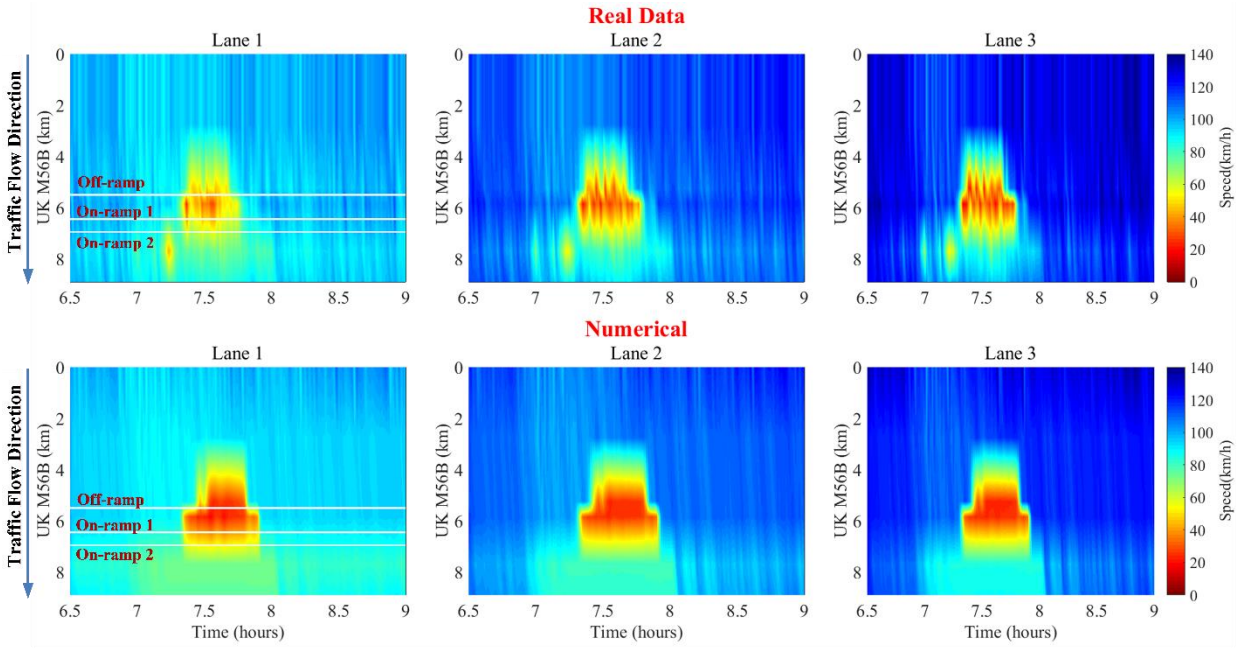

FIGURE 4.20: *(Multilane U.K. network) Phase space speed dynamics for real measured speed (upper) and the GKT model prediction (lower) for the* ***validation date****.*

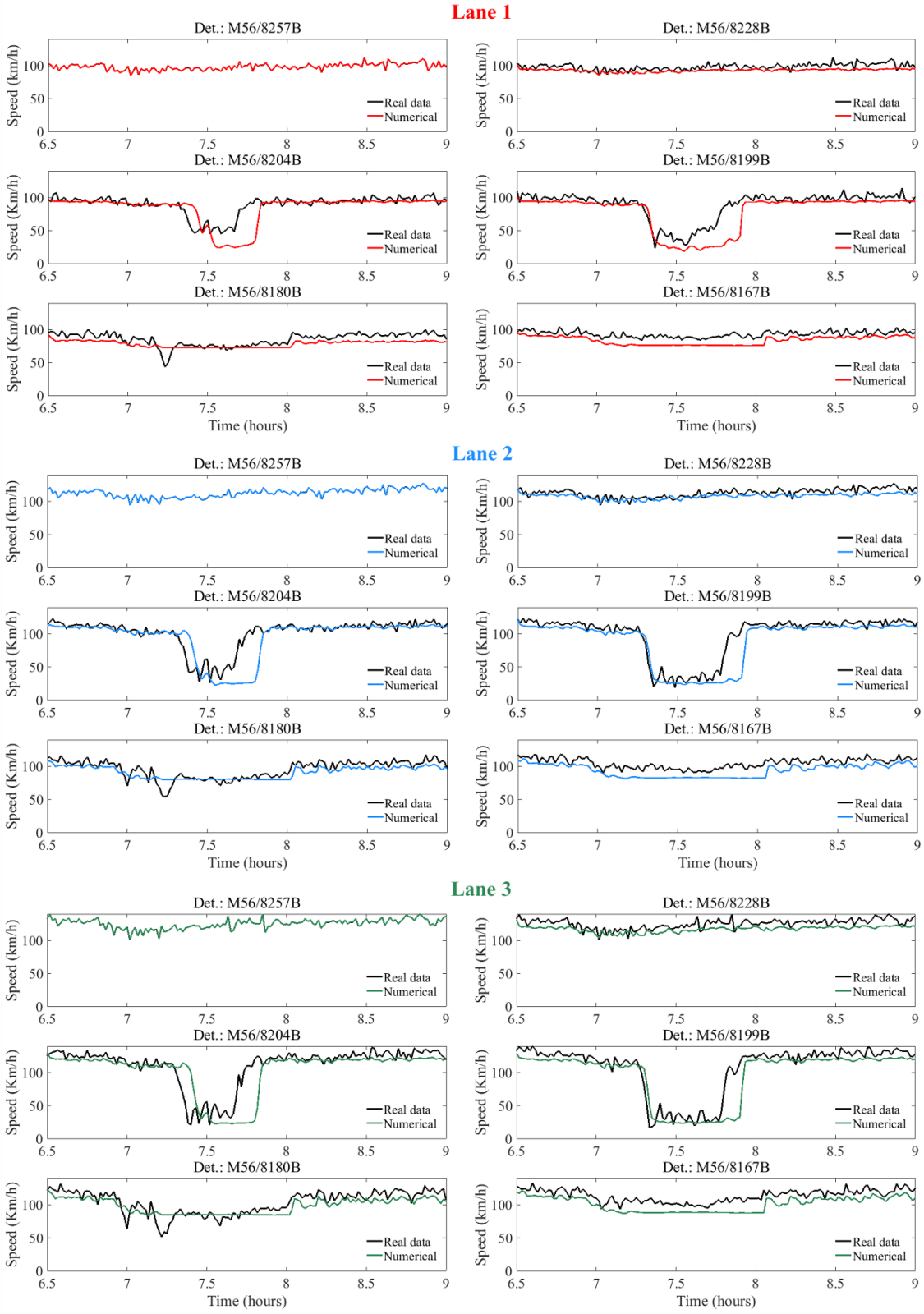

FIGURE 4.21: *(Multilane U.K. network) Time-series of the real speed measurements (black) and the GKT model prediction of speed at various detector locations for the* ***validation day.***

4.4.3 Calibration and Validation of the single-lane GKT Model Using Synchronous and Asynchronous Parallel Metamodel-Assisted DE Algorithm (Attiki Odos)

The next benchmark problem encountered in this study considers the employment of the two versions of the developed parallel metamodel-assisted DE algorithm (the synchronous and the asynchronous one), as described in Section 3.3, for the automated calibration of the parameters of a second-order macroscopic GKT traffic flow model, using real traffic data from Attiki Odos freeway (see Section 4.2.2). Hence, the model is first calibrated to identify the optimal parameter values for the examined freeway test network, using measured data from a specific date. Eventually, in order to investigate the extent to which the proposed model replicates the traffic conditions of the considered site, the optimal parameters values resulting from the calibration process are applied to the same freeway network for a different day. A comparison between the synchronous and asynchronous DE algorithms, with respect to their convergence rate, is also presented.

4.4.3.1 Calibration Results

The real traffic data used for the calibration process were collected on the Attiki Odos freeway in Greece on the 16th of June, 2009. The GKT model parameters, with their respective upper and lower bounds, being also in line with those given in Treiber *et al.*, 1999, Helbing *et al.*, 2001, Treiber & Kesting, 2013 and Delis *et al.*, 2014, are presented in Table 4.5. The synchronous version of the parallel DE algorithm was used first to calibrate the traffic flow model. A detailed presentation of the calibration and validation results of the GKT model will be presented only for the optimization run using the synchronous version of the parallel DE algorithm. The reason is that the results, concerning the optimal parameters vector, obtained by the synchronous and the asynchronous versions of the DE are almost identical, as it can be observed in Table 4.6. A comparison between the optimization runs using the two versions of the parallel DE algorithm will be presented in the following Section 4.4.3.3. The population size of the synchronous DE algorithm was defined equal to 60, while the algorithm was executed for 2000 generations. The control parameters for the mutation and crossover operations were $F = 0.6$ and $C_r = 0.45$, respectively.

TABLE 4.5: *(Attiki Odos – as single lane) Admissible range of the parameter vector used for the GKT model calibration.*

Model parameters	***Units***	***Bounds***
Desired free speed, u_{max},	km/h	[110, 130]
Maximum density, ρ_{max}	veh/km	[100, 200]
Critical density, ρ_{cr}	veh/km	[30, 60]
Desired time gap, T	s	[0.8, 2.2]
Anticipation factor, γ		[1, 2]
Relaxation time, τ	s	[10, 40]
Variance pre-factor for free traffic, A_0		[0.0025, 0.015]
Pre-factor, δA		[0.03, 0.035]
Transition width, $\delta\rho$	veh/km	[3.5, 20]

TABLE 4.6*: (Attiki Odos – as single lane) Cost function values and the resulted optimal parameter values for the calibration phase.*

Model Parameters	u_{max} ***(km/h)***	ρ_{max} ***(veh/km)***	ρ_{cr} ***(veh/km)***	T ***(s)***	γ	τ ***(s)***	A_0	δA	$\delta\rho$ ***(veh/km)***	***Cost Function (%)***
Optimal values (Synchronous)	110	172	30	1.059	1.999	30.42	0.015	0.03	20	4.983
Optimal values (Asynchronous)	110	172	30	1.058	1.999	30.46	0.015	0.03	20	4.892

The considered 6.2 km stretch was simulated for 6 morning hours (i.e. from 6: 00 a.m. to 12: 00 p.m.), whereas the space discretization was for $\Delta x = 50$ m and the CFL was set equal to 0.4. The wall clock computational time for the synchronous run and for 2000 generations was 1752 min. The resulted optimal model parameters and the minimum value of the cost function are presented in Table 4.6. In Figure 4.22, the convergence history for the cost function of the best chromosome in each generation is presented as a function of the generation number and as a function of the number of exact evaluations, for the synchronous DE run.

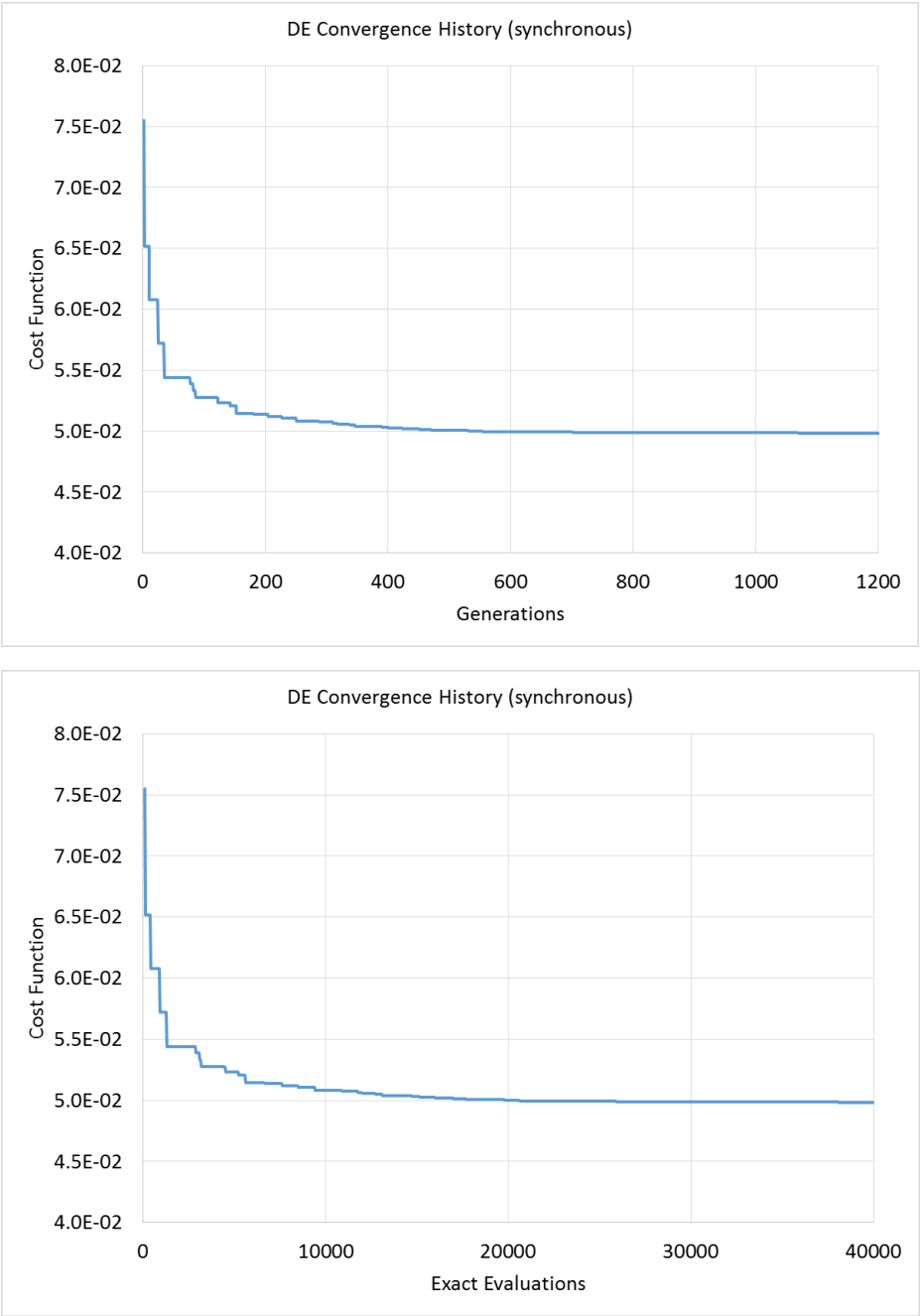

FIGURE 4.22: *(Attiki Odos – as single-lane) The convergence history of the best solution of each generation of the DE algorithm as a function of the generation number (top) and as a function of exact evaluations (bottom) (synchronous DE version).*

Figure 4.23 presents the space-time diagrams of the real measured speeds, contrasted to the numerical model's estimation of speed for the calibration day using the computed optimal parameters. As it can be seen, the model is able to accurately reproduce the spatiotemporal behavior of the speed dynamics. More precisely, following the early morning hours and their free flow conditions, the initiation time (at 8:00 a.m.) and location (close to the E-11-1 off-ramp) of the congestion, as well as its duration (up to 10:00 a.m) along with the average speed reduction are well reproduced. Further, the upstream propagation of the congestion (up to the 32nd km) for this date is also accurately represented by the model. It is noted that, the perfect agreement at the detection station located at the 34th km is due to the

use of the real measurements from this detector as upstream boundary condition in the numerical model.

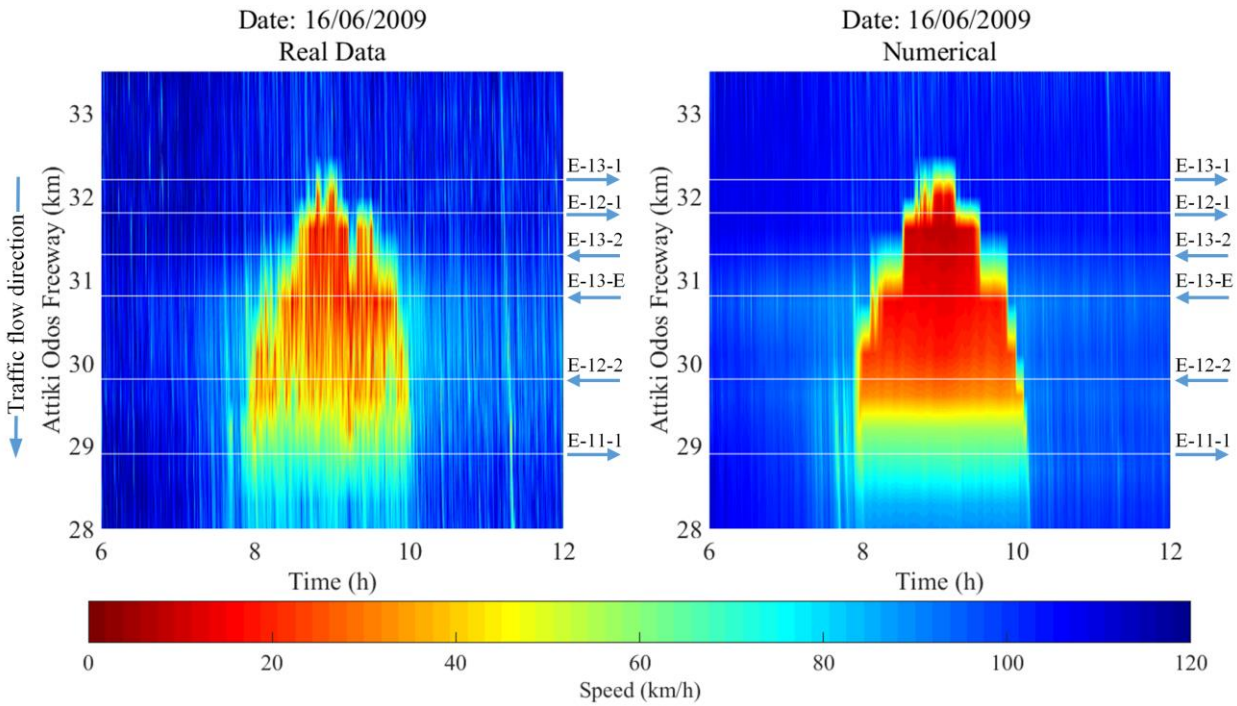

FIGURE 4.23: *(Attiki Odos – as single lane) Phase space speed dynamics for real measured speed (left) and the GKT model prediction (right) for the* ***calibration day****.*

Figure 4.24 displays the measured and estimated speed dynamics, in time, for all detector stations (whose locations are depicted in Figure 4.6). As it can be seen, the reduction in speed (indicating the initiation of congestion) originates close to the 29th km at 8: 00 a.m. and propagates upstream up to the 32nd km. This reduction can reach the values of $15 - 20$ km/h and lasts for up to two hours for certain locations in the motorway. In addition, the model is able to reflect realistically the vehicle acceleration downstream of the congestion creation area (29th km), since this model acknowledges the limited acceleration ability of vehicles. Hence, the overall agreement of the real measurement time series with those produced by the GKT model for all detector stations is almost perfect.

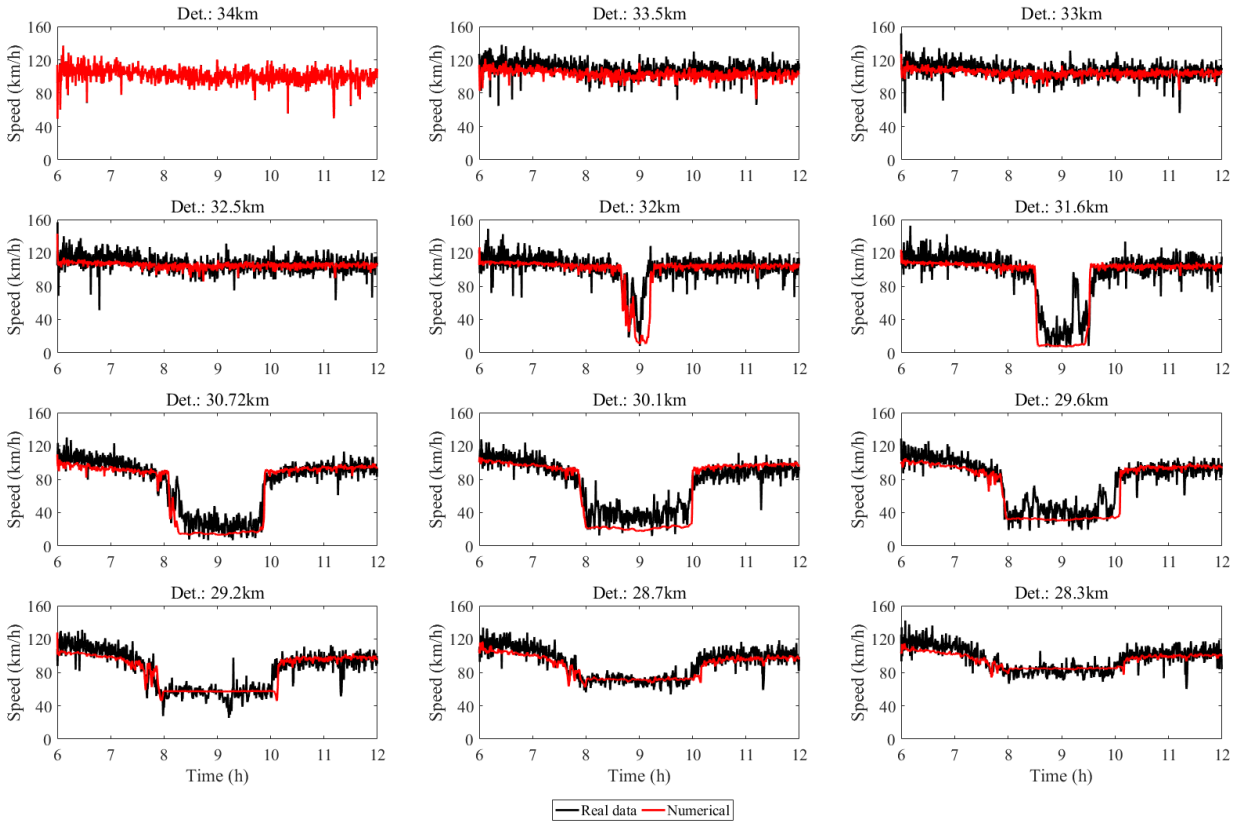

FIGURE 4.24: *(Attiki Odos – as single lane) Time series of the real speed measurements (black) and the GKT model prediction of speed (red) at various detector locations for the* ***calibration day****.*

In Figure 4.25 the corresponding average flow (veh/h) dynamics comparison is given for all detector stations. Flow measurements are important as to realize the correct behavior of the model in terms of density and flow conservation (also related to the correct treatment in the model of the on- and off-ramp flows). Again the variation of the real flow is correctly reproduced by the GKT model. An important point here is the ability of the model to reproduce relatively accurate the reduced (discharge) flow rate following the onset of congestion. These flow reductions, also well-known as capacity drops, are typically measured by comparing the queue discharge flow rate to the maximum pre-queue discharge flow rate. This is particularly evident in the detector stations between 28.3 and 31.6 km.

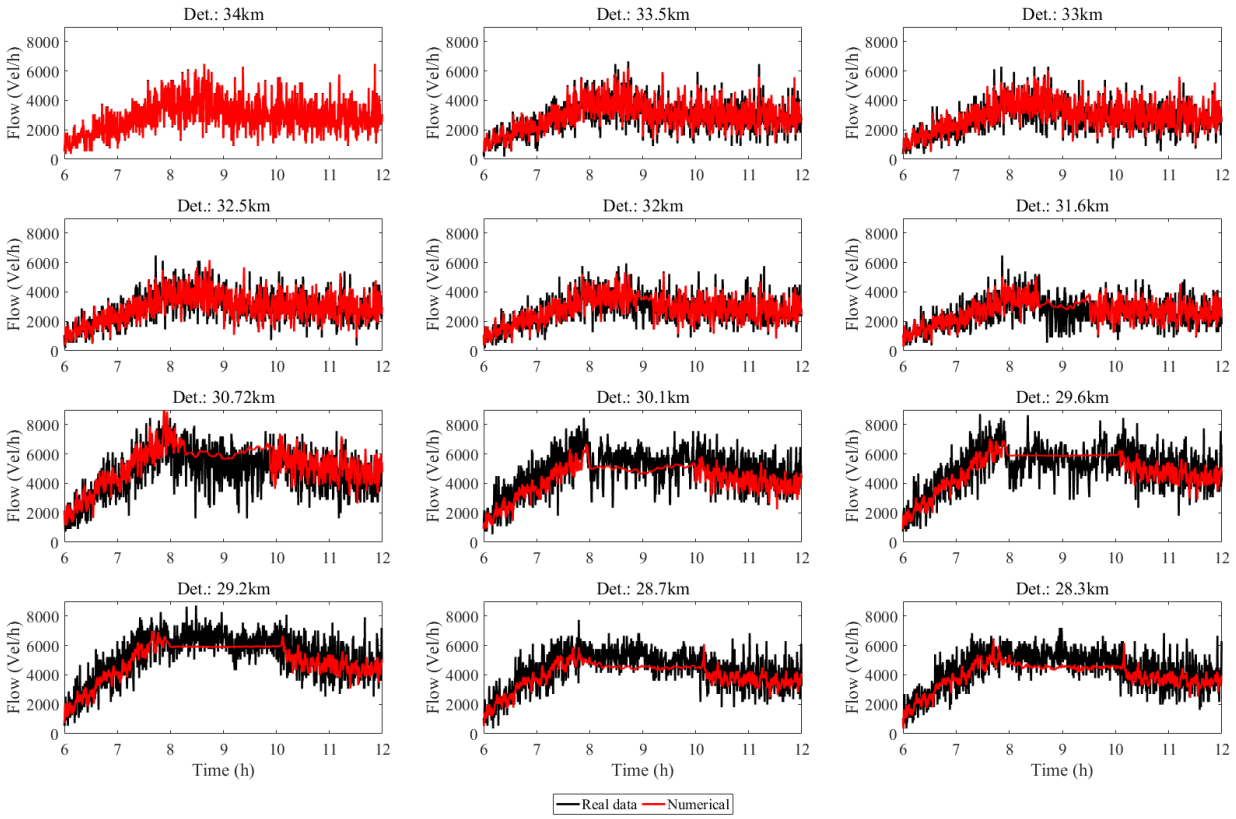

FIGURE 4.25: *: (Attiki Odos – as single lane) Time series of the real flow measurements (black) and the GKT model prediction of flow (red) at various detector locations for the* ***calibration day****.*

4.4.3.2 Validation Results

To test and assess the performance and robustness of the resulting GKT model, the optimal parameters resulting from the previous calibration procedure (Section 4.4.3.1) were applied to the same freeway stretch in Attiki Odos, but for a different day, the 23rd of June 2009. For the validation day, the recurrent congestion in the traffic flow behavior is similar to the one of the calibration day. The cost function value obtained for the validation procedure was 14%.

The validation results are presented in Figures 4.26, 4.27 and 4.28 following the same presentation as for the calibration day (in Figures 4.23, 4.25). The real traffic flow conditions indicate a similar behavior with that of the calibration date. The only differences being the time duration of the congestion (which starts at about 8: 30 a.m.) but now propagates up to the 33rd km. The validation results show that the model is able to reproduce traffic congestion due to the over-spilling off-ramp with sufficient accuracy.

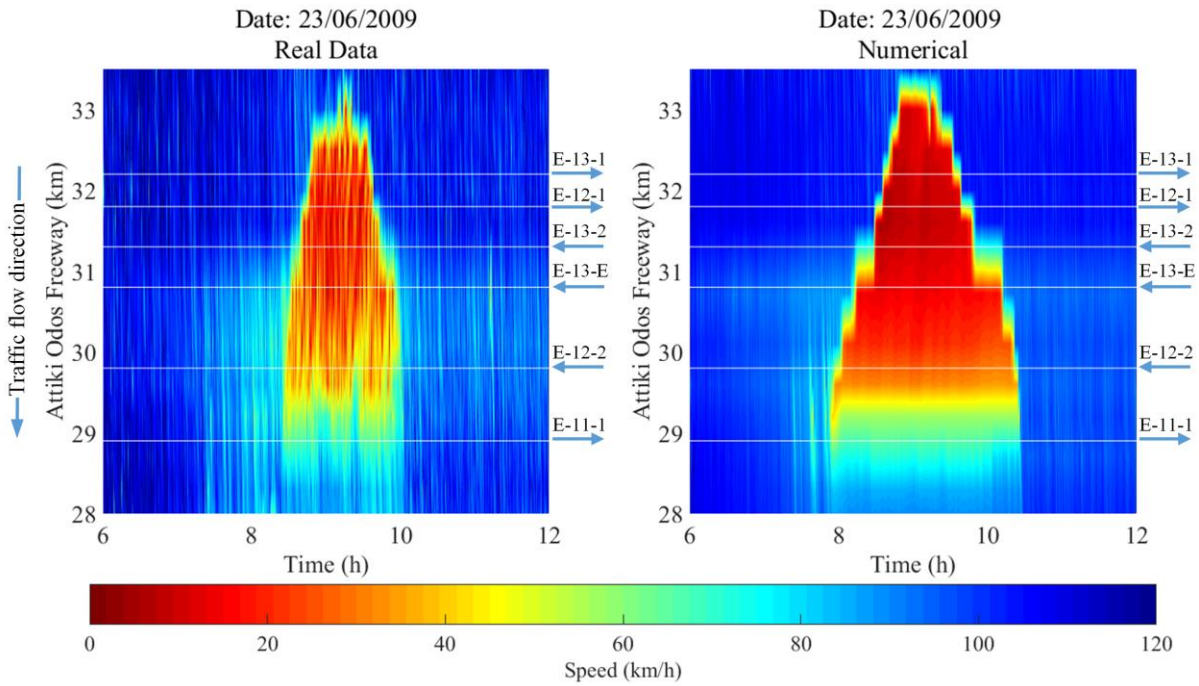

FIGURE 4.26: *(Attiki Odos – as single lane) Phase space speed dynamics for real measured speed (left) and the GKT model prediction (right) for the* ***validation day****.*

Figure 4.26 presents the space-time diagrams of the real measured speeds, in comparison to the numerical model's estimation of speed for this day using the computed optimal parameters obtained from the calibration date. The GKT model was able to reproduce the congestion extend as well as the average speed reduction but slightly overestimated its duration (starting earlier and finished later) at some locations. This is also evident in Figure 4.27, since at some detectors (those at 29.6, 30.1 and 30.72 km) the time duration of the congestion is slightly larger. However, the overall comparison, also in terms of the average predicted speed, is considered as satisfactory, given the complexity of the traffic flow phenomena. Further, in Figure 4.28 the corresponding average flow dynamics comparison is given for all detector stations. Again the variation of the real flow is almost correctly reproduced by the model with only some discrepancies appearing in some detectors, where the flow emerging from the congestion (discharge) is somehow lower compared to the real one, on average.

In general, it is observed that the model is able to reproduce/replicate the traffic conditions of other days with sufficient accuracy, predicting the congestion at almost the right time period and for the right space-time extent; although it is seen to produce slightly longer congestion duration at certain locations.

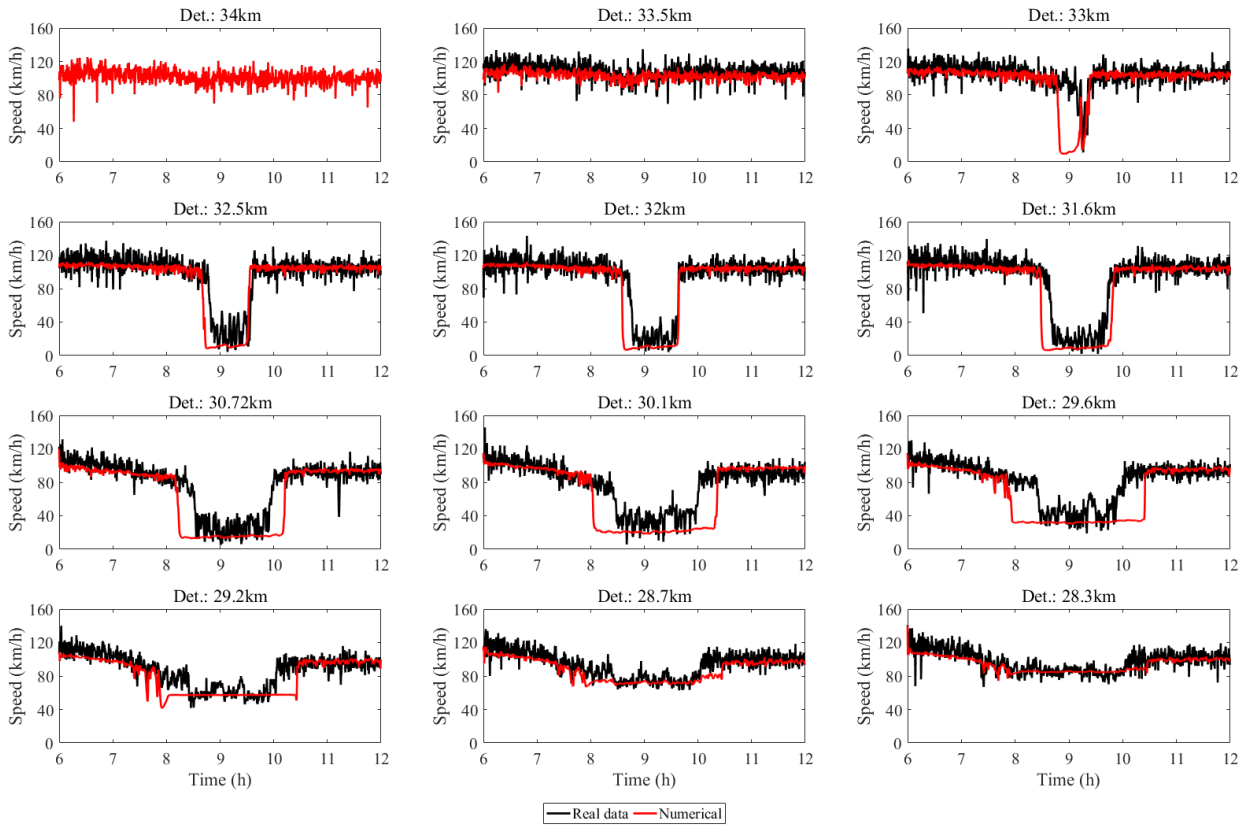

FIGURE 4.27: *(Attiki Odos – as single lane) Time series of the real speed measurements (black) and the GKT model prediction of speed (red) at various detector locations for the* ***validation day****.*

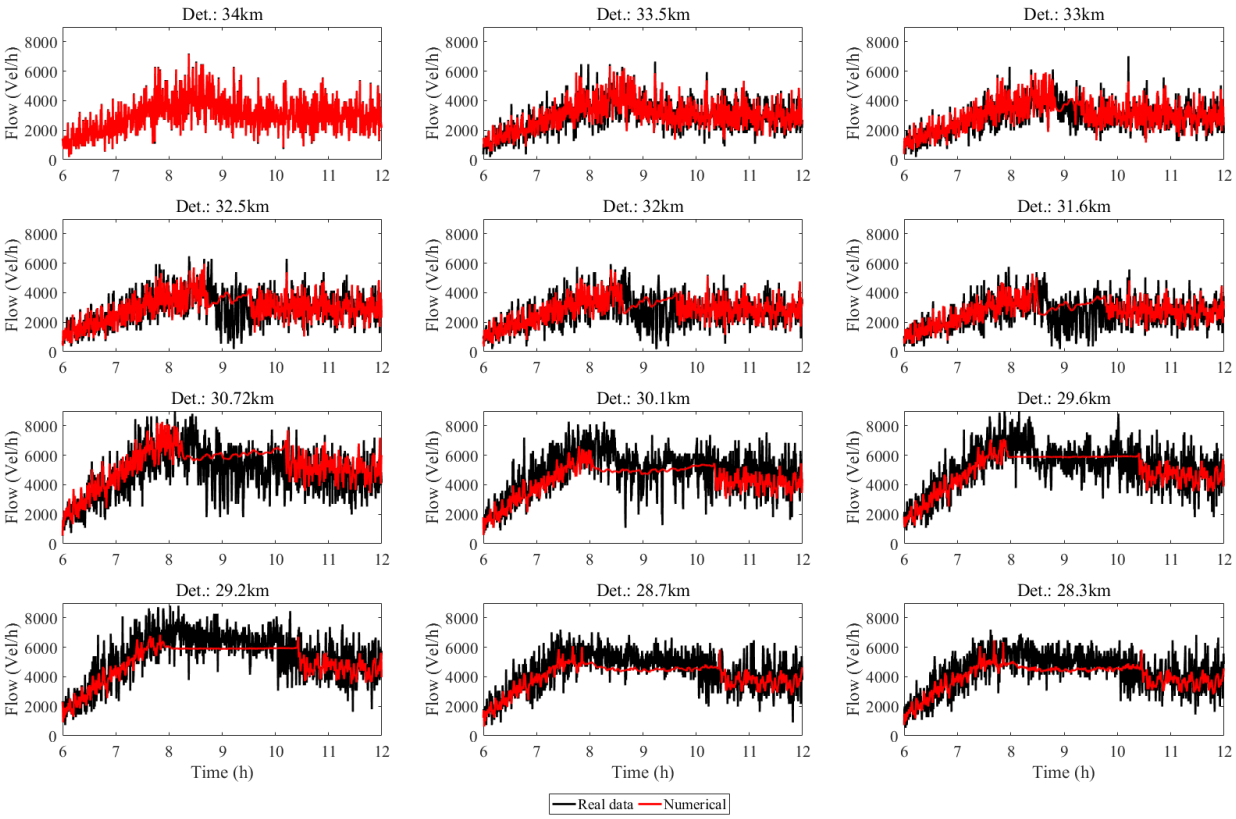

FIGURE 4.28: *(Attiki Odos – as single lane) Time series of the real flow measurements (black) and the model prediction of flow (red) at various detector locations for the* ***validation day****.*

4.4.3.3 *Comparison between Synchronous and Asynchronous Parallel Differential Evolution Runs (Attiki Odos – as single lane)*

In the following, a comparison between the two versions of the parallel DE algorithm is presented, with respect to the calibration of the single-lane GKT model for Attiki Odos case. Both parallel DE versions (synchronous and asynchronous) were run for 2000 generations, and converged practically to the same optimal solution (the one depicted in Table 4.6). Figure 4.29 contains the convergence histories for the two parallel DE versions with respect to the generation number (top) and the number of exact evaluations (bottom). The minimum value of the cost function in each generation (the cost function of the best member of the population) is plotted against the generation number (as previously defined for the asynchronous version) in the first case (Figure 4.29 (top)). It can be easily observed that, although both versions converge to almost the same cost function value, the asynchronous version has a steeper convergence rate at the beginning of the optimization procedure, reaching faster a region close to the final optimal solution. However, if we compare the two versions with respect to the number of exact evaluations, a very similar behavior is observed, which will be explained later.

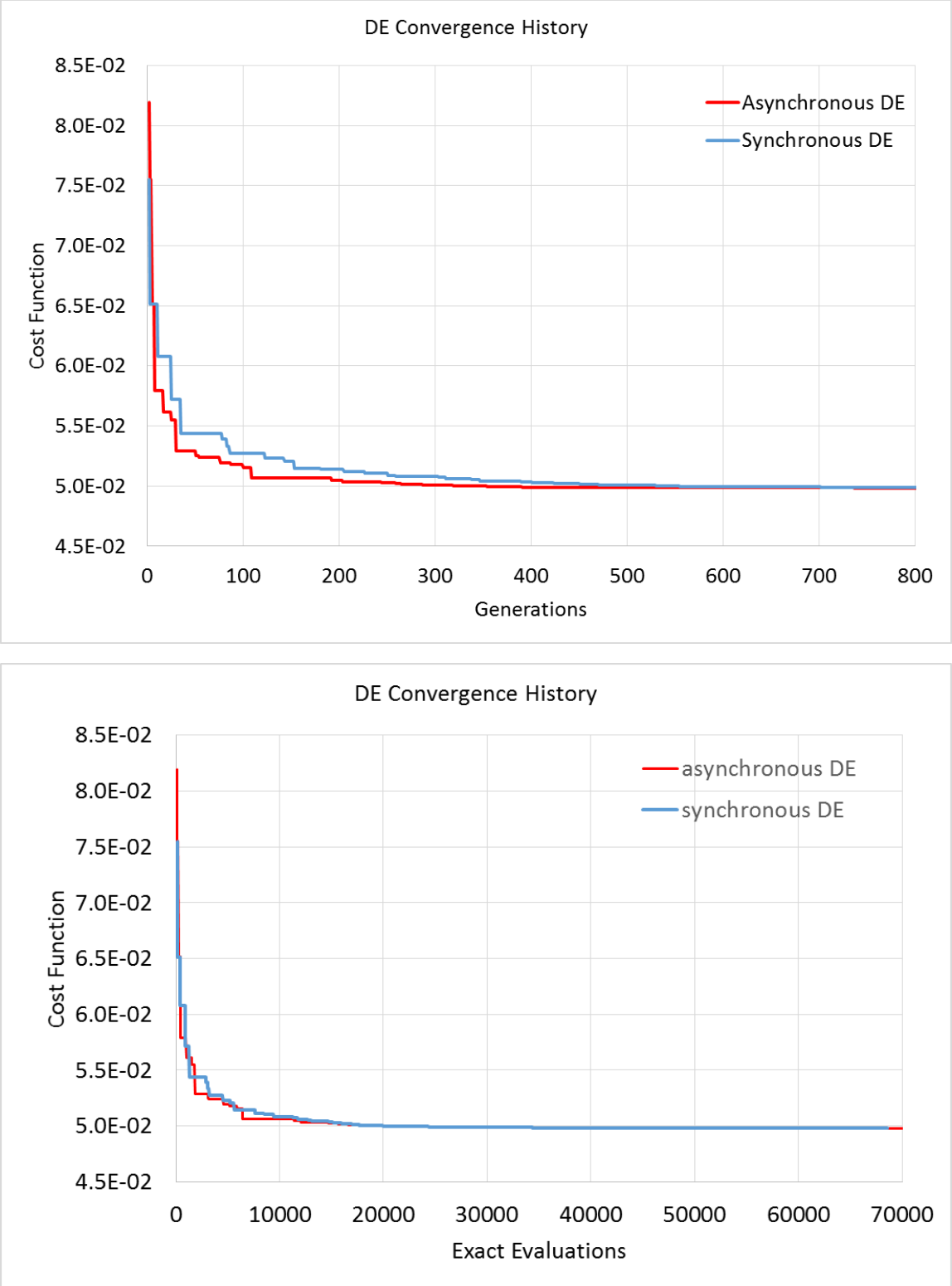

FIGURE 4.29: *(Attiki Odos – as single lane) Convergence histories of the synchronous and asynchronous versions of the parallel DE algorithm, for the calibration of the GKT model: as a function of generation number (top), and as a function of exact evaluations (bottom).*

Figures 4.30 and 4.31 contain the histories of the training and testing errors for the two surrogates (RBF and MLP Artificial Neural Networks), for the synchronous parallel DE run. The MLP surrogate demonstrates a much smoother behavior of its errors, compared to the

RBF one, but the latter provides much smaller training and testing errors. As a result, it is the RBF network that is used for the pre-evaluation phase for all generations in the synchronous run.

Figures 4.32 and 4.33 contain the histories of the training and testing errors for the two surrogate models, for the asynchronous parallel DE run. Their behavior is very similar to the synchronous run (with slightly lower error values, due to the faster convergence of the asynchronous DE version). The RBF again demonstrates much lower training and testing errors for all generations, and it is always (automatically) selected for the pre-evaluation phase of the trial vectors. It should be mentioned here that the automatic selection of the best surrogate model in each generation (based on the lower value of the corresponding testing error) makes the surrogate-assisted optimization procedure very easily adaptable to different cost functions and search spaces.

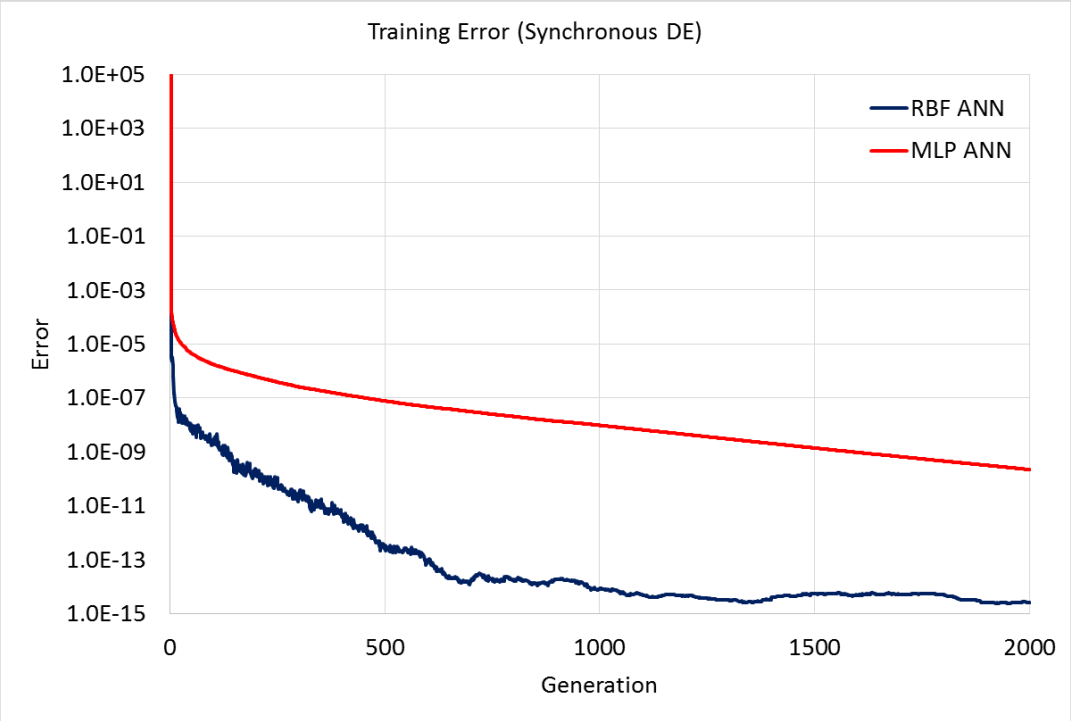

FIGURE 4.30: *(Attiki Odos – as single lane) The history for the Training Error for both surrogate models, for the synchronous DE run.*

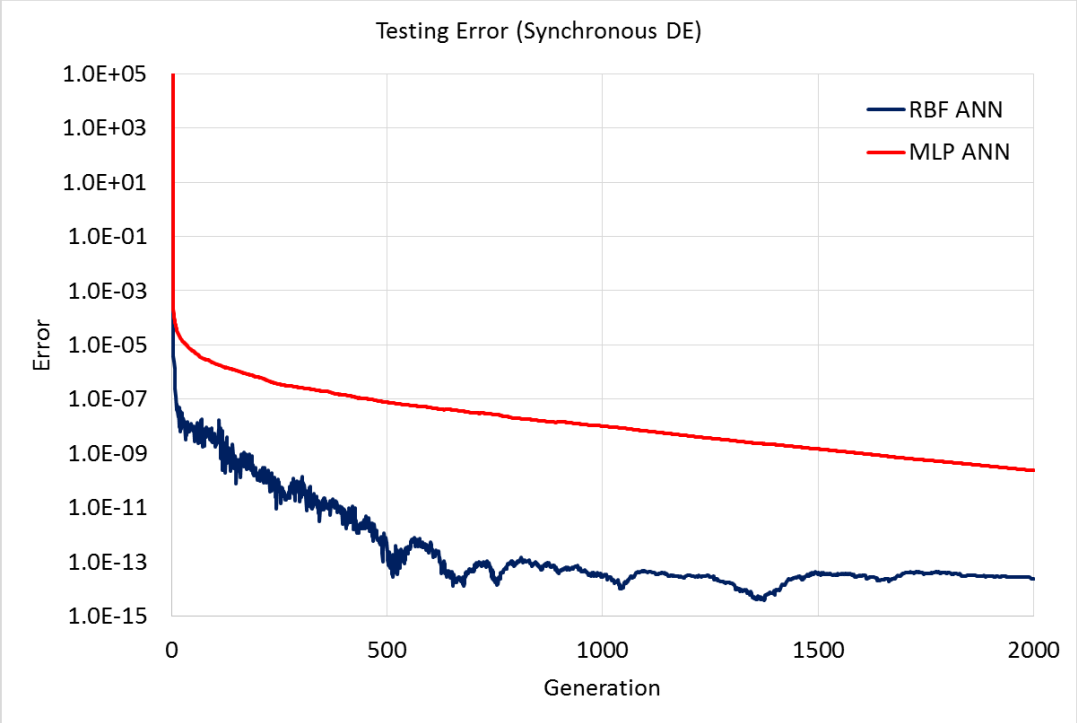

FIGURE 4.31: *(Attiki Odos – as single lane) The history for the Testing Error for both surrogate models, for the synchronous DE run.*

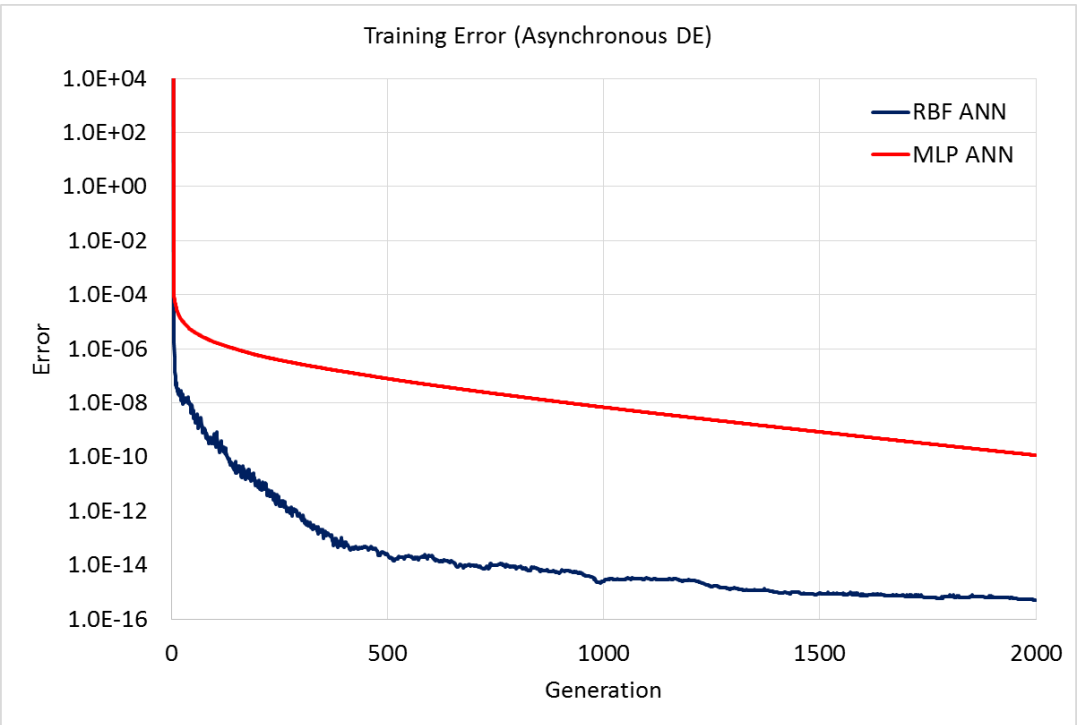

FIGURE 4.32: *(Attiki Odos – as single lane) The history for the Training Error for both surrogate models, for the asynchronous DE run.*

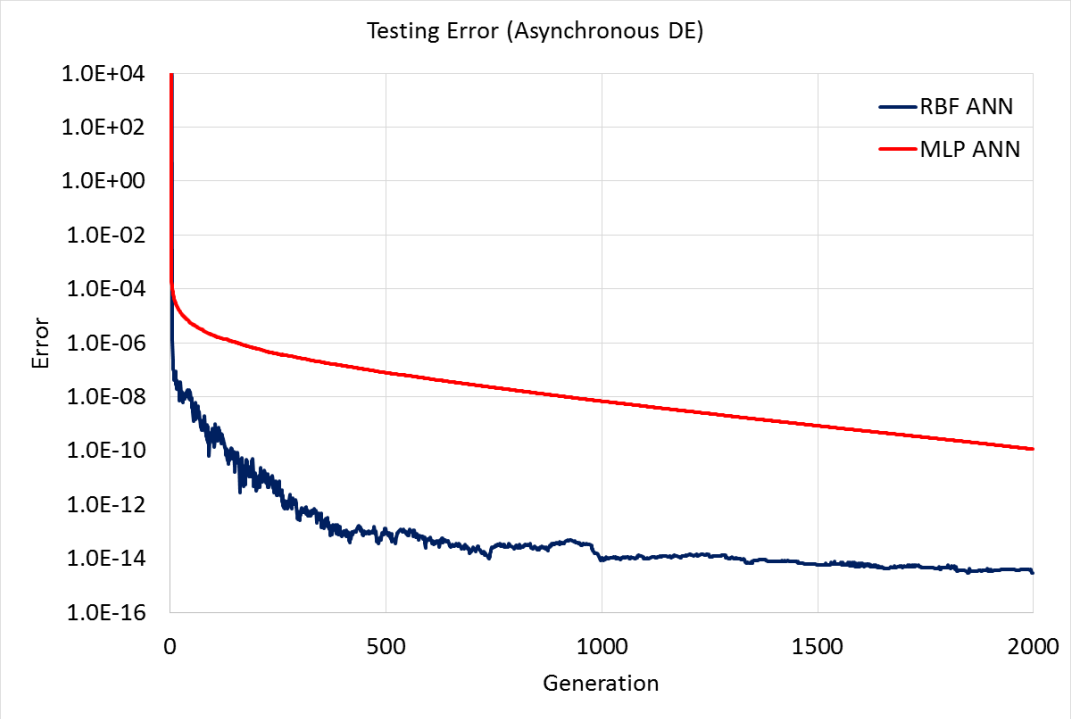

FIGURE 4.33: *(Attiki Odos – as single lane) The history for the Testing Error for both surrogate models, for the asynchronous DE run.*

Figure 4.34 contains the history for the exact evaluations per generation for the synchronous and the asynchronous DE runs. For the synchronous run, it is evident that for almost half the members of each population an exact evaluation is used after the pre-evaluation phase. This number slightly decreases with increasing generation number. The number of exact evaluations per generation depends on the optimization problem at hand and on the selected surrogate model as well. In general, when the RBF network is selected as the surrogate model, a large number of exact evaluations is observed in each generation, but when the MLP network is selected, only few calls to the exact evaluation procedure are observed in each generation (Nikolos, 2013). For the asynchronous run a completely different situation can be observed. Due to the fact that the "generation" is rather an artificial time period (defined by the master node), and due to the absence of synchronization between the parallel processes, a large number of exact evaluations takes place in each generation, which may be even higher than the number of available processors (being equal to 60). This unusual observation is explained by the fact that the master node (which defines the time duration of each "generation" in the asynchronous version), besides the evaluation of its individuals, has to perform all the DE processes, including the re-training and re-testing of both surrogate models. The resulting delay in the completion of its "generation" requires additional time, which is used by the rest of the processors to evaluate more individuals in an asynchronous (thus more efficient) manner. This explains also the faster convergence of the asynchronous DE compared to the synchronous one, with respect to the generation number (Figure 4.29 (top)). In each "generation", the asynchronous version completes many more evaluations (exact and inexact), thus it evolves its population faster. However, if the convergence is plotted with respect to the exact evaluations (Figure 4.29 (bottom)), both versions show similar performance. This observation unveils the fact that the cost function value convergence rate is directly connected to the number of exact evaluations, regardless the way such evaluations

are accomplished (synchronously or asynchronously). In the latter case (Figure 4.29 (bottom)), as the asynchronous evaluations result in a more efficient utilization of the available computational resources, this observation has the effect of faster convergence rate. To demonstrate that, the two runs (synchronous and asynchronous) had almost the same wall clock run times for 2000 generations (105,132 s and 100,585 s, respectively). However, these run times correspond to 68,575 exact evaluations for the synchronous parallel DE run and to 118,055 ones for the asynchronous one.

In order to further test the predictive ability of the surrogate models, an experiment was conducted for the synchronous version of the parallel DE algorithm. For this experiment the algorithm was modified as to exactly evaluate all the candidate solutions in each generation, so that the predictive capability of the utilized surrogate model to be evaluated. Figure 4.35 contains the percentage (in each generation) of the correct worse-fitted forecast by the surrogate model for this implementation (how many candidate solutions predicted by the surrogate model as worse-fitted than their parents are actually worse-fitted). As it can be observed in Figure 4.35, this percentage is very high (in the order of 95%), which supports the use of the surrogate model to predict the less-promising candidate solutions.

Finally, Figure 4.36 contains the percentage (in each generation) of the correct better-fitted forecast by the surrogate model (how many candidate solutions predicted by the surrogate model as better-fitted than their parents are actually better-fitted). As it can be observed in Figure 4.36, this percentage is relatively low. However, this prediction does not have a negative effect on the accuracy and the robustness of the DE algorithm as it is followed by an exact evaluation. This low-accuracy prediction can be explained by the fact that the new candidates are outside the region used to train the surrogate models. At the same time this region becomes shorter as the generation number gets higher.

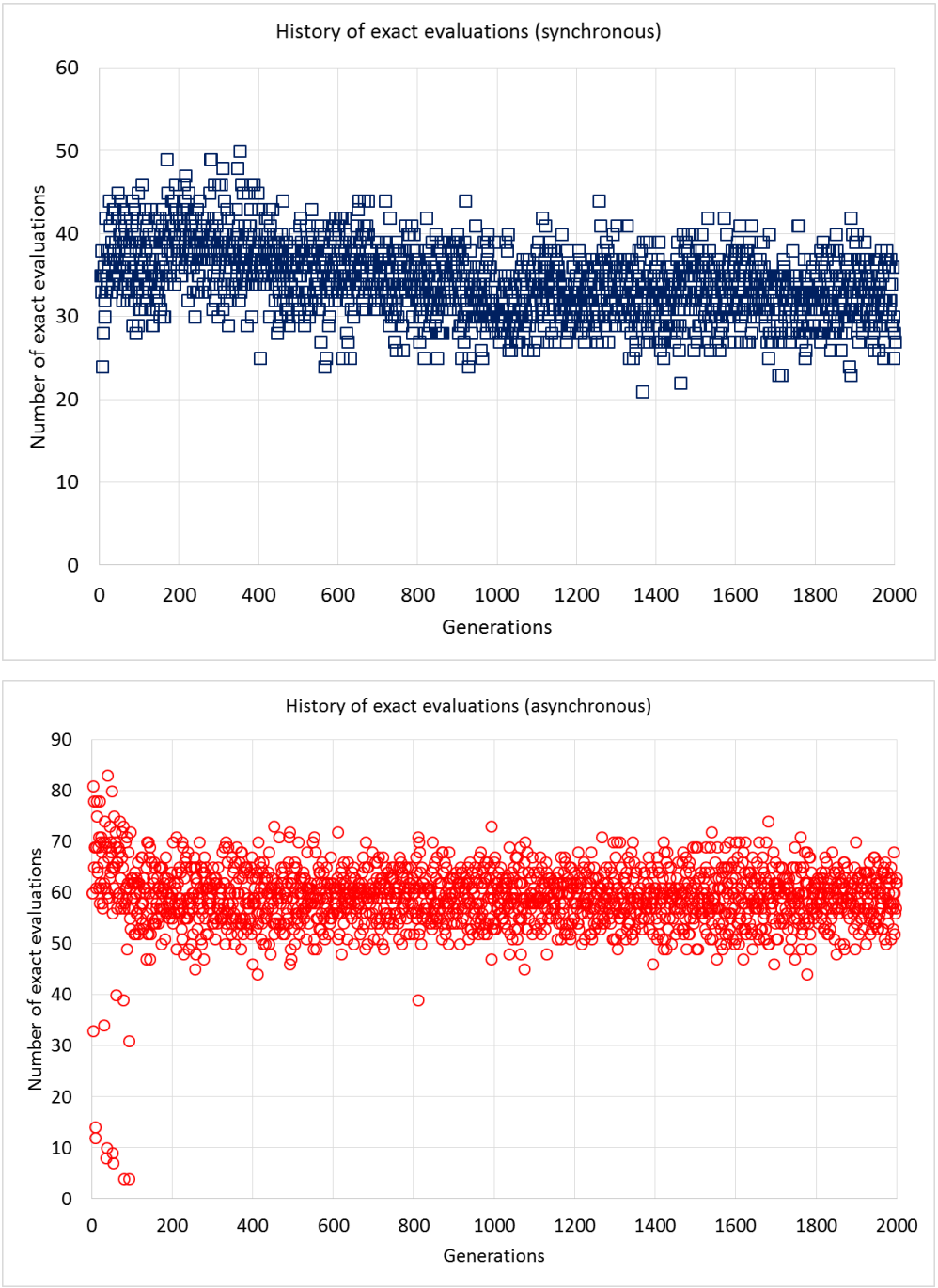

FIGURE 4.34: *(Attiki Odos – as single lane) The history of the exact evaluations per generation for the synchronous DE run (top) and the asynchronous one (bottom).*

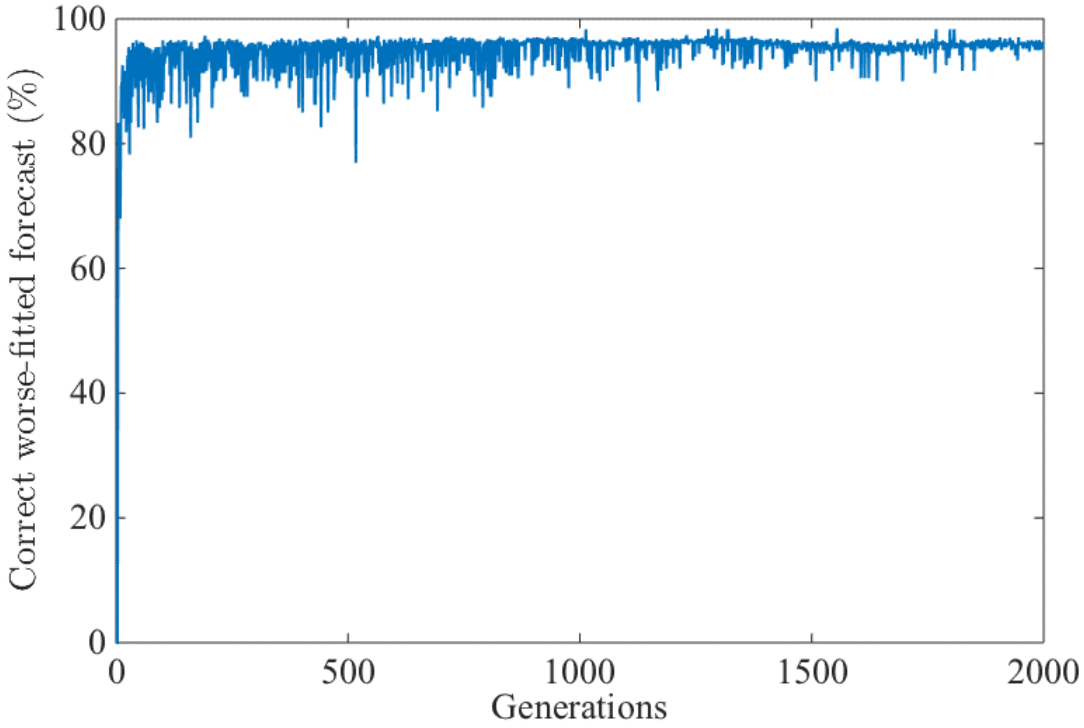

FIGURE 4.35: *(Attiki Odos – as single lane) The history of the percentage of the correct worse-fitted forecast by the surrogate model for the synchronous implementation.*

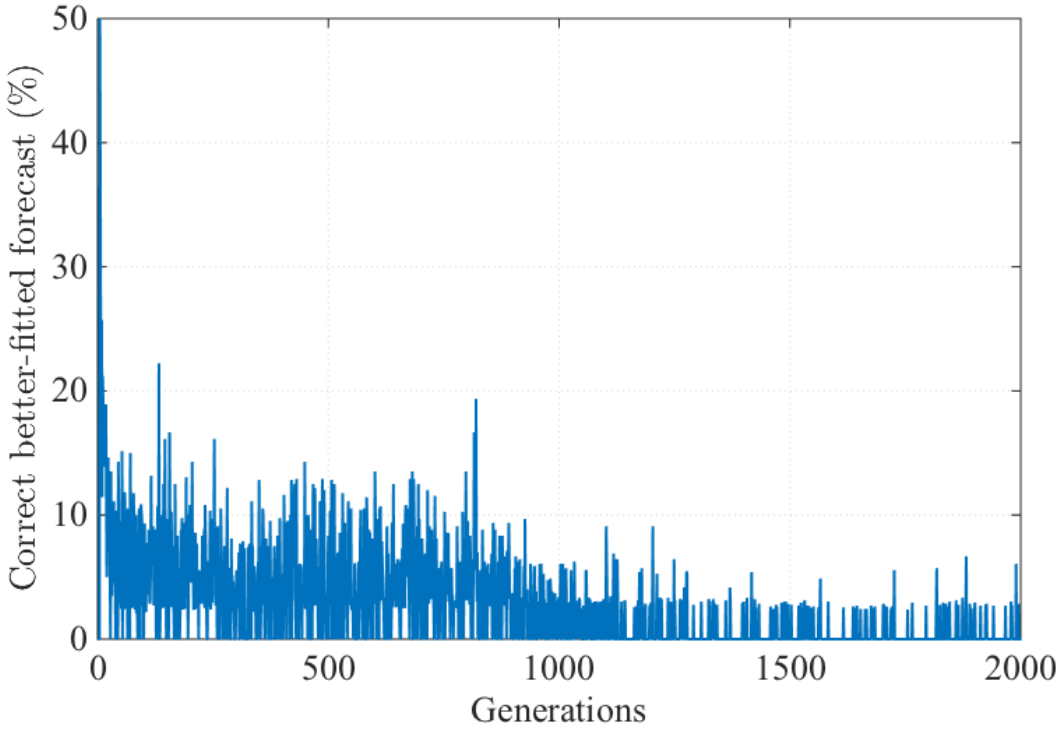

FIGURE 4.36: *(Attiki Odos – as single lane) The history of the percentage of the correct better-fitted forecast by the surrogate model for the synchronous implementation.*

4.4.4 Comparative Calibration and Validation of the GKT and METANET Models Using Synchronous Parallel Metamodel-Assisted DE Algorithm (U.K. network – as single lane)

The last calibration testing encountered in this study concerns the employment of the synchronous, parallel, metamodel-assisted DE algorithm for the automated calibration of the parameters of the two second-order macroscopic traffic flow models (as single-lane). In particular, the numerically approximated second-order GKT model and the discrete second-order METANET model were compared, regarding the reproduction of traffic congestion created at freeways close to on/off-ramps. To this end, the selected models were first calibrated using real traffic data from the freeway stretch in U.K. and then validated and compared using real traffic data for a different day from the same freeway network.

4.4.4.1 Calibration Results

As in the first test case (Section 4.4.1.1), the calibration results were obtained using real traffic data from the M56 motorway in U.K. on the 3rd of June, 2014. The GKT model parameters, with their respective upper and lower bounds, according to Treiber *et al.*, 1999, Helbing *et al.*, 2001, Treiber & Kesting, 2013 and Delis *et al.*, 2014, are presented in Table 4.7. Moreover, the population size of the DE algorithm was defined equal to 50, whereas the maximum number of generations was 1100; the control parameters F and C_r for the mutation and crossover operations were set equal to 0.6 and 0.45, respectively.

TABLE 4.7: *(U.K. network – as single lane) Admissible range of the parameter vector used for the GKT model calibration.*

Model parameters	***Units***	***Bounds***
Desired free speed, u_{max},	km/h	[105, 135]
Maximum density, ρ_{max}	veh/km	[100, 200]
Critical density, ρ_{cr}	veh/km	[30, 60]
Desired time gap, T	s	[0.5, 2.5]
Anticipation factor, γ		[1, 2]
Relaxation time, τ	s	[10, 40]
Variance pre-factor for free traffic, A_0		[0.0025, 0.015]
Pre-factor, δA		[0.01, 0.03]
Transition width, $\delta\rho$	veh/km	[3.5, 20]

The examined freeway stretch of 9.45 km was also simulated from 6:00 a.m. to 9:00 a.m.), with the space discretization equal to 100 m and the CFL value equal to 0.5. Figure 4.37 illustrates the convergence history of the best solution of each generation, which achieves a low value already from the first 400 iterations. Table 4.8 presents the resulting optimal model parameters and the minimum of the cost function, calculated using equation (4.1). Figure 4.38 displays the space-time evolution of real measured speed, contrasted to the model prediction for the calibration day. Figure 4.39 depicts the measured and simulated speed dynamics for all detector stations around the traffic congestion area, using the optimal parameters values of Table 4.8; as it can be observed, the calibrated model reproduces with sufficient accuracy

the real traffic conditions, capturing the occurring congestion at the accurate location and time in both duration and extent.

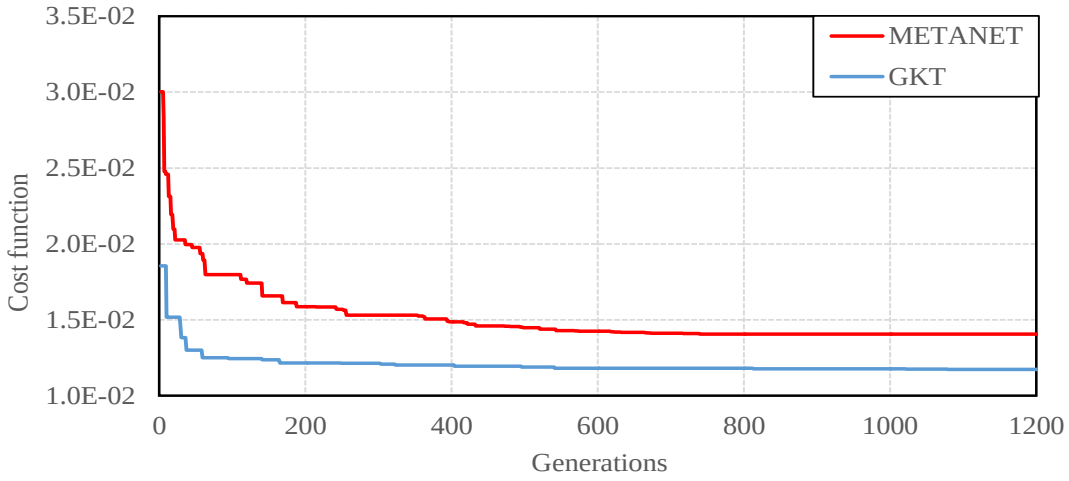

FIGURE 4.37: *(U.K. network – as single lane) DE algorithm convergence history during the calibration of the GKT and the METANET models.*

TABLE 4.8: *(U.K. network – as single lane) Cost function values and the resulted optimal parameter values for the calibration phase of the GKT model.*

Model parameters	u_{max} ***(km/h)***	ρ_{max} ***(veh/km)***	ρ_{cr} ***(veh/km)***	T ***(s)***	γ	τ ***(s)***	A_0	δA	$\delta\rho$ ***(veh/km)***
Optimal values	115	170	42	2	2	20	0.0025	0.015	10
Cost function (%)	1.16								

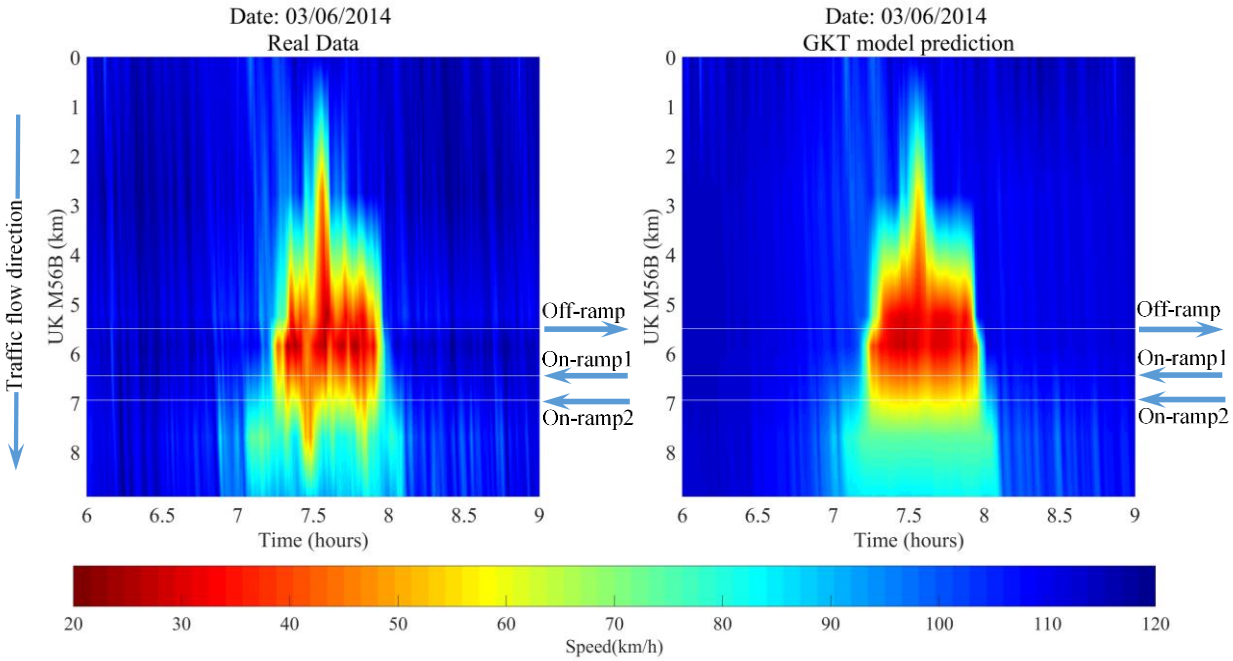

FIGURE 4.38: *(U.K. network – as single lane) Phase space speed dynamics for real measured speed (left) and the GKT model estimation (right) for the* ***calibration date****.*

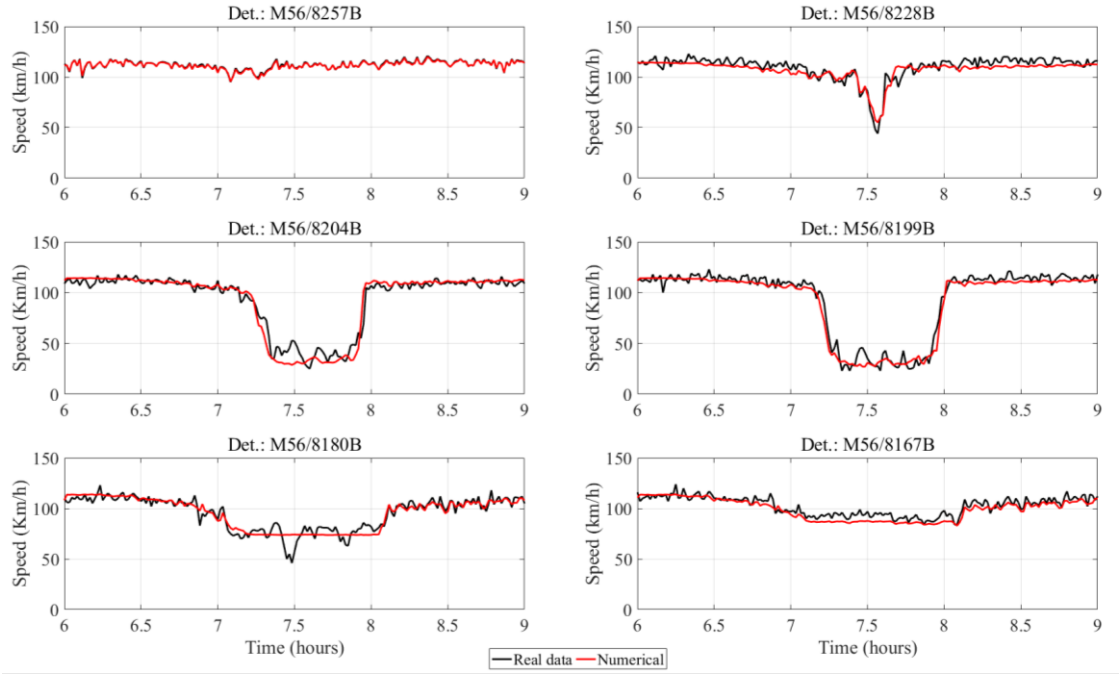

FIGURE 4.39: *(U.K. network – as single lane) Time series of the real speed measurements (black) and the GKT model prediction of speed (red) at various detector locations for the* ***calibration day****.*

Regarding the METANET model, the parameter vector consists of the free flow speed u_f, the critical density ρ_{cr} and the parameters a, τ, ν and δ, which are common for all the freeway sections. Moreover, the model includes two extra parameters which are known from

previous validation exercises to be of minor importance and are, therefore, given constant values, in order to reduce the dimension of the parameter vector. In particular, κ is set equal to 10 $veh/km/lane$ and u_f is set to 7 km/h. Thus, one single fundamental diagram is considered for all freeway sections in this model. The METANET model parameters, with their respective upper and lower bounds are presented in Table 4.9. Again, the DE was employed with population size equal to 50, maximum number of generations 1100 and control parameters $F = 0.6$ and $C_r = 0.45$; the consider network was also simulated from 6:00 a.m. to 9:00 a.m. as in the case of the GKT model.

TABLE 4.9: *(U.K. network – as single lane) Admissible range of the parameter vector used for the METANET model calibration.*

Model parameters	***Units***	***Bounds***
Free flow speed, u_f,	km/h	[80, 150]
Critical density, ρ_{cr}	veh/km/lane	[5, 80]
Model parameter, a		[1800, 2500] (capacity bounds)
Time constant, τ	s	[5, 80]
Anticipation constant, ν	km²/h	[15, 40]
Model parameter, δ	h/km	[0, 10]

Figure 4.37 presents the DE convergence history of the best value of the cost function in each generation, which also achieves a low value already from the first 450 iterations. Table 4.10 contains the optimal parameter set, obtained for the specific cost function (4.1) as well the corresponding minimum value. The space-time evolution of the model estimation of speed in comparison with the real measured data for the calibration day is illustrated in Figure 4.40. Figure 4.41 displays the observed and estimated speed dynamics for all detector locations, using the optimal parameters values included in Table 4.10. In both figures, it can be seen that the model predictions are very close to the real measurements, as for the previous model.

TABLE 4.10: *(U.K. network – as single lane) Cost function values and the resulted optimal parameter values for the calibration phase of the METANET model.*

Model parameters	u_f ***(km/h)***	ρ_{cr} ***(veh/km/lane)***	a	τ ***(s)***	ν ***(km²/h)***	δ ***(h/km)***
Optimal values	114	34.5	2.3	19.8	29.7	0.66
Cost function (%)	1.4					

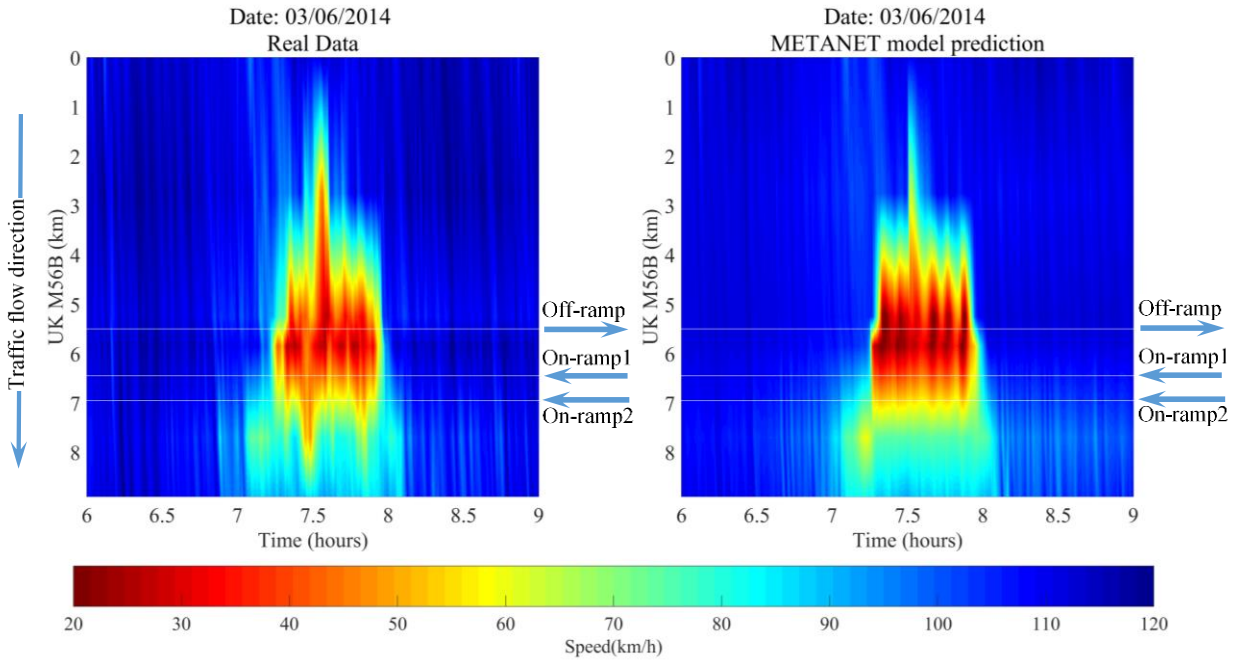

FIGURE 4.40: *(U.K. network – as single lane) Phase space speed dynamics for real measured speed (left) and the METANET model estimation (right) for the* ***calibration date****.*

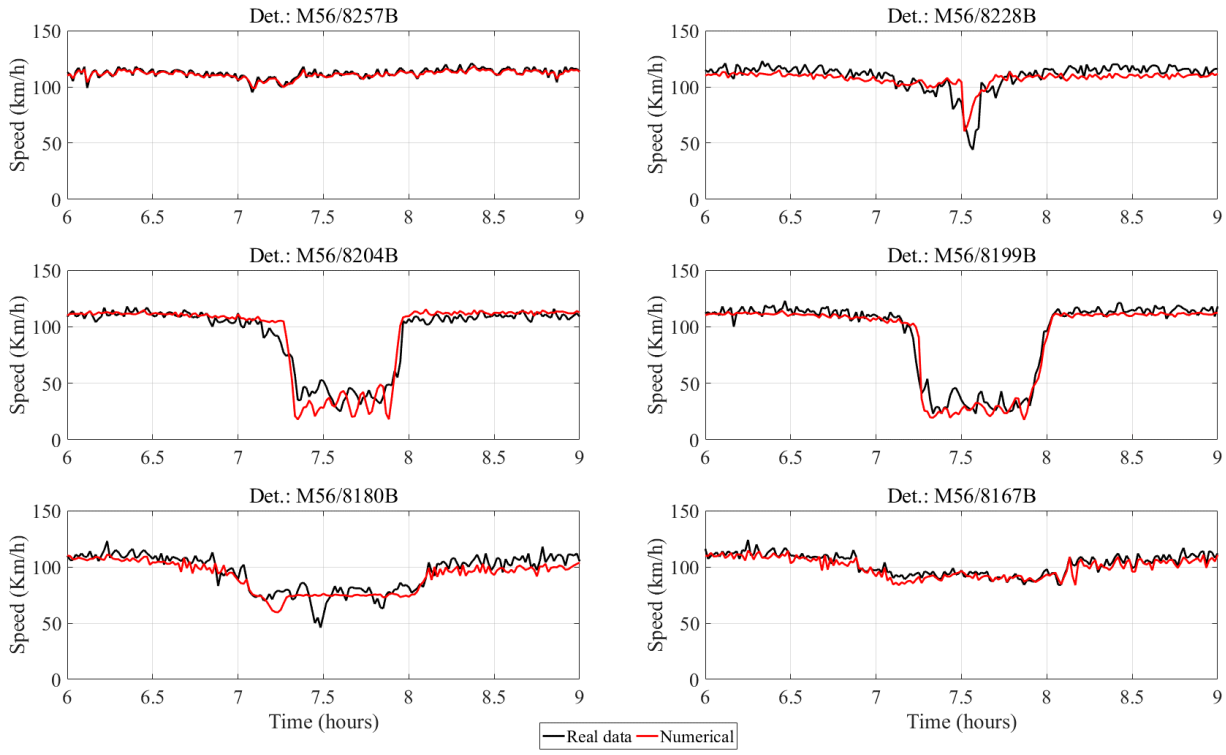

FIGURE 4.41: *(U.K. network – as single lane) Time series of the real speed measurements (black) and the METANET model prediction of speed (red) at various detector locations for the* ***calibration day****.*

4.4.4.2 *Validation Results*

In order to test and evaluate the robustness of the produced optimal parameters of the previous calibration procedure (Section 4.4.4.1), the resulting macroscopic traffic flow models were validated using a different data set than the one utilized for their calibration. Hence, both models were validated using real traffic data in the U.K. site from 24th June, 2014, with particular emphasis on the recurrent congestion in traffic flow, which persists between 7:00 a.m. and 8:00 a.m., as in the calibration day.

Figure 4.42 displays the space-time diagrams of the real measured speeds, contrasted to the models' prediction of speed for the validation day. The comparison between the real speed data and the simulated speed data can be seen in Figure 4.43 for the GKT model and in Figure 4.44 for METANET model. It is observed that both models are able to reproduce the real traffic condition for the specific freeway stretch in U.K. also for the validation day, simulating the congestion for the correct duration and extent, as observed in the real traffic data; although the METANET model is seen to produce a congestion that spills back further onto the freeway mainstream and spreads almost all over the network. The cost function value for this validation procedure was 1.6 % for the GKT model and 1.5 % for the METANET model.

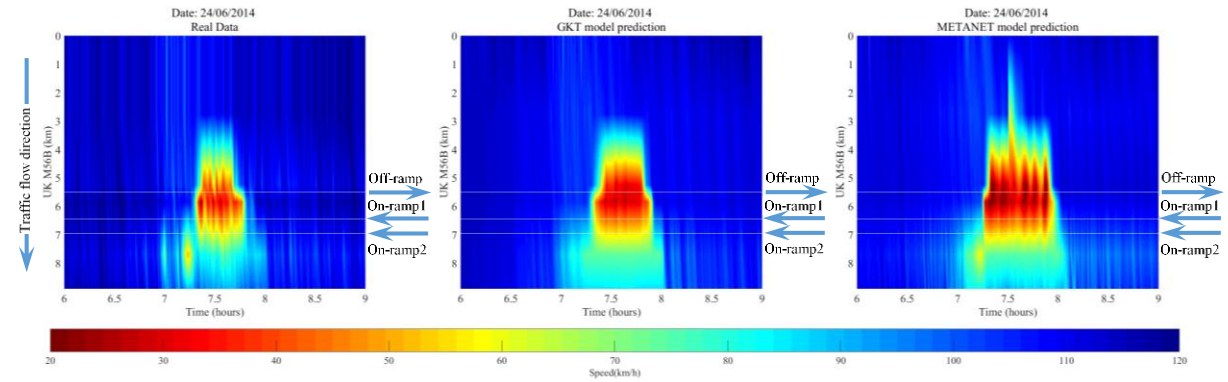

FIGURE 4.42: *(U.K. network – as single lane) Phase space speed dynamics for real measured speed and the models' estimation for the* ***validation date*** *(left: measured, center: GKT, right: METANET).*

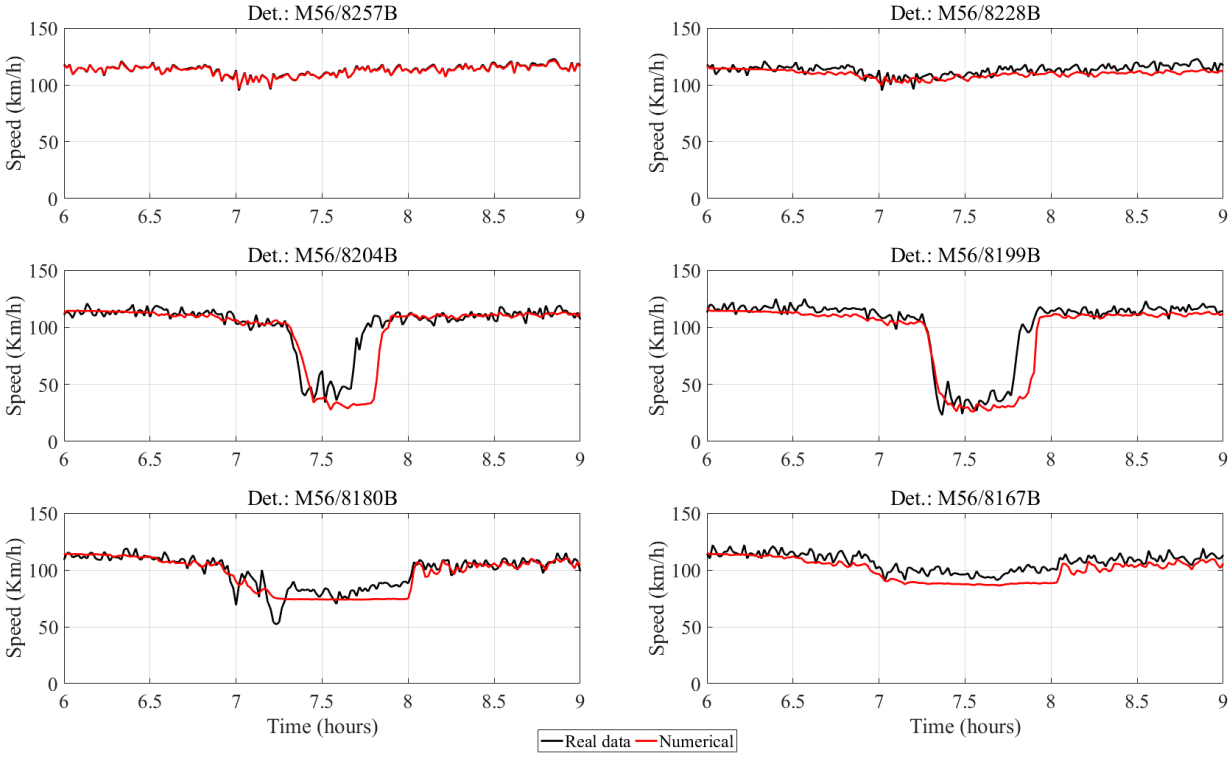

FIGURE 4.43: *(U.K. network – as single lane) Time series of the real speed measurements (black) and the GKT model prediction of speed (red) at various detector locations for the* ***validation day****.*

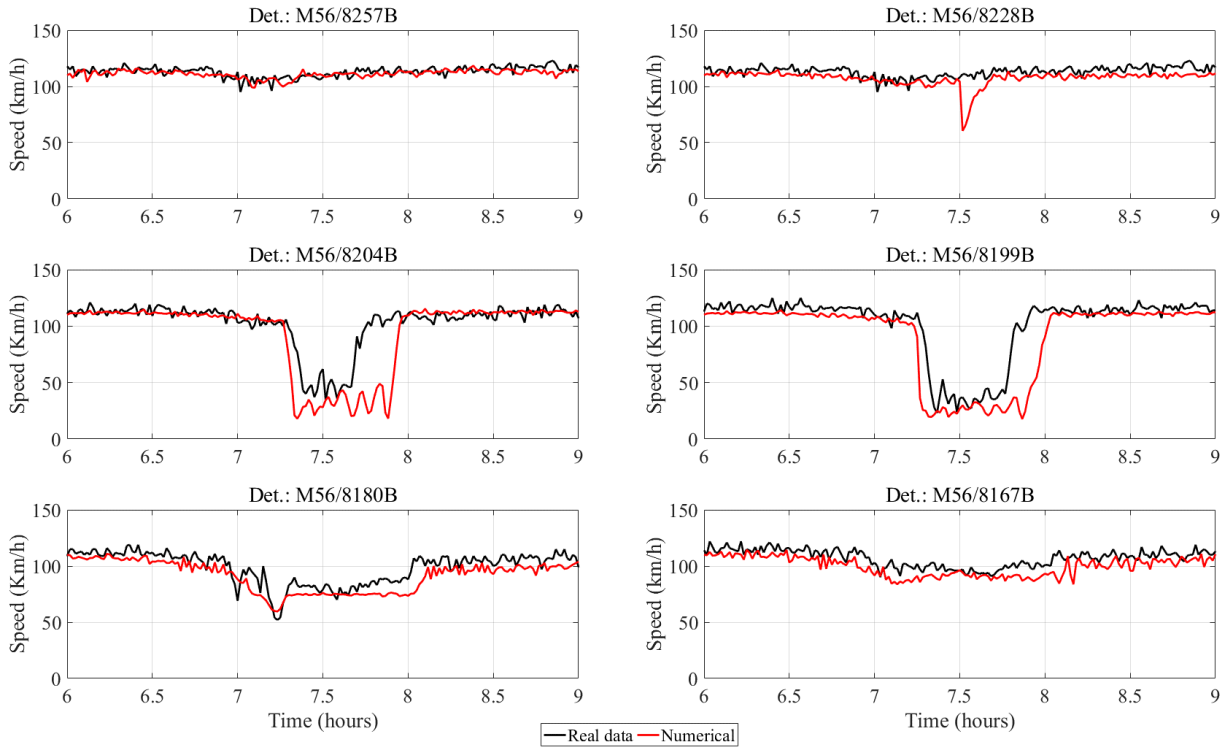

FIGURE 4.44: *(U.K. network – as single lane) Time series of the real speed measurements (black) and the METANET model prediction of speed (red) at various detector locations for the* ***validation day****.*

4.5 Final Remarks and Conclusions

In this chapter, the parallel metamodel-assisted DE algorithm was employed for the automated calibration of the parameters of a second-order macroscopic GKT traffic flow model, using real traffic data. Specifically, the GKT model was calibrated and validated by employing both the synchronous and the asynchronous version of the DE algorithm using real traffic data from the U.K. motorway and from Attiki Odos freeway in Athens; in the first network traffic congestion is created due to high on-ramp flows during the morning hours, whereas in the second network recurrent congestion is triggered by a saturated off-ramp during the morning peak hours, as well. Furthermore, the extended GKT model for the simulation of multi-lane traffic dynamics was also evaluated using real traffic data from the motorway network in the U.K. (by employing the synchronous version of the DE algorithm). Subsequently, by implementing the same optimization scheme for the same network in U.K., the GKT model was compared with the well-known METANET model.

Following from the numerical results, both parallel DE algorithms proved to be viable candidates and versatile tools for the calibration of macroscopic traffic flow models, having counteracting calibration parameters in which the cost function exhibits multi-optimal values. Specifically, the resulted optimal values of the model parameters indicated that the proposed DE algorithms guarantee the convergence to the best solutions as well as that the GKT model is able to replicate and predict with sufficient accuracy the prevailing traffic flow conditions; especially, in the case of the calibration of the complicated multi-lane GKT model, which have a relatively large number of (usually) counteracting calibration parameters, the synchronous DE algorithm also proved to be a promising and robust tool. It is also worth to highlight that the DE algorithms have the advantage that they can be used without the need of tuning its

parameters for the problem at hand, while wide bounds can be used for the unknown vector without convergence problems.

Regarding the implementation of the (synchronous) DE algorithm for the comparison of the GKT and METANET model, simulations results showed that the performance of the two models is comparable; both the GKT and METANET model were able to reproduce accurately and similarly the real traffic dynamics, including congestion. Moreover, by comparing the two versions of the DE algorithm, the asynchronous version had a faster convergence rate (especially at the first steps of the optimization procedure), compared to the synchronous one, as it was expected. Further, for the addressed optimization problem, the Radial Basis Function (RBF) Artificial Neural Network (ANN) featured the lowest training and testing errors for all generations and for both versions of the DE optimizer. As such, it was constantly (automatically) selected as surrogate model for the pre-evaluation phase, in both cases. Finally, the robustness of the calibrated parameters was demonstrated through the validation process, indicating that both the single- and multi-lane GKT models, as well as the METANET model, are able to reproduce with sufficient accuracy the traffic flow conditions of the particular networks also for different than the calibration date.

Part II

Macroscopic Modelling of ACC/CACC traffic: Stability Analyses

Chapter 5: Macroscopic Traffic Flow Modelling with Adaptive and Cooperative Adaptive Cruise Control

5.1 Introduction

During the last decades, there has been an enormous effort to develop a variety of VACS that are expected to bring radical changes in the way that traffic flow will be controlled and optimized. VACS, such as ACC and CACC systems, were initially developed with particular emphasis put on improving comfort, convenience, and safety. The benefits of the ACC and CACC framework are also highlighted in terms of improved capacity and stability. Indeed, for specific values of their parameters, such systems appear to be a potential remedy to reduce the amplitude or even to eliminate the formation of traffic flow instabilities, which are usually related to traffic jams. This advanced feature, along with the expected spreading of such systems, are likely to effectively contribute to the diminution of the existing and rising traffic congestion.

Motivated by such facts, the automotive industry and many research institutes have made a massive interdisciplinary effort to develop and test VACS, while several different types of equipped vehicles are already available in the market. The ACC technology, for example, enables drivers to automatically follow a preceding vehicle by controlling the throttle and the brake actuators. Specifically, using headway sensors, such as a radar or LIDAR, an ACC system is able to continuously measure the time-gap and the speed to the front vehicle, usually referred to as the leader. Hence, in cases that the ACC sensors detect that the leading vehicle travels at a lower speed, ACC automatically adjusts the speed of the equipped vehicle in order to realize the pre-selected by the user desired distance (gap-control mode). On the other hand, when the leader is out of the range of the equipped vehicle's sensors, the ACC vehicle operates in a speed-control mode, maintaining the user-defined free-speed.

An enhancement of the ACC functionality is the CACC system, which is based on inter-vehicle exchange of information among the equipped vehicles via wireless technology or ad-hoc networks, resulting in remarkably higher accuracy and faster response. Thus, even though ACC systems have been focused on increasing driving comfort, safety and collision avoidance, as the driver is relieved from continuous speed adjustments to the speed of the leader, CACC systems additionally offer high potential to further improve the traffic flow capacity and safety, reducing the traffic congestion as well. The latter is the prospective result of the main aspiration of the CACC concept to decrease time gaps between consecutive vehicles, as well as to eliminate the traffic disturbances. Compared to ACC, the literature on CACC systems is still very premature and relevant studies do not usually investigate the traffic flow effects of CACC quantitatively in terms of throughput, capacity, and congestion reduction, but aim at creating design frameworks which will standardize and optimize the use of such technology.

A lot of active approaches relying on microscopic traffic flow simulation have been reported, representing the vehicle behavior in presence of ACC and CACC systems at

individual level (see, e.g., Ioannou & Chien, 1993; Swaroop *et al.*, 1994; Swaroop & Hedrick, 1996; Liang & Peng, 1999, 2002; Swaroop & Rajagopal, 1999; Alkim *et al.*, 2000; Marsden *et al.*, 2001; VanderWerf *et al.*, 2001; Davis, 2004, 2007; Rajamani *et al.*, 2005; Kesting *et al.*, 2006, 2008, 2010; van Arem *et al.*, 2006; Nowakowski *et al.*, 2011; Shladover *et al.*, 2012; Arnaout & Bowling, 2014; Milanés *et al.*, 2014; Milanés & Shladover, 2014; Wang *et al.*, 2014; Ntousakis *et al.*, 2015). On the contrary, the corresponding literature pertaining to macroscopic models is rather limited. However, macroscopic models in general have specific advantages, compared to microscopic ones, as they require less computational resources, involve fewer parameters, and need lower calibration and validation effort. Hence, the development of macroscopic models for the real-time simulation of ACC and CACC traffic, evaluating also their impact on traffic dynamics, could be of major significance in the near future.

In Swaroop & Rajagopal, 1999, a design approach for an ACC strategy of vehicles in an Automated Highway System, based on macroscopic traffic flow stability analysis, was presented. In this study, in order to analyze the effect of the ACC laws on the behavior of traffic flow, an open stretch highway with inlets and exits was considered, having a small constant inflow from an on-ramp, where all the equipped vehicles employed constant-time headway policy; the results showed that the constant-time headway policy leads to characteristics inappropriate for automated traffic flow. Furthermore, Yi & Horowitz, 2002, presented a macroscopic model with velocity saturation for traffic flow that also takes into account a constant-time headway policy in order to study the behavior of ACC vehicles.

In Lenz, 1999, and Hoogendoorn & Bovy, 2001, the macroscopic formulation of a kinetic model to variable speed control was applied, using Variable Message Signs (VMS). In the first work, a sliding mode controller that was able to extinguish stop-and-go waves by increasing the flow above some density and by decreasing the flow below this density, adapting suitable speed limits on the VMS, was applied. In the second work, a similar approach was adopted, in which VMS were used to inform drivers of slower traffic ahead. The authors assumed that drivers decrease their desired velocity when control is active and applied the variable average desired speed in the macroscopic implementation of the model. As a result, the occurrence of the so-called phantom traffic jams was prevented, as long as the speed adaptation by drivers was sufficiently high.

An analysis of ACC systems based on macroscopic traffic flow modelling was also conducted by Demir, 2003. In particular, the already existing macroscopic model of Payne was modified including parameters to represent ACC policies, by being calibrated using a microscopic simulation model incorporated in ACC vehicles. Following from the simulation results, lower time headways increased the traffic flow rate while congestion disappeared faster, even with small penetration rates of ACC vehicles. Specifically, up to a penetration rate of 30 % the traffic flow rate was increasing, whereas an additional increase of the penetration rate did not provide any further benefits.

An extended multiclass gas-kinetic theory was proposed by Ngoduy *et al.*, 2009, to integrate the cooperative concepts into traffic flow modelling, allowing the equipped vehicles to adapt their desired speed to the speed of the congested traffic flowing downstream; the derived macroscopic model was based on the method of moments. In this way, the equipped vehicles lead to a delay in traffic inflowing the congested area, adopting a deceleration situation close to lower speed areas. Through the numerical tests it became apparent that the presence of equipped vehicles contributes to substantial improvements of traffic flow stability and total travel time, as well as to the suppression of traffic congestion. The same method of moments was applied by Ngoduy, 2012a, to derive a macroscopic formulation for a multiclass

gas-kinetic model able to simulate mixed traffic flow of both manual and ACC vehicles. Based on the numerical simulation results, it was demonstrated that increasing the penetration rate of ACC vehicles contributes to more stable traffic flow, while a rate of 30 % ACC vehicles results in remarkably improved capacity and reduced travel time. Furthermore, the development of a macroscopic model for CACC traffic flow dynamics was presented by Ngoduy, 2013a, also based on the gas-kinetic approach. The numerical results indicated that CACC systems better enhance the dynamic equilibrium capacity, compared to ACC vehicles, which potentially lead to jam suppression effects at bottlenecks. Finally, recent works regarding the platoon-based driving behavior (Ngoduy, 2013b) and the multi-anticipative driving behavior (Ngoduy & Wilson, 2014), are also derived from the modified gas-kinetic theory.

In the following Section 5.2, a new approach to develop a second order macroscopic model for traffic flow by Delis *et al.*, 2015a, is presented, which reflects ACC and CACC traffic dynamics in the GKT model (see Section 3.2.1). In particular, modelling is based on the introduction of a relaxation term in a GKT model that satisfies the time-gap principle of ACC or CACC systems and allows for consideration of mixed traffic of manual and ACC/CACC vehicles. The relaxation time is assigned to multiple leading vehicles in the CACC case, whereas in the ACC case it's only related to the direct leading vehicle. Appendix B presents the related mathematical background for the development of the macroscopic models for ACC and CACC traffic flow dynamics of Ngoduy, 2012a, and Ngoduy, 2013a, for comparative reasons.

5.2 The GKT Model for ACC and CACC Systems

In this section, the developed second-order macroscopic traffic flow model, incorporating the behavior of ACC and CACC equipped vehicles, is reviewed (Delis *et al.*, 2015a; Nikolos *et al.*, 2015). The model has been implemented based on the gas-kinetic traffic flow model, which was first established in the 1960s with a quite simple model by Prigogine & Andrews, 1960, and Prigogine, 1961. However, in the last years an increasing interest can be observed for the GKT model, by applying it to derive alternative continuum macroscopic traffic flow models (Treiber *et al.*, 1999; Helbing *et al.*, 2001; Treiber *et al.*, 2010; Ngoduy, 2012a; 2013a; 2013b). The macroscopic traffic flow equations are derived from the gas-kinetic ones using the so-called method of moments (see, e.g., Helbing, 1997b; Treiber *et al.*, 1999; Ngoduy, 2006, 2009; Ngoduy *et al.*, 2009; Ngoduy & Tampere, 2009; Ngoduy, 2012a). Specifically, as the gas-kinetic models describe the dynamics of the phase-space density, which reflect the dynamics of the velocity distribution functions of vehicles in traffic flow, one knowing the phase-space density profile and using the method of moments can define the macroscopic traffic flow variables such as the density, the mean speed, or the flow rate. It should also be noted at this point that the crucial difference between the GKT model and other macroscopic traffic flow models is its non-local interaction term, which has beneficial properties regarding the rapidity and robustness of numerical integration methods. Therefore, the GKT model allows for real world application ensuring accuracy, robustness and computational efficiency, even in case of large freeway network (Treiber *et al.*, 1999). Moreover, the non-local GKT model is capable to describe the "synchronized traffic", namely the hysteretic phase transitions to congested traffic, which is the most frequent form of congested states, typically occurring behind on-ramps, gradients, or other bottlenecks of crowded highways (Helbing & Treiber, 1998; Treiber

et al., 1999; Treiber & Helbing, 1999). For a more detailed review of the features of the GKT model with the corresponding mathematical form, see Section 3.2.1.

By denoting again $\rho(x,t)$ the traffic density, $u(x,t)$ the average speed and $q = \rho u$ the traffic flow rate as functions in space, x and time instant t, the modified single-lane GKT model, in its conservation law form with source terms (without on/off-ramps) is given as,

$$\partial_t(\rho) + \partial_x(\rho u) = 0\,, \tag{5.1}$$

$$\partial_t(\rho u) + \partial_x(\rho u^2 + \theta\rho) = \rho\left(\frac{V_e^*(\rho) - u}{\tau}\right)[1 - pF(\rho)] + pV_{acc/cacc}\,. \tag{5.2}$$

From the momentum equation (5.2), it can be seen that the contribution of ACC and CACC vehicles lies in the terms of $pV_{acc/cacc}$ and $[1 - pF(\rho)]$, where p is the penetration rate of the ACC/CACC-equipped vehicles. By setting the coefficient p equal to zero the original GKT model equations for manual driving are obtained, as described in Section 3.2.1. Moreover, the definition of the GKT models' parameters, such as the pressure-like term, θ, the equilibrium speed, $V_e^*(\rho)$ and the relaxation time, τ remains the same with their definition in Section 3.2.1.

Next, the incorporation of the ACC and CACC traffic dynamics in the GKT model is presented. This is done through the terms, $pV_{acc/cacc}$ and $[1 - pF(\rho)]$, in equation (5.2), with $p = 1$. One major difference of this new approach compared to others, is that the ACC/CACC terms contribute to the non-local relaxation term in the momentum equation of the GKT model, which controls the speed dynamics in traffic flow. In addition, the proposed model enables the explicit definition of the significant for cooperative systems time-gap principle, allowing the simulation of ACC and CACC flows with different time-gap settings, leading to different dynamic equilibrium capacities and dynamic behavior.

The proposed model is based on the prerequisite control objectives that the ACC systems should adopt, and by extension the CACC systems, as they have similar control objectives with the important difference being in their desired time gaps, according to Shladover *et al.*, 2012:

I. *Speed control mode*: to travel close to the pre-set by the driver maximum velocity, in cases where no leading vehicles are detected and identified by the sensor systems, or leading vehicles are detected but their speeds are higher than the driver-defined maximum velocity.

II. *Gap control mode*: to adjust the velocity of the equipped vehicle equal to the velocity of the leading vehicle, so as to maintain the user-defined desired gap, in cases that the leading vehicle is identified by the sensor systems and its velocity is lower than the pre-set by the user maximum speed.

III. The two aforementioned control modes are required to operate with robust, stable and smooth transitions between them, in order to avoid discomfort to the passengers, on account of sudden, abrupt changes in velocity.

At this point, it is essential to clarify the terms headway and gap. Time/space-headway is defined as the time/space interval between the front bumpers of two successive vehicles following each other, while time/space-gap is defined as the time/space interval between the rear bumper of the leading vehicle and the front bumper of the following vehicle (Treiber &

Kesting, 2013). Moreover, the proposed model was induced by an appealing control policy for ACC (and -in extension- CACC) systems, the ''Constant Time Headway (CTH) policy'', where the desired inter-vehicle distance is proportional to the vehicle's velocity (Zhou & Peng, 2005).

The following are the underlying assumptions for the developed model, satisfying simultaneously the aforementioned objectives:

- At densities explicitly below the critical threshold ρ_{acc} (being lower than or equal to the critical density ρ_{cr}) the additional term to the GKT model has no influence, since it is supposed that the drivers react by setting their maximum desired speeds as in a manual manner. At densities around ρ_{acc} a smooth but fast transition between the previous manual case and the ACC or CACC model is established, using the Fermi function:

$$F(\rho) = \frac{1}{2}\left[1 + tanh\left(\frac{\rho - \rho_{acc}}{\Delta\rho}\right)\right]. \tag{5.3}$$

- When the gap control mode is activated, the desired constant time gap T^* is imposed through its corresponding influence on a desired density ρ^*, given as:

$$\rho^* = \frac{1}{1/\rho_{max} + T^* u^*} \tag{5.4}$$

in which the denominator reflects the desired space headway, with $1/\rho_{max}$ being the vehicle's length and $u^* = u(x^*)$ being the velocity of the preceding vehicle, computed at "interaction" position:

$$x^* = x + \gamma^*(1/\rho_{max} + T^* u)\,, \quad \gamma^* \in [1, 2]\,. \tag{5.5}$$

Additionally, after a relaxation time τ^* the desired speed relaxes to the speed of the preceding vehicle u^*. Accordingly, the corresponding source term of equation (5.2) that reflects the behavior of ACC systems can be expressed mathematically as

$$V_{acc}(\rho, u, \rho^*, u^*) = F(\rho)\left(\frac{\rho^* u^* - \rho u}{\tau^*}\right). \tag{5.6}$$

In the work of Marsden *et al.*, 2001, it was demonstrated that the minimum time-gap that can be achieved by ACC vehicles is 0.8s. In general, indicated values for ACC-equipped vehicles should be $T^* \in [0.8, 2.2]s$, following [ISO 15622, 2010] standards, while $\tau^* \approx 1s$.

In the following, in order to model the impact of CACC vehicles in traffic flow dynamics, a similar approach is utilized, with the only difference being that the vehicle can exchange information with multiple preceding vehicles, each one of which has a different relaxation time. As a result, the corresponding source term of equation (5.2) is modified, taking into consideration the velocities of the respective preceding vehicles, enhancing in this way the smoothing effect of this term. It is also worth mentioning that this feature for exchanging information from far downstream enables a considerable reduction in the size of time gaps, resulting in a significant increase of traffic flow density and efficiency without compromising safety. Thus, the corresponding source term of the momentum equation takes the form

$$V_{cacc}(\rho,u,\rho^*,u^*) = F(\rho)\sum_{i=1}^{M}\left(\frac{\rho^* u_i^* - \rho u}{\tau_i^*}\right) \tag{5.7}$$

where $u_i^* = u(x_i^*)$ with $x_i^* = x + \ i\cdot\gamma^*(1/\rho_{max} + T^*\cdot u), \quad i = 1,\dots,M$, and

$$\rho^* = \frac{1}{1/\rho_{max} + T^* u_1^*}. \tag{5.8}$$

In this work indicated values for CACC systems should be $M = 3$, while $[\tau_1^*, \tau_2^*, \tau_2^*] = [2,3,6]$.

5.3 Qualitative comparison between the utilized ACC model and that proposed by Ngoduy

In this section, the developed second-order macroscopic traffic flow model, incorporating the behavior of ACC-equipped vehicles (Delis *et al.*, 2015a; Nikolos *et al.*, 2015) is qualitatively compared with the one proposed by Ngoduy, 2012c.

By denoting $\rho(x,t)$ the traffic density, $u(x,t)$ the average speed and $q = \rho u$ the traffic flow rate as functions in space, x and time instant t, the modified single-lane GKT model, in its conservation law form with source terms (without on/off-ramps) is given as,

$$\frac{\partial\rho}{\partial t} + \frac{\partial(\rho u)}{\partial x} = 0 \tag{5.9}$$

$$\frac{\partial(\rho u)}{\partial t} + \frac{\partial[\rho(u^2+\theta)]}{\partial x} = \rho\left(\frac{V_e^*(\rho) - u}{\tau}\right)[1 - pF(\rho)] + pV_{acc} \Rightarrow \tag{5.10}$$

$$\frac{\partial(\rho u)}{\partial t} + \frac{\partial[\rho(u^2+\theta)]}{\partial x} = \rho\left(\frac{V_e^*(\rho) - u}{\tau}\right)[1 - pF(\rho)] + pF(\rho)\left(\frac{\rho^* u^* - \rho u}{\tau^*}\right), \tag{5.11}$$

where the Fermi function is given as

$$F(\rho) = \frac{1}{2}\left[1 + tanh\left(\frac{\rho - \rho_{acc}}{\Delta\rho}\right)\right] \tag{5.12}$$

and the desired constant time gap T^* of the ACC vehicle is imposed through its corresponding influence on a desired density ρ^*, given as

$$\rho^* = \frac{1}{1/\rho_{max} + T^* u^*}\ , \tag{5.13}$$

where the denominator reflects the desired space headway, with $1/\rho_{max}$ being the vehicle's length and $u^* = u(x^*)$ being the velocity of the preceding vehicle, computed at "interaction" position

$$x^* = x + \ \gamma^*(1/\rho_{max} + T^* u)\,, \quad \gamma^* \in [1,2]\,. \tag{5.14}$$

For penetration rate of the ACC-equipped vehicles $p = 0$, the original GKT model results

$$\frac{\partial(\rho u)}{\partial t}+\frac{\partial[\rho(u^2+\theta)]}{\partial x}=\rho\left(\frac{V_e^*(\rho)-u}{\tau}\right). \tag{5.15}$$

For penetration rate of the ACC-equipped vehicles $p=1$, the modified model becomes

$$\frac{\partial(\rho u)}{\partial t}+\frac{\partial[\rho(u^2+\theta)]}{\partial x}=\left(\frac{\rho V_e^*-\rho u}{\tau}\right)[1-F(\rho)]+F(\rho)\left(\frac{\rho^* u^*-\rho u}{\tau^*}\right). \tag{5.16}$$

The additional source term

$$\left(\frac{\rho^* u^*-\rho u}{\tau^*}\right) \tag{5.17}$$

smoothly [due to $F(\rho)$] replaces the original GKT source term

$$\left(\frac{\rho V_e^*-\rho u}{\tau}\right) \tag{5.18}$$

for $\rho>\rho_{acc}$. As a result, for densities below ρ_{acc}, the additional term has no influence, and the ACC-equipped vehicles tend to reach the maximum desired speeds set by their drivers, similarly to the manual manner. However, for $\rho>\rho_{acc}$ the original source term is smoothly deactivated and the ACC vehicles turn into the gap control mode, trying to reach a pre-specified constant time gap T^* (indirectly, through ρ^*) and the speed of the preceding vehicle $u^*=u(x^*)$, within a relaxation time τ^*.

The proposed modification was based on rational thinking rather on formal mathematical derivation, in order to fulfill the ACC/CACC control objectives described by Shladover *et al.*, 2012 and the Constant Time Headway (CTH) policy (Zhou & Peng, 2005). It provides the major advantage that the only modification to the original GKT model is in the source term of the momentum equation, without changing the corresponding LHS. This results in a very easy numerical implementation of the corresponding modification. Additionally, the ACC penetration rate is easily and explicitly defined.

The corresponding ACC model proposed by Ngoduy, 2012c, is also based on the original GKT model; however, its derivation is purely analytic, based on the method of moments (see Appendix B, where a detailed derivation is included). For the case of a 100% penetration rate of ACC-equipped vehicles, the model's equations are:

$$\frac{\partial\rho}{\partial t}+\frac{\partial(\rho u)}{\partial x}=0\,, \tag{5.19}$$

$$\frac{\partial(\rho u)}{\partial t}+\frac{\partial[\rho(u^2+\theta)]}{\partial x}-\frac{\gamma}{\tau^*}\frac{\partial u}{\partial x}=\rho\left(\frac{V_e^*(\rho)-u}{\tau}\right), \tag{5.20}$$

where τ^* denotes the relaxation time of the ACC vehicle. From the equation above it is clear that the contribution of the ACC vehicles lies in the convection term, which consequently results in the propagation of the shock waves (Ngoduy, 2012c). According to this model, the impact of ACC vehicles on the wave propagation is indicated through τ^*, which has as result that the waves propagate faster upstream and slower downstream in free-flow traffic conditions. It was experimentally shown that the impact of ACC vehicles on traffic dynamics becomes insignificant when $\tau^*>\tau$.

A major difference of the model of Ngoduy, 2012c, compared to the examined one (Delis *et al.*, 2015a; Nikolos *et al.*, 2015) is the fact that the ACC additional term is in the LHS of the momentum equation, which requires more significant modifications to the original GKT model for its numerical discretization.

Another difference between the two models is that the desired ACC time gap is not explicitly defined within the momentum equation in the model of Ngoduy, 2012c. Moreover, the additional term is active in the whole density regime (congested and uncongested traffic flow), which is not compatible with the objectives of the ACC systems (Shladover *et al.*, 2012).

A more thorough comparison between the two models should involve numerical experiments in common test-cases. This requires the programming of the model proposed by Ngoduy, 2012c, which is beyond the scope of this thesis and remains as a topic for future work.

Chapter 6: Macroscopic Traffic Flow Stability Analysis for Adaptive and Cooperative Adaptive Cruise Control Systems

6.1 Introduction

In recent years, many efforts have been made aiming to investigate the formation and diffusion of traffic flow instabilities; it is well known that even small perturbations resulting from the response of drivers to a stimulus, can lead to the formation of traffic jams. In many occasions, these emergent traffic jams could present a serious problem rather than just a small inconvenience, deteriorating the overall traffic performance, increasing fuel consumption, as well as leading to severe infrastructure underutilization. Moreover, such traffic jams are usually associated with traffic flow instabilities, including stop-and-go waves, which, under congested states, can grow and travel against traffic direction. In general, the application of new technologies in the field of VACS, such as ACC and CACC systems, can provide additional tools for the remedy of the aforementioned traffic flow problems, reducing the adverse impacts of traffic flow instabilities through the selection of suitable operating parameters. To this end, in this chapter both linear and nonlinear stability analysis is performed, in order to derive the stability threshold(s) of the recently developed second-order macroscopic traffic flow model that is able to simulate the effects in traffic flow when ACC and CACC vehicles are present; the adopted macroscopic model is based on the GKT model (see Chapter 5). Thus, the influence of the equipped vehicles on the traffic flow stabilization is considered with respect to both small and large perturbations around the equilibrium state.

More specifically, traffic flow perturbation phenomena, such as abrupt decelerations of vehicles, bottlenecks, rear-end collisions, or non-uniformity of the flow entering a highway from an on-ramp, are likely to develop into stop-and-go waves traveling upstream, or even traffic jams, under certain traffic flow conditions; thus, resulting in a reduction of traffic efficiency and negative influence on total travel time, energy consumption, and traffic accidents. Consequently, it is of significant importance to evaluate the capability of ACC- and CACC-equipped vehicles to reduce potential traffic instability, and identify their crucial parameters that result to a stable or unstable response after the introduction of a disturbance to the traffic flow.

Various researchers have demonstrated that such cooperative systems can improve the traffic flow stability (Hasebe *et al.*, 2003; Davis, 2004; van Arem *et al.*, 2006; Naus *et al.*, 2010), while others appear more conservative regarding their stabilization effects (Marsden *et al.*, 2001). In the former case also belongs the study of an ACC CTH policy in the work by Zhou & Peng, 2005, concluding that ACC systems are required to ensure string or traffic flow stability, otherwise the traffic safety and congestion would be deteriorated instead of improving.

Scientists have been particularly interested in understanding the occurrence of traffic flow instabilities since the '50s (see, e.g., Herman *et al.*, 1959), as it is considered to be one of

the fundamental problems in traffic theory. Indeed, much work has been devoted to the application of both linear and nonlinear stability methods in order to derive stability criteria, using either microscopic models (Herman *et al.*, 1959; Wilson *et al.*, 2004; Treiber *et al.*, 2006; Kesting & Treiber, 2008; Yu *et al.*, 2008; Li *et al.*, 2009, 2013; Tian *et al.*, 2011; Treiber & Kesting, 2011, 2013; Peng *et al.*, 2012; Tang *et al.*, 2012; Zheng *et al.*, 2012; Ngoduy, 2013c) or macroscopic ones (Wilson *et al.*, 2004; Gupta & Katiyar, 2005, 2006; Tampere *et al.*, 2005; Zhang & Wong, 2006; Tang *et al.*, 2008, 2011; Helbing & Johansson, 2009; Ngoduy & Tampere, 2009; Zhang *et al.*, 2009; Tian *et al.*, 2011; Ngoduy, 2012b, 2014; Treiber & Kesting, 2013; Gupta & Dhiman, 2014). At this point, it is necessary to provide a clear distinction on the definition of stability analysis between microscopic and macroscopic traffic flow models. Stability analysis in a macroscopic level is referred to as flow stability, describing the way aggregated density and speed evolve, depending on variations in traffic flow caused by speed or density perturbations. On the other hand, the stability analysis obtained at a vehicle level is called string stability of a platoon of vehicles, referring to the way the perturbations from the deceleration of the leading vehicles are propagated upstream against the traffic flow (Swaroop & Rajagopal, 1999; Treiber & Kesting, 2013). For a more detailed review of the overall classification of traffic flow models with the corresponding stability method for each class, we refer to the work by Treiber & Kesting, 2013.

Although much work of microscopic approaches for analyzing linear or nonlinear instabilities of traffic flow has been reported, in order to evaluate the impact of the penetration of ACC and CACC systems on traffic dynamics (see, for instance, Ioannou & Chien, 1993; Swaroop *et al.*, 1994; Swaroop & Hedrick, 1996; Liang & Peng, 1999; 2000; Treiber & Helbing, 2001; Bareket *et al.*, 2003), corresponding approaches pertaining to macroscopic or gas-kinetic traffic flow models are relatively rare. Swaroop & Rajagopal, 1999 first studied the traffic flow stability under an ACC spacing policy, using an aggregated macroscopic traffic flow model for an open stretch highway with entries and exits. Using a linearized stability analysis they concluded that the traffic flow equilibrium state was marginally stable, but traffic flow was unstable when using spatially discretized stability analysis for a CTH policy. It should be stressed, however, that the findings appear to contradict those reported in the work by Li & Shrivastava, 2002, where the traffic flow stability on a circular highway with no entries and exits was studied, concluding that the traffic flow induced by the CTH policy is stable.

Further, a framework to study traffic flow propagation stability using a generalized macroscopic model for vehicles controlled by ACC policies was presented by Yi & Horowitz, 2006. The nonlinear stability condition was derived using a wavefront expansion method, resulting in necessary and mandatory conditions to predict the traffic flow stability under ACC systems and having the ability to be used for the design and validation of ACC systems with different spacing policies as well.

A linear stability analysis was also used by Ngoduy, 2012c, showing analytically that the proposed approach of ACC systems, based on an extension of the multiclass gas-kinetic theory, stabilizes the traffic flow with respect to small perturbations. The numerical simulation results in a circular homogeneous freeway were supported by the analytical results. The same linear stability method was implemented in recent works regarding the platoon-based driving behavior (Ngoduy, 2013a) and the multi-anticipative driving behavior (Ngoduy & Wilson, 2014); based on the linear stability diagrams, the developed models enhance the stabilization of traffic flow with respect to a small perturbation. Finally, stability diagrams were constructed from the developed macroscopic model for CACC traffic flow dynamics by Ngoduy, 2013b, based on both linear and non-linear stability methods for a

certain model parameter set. The numerical results indicated that the CACC vehicles enhance the stabilization of traffic flow with respect to both small and large perturbations, compared to the ACC vehicles.

The outline of this chapter is as follows. In Section 6.2, using both the linear (6.2.1) and nonlinear (6.2.2) methods, we derive analytically the influencing conditions to the stability of traffic flow based on the developed model. Section 6.3 presents a numerical study to support qualitatively the analytical findings.

6.2 Stability Analysis for ACC and CACC Systems

Inherently, the stability analysis concerns the study of solutions and trajectories of a dynamic system with respect to smaller or larger introduced perturbations in the homogeneous flow, which are primarily responsible for the deterioration of traffic flow stability. Regarding traffic flow theory, drivers' response under hazardous driving conditions, such as an abrupt or sudden deceleration/acceleration, results in the formation of perturbations that, in congested traffic flow, can grow and eventually give rise to "phantom traffic jams", propagating against the direction of the vehicle flow. Thus, it is of high importance to derive the specific instability conditions under which emergent waves are expected to occur even in case of small introduced perturbations (Treiber & Kesting, 2013).

Towards this direction, this section aims to investigate the qualitative properties and the influences of the macroscopic characteristics of ACC and CACC vehicles exhibited by the developed model, as presented in Chapter 5, on traffic flow stability. To this end, a proper stability threshold is derived based on linear and nonlinear stability analyses, in reference to small and large perturbations, respectively. At this point it is important to highlight the difference between small and large perturbations in the stability analysis of traffic flow systems. Mathematically, dynamics of small perturbations can be approximately characterized by linear differential equations around an equilibrium point using Taylor series expansion. However, the outcome of such linear approximations is that, even if the traffic system is linearly stable, it might actually still be nonlinearly unstable with respect to large perturbations; small perturbations can be eradicated or delimited with the course of time but large ones may be amplified generating persistent traffic waves. Hence, the linear stability method is valid only in cases of small perturbations, since the higher order terms in this technique are neglected. Indeed, as pointed out by Whitham, 1974, in cases where the amplitude of the perturbations is considerably large (caused, e.g., by hard braking maneuvers or reckless lane changes), the aforementioned linear stability approach is likely to result in incorrect outcomes. Therefore, there has been a need to adopt alternative nonlinear methods to derive the stability conditions, under which a large perturbation travels against the traffic flow, such as the wavefront expansion method that is also followed in this thesis (Yi *et al.*, 2003). At this point, it should be highlighted that both linear and nonlinear stability methods can complementary provide a valuable insight into the general behavior of the model in the presence of ACC or CACC vehicles and its numerical solution (Swaroop & Rajagopal, 1999; Ngoduy, 2012c, 2013b).

6.2.1 Linear Stability Analysis for ACC and CACC Systems

Let's start with finding the unstable traffic regions by the linear stability analysis of the presented model, taking primarily into account the case where only ACC vehicles are present in the flow, i.e. $p = 1$ (100% penetration rate) in equation (5.2). In order to simplify the analysis, it is assumed that the flow is congested (thus the value of $F(\rho) \to 1$ in equation (5.6) and only the ACC-term is activated in the source term of equation (6.2)). Accordingly, equations (5.1) and (5.2) are transformed in the following form:

$$\partial_t(\rho) + u\partial_x(\rho) + \rho\partial_x(u) = 0\,, \tag{6.1}$$

$$\partial_t(u) + u\partial_x(u) + \frac{1}{\rho}\Big(\partial_\rho(P)\partial_x(\rho) + \partial_u(P)\partial_x(u)\Big) = \frac{1}{\rho}\left(\frac{\rho^* u^* - \rho u}{\tau^*}\right), \tag{6.2}$$

where $P = \theta\rho$, while the shortened notations for partial derivatives are defined as

$$\partial_a(\cdot) = \frac{\partial(\cdot)}{\partial a}. \tag{6.3}$$

The whole procedure begins supposing that the stationary and spatially homogeneous (i.e. time- and location-independent) solution vector of the system of partial differential equations (6.1) and (6.2) is the constant density ρ_0 and velocity u_0 (Helbing & Johansson, 2009; Treiber & Kesting, 2013). Thus, in this initial equilibrium state of homogenous flow all vehicles have equal speed, constant spacing and zero acceleration. Subsequently, small deviations are considered around this solution pair ρ_0 and u_0, represented by $\delta\rho(x,t)$ and $\delta u(x,t)$, which result in

$$\delta\rho(x,t) = \rho(x,t) - \rho_0 \quad \text{and} \quad \delta u(x,t) = u(x,t) - u_0\,. \tag{6.4}$$

The dominant essence of the traffic flow stability analysis is to find the threshold under which the magnitude of the perturbations $\delta\rho(x,t)$ and $\delta u(x,t)$ decreases, in order to gradually restore the equilibrium state.

Next, by setting $\rho(x,t) = \rho_0 + \delta\rho(x,t)$ and $u(x,t) = u_0 + \delta u(x,t)$ into the reformed continuity equation (6.1), and performing linear Taylor approximations, where is necessary, and dropping all nonlinear terms because of the assumption of small perturbations $\delta\rho(x,t)/\rho_0 \ll 1$ and $\delta u(x,t)/u_0 \ll 1$, the following linearized equation is derived

$$\partial_t(\delta\rho) + u_0\partial_x(\delta\rho) + \rho_0\partial_x(\delta u) = 0\,. \tag{6.5}$$

In the same way, and noticing that $\rho^* u^*$ is independent of ρ, the linearized equation for the momentum dynamics equation (6.2), describing the behavior of ACC vehicles, becomes

$$\partial_t(\delta u) + u_0\partial_x(\delta u) + \frac{1}{\rho_0}\left[\partial_u(P)\partial_x(\delta u) + \partial_\rho(P)\partial_x(\delta\rho) - \frac{1}{\tau^*}\partial_u(\rho^* u^*)\delta u\right] + \frac{\delta u}{\tau^*} = 0. \tag{6.6}$$

In principle, the stability analysis highly depends on the form of the perturbed initial conditions, which is essential to be defined in a way that the linear approach is as general as possible. Indeed, any conventional functional form is possible to be implemented for the perturbations of the initial uniform state. However, any periodic function can be written as a

discrete sum (or integral in cases of non-periodic functions) of sine and cosine functions. If the model is stable with respect to any function of sines or cosines, it will be stable for any linear combination of these functions as well. Therefore, proving the stability conditions of the model in relation to sine or cosine perturbations, also proves the general stability conditions to any functional form of the perturbations (Helbing & Johansson, 2009). Accordingly, it is considered that the corresponding functions of the deviations are determined as shown below:

$$\delta\rho(x,t) = \delta\rho_0 e^{\lambda t + i\omega x}\,, \tag{6.7}$$

$$\delta u(x,t) = \delta u_0 e^{\lambda t + i\omega x} \tag{6.8}$$

in which the wave frequency λ and the wave number ω are complex numbers: $\lambda,\ \omega \in \mathbb{C}$, i denotes the imaginary unit, and $\delta\rho_0$ and δu_0 are constants.

The remainder of the linear stability analysis concentrates on finding the conditions so that two restrictions are met (Helbing & Johansson, 2009; Treiber & Kesting, 2013):

I. The deviation pair $\delta\rho(x,t)$ and $\delta u(x,t)$ is a solution of equations (6.1) and (6.2) and

II. This solution is stable, which means that the amplitude of the perturbation should diminish with time; the latter is true if the real part of λ is strictly negative.

In order to satisfy the former condition we substitute the definitions for the perturbations $\delta\rho(x,t)$ and $\delta u(x,t)$ (equations (6.7) and (6.8)) are substituted in the linearized equations (6.5) and (6.6), which yields the following linear system (which can be considered as an eigenvalue problem)

$$\underbrace{\begin{pmatrix} \lambda - a_{11} & a_{12} \\ a_{21} & \lambda - a_{22} \end{pmatrix}}_{\mathcal{J}} \begin{pmatrix} \delta\rho_0 \\ \delta u_0 \end{pmatrix} = \begin{pmatrix} 0 \\ 0 \end{pmatrix} \tag{6.9}$$

using the following abbreviations

$$a_{11} = -i\omega u_0 \tag{6.10}$$

$$a_{12} = i\omega\rho_0 \tag{6.11}$$

$$a_{21} = i\omega \frac{1}{\rho_0}\partial_\rho(P) \tag{6.12}$$

$$a_{22} = -i\omega\left(u_0 + \frac{1}{\rho_0}\partial_u(P)\right) + \frac{1}{\rho_0\tau^*}\partial_u(\rho^* u^*) - \frac{1}{\tau^*}. \tag{6.13}$$

These eigenvalues of λ result by solving the characteristic polynomial of second order in λ, which is obtained by determining the determinant of the matrix $\mathcal{J}$, and requiring that it becomes equal to zero. So, the corresponding characteristic polynomial is given as

$$det(\mathcal{J}) = 0 \Leftrightarrow \lambda^2 - (a_{11} + a_{22})\lambda + (a_{11}a_{22} - a_{12}a_{21}) = 0\,, \tag{6.14}$$

which results in

$$\lambda_1 = 0.5\left(a_{11} + a_{22} + \sqrt{(a_{11} - a_{22})^2 + 4a_{12}a_{21}}\right) \tag{6.15}$$

and

$$\lambda_2 = 0.5\left(a_{11} + a_{22} - \sqrt{(a_{11} - a_{22})^2 + 4a_{12}a_{21}}\right). \tag{6.16}$$

Condition II is strictly fulfilled if the real part of λ_1, λ_2 is strictly negative, i.e. $Re(\lambda_{1,2}) < 0$. Thus,

$$Re(a_{11} + a_{22}) = \frac{1}{\rho_0 \tau^*}\frac{\partial(\rho^* u^*)}{\partial u} - \frac{1}{\tau^*} = -\frac{1}{\tau^*}\left(1 - \frac{1}{\rho_0}\frac{\partial(\rho^* u^*)}{\partial u}\right). \tag{6.17}$$

Under the assumption of small perturbations around the initial state, it can be written that

$$\frac{1}{\rho_0}\frac{\partial(\rho^* u^*)}{\partial u} \approx \frac{1}{\rho_0}\frac{\partial(\rho^* u)}{\partial u} = \frac{1}{\rho_0}\frac{\rho_{max}}{(1 + T^*\rho_{max}u)^2}, \tag{6.18}$$

which for $\rho_0 \in [\rho_{cr}, \rho_{max}]$ takes values always less than one. Thus, the value of $Re(a_{11} + a_{22})$ is always negative.

Owing to the fact that the square root of equations (6.15) and (6.16) contains a complex number the following useful formula is applied for separating the real part R and imaginary part I for a complex number $z = R + iI$ (which is described in detail in the Appendix A):

$$\sqrt{R \pm i|I|} = \sqrt{0.5\left(\sqrt{R^2 + I^2} + R\right)} \pm i\sqrt{0.5\left(\sqrt{R^2 + I^2} - R\right)}. \tag{6.19}$$

By applying (6.18) to the square root terms of $\lambda_{1,2}$, eventually results in

$$Re\left(\sqrt{(a_{11} - a_{22})^2 + 4a_{12}a_{21}}\right) = \sqrt{0.5\left(\sqrt{R^2 + I^2} + R\right)}, \tag{6.20}$$

where now

$$R = \frac{1}{\tau^{*2}}\left(1 - \frac{1}{\rho_0}\partial_u(\rho^* u^*)\right)^2 - \left(\frac{\omega}{\rho_0}\partial_u(P)\right)^2 - 4\omega^2\partial_\rho(P) \tag{6.21}$$

and

$$I = \frac{2\omega}{\rho_0 \tau^*}\partial_u(P)\left(1 - \frac{1}{\rho_0}\partial_u(\rho^* u^*)\right). \tag{6.22}$$

Thus, from equations (6.17) and (6.20), and simultaneously taking into account that a change from stable to unstable behavior, i.e. the transition from negative to positive values of $Re(\lambda_{1,2})$ occurs only for eigenvalue λ_1, the inequality $Re(\lambda_1) < 0$ results in:

$$\begin{aligned} &\frac{1}{\rho_0 \tau^*}\partial_u(\rho^* u^*) - \frac{1}{\tau^*} < -\sqrt{0.5\left(\sqrt{R^2 + I^2} + R\right)} \Leftrightarrow \\ &\left(\frac{1}{\rho_0 \tau^*}\partial_u(\rho^* u^*) - \frac{1}{\tau^*}\right)^2 > 0.5\left(\sqrt{R^2 + I^2} + R\right) \Leftrightarrow \end{aligned} \tag{6.23}$$

$$2\left(\frac{1}{\rho_0\tau^*}\partial_u(\rho^*u^*)-\frac{1}{\tau^*}\right)^2>\left(\sqrt{R^2+I^2}+R\right)\Leftrightarrow$$
$$4\left(\frac{1}{\rho_0\tau^*}\partial_u(\rho^*u^*)-\frac{1}{\tau^*}\right)^4>\left(\sqrt{R^2+I^2}+R\right)^2\Leftrightarrow$$
$$4\left(\frac{1}{\rho_0\tau^*}\partial_u(\rho^*u^*)-\frac{1}{\tau^*}\right)^4-4\left(\frac{1}{\rho_0\tau^*}\partial_u(\rho^*u^*)-\frac{1}{\tau^*}\right)^2R>I^2\Leftrightarrow$$
$$\partial_\rho(P)\left(\frac{1}{\tau^*}-\frac{1}{\rho_0\tau^*}\partial_u(\rho^*u^*)\right)^2>0\,.$$

Using equation (6.18), the following inequality is conducted

$$\mathcal{B}\left(\frac{1}{\tau^*}\right)^2\left(1-\frac{1}{\rho_0}\mathcal{A}\right)^2>0 \tag{6.24}$$

where $\mathcal{B}=\partial_\rho(P)$, $\mathcal{A}=\frac{\rho_{max}}{(1+T^*\rho_{max}u)^2}$.

From the last inequality, provided that the term $\mathcal{B}=\partial_\rho(P)$ is positive (which is true in our case, where the pressure term P is modelled as $P=\rho A(\rho)u^2$), the stability condition for linear stability is always fulfilled. As a special case, the stability threshold is derived for

$$\left(1-\frac{1}{\rho_0}\mathcal{A}\right)^2=0\Leftrightarrow\rho_0=\mathcal{A}=\frac{\rho_{max}}{(1+T^*\rho_{max}u)^2}$$
$$\Leftrightarrow T^*=\frac{-1+\sqrt{\frac{\rho_{max}}{\rho}}}{\rho_{max}u}\,. \tag{6.25}$$

The possible values of $T^*\in[T^*_{min},T^*_{max}]$. From equation (6.25), arises:

$$u=\frac{1}{T^*}\frac{-1+\sqrt{\frac{\rho_{max}}{\rho}}}{\rho_{max}}\,. \tag{6.26}$$

Following an analogous derivation method, and taking into consideration the case of having only CACC-equipped vehicles (see Chapter 5), the linear stability conditions for equations (5.1) and (5.2) are obtained as:

$$\partial_\rho(P)\left(\sum_{i=1}^{M}\frac{1}{\tau_i^*}-\sum_{i=1}^{M}\frac{1}{\rho_0\tau_i^*}\frac{\rho_{max}}{(1+T^*\rho_{max}u)^2}\right)^2>0\,. \tag{6.27}$$

The term in the left-hand-side of equation (6.27) can be written as:

$$\partial_\rho(P)\left(\sum_{i=1}^{M}\frac{1}{\tau_i^*}\left(1-\frac{1}{\rho_0}\frac{\rho_{max}}{(1+T^*\rho_{max}u)^2}\right)\right)^2=\partial_\rho(P)\left(\sum_{i=1}^{M}\frac{1}{\tau_i^*}\left(1-\frac{1}{\rho_0}\mathcal{A}\right)\right)^2$$
$$=\partial_\rho(P)\left(1-\frac{1}{\rho_0}\mathcal{A}\right)^2\left(\sum_{i=1}^{M}\frac{1}{\tau_i^*}\right)^2\,. \tag{6.28}$$

As the third term in equation (6.28) is always positive, the stability threshold results in this case in the same way as for the previous ACC analysis (equations (6.25) and (6.26)).

6.2.2 Nonlinear Stability Analysis for ACC and CACC Systems

Since the linear stability analysis of the ACC/CACC system presented in Section 6.2.1 is only valid when the magnitude of perturbations is small, as for the linear approximation to be valid, in this Section the nonlinear stability analysis follows. The propagation stability conditions for the developed ACC and CACC traffic flow model are derived using a wavefront expansion method with respect to large perturbations around an equilibrium traffic state. In principle, if a perturbation begins at a certain location x_0 in a homogenous equilibrium state (i.e. uniform flow) (ρ_0, u_0), the wavefront is the propagation curve of the perturbation inside this homogenous flow. If the perturbation maintains its initial modulation magnitude during propagation, the traffic flow is considered to be nonlinearly stable. In contrast, if the perturbation travels upstream with increasing amplitude, traffic will become gradually unstable, forming for example shock waves or stop-and-go waves; the wavefront in a traffic system can be considered as a separation curve between disturbed and undisturbed flow regions (Yi *et al.*, 2003).

In what follows, the wavefront expansion method is adopted in order to find the unstable traffic regions of traffic flow via model equations (5.1) and (5.2), which incorporate the modelling of ACC and CACC vehicles (see Chapter 5). First of all, only the case of ACC-equipped vehicles is taken into account, while the same procedure will be expanded subsequently to the case of CACC-equipped vehicles. Hence, equations (5.1) and (5.2) are considered in their simplified form, presented in equations (6.1) and (6.2).

To derive the influencing conditions to traffic flow stability under a large perturbation, the macroscopic traffic flow variables, $\rho(x,t)$ and $u(x,t)$, need to be expanded, as well as their time and space partial derivatives, around the wavefront, as a power series of a small deviation

$$\xi = x - X(t)\,, \tag{6.29}$$

with $X(t)$ being the location of the wavefront at time instant t, and

$$\dot{X}(t) = \frac{dX}{dt} = u_0 + u_c\,, \tag{6.30}$$

where u_c denotes the relative characteristic speed, which will be defined later. Thus, using equation (6.29), the aforementioned flow variables ρ and u are expanded downstream the wavefront in a power series of ξ as

$$\rho(x,t) = \rho_0 + \xi\partial_x(\rho(t)) + \frac{1}{2}\xi^2\partial_{xx}(\rho(t)) + \cdots \tag{6.31}$$

$$u(x,t) = u_0 + \xi\partial_x(u(t)) + \frac{1}{2}\xi^2\partial_{xx}(u(t)) + \cdots \tag{6.32}$$

$$\partial_t(\rho) = -\dot{X}(t)\partial_x\big(\rho(t)\big) + \xi\dot{\rho}_x(t) + \xi\left(-\dot{X}(t)\partial_{xx}\big(\rho(t)\big)\right) + \frac{1}{2}\xi^2\dot{\rho}_{xx}(t) + \cdots \tag{6.33}$$

$$\partial_t(u) = -\dot{X}(t)\partial_x\big(u(t)\big) + \xi\dot{u}_x(t) + \xi\left(-\dot{X}(t)\partial_{xx}\big(u(t)\big)\right) + \frac{1}{2}\xi^2\dot{u}_{xx}(t) + \cdots \tag{6.34}$$

$$\partial_x(\rho) = \partial_x\big(\rho(t)\big) + \xi\partial_{xx}\big(\rho(t)\big) + \frac{1}{2}\xi^2\partial_{xxx}\big(\rho(t)\big) + \cdots \tag{6.35}$$

$$\partial_x(u) = \partial_x\big(u(t)\big) + \xi\partial_{xx}\big(u(t)\big) + \tfrac{1}{2}\xi^2\partial_{xxx}\big(u(t)\big) + \cdots, \tag{6.36}$$

where the abbreviations for derivatives are defined as

$$\begin{aligned}
\dot{\rho}_x(t) &= \frac{d(\partial_x(\rho(t)))}{dt}, & \dot{u}_x(t) &= \frac{d(\partial_x(u(t)))}{dt},\\
\dot{\rho}_{xx}(t) &= \frac{d(\partial_{xx}(\rho(t)))}{dt}, & \dot{u}_{xx}(t) &= \frac{d(\partial_{xx}(u(t)))}{dt},\\
\partial_x(\rho(t)) &= \frac{\partial\rho}{\partial x}\Big|_{X(t),t}, & \partial_x(u(t)) &= \frac{\partial u}{\partial x}\Big|_{X(t),t},\\
\partial_{xx}(\rho(t)) &= \frac{\partial^2\rho}{\partial x^2}\Big|_{X(t),t}, & \partial_{xx}(u(t)) &= \frac{\partial^2 u}{\partial x^2}\Big|_{X(t),t},\\
\partial_{xxx}(\rho(t)) &= \frac{\partial^3\rho}{\partial x^3}\Big|_{X(t),t}, & \partial_{xxx}(u(t)) &= \frac{\partial^3 u}{\partial x^3}\Big|_{X(t),t}.
\end{aligned} \tag{6.37}$$

Correspondingly, the derivatives of traffic pressure in relation to the local density and speed are expressed as

$$\partial_\rho(P) = \partial_\rho(P_0) + \xi\big[\partial_{\rho\rho}(P_0)\partial_x\big(\rho(t)\big) + \partial_{\rho u}(P_0)\partial_x(u(t))\big] + \cdots \tag{6.38}$$

$$\partial_u(P) = \partial_u(P_0) + \xi\big[\partial_{u\rho}(P_0)\partial_x\big(\rho(t)\big) + \partial_{uu}(P_0)\partial_x(u(t))\big] + \cdots \tag{6.39}$$

Similarly, the desired density $\rho^*$and speed u^* in the ACC model at the relative position (with respect to the front) $(x^* - X) = (d^* + \xi)$, with $d^* = x^* - x$, are expanded as

$$\begin{aligned}
\rho^* &= \rho_0 + (d^* + \xi)\partial_x\big(\rho(t)\big) + \frac{1}{2}(d^* + \xi)^2\partial_{xx}\big(\rho(t)\big)\\
&= \rho_0 + (d^* + \xi)\partial_x\big(\rho(t)\big) + \frac{1}{2}((d^*)^2 + \xi^2 + 2d^*\xi)\partial_{xx}\big(\rho(t)\big)\\
&= \rho_0 + \xi\partial_x\big(\rho(t)\big) + d^*\Big(\partial_x\big(\rho(t)\big) + \xi\partial_{xx}\big(\rho(t)\big)\Big) + \cdots,
\end{aligned} \tag{6.40}$$

and similarly

$$u^* = u_0 + \xi\partial_x\big(u(t)\big) + d^*\Big(\partial_x\big(u(t)\big) + \xi\partial_{xx}\big(u(t)\big)\Big) + \cdots, \tag{6.41}$$

where $P_0 = P(\rho_0, u_0)$. Further, the following abbreviations have been used

$$\begin{aligned}
\partial_\rho(P_0) &= \frac{\partial P}{\partial\rho}\Big|_{X(t),t}, & \partial_{\rho\rho}(P_0) &= \frac{\partial^2 P}{\partial\rho^2}\Big|_{X(t),t},\\
\partial_u(P_0) &= \frac{\partial P}{\partial u}\Big|_{X(t),t}, & \partial_{uu}(P_0) &= \frac{\partial^2 P}{\partial u^2}\Big|_{X(t),t},
\end{aligned} \tag{6.42}$$

$$\partial_{\rho u}(P_0) = \left.\frac{\partial^2 P}{\partial \rho \partial u}\right|_{X(t),t}, \qquad \partial_{u\rho}(P_0) = \left.\frac{\partial^2 P}{\partial \rho \partial u}\right|_{X(t),t}.$$

Thereafter, substituting equations (6.31)-(6.36) and (6.38)-(6.41) into the system equations (6.1) and (6.2), and neglecting terms including $\xi^2$and $(d^*)^2$, two sets of equations are obtained, one for the original position (ξ^0) (for $\xi = 0$) and one for the disturbed position (ξ^1), taking also into account equation (6.30). Thus, conservation equation (6.1) provides the following expressions:

$$\boldsymbol{\xi^0}: \; -\partial_x(\rho)u_c + \rho_0 \partial_x(u) = 0\,, \tag{6.43}$$

$$\boldsymbol{\xi^1}: \dot{\rho}_x - \partial_{xx}(\rho)u_c + 2\partial_x(\rho)\partial_x(u) + \rho_0 \partial_{xx}(u) = 0\,. \tag{6.44}$$

Similarly, for the momentum dynamics equation (5.2), the following expressions are obtained (using also equations (6.43) and (6.44)):

$$\boldsymbol{\xi^0}: -u_c\partial_x(u) + \frac{1}{\rho_0}\left(\partial_\rho(P_0)\partial_x(\rho) + \partial_u(P_0)\partial_x(u)\right) = \frac{1}{\rho_0}\left(\frac{d^*}{\tau^*}\right)\left(\rho_0\partial_x(u) + u_0\partial_x(\rho)\right), \tag{6.45}$$

$$\begin{aligned}
&\boldsymbol{\xi^1}: \; \dot{u}_x - u_c\partial_{xx}(u) + \left(\partial_x(u)\right)^2 - u_c\frac{\partial_x(\rho)}{\rho_0}\partial_x(u) \\
&+\frac{1}{\rho_0}\,\partial_\rho(P_0)\partial_{xx}(\rho) + \frac{1}{\rho_0}\,\partial_{\rho\rho}(P_0)\left(\partial_x(\rho)\right)^2 + \frac{2}{\rho_0}\partial_{\rho u}(P_0)\partial_x(\rho)\partial_x(u) \\
&+\frac{1}{\rho_0}\,\partial_u(P_0)\partial_{xx}(u) + \frac{1}{\rho_0}\partial_{uu}(P_0)\left(\partial_x(u)\right)^2 \\
&= \left(\frac{d^*}{\tau^*}\right)\left(\partial_{xx}(u) + \frac{2}{\rho_0}\partial_x(\rho)\partial_x(u) + \frac{1}{\rho_0}u_0\partial_{xx}(\rho)\right).
\end{aligned} \tag{6.46}$$

Equation (6.43) leads to

$$\partial_x(\rho) = \frac{\rho_0\partial_x(u)}{u_c}. \tag{6.47}$$

Thus, by substituting equation (6.47) into equation (6.45), the following relation for the characteristic velocities u_c is derived,

$$u_c{}^2 - \left(\frac{1}{\rho_0}\,\partial_u(P_0) - \left(\frac{d^*}{\tau^*}\right)\right)u_c + \left(\frac{d^*}{\tau^*}\right)u_0 - \partial_\rho(P_0) = 0\,, \tag{6.48}$$

which gives

$$u_{c\pm} = \frac{1}{2}\left(\frac{1}{\rho_0}\,\partial_u(P_0) - \left(\frac{d^*}{\tau^*}\right)\right) \pm \sqrt{\left(\frac{1}{2\rho_0}\,\partial_u(P_0) - \frac{1}{2}\left(\frac{d^*}{\tau^*}\right)\right)^2 + \partial_\rho(P_0) - \left(\frac{d^*}{\tau^*}\right)u_0}\,. \tag{6.49}$$

In general, in free-flow traffic condition, related to low traffic demand, disturbances propagate downstream with positive characteristic velocity u_{c+}. In contrast, under congested flow conditions they travel upstream, with negative characteristic velocity u_{c-}. However, as pointed out by Yi *et al.*, 2003, the positive characteristic velocity u_{c+} will decay to zero very

quickly in the course of time without having a particularly relevant role. Therefore, in the remainder of the nonlinear stability analysis, the branch corresponding to the perturbation moving downstream is neglected, concentrating only on the upstream propagation with characteristic velocity $u_{c\_}$.

Subsequently, the second-order partial derivatives $\partial_{xx}(\rho)$ and $\partial_{xx}(u)$ in equations (6.44) and (6.46) can be eliminated. This is feasible by multiplying expressions (6.44) and (6.46) with the terms $\{-u_{c\_}\}$ and $\left\{\frac{1}{\rho_0}\left(\left(\frac{d^*}{\tau^*}\right)u_0 - \partial_\rho(P_0)\right)\right\}$, respectively, and using properly equation (6.48), whereby the resulting equations are added to one another. Consequently, after some algebraic manipulation, we obtain the reduced equation

$$\dot{u}_x + a\partial_x(u) + \beta\left(\partial_x(u)\right)^2 = 0\,, \tag{6.50}$$

in which

$$a = 0\,, \tag{6.51}$$

$$\beta = \frac{2\partial_\rho(P_0) + \rho_0\partial_{\rho\rho}(P_0) + 2u_{c\_}\partial_{\rho u}(P_0) + \frac{\left(u_{c\_}\right)^2}{\rho_0}\partial_{uu}(P_0) - 2u_0\left[\frac{d^*}{\tau^*}\right] - 2u_{c\_}\left[\frac{d^*}{\tau^*}\right]}{\left(u_{c\_}\right)^2 + \partial_\rho(P_0) - u_0\left[\frac{d^*}{\tau^*}\right]}\,.$$

The solution of equation (6.50) is given as

$$\partial_x(u(t)) = \frac{\partial_x(u(0))}{\partial_x\left(u(0)\right)\beta t + 1}\,, \tag{6.52}$$

where $\partial_x(u(0))$ is the initial condition for $\partial_x(u(t))$. From equation (6.52), the trend of $\partial_x(u(t))$ can be determined using the derivative

$$\frac{d\left(\partial_x(u(t))\right)}{dt} = \frac{-\left(\partial_x(u(0))\right)^2\beta}{\left(\partial_x\left(u(0)\right)\beta t + 1\right)^2}\,. \tag{6.53}$$

According to equation (6.52), if the denominator tends to zero, then $\partial_x\left(u(t)\right)$ tends to infinity and traffic becomes nonlinearly unstable. More precisely, this can happen when $\partial_x\left(u(0)\right)\beta t + 1 = 0$ or when $t = -1/(\partial_x u(0)\beta)$. As t is always positive, for the satisfaction of the previous condition, $\partial_x\left(u(0)\right)\beta < 0$ should be applied. Thus, for the unstable regions, the solution must satisfy the following two restrictions: $\{\partial_x\left(u(0)\right) < 0\ and\ \beta > 0\}$ or $\{\partial_x\left(u(0)\right) > 0\ and\ \beta < 0\}$. However, for most second-order models, $\beta > 0$ (Yi *et al.*, 2003; Ngoduy, 2013b); thus it is expected that unstable regions emerge when $\partial_x\left(u(0)\right) < 0$.

Similarly, following the aforementioned derivation nonlinear stability method including the contribution of CACC elements, the reduced equation is given as:

$$\dot{u}_x + a\partial_x(u) + \beta\left(\partial_x(u)\right)^2 = 0\,, \tag{6.54}$$

where

$$a = 0\,, \tag{6.55}$$

$$\beta = \frac{2\partial_\rho(P_0) + \rho_0\partial_{\rho\rho}(P_0) + 2u_{c\_}\partial_{\rho u}(P_0) + \frac{(u_{c\_})^2}{\rho_0}\partial_{uu}(P_0) - 2u_0\sum_{i=1}^{M}\frac{d^*}{\tau_i^*} - 2u_{c\_}\sum_{i=1}^{M}\frac{d^*}{\tau_i^*}}{(u_{c\_})^2 + \partial_\rho(P_0) - u_0\sum_{i=1}^{M}\frac{d^*}{\tau_i^*}}.$$

6.3 Numerical Study for Nonlinear Stability Analysis of ACC Systems

In this section, we investigate numerically the findings of the theoretical analysis, assuming the traffic flow inside a single-lane ring road of circumference $L = 10$ km; periodic boundary conditions were implemented at the boundaries of the discretized section. The second order model is numerically approximated by an accurate and robust high-resolution finite volume relaxation scheme, where the nonlinear system of partial differential equations is first recast to a diagonalizable semi-linear system and is then discretized by a higher-order WENO scheme (Delis *et al.*, 2014, 2015a).

We consider an initial perturbation of the average density, as it is depicted in Figure 6.1, given as

$$\rho = \bar{\rho} - \Delta\rho\frac{1}{2}\left[1 + tanh\left(\frac{x - x_1}{\Delta x}\right)\right] + \Delta\rho\frac{1}{2}\left[1 + tanh\left(\frac{x - x_2}{\Delta x}\right)\right], \tag{6.56}$$

where $\bar{\rho} = 45$ veh/km, $\Delta\rho = 5$ veh/km, $\Delta x = 400$ m, $x_1 = 4000$ m, and $x_2 = 7000$ m. The resulting velocity perturbation is also presented in Figure 6.1. The initial perturbation was selected in order to produce the condition $\partial_x(u(0)) < 0$.

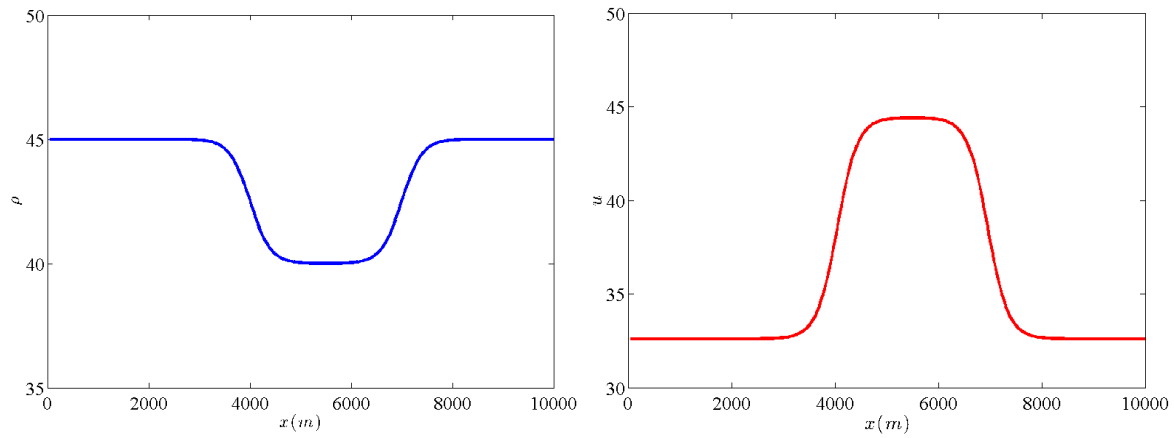

FIGURE 6.1: *The initial perturbation in ρ (left) and u (right), applied for the numerical example.*

The ring was discretized with $npts = 400$ grid points, while the model parameters used in the simulation of the GKT model were $u_{max} = 110$ km/h, $\rho_{max} = 160$ veh/km, $\rho_{cr} = 0.27\rho_{max}$, $\tau = 35$ s, $A_0 = 0.008$, $\delta A = 0.02$, $\delta\rho = 0.05\rho_{max}$, $T = 1.8$ s, $\gamma = 1.2$. Simulations are reported up to 1200 s. First the manual flow was simulated (by setting $p = 0$ in equation (5.2)).

The simulation results for manual cars are presented in Figures 6.2 and 6.3 for density and velocity, respectively; a cascade of stop-and-go waves emerges from the perturbation in the initial condition.

The corresponding simulation results for ACC traffic (by setting $p = 1$ in equation (5.2)) are presented in Figures 6.4 and 6.5, for density and velocity evolution respectively. The

same initial perturbation was used as for the flow with manual vehicles. All cars are supposed to be equipped with the same type of ACC, with the same parameters; the time gap was set equal to $T^* = 1$ s, while $\rho_{acc} = 0.9\rho_{cr}$, $\gamma^* = 1$ and $\tau^* = 0.5$ s. As it can be observed, the original cascade of stop-and-go waves (produced in the manual traffic) has been eliminated; however, a series of growing instabilities emerges from the region where $\partial_x(u(0)) < 0$ in the initial condition. This observation is compatible with the findings of the theoretical investigation.

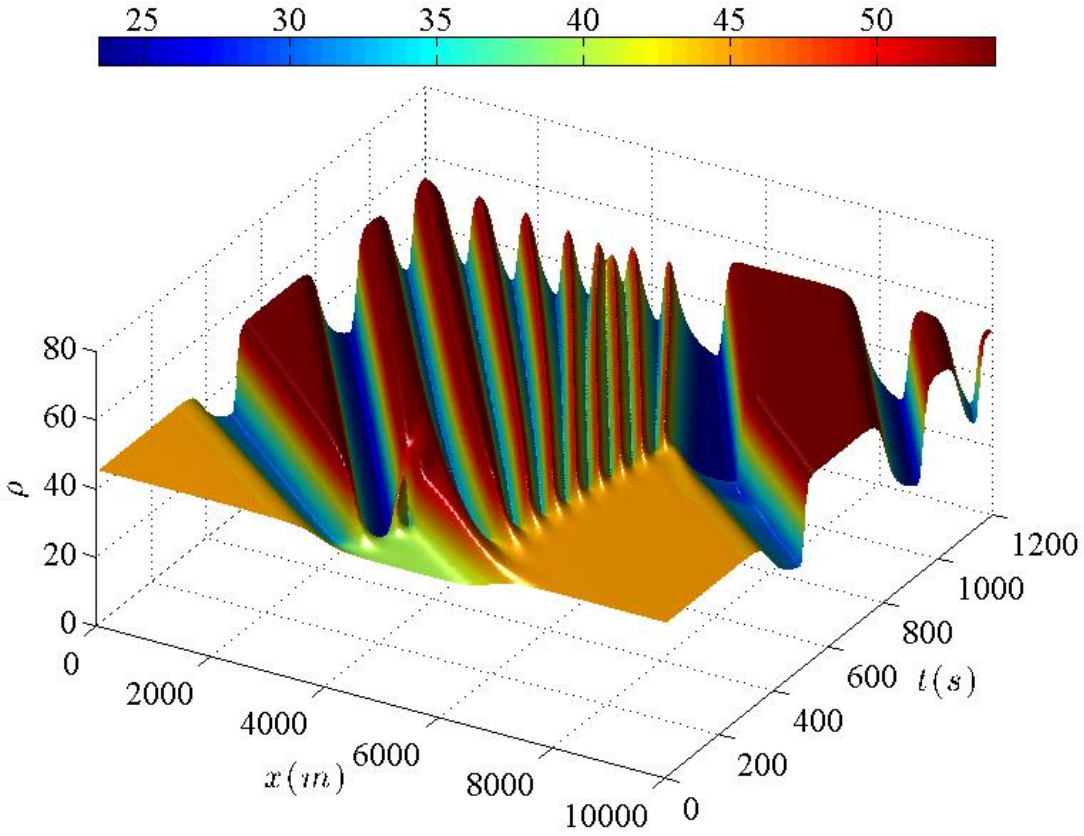

FIGURE 6.2: *Density evolution for manually driven cars.*

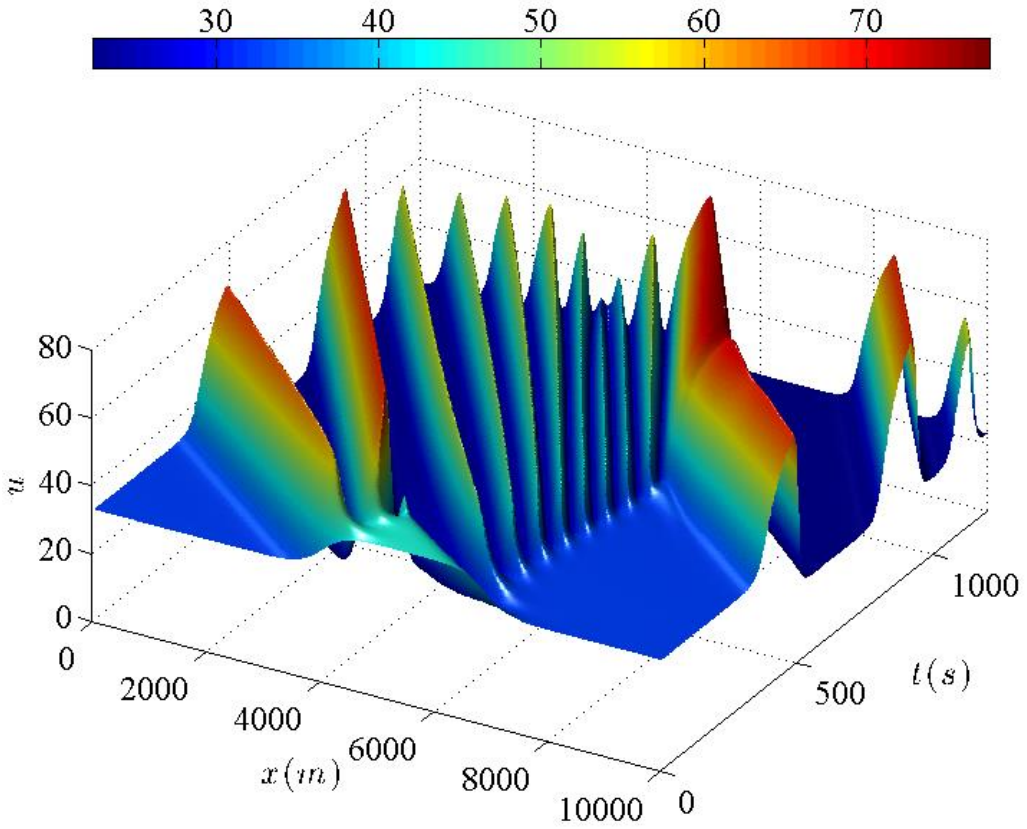

FIGURE 6.3: *Velocity evolution for manually driven cars.*

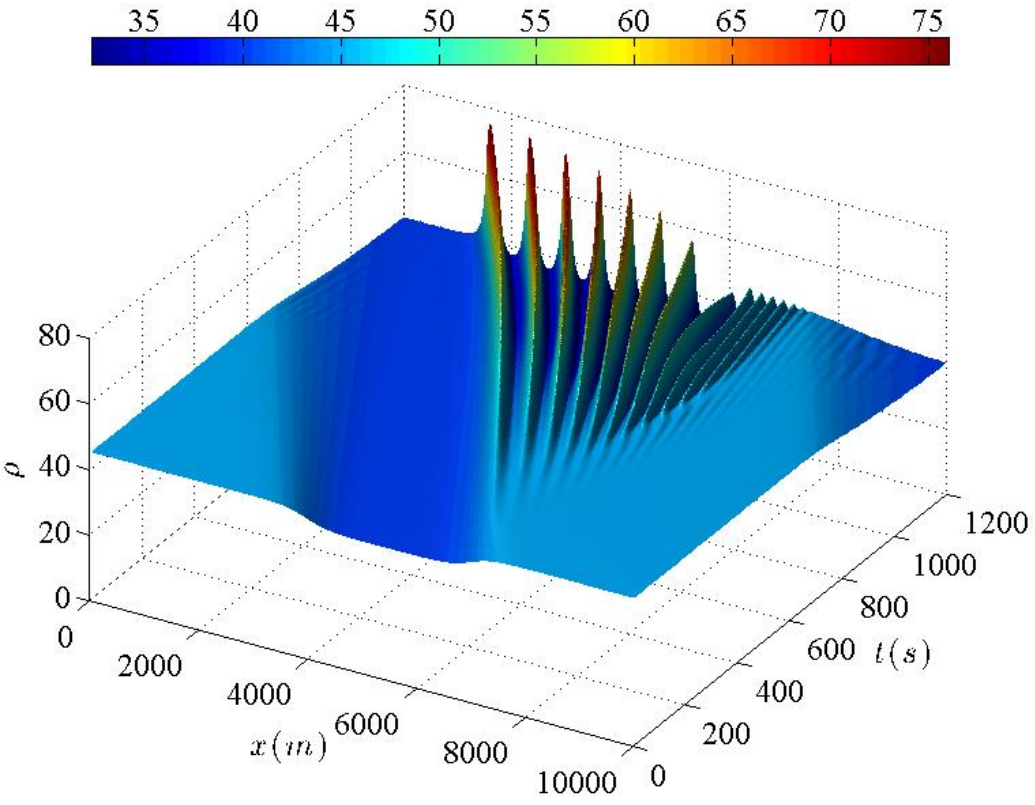

FIGURE 6.4: *Density evolution for ACC traffic.*

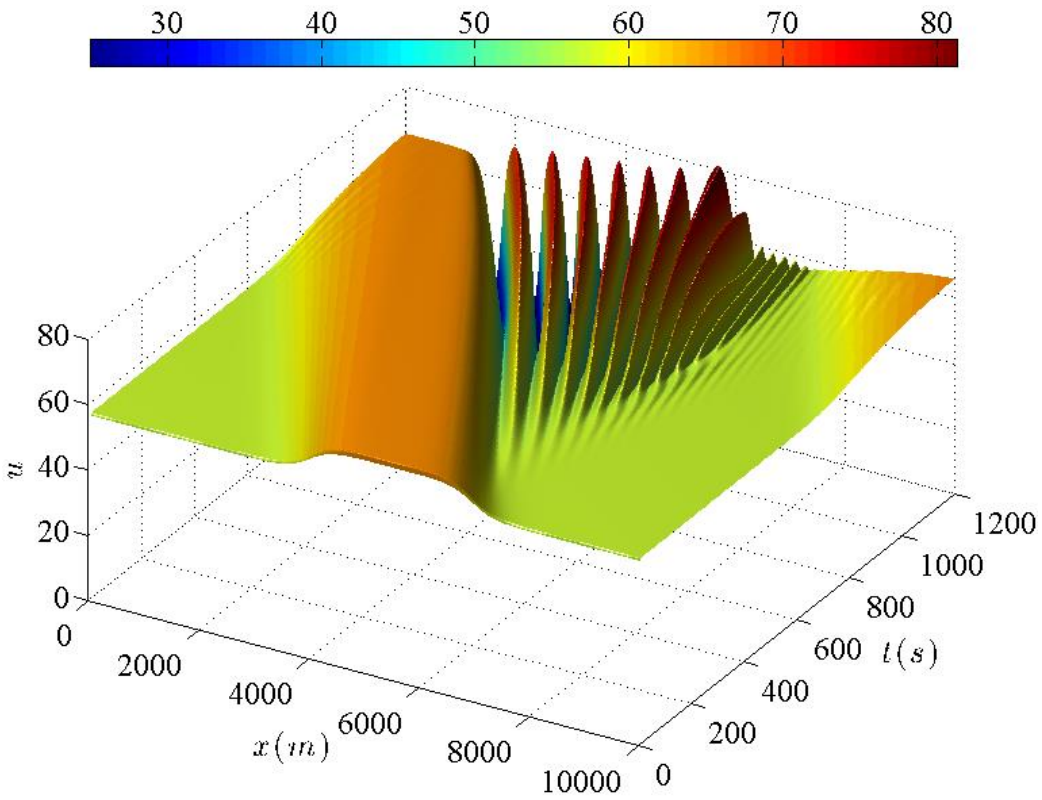

FIGURE 6.5: *Velocity evolution for ACC traffic.*

Chapter 7: Conclusions and Future Work

This final chapter summarizes the findings and results of this thesis. In particular, Section 7.1 gives a summary of the study and highlights the main results and contributions of the thesis, while Section 7.2 indicates future research aspects that could be considered to extend the investigation results.

7.1 Concluding remarks

In the last few decades, traffic flow theory, modelling, and simulation have gained considerable attention since overall traffic demand has increased and more data as well as easy access to computing power has become available. Moreover, this growing interest to traffic flow modelling stems also from the need for reliable traffic management, so as to optimize traffic efficiency and safety under various traffic flow conditions. One of the main issues, regarding traffic flow models, is their level of proximity to reality and its representation. Hence, to ensure the validity of any model in performing real-world simulations and provide results that are reliable, the application of calibration and validation processes is deemed mandatory.

Concurrently, traffic congestion originating from off-ramp areas is a particular, but quite frequent case of (recurrent) congestion, which is appearing usually at urban or peri-urban freeways during the peak periods and is difficult to deal with. Moreover, within the traffic flow modelling literature there are, so far, no studies undertaking validation of second-order traffic flow models regarding the reproduction of traffic conditions at congested freeway on/off-ramp areas. The emergence of traffic flow models that are able to reproduce such cases with satisfactory accuracy is deemed important as it may trigger the development of innovative traffic control strategies that face this particular type of freeway congestion. This gap in the literature was addressed within this thesis, which focuses on the validation of traffic flow modelling for congested freeway off-ramp areas.

In addition, the frequent occurrence of perturbations in traffic flow, such as sudden deceleration of vehicles, or the non-uniformity of the flow entering a highway from an on-ramp, is likely to develop into stop-and-go waves traveling upstream, or traffic jams when the amplitude of perturbations is large enough, resulting in considerable time-delays, increased fuel consumption and air pollution, as well as a serious under-utilization of the available infrastructure. Consequently, traffic flow stability analysis is considered to be one of the fundamental problems in traffic theory, and scientists have been particularly interested in understanding the formation and evolution of such traffic flow instabilities since the early days of traffic engineering. Recent developments in the field of ITS and VACS, such as ACC and CACC systems, besides their contribution in safety and convenience of the passengers, is believed to be a potential remedy to the aforementioned traffic flow problems, and be capable of reducing the effects of traffic flow instabilities with the appropriate selection of their operation parameters. This advanced feature, in conjunction with the expected extensive use of such systems in the near future, can provide additional tools for the mitigation of the rapidly growing problem of traffic congestion. Towards this direction, this thesis attempts to

perform both a linear and a nonlinear stability analysis of a recently developed second order macroscopic traffic flow model able to simulate the flow of ACC/CACC-equipped vehicles, and identify the ways that ACC and CACC systems influence the stability of traffic flow, in relation with both small and large traffic disturbances around the equilibrium state.

In particular, in the first part of the thesis (Chapter 3 − Chapter 4), a parallel, synchronous and asynchronous, metamodel-assisted DE algorithm was employed for the automated calibration of the parameters of a second-order GKT traffic flow model (along with its multi-lane extension), in order to evaluate the representation of traffic conditions at congested freeway on/off-ramp areas. The model was first calibrated using real traffic data from two different motorway networks; a motorway stretch in the U.K., where severe traffic congestion is created due to high on-ramp flows during the morning peak periods, and a freeway stretch in Greece, where recurrent congestion is triggered by a saturated off-ramp during the morning peak hours. Then the resulted model was validated using different traffic data sets from the same freeway sites. Finally, this thesis evaluates the implementation of the proposed DE algorithm for the comparison of the GKT model and the well-known METANET model, with respect to their accuracy in reproducing real traffic dynamics using data from the freeway stretch in U.K.

The results demonstrated that the parallel, metamodel-assisted DE algorithm can be considered as a useful and versatile tool for the calibration of macroscopic traffic flow models in which the cost function exhibits multi-optimal values. It also has the advantage that it can be used without the need of tuning its parameters for the problem at hand, while wide bounds can be used for the unknown vector of parameters without convergence problems. The well-known computational inefficiency of evolutionary algorithms was successfully addressed in our implementation with parallel processing and surrogate-model assistance. Moreover, both the GKT and the METANET model achieved satisfactory reproduction of the network traffic conditions for the calibration date. Finally, the calibration and validation of both models indicated that they are both able to reproduce the traffic conditions of the examined networks also for other dates, while the GKT model achieves a lower cost function value comparing to the METANET model for the calibration date.

The second part of the thesis (Chapter 5 - Chapter 6) aims to derive the stability conditions of a recently proposed second-order macroscopic traffic flow model, as to investigate the effects of the incorporated ACC and CACC characteristics on the stabilization of traffic flow under small and large perturbations around the equilibrium state, applying both linear and nonlinear stability analyses. The macroscopic model under investigation has been derived based on the well-known GKT model, taking into account the impacts of ACC and CACC equipped vehicles by adding a proper source term in the momentum equation of the GKT model. This term controls the speed dynamics, contributing to the relaxation term in the GKT model equations and also takes explicitly into account the major time/space-gap principle of ACC and by extension CACC systems.

Considering the above, the main contributions and findings of the thesis can be summarized as follows:

- The numerically approximated second-order GKT model via a high resolution finite volume relaxation scheme was calibrated by implementing a parallel, synchronous & asynchronous, metamodel-assisted Differential Evolution (DE) algorithm. The DE algorithm was also applied for the calibration of the discrete second order METANET

model. The calibration procedure proved to be problem-free for both macroscopic models, for single- and multi-lane variants and for all test-cases considered.

- The optimization results showed that the DE algorithm can be considered as a useful, effective, and versatile tool for the calibration of macroscopic traffic flow models. It provides the ability to calibrate a large number of parameters, in a fully automated way, without human interaction, and with wide initial bounds for the parameters' vector. The large number of evaluations, required by all EAs, was successfully addressed through parallel processing and ANN surrogate models.

- The asynchronous version of the parallel DE proved to be more time efficient than the synchronous one, with a steeper convergence rate at the beginning of the procedure. Both versions provided almost identical optimal solutions.

- Both GKT and METANET macroscopic models showed that they can reproduce accurately and similarly real traffic dynamics, including congestion. The METANET model showed a longer congestion time, compared to the GKT one, for the validation date.

- The qualitative properties of the developed macroscopic model to reflect the effects of ACC/CACC-equipped vehicles on traffic flow stability were investigated through a linear stability method, which refers to linear Taylor approximations, used throughout the analysis. However, the consequence of using such linear approximations is that even if the traffic system is linearly stable, might actually still display nonlinear instability with respect to large perturbations. Thus, subsequently, a wavefront expansion method, with respect to large perturbations, was applied to analytically derive the stability region of the developed model. The procedure was proved not a trivial task, however, provided interesting findings: a perturbation in the initial conditions with $\partial_x\big(u(0)\big) < 0$ leads to growing instabilities.

- The theoretical findings for the ACC model were supported by the simulation results derived for a numerical test in a single-lane ring road with a perturbation in the initial conditions of density and speed. The simulation results revealed that a series of growing instabilities emerges from the region in the initial conditions where the previous instability criterion is valid.

7.2 Further research

There are various ways to extend the investigations presented in this thesis. Few of them are listed in the following:

- Investigate how the instability region resulted for the ACC/CACC model can be alleviated/eliminated with a proper selection of parameters (especially the time gap).

- Perform experimental analysis (for the examined test cases and additional ones) to study the effect of the use of ACC/CACC equipped vehicles (with various penetration rates) on the observed congestion and its characteristics.

- Perform comparative studies of the examined macroscopic ACC/CACC model with other macroscopic ones (such as the one proposed by Ngoduy), for specific test cases, in order to compare their performance and analyze their credibility.

- Compare the examined macroscopic ACC/CACC model to microscopic ones, to evaluate their performance and efficiency.

- Extend the proposed combination of the macroscopic model and the calibration (optimization) algorithm to a software package, with a friendly user interface, to be used as a tool for traffic Engineers and planners.

Appendix A

This section describes how to derive equation (6.19) in order to recast the square root of a complex number. Recalling that complex numbers extend to the two-dimensional space, every complex number can be written in the following notation:

$$z = R + iI\,, \tag{A.1}$$

where (R, I) are real numbers in Cartesian coordinates and i is the imaginary unit defined as: $i^2 = -1$. In the former equation R represents the real part of z, written as $R = Re(z)$, while I the imaginary part, written as $I = Im(z)$.

The square root of a complex number can be easily found using the polar form, thus, by switching to polar coordinates (r, θ), the nonzero complex number z can be defined as

$$z = r\,cos(\theta) + ir\,sin(\theta)\,, \tag{A.2}$$

where $r\cos(\theta) = Re(z)$ and $r\sin(\theta) = Im(z)$ the real and the imaginary parts, respectively. The absolute value or modulus r is given as

$$r = \sqrt{R^2 + I^2} = \sqrt{(R + iI)(R - iI)} = \sqrt{z\bar{z}} = |z|\,, \tag{A.3}$$

where $\bar{z} = R - iI$ is the complex conjugate number, whereas the polar angle θ is determined by

$$tan(\theta) = \frac{sin(\theta)}{cos(\theta)} = \frac{I}{R} = \frac{Im(z)}{Re(z)}\,. \tag{A.4}$$

Next, using the following Euler's formula

$$e^{i\theta} = cos(\theta) + i\,sin(\theta) \tag{A.5}$$

the aforementioned polar form of a complex number can be rewritten into its exponential form as:

$$z = r[cos(\theta) + i\,sin(\theta)] = r\,e^{i\theta}\,. \tag{A.6}$$

The exponential function can be defined on the complex plane by an infinite series expansion

$$exp(z) = e^z = \sum_{n=0}^{\infty} \frac{z^n}{n!}\,. \tag{A.7}$$

Therefore, the relationships for exponential functions are also applied to the case of complex numbers, getting the useful formulas for the product or quotient of complex numbers; i.e. the product of two complex numbers $z_1 = R_1 + iI_1 = r_1 e^{i\theta_1}$ and $z_2 = R_2 + iI_2 = r_2 e^{i\theta_2}$ is given by

$$\begin{aligned} z_1 z_2 &= (R_1 R_2 - I_1 I_2) + i(R_1 R_2 + I_1 I_2) = r_1 e^{i\theta_1} r_2 e^{i\theta_2} = r_1 r_2 e^{i(\theta_1 + \theta_2)} \\ &= r_1 r_2\,cos(\theta_1 + \theta_2) + i r_1 r_2\,sin(\theta_1 + \theta_2)\,. \end{aligned} \tag{A.8}$$

Since the real and imaginary parts are linearly independent of each other, this yields that $R_1 R_2 - I_1 I_2 = r_1 r_2 \cos(\theta_1 + \theta_2)$ and $R_1 R_2 + I_1 I_2 = r_1 r_2 \sin(\theta_1 + \theta_2)$. Moreover, the inverse of any nonzero complex number is given by

$$\frac{1}{z} = \frac{1}{r\,e^{i\theta}} = \frac{e^{-i\theta}}{r}, \tag{A.9}$$

where $i = \sqrt{-1} = e^{i\pi/2}$.

In general, the square of complex numbers in the form

$$z = r\,e^{\pm i\theta} = r[cos(\theta) \pm i\,sin(\theta)] \tag{A.10}$$

can be written either as

$$z^2 = r^2[cos^2(\theta) \pm 2i\,cos(\theta)\,sin(\theta) - sin^2(\theta)] \tag{A.11}$$

or, using the familiar additive property $e^{x_1} \cdot e^{x_2} = e^{x_1+x_2}$ of the exponential function, the alternative representation is given as

$$z^2 = r^2\left(e^{\pm i\theta}\right)^2 = r^2 e^{\pm i2\theta} = r^2[cos(2\theta) \pm i\,sin(2\theta)]\,. \tag{A.12}$$

Thus, comparing the real parts and using the trigonometric identity $\cos^2(\theta) + \sin^2(\theta) = 1$, we find

$$cos(2\theta) = 1 - 2\,sin^2(\theta) = 1 - 2[1 - cos^2(\theta)] = 2\,cos^2(\theta) - 1 \tag{A.13}$$

from which the following trigonometric types are derived:

$$\begin{aligned} \cos^2(\theta/2) &= \frac{1}{2}[1 + \cos(\theta)]\,, \\ \sin^2(\theta/2) &= \frac{1}{2}[1 - \cos(\theta)]\,. \end{aligned} \tag{A.14}$$

Consequently, the square root of a complex number is defined as

$$\begin{aligned} \sqrt{z} &= \sqrt{r}e^{\pm i\theta/2} = \sqrt{r}[\cos(\theta/2) \pm i\sin(\theta/2)] \\ &= \sqrt{\frac{1}{2}[r + \mathrm{r}\cos(\theta)]} \pm i\sqrt{\frac{1}{2}[r - \mathrm{r}\cos(\theta)]}\,. \end{aligned} \tag{A.15}$$

Taking into account that $R = r\cos(\theta)$ and $I = r\sin(\theta)$, the following desired equation form is obtained:

$$\sqrt{R \pm i|I|} = \sqrt{\frac{1}{2}\left(\sqrt{R^2 + I^2} + R\right)} \pm i\sqrt{\frac{1}{2}\left(\sqrt{R^2 + I^2} - R\right)}\,. \tag{A.16}$$

Appendix B

B.1 Macroscopic Model Development for ACC traffic flow based on GKT theory

The work reported here contains a detailed derivation of the equations for the macroscopic traffic flow simulation with ACC traffic dynamics (Ngoduy, 2012c), obtained from the classic multi-class GKT theory, using the well-known method of moments. It is actually based on the work of Hoogendoorn & Bovy, 2000, and Ngoduy, 2012c. This derivation was performed in order to verify the procedure followed in Ngoduy, 2012c, and highlight the details of this procedure, so as to be able to compare the utilized ACC model (Chapter 5) with that in Ngoduy, 2012c.

B.1.1 Underlying gas-kinetic model for ACC vehicles

This section introduces the so-called gas-kinetic equations describing multiple user-class traffic operations (Hoogendoorn & Bovy, 2000) and its extension to mixed traffic flow of manual and ACC vehicles. In general, the gas-kinetic model describes the behavior characteristics of group of vehicles, determined by their location, x, (space), current speed, v, and desired speed, v^0, at a particular instant in time, t, (phase). Let us first denote the class specific phase-space density $\rho_u(x,t,v,v^0)$, hereafter ρ_u for short, which represents the expected number of vehicles class u on (x,t) driving with speed v while having desired speed v^0 per unit roadway length. In what follows, $u=1$ indicates the manual vehicle while $u=2$ indicates the ACC vehicle. Let $\psi_u(v,v^0)$ denotes the joint probability function of the current speed and the desired speed of vehicle class u. By definition, $\rho_u = \psi_u r_u$, with $r_u = r_u(x,t)$, being the class specific density at location x and time t. The multi-class gas-kinetic theory of Hoogendoorn & Bovy, 2000, describes the changes of the class specific phase-space density ρ_u due to the continuum process and non-continuum process. In particular, the continuum process produces smooth changes of ρ_u, due to inflow and outflow in the phase-space consisting of vector $\mathcal{F} = (x,v,v^0)$, while the non-continuum process reflects non-smooth changes of ρ_u caused by the interaction between and within vehicle classes. The generalized governing gas-kinetic equation for multi-class traffic flow is defined as (Hoogendoorn & Bovy, 2000; Ngoduy, 2012c):

$$\frac{\partial \rho_u}{\partial t} + \underbrace{\nabla\left(\rho_u \frac{d\mathcal{F}}{dt}\right)}_{continuum} = \underbrace{\left(\frac{\partial \rho_u}{\partial t}\right)^{int}}_{non-continuum}, \tag{B.1}$$

where ∇ is the so-called Nabla operator defined by:

$$\nabla = \left(\frac{\partial}{\partial x}, \frac{\partial}{\partial v}, \frac{\partial}{\partial v^0}\right). \tag{B.2}$$

Assuming that drivers do not change their desired speed during their trip, the first and the third term of $\frac{d\mathcal{F}}{dt}$ in equation (B.1) becomes:

$$\frac{dx}{dt} = v, \quad \frac{dv^0}{dt} = 0\,. \tag{B.3}$$

While the second term $\frac{d\mathcal{F}}{dt}$ is actually the acceleration/deceleration law and is determined for manual vehicles as $\frac{dv}{dt} = \frac{v^0 - v}{\tau_u}$, while for ACC vehicles is specified as (Davis, 2004):

$$\frac{dv}{dt} = \underbrace{\frac{v^0 - v}{\tau_u}}_{1} + \underbrace{\kappa(w - v)}_{2}\,. \tag{B.4}$$

In the above equation, τ_u is the relaxation time of the vehicle towards the desired speed and κ is the coefficient of the ACC system in response to the speed difference with the leader. Term (1) represents the relaxation of the vehicle towards the desired speed, while term (2) reflects the relaxation of the ACC vehicle towards the speed of the leader w. Based on the space-headway policy, the speeds of the ACC vehicle and its leader are related to each other as: $w = v(x + \Delta x, t)$, where Δx is the space headway between two consecutive vehicles.

In the non-continuum process (vehicular interaction), the term $\left(\frac{\partial \rho_u}{\partial t}\right)^{int}$ reflects the interactions among vehicle classes or within a vehicle class (Treiber *et al.*, 1999; Hoogendoorn & Bovy, 2000; Helbing *et al.*, 2001).

B.1.2 Governing macroscopic traffic equations

In the remainder, a multi-class macroscopic model incorporating mixed ACC traffic dynamics will be derived from the gas-kinetic model proposed above, using the so-called method of moments (Hoogendoorn & Bovy, 2000).

Helpful Calculations:

$$\frac{d\mathcal{F}}{dt} = \frac{d}{dt}(x, v, v^0) = \left(\frac{dx}{dt}, \frac{dv}{dt}, \frac{dv^0}{dt}\right) = \left(v, \frac{dv}{dt}, 0\right), \tag{B.5}$$

$$\begin{aligned} \nabla\left(\rho_u \frac{d\mathcal{F}}{dt}\right) &= \left(\frac{\partial}{\partial x}, \frac{\partial}{\partial v}, \frac{\partial}{\partial v^0}\right)\rho_u \left(\frac{dx}{dt}, \frac{dv}{dt}, \frac{dv^0}{dt}\right) = \left(\frac{\partial}{\partial x}, \frac{\partial}{\partial v}, \frac{\partial}{\partial v^0}\right)\left(\rho_u v, \rho_u \frac{dv}{dt}, 0\right) \\ &= \frac{\partial}{\partial x}(\rho_u v) + \frac{\partial}{\partial v}\left(\rho_u \frac{dv}{dt}\right) + 0\,. \end{aligned} \tag{B.6}$$

Thus, the left-hand side of equation (B.1) becomes

$$(LHS) = \frac{\partial \rho_u}{\partial t} + \frac{\partial}{\partial x}(\rho_u v) + \frac{\partial}{\partial v}\left(\rho_u \frac{dv}{dt}\right). \tag{B.7}$$

Method of Moments

Afterwards, the left-hand side of equation (B.1) is multiplied with the "k moments" of the variable v, v^k and subsequently the resulting equation is integrated over the physical range of speed v and desired speed v^0

$$(LHS) = \frac{\partial}{\partial t}(\rho_u)v^k + \frac{\partial}{\partial x}(\rho_u v)v^k + \frac{\partial}{\partial v}\left(\rho_u \frac{dv}{dt}\right)v^k \implies$$
$$(LHS) = \int_v \int_{v^0} \frac{\partial}{\partial t}\rho_u v^k dv^0 dv + \int_v \int_{v^0} \frac{\partial}{\partial x}\rho_u v^{k+1} dv^0 dv + \int_v \int_{v^0} v^k \frac{\partial}{\partial v}\left(\rho_u \frac{dv}{dt}\right) dv^0 dv\,. \tag{B.8}$$

Taking into account that $\rho_u = r_u\psi_u = r_u(x,t)\psi_u(v,v^0)$ the above equation (B.8) becomes

$$(LHS) = \underbrace{\int_v \int_{v^0} \frac{\partial}{\partial t} r_u(x,t) v^k \psi_u(v,v^0) dv^0 dv}_{A} + \underbrace{\int_v \int_{v^0} \frac{\partial}{\partial x} r_u(x,t) v^{k+1} \psi_u(v,v^0) dv^0 dv}_{B}$$
$$+ \underbrace{\int_v \int_{v^0} v^k \frac{\partial}{\partial v}\left(\rho_u \frac{dv}{dt}\right) dv^0 dv}_{C}\,. \tag{B.9}$$

The following mean operator, $\langle . \rangle_u$, of vehicle class u is applied to any function $y(v,v^0)$:

$$\langle y(v,v^0)\rangle_u = \int_v \int_{v^0} y(v,v^0)\psi_u(v,v^0) dv^0 dv\,. \tag{B.10}$$

For example:

$$\int_v \int_{v^0} v^k \psi_u(v,v^0) dv^0 dv = \langle v^k \rangle_u\,. \tag{B.11}$$

So, the macroscopic traffic variables are defined as below:

- **Density**: $r = \int_v \rho\, dv$
- **Mean speed**: $V_u = \langle v \rangle_u$
- **Mean speed variance**: $\Theta_u = \langle v^2 \rangle_u - (V_u)^2 \Rightarrow \langle v^2 \rangle_u = \Theta_u + (V_u)^2$
- **Mean desired speed**: $V_u^0 = \langle v^0 \rangle_u$

Applying partial integration to equation (B.9) results in

Term A:

$$A = \frac{\partial}{\partial t} r_u(x,t) \int_v \int_{v^0} v^k \psi_u(v,v^0) dv^0 dv = \frac{\partial}{\partial t} r_u \langle v^k \rangle_u \tag{B.12}$$

Term B:

$$B = \frac{\partial}{\partial x} r_u(x,t) \int_v \int_{v^0} v^{k+1} \psi_u(v, v^0) dv^0 dv = \frac{\partial}{\partial x} r_u \langle v^{k+1} \rangle_u \tag{B.13}$$

Term C (taking also into account the following equations (B.15), (B.16), (B.17)):

$$C = \int_v \int_{v^0} v^k \frac{\partial}{\partial v}\left(\rho_u \frac{dv}{dt}\right) dv^0 dv = \int_v \int_{v^0} \left[\frac{\partial}{\partial v}\left(v^k \rho_u \frac{dv}{dt}\right) - \frac{\partial}{\partial v}(v^k)\rho_u \frac{dv}{dt}\right] dv^0 dv \,. \tag{B.14}$$

Specifically, in the above equation

$$\int_v \int_{v^0} \frac{\partial}{\partial v}\left(v^k \rho_u \frac{dv}{dt}\right) dv^0 dv = \int_{v^0} v^k \rho_u \frac{dv}{dt} dv^0 \to 0 \tag{B.15}$$

and hence the term C is equivalent to

$$C = -\int_v \int_{v^0} k v^{k-1} r_u \psi_u(v, v^0) \frac{dv}{dt} dv^0 dv \,. \tag{B.16}$$

By substituting equation (B.4) into equation (B.16) the term C is obtained as

$$\begin{aligned} C &= -k r_u \int_v \int_{v^0} v^{k-1} \frac{dv}{dt} \psi_u dv^0 dv \\ &= -k r_u \int_v \int_{v^0} \frac{v^{k-1} v^0 - v^{k-1} v}{\tau_u} + \frac{v^{k-1} w - v^{k-1} v}{\tau^*} \psi_u dv^0 dv \\ &= -k r_u \int_v \int_{v^0} \frac{v^{k-1} v^0 - v^k}{\tau_u} \psi_u dv^0 dv + \int_v \int_{v^0} \frac{v^{k-1} w - v^k}{\tau^*} \psi_u dv^0 dv \\ &= -k r_u \left[\left\langle \frac{v^{k-1} v^0 - v^k}{\tau_u} \right\rangle + \left\langle \frac{v^{k-1} w - v^k}{\tau^*} \right\rangle \right]. \end{aligned} \tag{B.17}$$

By setting $k = 0$ and $k = 1$, the aggregated left-hand side becomes

- **For $k = 0$**

$$A = \frac{\partial}{\partial t}\left(r_u \langle v^k \rangle_u\right) = \frac{\partial}{\partial t}\left(r_u \langle v^{(0)} \rangle_u\right) = \frac{\partial}{\partial t}(r_u 1) = \frac{\partial (r_u)}{\partial t}, \tag{B.18}$$

$$B = \frac{\partial}{\partial x}\left(r_u \langle v^{(k+1)} \rangle_u\right) = \frac{\partial}{\partial x}\left(r_u \langle v^{(0+1)} \rangle_u\right) = \frac{\partial}{\partial x}(r_u \langle v \rangle_u) = \frac{\partial}{\partial x}(r_u V_u) \,, \tag{B.19}$$

$$C = 0 \,. \tag{B.20}$$

Finally,

$$\begin{aligned} (LHS) = (term\ A + term\ B = term\ C) = \frac{\partial (r_u)}{\partial t} + \frac{\partial}{\partial x}(r_u V_u) + 0 \Longrightarrow \\ (LHS) = \frac{\partial (r_u)}{\partial t} + \frac{\partial}{\partial x}(r_u V_u) \end{aligned} \tag{B.21}$$

- **For k=1:**

$$A = \frac{\partial}{\partial t}\left(r_u\langle v^k\rangle_u\right) = \frac{\partial}{\partial t}\left(r_u\langle v^{(1)}\rangle_u\right) = \frac{\partial}{\partial t}\left(r_u\langle v\rangle_u\right) = \frac{\partial}{\partial t}\left(r_u V_u\right), \tag{B.22}$$

$$B = \frac{\partial}{\partial x}\left(r_u\langle v^{(k+1)}\rangle_u\right) = \frac{\partial}{\partial x}\left(r_u\langle v^{(1+1)}\rangle_u\right) = \frac{\partial}{\partial x}\left(r_u\langle v^2\rangle_u\right), \tag{B.23}$$

$$\begin{aligned} C &= -kr_u\left[\langle\frac{v^{k-1}v^0 - v^k}{\tau_u}\rangle + \langle\frac{v^{k-1}w - v^k}{\tau^*}\rangle\right] = -r_u\left[\langle\frac{v^{1-1}v^0 - v^1}{\tau_u}\rangle + \langle\frac{v^{1-1}w - v^1}{\tau^*}\rangle\right] \\ &= -r_u\left[\langle\frac{v^{(0)}v^0 - v}{\tau_u}\rangle + \langle\frac{v^{(0)}w - v}{\tau^*}\rangle\right] = -r_u\left[\langle\frac{v^0 - v}{\tau_u}\rangle + \langle\frac{w - v}{\tau^*}\rangle\right] \\ &= -r_u\left[\frac{\langle v^0\rangle - \langle v\rangle}{\langle\tau_u\rangle} + \langle\frac{w - v}{\tau^*}\rangle\right] = -r_u\left[\frac{V^0 - V}{\tau_u} + \langle\frac{w - v}{\tau^*}\rangle\right]. \end{aligned} \tag{B.24}$$

Finally,

$$(LHS) = \frac{\partial(r_u V_u)}{\partial t} + \frac{\partial}{\partial x}\left(r_u\langle v^2\rangle_u\right) - r_u\frac{V_u^0 - V_u}{\tau_u} - \gamma_u r_u\langle\frac{w - v}{\tau^*}\rangle \tag{B.25}$$

where $\gamma_u = 0$ for manual vehicles and $\gamma_u = 1$ for ACC vehicles.

Let $\varphi(\Delta x)$ denotes the space headway distribution between two consequent vehicles, regardless of the class. By substituting $w = v(x + \Delta x, t) = v(x, t) + \Delta x\frac{\partial v}{\partial x}$ into the mean operator $\langle w - v\rangle$, we obtain:

$$\langle w - v\rangle = \int_{v^0}\int_{v}\int_{\Delta x}\Delta x\frac{\partial v}{\partial x}\varphi(\Delta x)\psi_u(v, v^0)d(\Delta x)dvdv^0. \tag{B.26}$$

Assume that $\varphi(\Delta x)$ is distributed as below:

$$\varphi(\Delta x) = \delta\left(\Delta x - \frac{1}{r(x + \delta x, t)}\right). \tag{B.27}$$

Here, $\delta(.)$ denotes the Dirac delta function and δx is defined as:

$$\begin{aligned} \delta x &= \frac{1}{2}\left(\int_v\int_{v^0}\rho(v, v^0)dv^0dv\right)^{-1} = \frac{1}{2}\left(\int_v\int_{v^0}r_u(x, t)\psi_u(v, v^0)dv^0dv\right)^{-1} \\ &= \frac{1}{2}\left(r\int_v\int_{v^0}\psi_u dv^0dv\right)^{-1} = \frac{1}{2}(r\cdot 1)^{-1} = \frac{1}{2r} \end{aligned} \tag{B.28}$$

Calculation of $\langle\Delta x\rangle$:

$$
\begin{aligned}
\langle \Delta x \rangle &= \int_{v^0} \int_{v} \int_{\Delta x} \Delta x \, \varphi(\Delta x) \psi_u(v, v^0) d(\Delta x) dv dv^0 \\
&= \int_{\Delta x} \Delta x \, \varphi(\Delta x) d(\Delta x) \int_{v^0} \int_{v} \psi_u(v, v^0) dv dv^0 \\
&= \int_{\Delta x} \Delta x \, \delta\left(\Delta x - \frac{1}{r(x+\delta x, t)}\right) d(\Delta x) \underbrace{\int_{v^0} \int_{v} \psi_u(v, v^0) dv dv^0}_{=1} \\
&= \int_{\Delta x} \Delta x \, \delta\left(\Delta x - \frac{1}{r(x+\delta x, t)}\right) d(\Delta x) .
\end{aligned}
\tag{B.29}
$$

By the properties of the Dirac delta function:

$$
\int_{\Delta x} \Delta x \, \delta\left(\Delta x - \frac{1}{r(x+\delta x, t)}\right) d(\Delta x) = \frac{1}{r(x+\delta x, t)} . \tag{B.30}
$$

By substituting equation (B.30) into equation (B.29), we obtain:

$$
\langle \Delta x \rangle = \frac{1}{r(x+\delta x, t)} . \tag{B.31}
$$

By applying the first-order Taylor expansion for $\varphi(\Delta x)$ with respect to location x, and using equation (B.28), we come up with

$$
\begin{aligned}
\langle \Delta x \rangle = \frac{1}{r(x+\delta x, t)} &= \frac{1}{r(x)} + \left[\frac{1}{r(x)}\right]_x^1 \delta x = \frac{1}{r} + \left[-\frac{1}{r^2}\frac{\partial r}{\partial x}\right] \delta x = \frac{1}{r} - \frac{1}{r^2}\frac{\partial r}{\partial x} \delta x \\
&= \frac{1}{r} - \frac{1}{r^2}\frac{\partial r}{\partial x}\frac{1}{2r} = \frac{1}{r} - \frac{1}{2r^3}\frac{\partial r}{\partial x} .
\end{aligned}
\tag{B.32}
$$

Neglecting the second-order terms

$$
\langle \Delta x \rangle = \frac{1}{r} . \tag{B.33}
$$

Finally, by substituting equations (B.27) and (B.33) into equation (B.26), we obtain:

$$
\begin{aligned}
\langle w - v \rangle &= \int_{v^0} \int_{v} \int_{\Delta x} \Delta x \frac{\partial v}{\partial x} \varphi(\Delta x) \psi_u(v, v^0) d(\Delta x) dv dv^0 \\
&= \int_{\Delta x} \Delta x \, \varphi(\Delta x) d(\Delta x) \int_{v^0} \int_{v} \frac{\partial v}{\partial x} \psi_u(v, v^0) dv dv^0 \\
&= \langle \Delta x \rangle \int_{v^0} \int_{v} \frac{\partial v}{\partial x} \psi_u(v, v^0) dv dv^0 = \langle \Delta x \rangle \frac{\partial}{\partial x} \int_{v^0} \int_{v} v \psi_u(v, v^0) dv dv^0 \\
&= \langle \Delta x \rangle \frac{\partial}{\partial x} \langle v \rangle_u = \langle \Delta x \rangle \frac{\partial}{\partial x} V_u = \frac{1}{r}\left(\frac{\partial V_u}{\partial x}\right) .
\end{aligned}
\tag{B.34}
$$

The derivation of the right-hand side (non-continuum term) of equation (B.5) has been specified in the papers of Treiber *et al.*, 1999, Hoogendoorn & Bovy, 2000 and Helbing *et al.*, 2001.

In more details, we can distinguish two types of non-continuum processes, namely adaptation of the desired velocity distribution to a reasonable desired velocity distribution, and the deceleration caused by vehicle interactions. An interaction event is determined by the

fact that a faster vehicle catches up with a slower one. In case of interaction, the fast vehicle needs to perform a remedial maneuver to avoid an imminent collision. Hence, in what follows, the impeded vehicle will be referred to as the active party, while we will refer to the impeding vehicle as the passive party (Treiber *et al.*, 1999).

Subsequently, let us first consider interacting vehicles of $\rho_u(x,t,v,v^0)$; interactions can either yield an increase or a decrease in $\rho_u(x,t,v,v^0)$, denoted by $(\partial\rho_u/\partial t)^+_{int}$ and $(\partial\rho_u/\partial t)^-_{int}$, respectively. That is:

$$\left(\frac{\partial\rho_u}{\partial t}\right)_{NC} = \left(\frac{\partial\rho_u}{\partial t}\right)^-_{int} + \left(\frac{\partial\rho_u}{\partial t}\right)^+_{int}. \tag{B.35}$$

Let us now consider the joint phase-space density of classes u and s, given by $\rho_{u,s}(x,t,v,w)$, with $v=(v,v^0)$ and $w=(w,w^0)$ being the velocity and desired velocity of vehicles 1 and 2, respectively. Specifically, $\rho_{u,s}$ denotes the expected pair of vehicles of class u having a velocity v and a desired velocity v^0 and a vehicle of class s with velocity w and desired velocity w^0 per unit length of a roadway. Subsequently, let $p_u = p_u(x,t,v,w)$ denotes the probability that slower vehicles can be immediately overtaken by a vehicle of class u. Then, based on the results established in Leutzbach, 1988, the reduction rate $(\partial\rho_u/\partial t)^-_{int}$ in $\rho_u(x,t,v,v^0)$ due to vehicles in $\rho_u(x,t,v,v^0)$ interacting with slower ones is given by:

$$\left(\frac{\partial\rho_u}{\partial t}\right)^-_{int} = \sum_s \int_{w'} \int_{w^0} \left(1-p_u = p_u(v,w')\right)(w'-v)\rho_{u,s}(v,v^0,w',w^0)dw^0dw'. \tag{B.36}$$

The increase rate $(\partial\rho_u/\partial t)^+_{int}$ due to vehicles in $\rho_u(x,t,w,v^0)$, with $w>v$, interacting with slower ones in $\rho_s(x,t,v,v^0)$ (irrespective of the desired velocity v^0) equals:

$$\left(\frac{\partial\rho_u}{\partial t}\right)^+_{int} = \sum_s \int_{v'=v}^{\infty} \int_{w^0} \left(1-p_u = p_u(v',v)\right)(v'-v)\rho_{u,s}(v',v^0,v,w^0)dw^0dv', \tag{B.37}$$

where it was speculated that slower vehicles are not affected by the interaction.

The probability $p_u = p_u(x,t,v,w)$ of immediate overtaking depends on several factors, such as the traffic flow conditions in a destination lane, the maneuverability and length of the vehicle, as well as the difference between the current velocity v and the velocity w of the impeding vehicle, the traffic composition (for example the percentage of heavy-vehicles), etc.

Next, using the expression $\rho_{u,s} = \rho_u\rho_s$ or $\rho_{u,s} = \rho_u\rho_s^f$, where ρ_s^f denotes the free-flowing vehicles in ρ_s, the resulting expressions for (B.35) and (B.36) can be approximated by:

$$\left(\frac{\partial\rho_u}{\partial t}\right)^-_{int} = \sum_s (1-\pi_{u,s}) \int_{w'=0}^{v} \int_{w^0} (w'-v)\,\rho_u(v,v^0)\rho_s^f(w',w^0)dw^0dw' \tag{B.38}$$

$$\left(\frac{\partial\rho_u}{\partial t}\right)^+_{int} = \sum_s (1-\pi_{u,s}) \int_{v'=v}^{\infty} \int_{w^0} (v'-v)\,\rho_u(v',v^0)\rho_s^f(v,w^0)dw^0dv', \tag{B.39}$$

in which $\pi_{u,s}$ defines the (v,v^0)-independent expected probability of immediate overtaking of vehicles of class u overtaking a vehicle of class s.

B.1.3 Method of Moments for the right-hand side

$$\int_v \int_{v^0} \left(\frac{\partial \rho_u}{\partial t}\right)_{NC} = v^k dv^0 dv$$

$$= \int_v \int_{v^0} \left[\sum_s (1-\pi_{u,s}) \int_{w'=0}^{v} \int_{w^0} (w'-v)\, \rho_u(v,v^0) \rho_s^f(w',w^0) dw^0 dw' \right] v^k dv^0 dv$$

$$+ \int_v \int_{v^0} \left[\sum_s (1-\pi_{u,s}) \int_{v'=v}^{\infty} \int_{w^0} (v'-v)\, \rho_u(v',v^0) \rho_s^f(v,w^0) dw^0 dv' \right] v^k dv^0 dv \,. \tag{B.40}$$

Using $\rho_u = \psi_u r_u$ and $\rho_s = \psi_s r_s$ (from the known mean operator) the equation (B.40) becomes:

$$\int_v \int_{v^0} \left[\sum_s (1-\pi_{u,s}) \int_{w'=0}^{v} \int_{w^0} (w'-v)\, \rho_u(v,v^0) \rho_s^f(w',w^0) dw^0 dw' \right] v^k dv^0 dv$$

$$= \int_v \int_{v^0} v^k \sum_s (1-\pi_{u,s}) dv^0 dv \int_{w'=0}^{v} \int_{w^0} (w'-v) r_u \psi_u \rho_s(w',w^0) dw^0 dw'$$

$$= \int_v \int_{v^0} v^k \sum_s (1-\pi_{u,s}) dv^0 dv \int_{w'=0}^{v} (w'-v) r_u \psi_u \left[\int_{w^0} \rho_s(w',w^0) dw^0 \right] dw'$$

$$= \int_v \int_{v^0} v^k \sum_s (1-\pi_{u,s}) dv^0 dv \int_{w'=0}^{v} (w'-v) r_u \psi_u \widetilde{\rho_s}(w')\, dw'$$

$$= \sum_s (1-\pi_{u,s}) r_u(x,t) \left[\int_v \int_{v^0} v^k dv^0 dv \int_{w'=0}^{v} (w'-v) \psi_u(v,v^0) \widetilde{\rho_s}(w')\, dw' \right] \tag{B.41}$$

$$= \sum_s (1-\pi_{u,s}) r_u \int_v \int_{v^0} v^k \psi_u(v,v^0) dv^0 dv \int_{w'=0}^{v} (w'-v) \widetilde{\rho_s}(w')\, dw'$$

$$= \sum_s (1-\pi_{u,s}) r_u \langle v^k \int_{w'=0}^{v} (w'-v) \widetilde{\rho_s}(w')\, dw' \rangle$$

$$= \sum_s (1-\pi_{u,s}) r_u F_{u,s} \,.$$

Similarly,

$$\int_v \int_{v^0} \left[\sum_s (1-\pi_{u,s}) \int_{v'=v}^{\infty} \int_{w^0} (v'-v)\, \rho_u(v',v^0) \rho_s^f(v,w^0) dw^0 dv' \right] v^k dv^0 dv$$

$$= \int_v \int_{v^0} v^k \sum_s (1-\pi_{u,s}) dv^0 dv \left[\int_{v'=v}^{\infty} \int_{w^0} (v'-v) \rho_u(v',v^0) \psi_s(v,w^0) r_s(x,t) dw^0 dv' \right] dv^0 dv$$

$$= \int_v v^k \sum_s (1-\pi_{u,s})\, r_s(x,t) dv \int_{v'=v}^{\infty} \int_{w^0} (v'-v) \widetilde{\rho_u}(v') \psi_s(v,w^0) dw^0 dv' \tag{B.42}$$

$$= \sum_s (1-\pi_{u,s}) r_s \int_v \int_{w^0} \left[v^k \int_{v'=v}^{\infty} \int_{w^0} (v'-v) \widetilde{\rho_u}(v') \psi_s(v,w^0) dv' \right] dw^0 dv$$

$$= \sum_s (1-\pi_{u,s}) r_s \langle v^k \int_{v'=v}^{\infty} \int_{w^0} (v'-v) \widetilde{\rho_u}(v') dv' \rangle = \sum_s (1-\pi_{u,s}) r_s H_{u,s} .$$

Let us define $\left(\frac{\partial \rho_u}{\partial t}\right)_{NC} = \left(\frac{\partial \rho_u}{\partial t}\right)_{NC}^{-} + \left(\frac{\partial \rho_u}{\partial t}\right)_{NC}^{+} \rightarrow R_{u,s}^{(k)} = F_{u,s}^{(k)} + H_{u,s}^{(k)}$

Hence,

$$\left(\frac{\partial \rho_u}{\partial t}\right)_{NC} = \left(\frac{\partial \rho_u}{\partial t}\right)_{int}^{-} + \left(\frac{\partial \rho_u}{\partial t}\right)_{int}^{+} = (1-\pi_{u,s}) r_u \sum_s R_{u,s}^{(k)} . \quad \text{(B.43)}$$

Finally, the aggregated right-hand side of equation (B.1) becomes (Ngoduy, 2012c):

- **For $k = 0$:** $(RHS) = 0$

- **For $k = 1$:** $(RHS) = -r_u(1-\pi_{u,s}) \sum_s R_{u,s}$, with $R_{u,s}$ being the interaction rate between a vehicle of class u and the leading vehicle of any class (denoted by s) and π_u being the probability that a vehicle of class u is able to immediately change lanes.

Consequently, the **macroscopic equations for mixed traffic of manual and ACC vehicles are determined as**

- **Conservation law:**

$$\frac{\partial r_u}{\partial t} + \frac{\partial r_u V_u}{\partial x} = 0 , \quad \text{(B.44)}$$

- **Momentum dynamics:**

$$\frac{\partial r_u V_u}{\partial t} + \underbrace{\frac{\partial r_u (V_u^2 + \Theta_u)}{\partial x} - \frac{\gamma_u}{\tau^*} \frac{\partial V_u}{\partial x}}_{convection} = \underbrace{r_u \frac{V_u^e - V_u}{\tau_u}}_{relaxation} , \quad \text{(B.45)}$$

where V_u^e is the equilibrium class specific speed:

$$V_u^e(r_u, V_u, \Theta_u) = V_u^0 - (1-\pi_u)\tau_u \sum_s R_{u,s} . \quad \text{(B.46)}$$

B.2 Macroscopic Model Development for CACC traffic flow based on GKT theory

Similarly to the previous Section B.1, the work reported here contains a detailed derivation of the equations for the macroscopic traffic flow simulation with CACC traffic dynamics (Ngoduy, 2013b), obtained from the classic GKT theory using the well-known method of moments. It is based on the work of Hoogendoorn & Bovy, 2000, and Ngoduy, 2013b. This derivation was performed in order to verify the procedure followed by Ngoduy, 2013b, and highlight the details of this procedure, so as to be able to compare the utilized CACC model (Chapter 5) with that in Ngoduy, 2013b.

B.2.1 Underlying gas-kinetic model for CACC vehicles

The macroscopic approach incorporating CACC traffic dynamics is extended from the gas-kinetic theory presented in the previous Section B.1 for ACC equipped vehicles. Thus, we will start by briefly recalling the GKT model for ACC vehicles presented in Section B.1. Let us first denote the phase space density $\rho(x,t,v,v^0)$, ρ for short, which represents the expected number of vehicles on (x,t) driving with speed v while having desired speed v^0 per unit roadway. With $\psi(v,v^0)$ the joint probability of the current speed and the desired speed of vehicles is denoted. By definition, $\rho = \psi r$, with $r = r(x,t)$, is the density at location x and time instant t. Based on the work of Hoogendoorn & Bovy, 2000, the gas-kinetic theory reflects the changes of the phase space density ρ due to both the continuum and non-continuum process; the continuum process yields smooth changes of ρ, due to inflow and outflow into the phase space consisting of vector $\mathcal{F} = (x,v,v^0)$, while the non-continuum process produces non-smooth changes of ρ by the interaction occurring between and within vehicle classes. The gas-kinetic equation describing the traffic dynamics for aggregate lane and aggregate vehicle class is given below (Ngoduy, 2013b)

$$\frac{\partial \rho}{\partial t} + \underbrace{\nabla\left(\rho \frac{d\mathcal{F}}{dt}\right)}_{continuum} = \underbrace{\left(\frac{\partial \rho}{\partial t}\right)^{int}}_{non-continuum}, \tag{B.47}$$

where the Nabla operator, ∇, is defined as

$$\nabla = \left(\frac{\partial}{\partial x}, \frac{\partial}{\partial v}, \frac{\partial}{\partial v^0}\right). \tag{B.48}$$

Assuming that drivers do not change their desired speed during their journey, the first and the third term of the non-continuum process $\frac{d\mathcal{F}}{dt}$ of equation (B.47) are determined as:

$$\frac{dx}{dt} = v, \quad \frac{dv^0}{dt} = 0\,. \tag{B.49}$$

In case of the second term of $\frac{d\mathcal{F}}{dt}$, which is actually the acceleration or deceleration term and is specified for manual vehicles as $\frac{dv}{dt} = \frac{v^0 - v}{\tau_u}$ for CACC vehicles, takes the following form:

$$\frac{dv}{dt} = \frac{v^0 - v}{\tau} + \sum_{n=1}^{N} \frac{w_n - v}{\tau_n^*}, \tag{B.50}$$

in which $n = 1,2,\dots,N$ with N being the number of preceding vehicles that the follower could exchange information (interact) with; w_n is the speed of the nth preceding vehicle. Following from the space-headway policy, the speeds of the follower are correlated with the speeds of its nth leader according to the following equation: $\langle w_n \rangle = \langle v(x + \Delta x_n, t) \rangle$, with Δx_n being the space headway between the follower and its nth leader. Moreover, the coefficient τ_n^* in equation (B.50) reflects the relaxation time of the CACC vehicle to the nth leader. Under the assumption that CACC vehicles takes longer time to relax to the speed of the furthest nth leader, it is supposed that $\tau_1^* < \tau_2^* < \cdots \tau_N^*$ and $\sum_{n=1}^{N} \frac{1}{\tau_n^*} = \frac{1}{\tau^*}$, where τ^* denotes the relaxation time of the ACC vehicle.

By substituting equation (B.50) into the generalized governing equation (B.47) we end up in the following gas-kinetic equation that incorporates CACC traffic dynamics:

$$\frac{\partial \rho}{\partial t} + \underbrace{\frac{\partial (\rho v)}{\partial x}}_{I} + \underbrace{\frac{\partial}{\partial v}\left(p \frac{v^0 - v}{\tau}\right)}_{II} + \underbrace{\frac{\partial}{\partial v}\left(\rho \sum_{n=1}^{N} \frac{w_n - v}{\tau_n^*}\right)}_{III} = \left(\frac{\partial \rho}{\partial t}\right)^{int}. \tag{B.51}$$

In the equation above, term I reflects the changes of the phase-space density ρ due to the motion of vehicles along the space variable x, term II denotes the changes of ρ due to the acceleration process (i.e. the vehicle accelerates to its the desired speed v^0), while term III depicts the changes of ρ due to the relaxation process towards the speeds of the preceding vehicles through the CACC system.

B.2.2 Governing macroscopic traffic equations

The macroscopic model for CACC traffic flow is derived from the gas-kinetic model proposed above, based on the so-called method of moments (Treiber *et al.*, 1999).

Helpful Calculations:

$$\frac{d\mathcal{F}}{dt} = \frac{d}{dt}(x, v, v^0) = \left(\frac{dx}{dt}, \frac{dv}{dt}, \frac{dv^0}{dt}\right) = \left(v, \frac{dv}{dt}, 0\right), \tag{B.52}$$

$$\begin{aligned} \nabla\left(\rho \frac{d\mathcal{F}}{dt}\right) &= \left(\frac{\partial}{\partial x}, \frac{\partial}{\partial v}, \frac{\partial}{\partial v^0}\right) \rho \left(\frac{dx}{dt}, \frac{dv}{dt}, \frac{dv^0}{dt}\right) = \left(\frac{\partial}{\partial x}, \frac{\partial}{\partial v}, \frac{\partial}{\partial v^0}\right)\left(\rho v, \rho \frac{dv}{dt}, 0\right) \\ &= \frac{\partial}{\partial x}(\rho v) + \frac{\partial}{\partial v}\left(\rho \frac{dv}{dt}\right) + 0 = \frac{\partial}{\partial x}(\rho v) + \frac{\partial}{\partial v}\left(\rho \frac{dv}{dt}\right). \end{aligned} \tag{B.53}$$

So, the left-hand side of equation (B.47) becomes:

$$(LHS) = \frac{\partial \rho}{\partial t} + \frac{\partial}{\partial x}(\rho v) + \frac{\partial}{\partial v}\left(\rho \frac{dv}{dt}\right). \tag{B.54}$$

Method of Moments

Afterwards, we multiply the left-hand side of equation (B.48) with the "k moments" of the variable v, v^k and subsequently the resulting equation is integrated over the physical range of speed v and desired speed v^0:

$$(LHS) = \frac{\partial}{\partial t}(\rho)v^k + \frac{\partial}{\partial x}(\rho v)v^k + \frac{\partial}{\partial v}\left(\rho\frac{dv}{dt}\right)v^k \Rightarrow$$
$$(LHS) = \int_v\int_{v^0}\frac{\partial}{\partial t}\rho v^k dvdv^0 + \int_v\int_{v^0}\frac{\partial}{\partial x}\rho v^{k+1}dvdv^0 + \int_v\int_{v^0} v^k\frac{\partial}{\partial v}\left(\rho\frac{dv}{dt}\right)dvdv^0 . \quad \text{(B.55)}$$

Taking into account that $\rho = r\psi = r(x,t)\psi(v,v^0)$, equation (B.55) becomes:

$$(LHS) = \underbrace{\int_v\int_{v^0}\frac{\partial}{\partial t}r(x,t)v^k\psi(v,v^0)dvdv^0}_{A} + \underbrace{\int_v\int_{v^0}\frac{\partial}{\partial x}r(x,t)v^{k+1}\psi(v,v^0)dvdv^0}_{B} + \underbrace{\int_v\int_{v^0} v^k\frac{\partial}{\partial v}\left(\rho\frac{dv}{dt}\right)dvdv^0}_{C} . \quad \text{(B.56)}$$

In the ensuing section, the following mean operator, $\langle . \rangle$, is applied to any function $y(v,v^0)$:

$$\langle y(v,v^0)\rangle = \int_v\int_{v^0} y(v,v^0)\psi(v,v^0)dvdv^0 . \quad \text{(B.57)}$$

For example:

$$\int_v\int_{v^0} v^k\psi(v,v^0)dvdv^0 = \langle v^k\rangle . \quad \text{(B.58)}$$

Thus, the macroscopic traffic variables are defined as below:

- **Density**: $r = \int_v \rho\, dv$
- **Mean speed**: $V = \langle v\rangle$
- **Mean speed variance**: $\Theta = \langle v^2\rangle - (V)^2 \Rightarrow \langle v^2\rangle = \Theta + (V)^2$
- **Mean desired speed**: $V^0 = \langle v^0\rangle$

Applying partial integration to equation (B.56) results in:

Term A:

$$A = \frac{\partial}{\partial t}r(x,t)\int_v\int_{v^0} v^k\psi(v,v^0)dvdv^0 = \frac{\partial}{\partial t}r\langle v^k\rangle \quad \text{(9.59)}$$

Term B:

$$B = \frac{\partial}{\partial x}r(x,t)\int_v\int_{v^0} v^{k+1}\psi(v,v^0)dvdv^0 = \frac{\partial}{\partial x}r\langle v^{k+1}\rangle \quad \text{(B.60)}$$

Term C (taking also into account the equations (B.62), (B.63), (B.64)):

$$C = \int_{v}\int_{v^0} v^k \frac{\partial}{\partial v}\left(\rho \frac{dv}{dt}\right) dvdv^0 = \int_{v}\int_{v^0} \left[\frac{\partial}{\partial v}\left(v^k \rho \frac{dv}{dt}\right) - \frac{\partial}{\partial v}(v^k)\rho \frac{dv}{dt}\right] dvdv^0. \tag{B.61}$$

In the above equation, obviously:

$$\int_{v}\int_{v^0} \frac{\partial}{\partial v}\left(v^k \rho \frac{dv}{dt}\right) dvdv^0 = \int_{v^0} v^k \rho \frac{dv}{dt} dv^0 \to 0\,. \tag{B.62}$$

So,

$$\int_{v}\int_{v^0} \frac{\partial}{\partial v}\left(v^k \rho \frac{dv}{dt}\right) dvdv^0 \to 0 \tag{B.63}$$

and the term C is equivalent to:

$$\begin{aligned} C &= -\int_{v}\int_{v^0} kv^{k-1} r\psi(v, v^0) \frac{dv}{dt} dvdv^0 \;\Rightarrow \\ C &= -kr \int_{v}\int_{v^0} \psi(v, v^0) \frac{dv}{dt} v^{k-1} dvdv^0\,. \end{aligned} \tag{B.64}$$

By substituting equation (B.50) into equation (B.64) the term C becomes:

$$\begin{aligned} C &= -kr \int_{v}\int_{v^0} v^{k-1} \frac{dv}{dt} \psi dvdv^0 \\ &= -kr \int_{v}\int_{v^0} \frac{v^{k-1}v^0 - v^{k-1}v}{\tau} + \left(v^{k-1} \sum_{n=1}^{N} \frac{w_n - v^k}{\tau_n^*}\right) \psi dvdv^0 \\ &= -kr \int_{v}\int_{v^0} \frac{v^{k-1}v^0 - v^k}{\tau} \psi dvdv^0 + \int_{v}\int_{v^0} \left(\sum_{n=1}^{N} \frac{v^{k-1}w_n - v^{k-1}v^k}{\tau_n^*}\right) \psi dvdv^0 \\ &= -kr \left[\left\langle \frac{v^{k-1}v^0 - v^k}{\tau} \right\rangle + \sum_{n=1}^{N} \left\langle \frac{v^{k-1}w_n - v^k}{\tau_n^*} \right\rangle\right]. \end{aligned} \tag{B.65}$$

By setting $k = 0$ and $k = 1$, the aggregated left-hand side takes the form:

- **<u>For $k = 0$:</u>**

$$A = \frac{\partial}{\partial t}\left(r\langle v^k \rangle\right) = \frac{\partial}{\partial t}\left(r\langle v^{(0)} \rangle\right) = \frac{\partial}{\partial t}(r\ 1) = \frac{\partial r}{\partial t}, \tag{B.66}$$

$$B = \frac{\partial}{\partial x}\left(r\langle v^{(k+1)} \rangle\right) = \frac{\partial}{\partial x}\left(r\langle v^{(0+1)} \rangle\right) = \frac{\partial}{\partial x}(r\langle v \rangle) = \frac{\partial}{\partial x}(rV)\,, \tag{B.67}$$

$$C = 0\,. \tag{B.68}$$

Therefore,

$$\begin{aligned} (LHS) &= (term\ A + term\ B = term\ C) = \frac{\partial r}{\partial t} + \frac{\partial}{\partial x}(rV) + 0 \Longrightarrow (LHS) \\ &= \frac{\partial r}{\partial t} + \frac{\partial}{\partial x}(rV)\,. \end{aligned} \tag{B.69}$$

- **For $k = 1$:**

$$A = \frac{\partial}{\partial t}\left(r\langle v^k\rangle\right) = \frac{\partial}{\partial t}\left(r\langle v^{(1)}\rangle\right) = \frac{\partial}{\partial t}\left(r\langle v\rangle\right) = \frac{\partial}{\partial t}(rV)\,, \tag{B.70}$$

$$B = \frac{\partial}{\partial x}\left(r\langle v^{(k+1)}\rangle\right) = \frac{\partial}{\partial x}\left(r\langle v^{(1+1)}\rangle\right) = \frac{\partial}{\partial x}\left(r\langle v^2\rangle\right) = \frac{\partial}{\partial x}[r(\Theta + V^2)]\,, \tag{B.71}$$

$$\begin{aligned} C &= -kr\left[\langle\frac{v^{k-1}v^0 - v^k}{\tau}\rangle + \sum_{n=1}^{N}\langle\frac{v^{k-1}w_n - v^k}{\tau_n^*}\rangle\right] \\ &= -r\left[\langle\frac{v^{1-1}v^0 - v^1}{\tau}\rangle + \sum_{n=1}^{N}\langle\frac{v^{1-1}w_n - v^1}{\tau_n^*}\rangle\right] \\ &= -r\left[\langle\frac{v^{(0)}v^0 - v}{\tau}\rangle + \sum_{n=1}^{N}\langle\frac{v^{(0)}w_n - v^1}{\tau_n^*}\rangle\right] \\ &= -r\left[\langle\frac{v^0 - v}{\tau}\rangle + \sum_{n=1}^{N}\langle\frac{w_n - v}{\tau_n^*}\rangle\right] = -r\left[\frac{\langle v^0\rangle - \langle v\rangle}{\langle\tau\rangle} + \sum_{n=1}^{N}\langle\frac{w_n - v}{\tau_n^*}\rangle\right] \\ &= -r\left[\frac{V^0 - V}{\tau} + \sum_{n=1}^{N}\langle\frac{w_n - v}{\tau_n^*}\rangle\right]. \end{aligned} \tag{B.72}$$

Finally,

$$\begin{aligned} (LHS) &= \frac{\partial(rV)}{\partial t} + \frac{\partial}{\partial x}\left(r\langle v^2\rangle\right) - r\frac{V^0 - V}{\tau} - r\sum_{n=1}^{N}\langle\frac{w_n - v}{\tau_n^*}\rangle \\ &= \frac{\partial(rV)}{\partial t} + \frac{\partial}{\partial x}[r(\Theta + V^2)] - r\frac{V^0 - V}{\tau} - r\sum_{n=1}^{N}\langle\frac{w_n - v}{\tau_n^*}\rangle\,. \end{aligned} \tag{B.73}$$

Let us now denote the space headway distribution between two successive vehicles, $\varphi(\Delta x)$. By substituting $\langle w_n\rangle = \langle v(x + \Delta x_n, t)\rangle = V(x,t) + \Delta x_n\frac{\partial v}{\partial x}$ into the mean operator $\langle w_n - v\rangle$ and $\langle\Delta x_n\rangle = n\Delta x$ (with Δx being the space headway between two successive vehicles) we end up with:

$$\langle w_n - v\rangle = \int_{v^0}\int_{v}\int_{\Delta x} n\Delta x\frac{\partial v}{\partial x}\varphi(\Delta x)\psi(v, v^0)d(\Delta x_n)dvdv^0\,. \tag{B.74}$$

Next, we assume that $\varphi(\Delta x)$ is distributed as follows:

$$\varphi(\Delta x) = \delta\left(\Delta x - \frac{1}{r(x + \delta x, t)}\right). \tag{B.75}$$

Here, $\delta(.)$ denotes the Dirac delta function and δx is defined as:

$$\begin{aligned}\delta x &= \frac{1}{2}\left(\int_{v}\int_{v^0}\rho(v,v^0)dvdv^0\right)^{-1} = \frac{1}{2}\left(\int_{v}\int_{v^0} r(x,t)\psi(v,v^0)dvdv^0\right)^{-1} \\ &= \frac{1}{2}\left(r\int_{v}\int_{v^0}\psi dvdv^0\right)^{-1} = \frac{1}{2}(r\cdot 1)^{-1} = \frac{1}{2r}.\end{aligned} \tag{B.76}$$

Calculation of $\langle \Delta x\rangle$:

$$\begin{aligned}\langle \Delta x\rangle &= \int_{v^0}\int_{v}\int_{\Delta x}\Delta x\,\varphi(\Delta x)\psi(v,v^0)d(\Delta x)dvdv^0 \\ &= \int_{\Delta x}\Delta x\,\varphi(\Delta x)d(\Delta x)\int_{v^0}\int_{v}\psi(v,v^0)dvdv^0 \\ &= \int_{\Delta x}\Delta x\,\delta\left(\Delta x-\frac{1}{r(x+\delta x,t)}\right)d(\Delta x)\underbrace{\int_{v^0}\int_{v}\psi(v,v^0)dvdv^0}_{=1} \\ &= \int_{\Delta x}\Delta x\,\delta\left(\Delta x-\frac{1}{r(x+\delta x,t)}\right)d(\Delta x).\end{aligned} \tag{B.77}$$

By the properties of the Dirac delta function:

$$\int_{\Delta x}\Delta x\,\delta\left(\Delta x-\frac{1}{r(x+\delta x,t)}\right)d(\Delta x) = \frac{1}{r(x+\delta x,t)}. \tag{B.78}$$

By substituting equation (B.78) into equation (B.77), we obtain:

$$\langle \Delta x\rangle = \frac{1}{r(x+\delta x,t)}. \tag{B.79}$$

By applying the first-order Taylor expansion for $\varphi(\Delta x)$ with respect to location x, and using equation (B.76), we come up with

$$\begin{aligned}\langle \Delta x\rangle = \frac{1}{r(x+\delta x,t)} &= \frac{1}{r(x)} + \left[\frac{1}{r(x)}\right]_{x}^{1}\delta x = \frac{1}{r} + \left[-\frac{1}{r^2}\frac{\partial r}{\partial x}\right]\delta x = \frac{1}{r} - \frac{1}{r^2}\frac{\partial r}{\partial x}\delta x \\ &= \frac{1}{r} - \frac{1}{r^2}\frac{\partial r}{\partial x}\frac{1}{2r} = \frac{1}{r} - \frac{1}{2r^3}\frac{\partial r}{\partial x}.\end{aligned} \tag{B.80}$$

Neglecting the second-order terms

$$\langle \Delta x\rangle = \frac{1}{r}. \tag{B.81}$$

Finally, by substituting equations (B.75) and (B.81) into equation (B.74), we obtain:

$$\begin{aligned}\langle w_n - v\rangle &= \int_{v^0}\int_{v}\int_{\Delta x} n\Delta x \frac{\partial v}{\partial x}\varphi(\Delta x)\psi(v,v^0)d(\Delta x)dvdv^0 \\ &= \int_{\Delta x} n\Delta x\,\varphi(\Delta x)d(\Delta x)\int_{v^0}\int_{v}\frac{\partial v}{\partial x}\psi(v,v^0)dvdv^0 \\ &= n\langle\Delta x\rangle\int_{v^0}\int_{v}\frac{\partial v}{\partial x}\psi(v,v^0)dvdv^0 = n\langle\Delta x\rangle\frac{\partial}{\partial x}\int_{v^0}\int_{v} v\psi(v,v^0)dvdv^0 \\ &= n\langle\Delta x\rangle\frac{\partial}{\partial x}\langle v\rangle = n\langle\Delta x\rangle\frac{\partial V}{\partial x} = \frac{n}{r}\left(\frac{\partial V}{\partial x}\right).\end{aligned} \tag{B.82}$$

The mean operator of the non-continuum term of equation (B.47) has been specified in the work of Treiber *et al.*, 1999, Hoogendoorn & Bovy, 2000 and Helbing *et al.*, 2001). In the following section we adopt the results concerning Treiber's work (Treiber *et al.*, 1999).

B.2.3 Underlying the gas-kinetic equation

In principle, the kinetic equation that describes the evolution of the coarse-grained phase-space density is given as

$$\begin{aligned}\tilde{\rho}(x,v,t) = \sum_{a}\int dt'\int dx'\int dv'\, g(t-t',x-x',v-v') \\ \times\,\delta(x'-x_\alpha(t))\delta(v'-v_\alpha(t))\,,\end{aligned} \tag{B.83}$$

and represents the probability density of finding, at a given time t, a vehicle α at position x_α having velocity v_α. The coarse graining is performed by taking local averages over a weighting function $g(t-t',x-x',v-v')$ satisfying $\int dt'\int dx'\int dv'\, g(t-t',x-x',v-v') = 1$, which is localized in a microscopically large and macroscopically small neighborhood around x and in appropriate neighborhoods around t and v (Treiber *et al.*, 1999).

Subsequently, taking the time derivative of the above equation (B.83), and inserting the microscopic equation $\frac{dv_a}{dt} = \frac{V_0 - v_a}{\tau} - \sum_{\beta\neq a}\bar{f}_{a\beta} + \xi_a(t)$, gives, by partial integration the kinetic evolution equation (B.86) for the phase-space density (Treiber *et al.*, 1999) :

$$\frac{\theta\tilde{\rho}}{\theta t} + \frac{\theta}{\theta x}(\tilde{\rho}v) + \frac{\theta}{\theta v}\left[\tilde{\rho}\frac{V_0 - v}{\tau}\right] = \frac{\theta}{\theta v}(\tilde{\rho}f_{int}) + \frac{\theta^2}{\theta v^2}(\tilde{\rho}D)\,, \tag{B.84}$$

in which the interaction term has the form

$$\begin{aligned}f_{int} = \tilde{\rho}^{-1}\sum_{a}\sum_{\beta\neq a}\int dt'\int dx'\int dv'\, g(t-t',x-x',v-v')\,\bar{f}_{a\beta}\delta(x'-x_\alpha(t))\delta(v' \\ - v_\alpha(t))\,.\end{aligned} \tag{B.85}$$

The microscopic braking interactions $\bar{f}_{a\beta}$ directly results in a Boltzmann-like interaction with a density-dependent prefactor $P(\rho)$:

$$\frac{\theta}{\theta v}(\tilde{\rho}f_{int}) = P(\rho)I(x,v,t)\,, \tag{B.86}$$

in which

$$I(x,v,t) = \int_{v'>v} dv'(\,v'-v)\tilde{\rho}(x,v',t)\,\tilde{\rho}(x_a,v,t) + \int_{v'<v} dv'(\,v-v')\tilde{\rho}(x,v,t)\,\tilde{\rho}(x_a,v',t)\,. \tag{B.87}$$

The first term of the right-hand side of equation (B.87) reflects the increase of the phase-space density $\tilde{\rho}(x,v,t)$ due to the deceleration of faster vehicles having velocity $v' > v$, which cannot overtake vehicles at x_a driving with velocity v, whereas the second term defines the decrease of the phase-space density due to deceleration of vehicles driving with velocity v, which cannot overtake slower vehicles at x_a driving with $v' < v$. The prefactor

$$P(\rho) = (1-p)\chi = \frac{1}{p} - 1 \tag{B.88}$$

is proportional to the probability $(1-p)$ that one cannot immediately overtake a slower vehicle, and to the correlation factor $\chi = \frac{1}{p}$ describing the increased interaction rate due to vehicular space requirements. To sum up, the kinetic phase-space equation, upon which the GKT model is based, is defined by

$$\frac{\theta\tilde{\rho}}{\theta t} + \frac{\theta}{\theta x}(\tilde{\rho}v) + \frac{\theta}{\theta v}\left[\tilde{\rho}\frac{V_0 - v}{\tau}\right] = \left(\frac{1}{p} - 1\right)\left[\int_{v'>v} dv'(\,v'-v)\tilde{\rho}(x,v',t)\,\tilde{\rho}(x_a,v,t) + \int_{v'<v} dv'(\,v-v')\tilde{\rho}(x,v,t)\,\tilde{\rho}(x_a,v',t)\right] + \frac{\theta^2}{\theta v^2}(\tilde{\rho}D)\,. \tag{B.89}$$

B.2.4 Derivation of the macroscopic equations

Next, macroscopic equations for the lowest velocity moments are derived from the kinetic equation (B.89). Consequently, the macroscopic vehicle density $\rho(x,t)$ and the average velocity $V(x,t)$ are determined as:

$$\rho(x,t) = \int_0^\infty dv\,\tilde{\rho}(x,v,t)\,, \tag{B.90}$$

$$V(x,t) = \langle v\rangle = \rho^{-1}\int_0^\infty dv\,v\,\tilde{\rho}(x,v,t)\,. \tag{B.91}$$

In particular, the macroscopic density equation depends on V, and the macroscopic equation for V on the variance

$$\theta(x,t) = \langle (v-V)^2\rangle = \rho^{-1}\int_0^\infty dv\,(v-V)^2\,\tilde{\rho}(x,v,t)\,. \tag{B.92}$$

In the GKT model, we make two assumptions. First, we assume that the variance θ is a function of density and average velocity. Second, we assume that the phase-space density is locally associated with a Gaussian velocity distribution

$$\tilde{\rho}(x,v,t) = \rho(x,t)\frac{e^{-[v-V(x,t)]^2/[2\theta(x,t)]}}{\sqrt{2\pi\theta(x,t)}}. \tag{B.93}$$

Finally, multiplying the phase-space equation (B.89) with 1 or v, respectively, and integrating over v, after straightforward but rather lengthy calculations lead to

$$\frac{\theta r}{\theta t} + \frac{\theta(rV)}{\theta x} = 0\,, \tag{B.94}$$

$$\left(\frac{\theta}{\theta t} + V\frac{\theta}{\theta x}\right)V = -\frac{1}{\rho}\frac{\theta(\rho\theta)}{\theta x} + \frac{V_0 - v}{\tau} - \frac{P(\rho_a)\rho_a(\theta+\theta_a)}{2}B(\delta v)\,. \tag{B.95}$$

In more detail, from equation (B.89) we obtain:

$$\begin{aligned}
&\int_0^\infty dv \int_{v'>v} dv'(v'-v)\tilde{\rho}(x,v',t)\,\tilde{\rho}(x_a,v,t) + \int_0^\infty dv \int_{v'<v} dv'(v-v')\tilde{\rho}(x,v,t)\,\tilde{\rho}(x_a,v',t) \\
&\quad = \int_0^\infty dv \int_{v'>v} dv' v'\tilde{\rho}(x,v',t)\,\tilde{\rho}(x_a,v,t) \\
&\quad - \int_0^\infty dv \int_{v'>v} dv' v\tilde{\rho}(x,v',t)\,\tilde{\rho}(x_a,v,t) \\
&\quad + \int_0^\infty dv \int_{v'<v} dv' v'\tilde{\rho}(x,v,t)\,\tilde{\rho}(x_a,v',t) \\
&\quad - \int_0^\infty dv \int_{v'<v} dv' v\tilde{\rho}(x,v,t)\,\tilde{\rho}(x_a,v',t)\,.
\end{aligned} \tag{B.96}$$

Using equations (B.90) and (B.91):

$$\int_0^\infty dv\,\tilde{\rho}(x,v,t) \int_{v'>v} dv'\,v'\tilde{\rho}(x,v',t) = \rho(x_a,t) \int_{v'>v} dv'\,v'\tilde{\rho}(x,v',t)\,, \tag{B.97}$$

$$\int_0^\infty dv\,v\tilde{\rho}(x_a,v,t) \int_{v'>v} dv'\,\tilde{\rho}(x,v',t) = \rho(x_a,t)V(x_a,t) \int_{v'>v} dv'\,\tilde{\rho}(x,v',t)\,, \tag{B.98}$$

$$-\int_0^\infty dv\,\tilde{\rho}(x,v,t) \int_{v'<v} dv' v'\,\tilde{\rho}(x_a,v',t) = -\rho(x,t) \int_{v'<v} dv' v'\,\tilde{\rho}(x_a,v',t)\,, \tag{B.99}$$

$$\int_0^\infty dv\,v\tilde{\rho}(x,v,t) \int_{v'<v} dv'\,\tilde{\rho}(x_a,v',t) = \rho(x,t)V(x,t) \int_{v'<v} dv'\,\tilde{\rho}(x_a,v',t)\,. \tag{B.100}$$

However,

$$\rho(x_a,t)\int_{v'>v} dv'v'\,\tilde{\rho}(x,v',t) = \rho(x_a,t)\rho(x,t)V(x,t)\,, \tag{B.101}$$

$$\rho(x_a,t)V(x_a,t)\int_{v'>v} dv'\,\tilde{\rho}(x,v',t) = \rho(x_a,t)V(x_a,t)\rho(x,t)\,, \tag{B.102}$$

$$\rho(x,t)\int_{v'<v} dv'\,v'\tilde{\rho}(x_a,v',t) = \rho(x,t)\rho(x_a,t)V(x_a,t)\,, \tag{B.103}$$

$$\rho(x,t)V(x,t)\int_{v'<v} dv'\,\tilde{\rho}(x_a,v',t) = \rho(x,t)V(x,t)\rho(x_a,t)\,. \tag{B.104}$$

So,

$$\begin{aligned}&\rho(x_a,t)\rho(x,t)V(x,t) - \rho(x_a,t)V(x_a,t)\rho(x,t) + \rho(x,t)\rho(x_a,t)V(x_a,t)\\ &\quad - \rho(x,t)V(x,t)\rho(x_a,t) = 0\,.\end{aligned} \tag{B.105}$$

Finally, the monotonically increasing macroscopic interaction term, $B(\delta v)$, of equation (B.95)

$$B(\delta v) = 2\left[\delta v\frac{e^{-\delta v^2/2}}{\sqrt{2\pi}} + (1+\delta v^2)\int_{-\infty}^{\delta v}\frac{e^{-y^2/2}}{\sqrt{2\pi}}dy\right] \tag{B.106}$$

describes the dependence of the braking interaction on the dimensionless velocity difference $\delta v = (V - V_a)/\sqrt{\theta + \theta_\alpha}$.

To sum up, the **macroscopic equations for CACC vehicles** are (Ngoduy, 2013b)**:**

- **Conservation law:**

$$\frac{\partial r}{\partial t} + \frac{\partial (rV)}{\partial x} = 0\,, \tag{B.107}$$

- **Momentum dynamics:**

$$\frac{\partial (rV)}{\partial t} + \frac{\partial [r(V^2+\Theta)]}{\partial x} - \frac{\partial V}{\partial x}\sum_{n=1}^{N}\frac{n}{\tau_n^*} = r\frac{V^e - V}{\tau}\,, \tag{B.108}$$

where $V^e = V^e(r,V,r^a,V^a)$ denotes the (dynamic) equilibrium speed, which depends not only on the local density r and mean speed V, but also on the nonlocal density r^a and mean speed V^a. Both r^a and V^a are computed at location $x^a = x + d$, with d being the safe distance gap, specified as $d = d_0 + \gamma TV$. Here, d_0 and T are the safe distance gap at the standstill and safe time headway, respectively. Typically, $d_0 = \frac{1}{r_{jam}}$ where r_{jam} denotes the jam density; γ is a scaled parameter. The dynamic equilibrium speed function of the nonlocal model is (Treiber *et al.*, 1999):

$$V^e(r,V,r^a,V^a) = V^0\left[1 - \frac{A(r)}{A(r_{jam})}\left(\frac{r_a d}{1-\frac{r_a}{r_{jam}}}\right)^2 B\left(\frac{V-V_\alpha}{\sqrt{\Theta}}\right)\right], \tag{B.109}$$

where *A(r)* is a variance factor, determined as:

$$A(r) = A_0 + \delta A\left[1 + tanh\left(\frac{r - r_{cr}}{\delta r}\right)\right], \tag{B.110}$$

in which r_{cr} is the critical density, reflecting the division between the free-flow and congested traffic situation; A_0, δA and δr are constants; $B(.)$ is defined as:

$$B(z) = 2[zN(z) + (1 + z^2)]E(z), \tag{B.111}$$

with $N(z) = 1/\sqrt{2\pi}exp(-z^2/2)$ and $E(z) = \int_{-\infty}^{z} N(y)dy$.

References

ACAMPORA, G., GAETA, M., & LOIA, V. (2011). Hierarchical optimization of personalized experiences for e-Learning systems through evolutionary models. *Neural Computing & Applications*, **20**(5), pp. 641–657.

ALBA, E. & DORRONSORO, B. (2005). The exploration/exploitation tradeoff in dynamic cellular genetic algorithms. *IEEE Transactions on Evolutionary Computation*, **9**(2), pp. 126–142.

ALBA, E., LUQUE, G., & NESMACHNOW, S. (2013). Parallel metaheuristics: recent advances and new trends. *International Transactions in Operational Research*, **20**(1), pp. 1–48.

ALBA, E. & TOMASSINI, M. (2002). Parallelism and evolutionary algorithms. *IEEE Transactions on Evolutionary Computation*, **6**(5), pp. 443–462.

ALBA, E. & TROYA, J.M. (1999). An analysis of synchronous and asynchronous parallel distributed genetic algorithms with structured and panmictic Islands. *Proceedings of the International Parallel Processing Symposium*, Springer, Berlin, Heidelberg, pp. 248–256.

ALBA, E. & TROYA, J.M. (2001). Analyzing synchronous and asynchronous parallel distributed genetic algorithms. *Future Generation Computer Systems*, Workshop on Bio-inspired Solutions to Parallel Computing problems, **17**(4), pp. 451–465.

ALKIM, T.P., SCHUURMAN, H., & TAMPERE, C.M.J. (2000). Effects of external cruise control and co-operative following on highways: an analysis with the MIXIC traffic simulation model. *Proceedings of the IEEE Intelligent Vehicles Symposium 2000 (Cat. No.00TH8511)*, pp. 474–479.

ARNAOUT, G.M. & BOWLING, S. (2014). A Progressive Deployment Strategy for Cooperative Adaptive Cruise Control to Improve Traffic Dynamics. *International Journal of Automation and Computing*, **11**(1), pp. 10–18.

AW, A. & RASCLE, M. (2000). Resurrection of "Second Order" Models of Traffic Flow. *SIAM Journal of Applied Mathematics*, **60**(3), pp. 916–938.

BANDO, M., HASEBE, K., NAKAYAMA, A., SHIBATA, A., & SUGIYAMA, Y. (1995). Dynamical model of traffic congestion and numerical simulation. *Physical Review E: Statistical Physics, Plasmas, Fluids, and Related Interdisciplinary Topics*, **51**(2), pp. 1035–1042.

BANDO, M., HASEBE, K., NAKANISHI, K., & NAKAYAMA, A. (1998). Analysis of optimal velocity model with explicit delay. *Physical Review E*, **58**(5), pp. 5429–5435.

BAREKET, Z., FANCHER, P.S., PENG, H., LEE, K., & ASSAF, C.A. (2003). Methodology for assessing adaptive cruise control behavior. *IEEE Transactions on Intelligent Transportation Systems*, **4**(3), pp. 123–131.

BOER, P.-T., KROESE, D.P., MANNOR, S., & RUBINSTEIN, R.Y. (2005). A Tutorial on the Cross-Entropy Method. *Annals of Operations Research*, **134**(1), pp. 19–67.

BOX, M.J. (1965). A New Method of Constrained Optimization and a Comparison With Other

Methods. *The Computer Journal. Section A / Section B*, **8**(1), pp. 42–52.

BROCKFELD, E., KÜHNE, R., & WAGNER, P. (2005). Calibration and Validation of Microscopic Models of Traffic Flow. *Transportation Research Record: Journal of the Transportation Research Board*, **1934**(1), pp. 62–70.

CANTU-PAZ, E. (1999). Designing Efficient and Accurate Parallel Genetic Algorithms (Parallel Algorithms) (PhD Thesis).

CARLSON, R.C., PAPAMICHAIL, I., PAPAGEORGIOU, M., & MESSMER, A. (2010). Optimal mainstream traffic flow control of large-scale motorway networks. *Transportation Research Part C: Emerging Technologies*, **18**(2), pp. 193–212.

CHANDLER, R.E., HERMAN, R., & MONTROLL, E.W. (1958). Traffic Dynamics: Studies in Car Following. *Operations Research*, **6**(2), pp. 165–184.

CIUFFO, B., PUNZO, V., & MONTANINO, M. (2012). The Calibration of Traffic Simulation Models : Report on the assessment of different Goodness of Fit measures and Optimization Algorithms, MULTITUDE Project – COST Action TU0903 - EU Science Hub - European Commission.

CREMER, M. & LUDWIG, J. (1986). A fast simulation model for traffic flow on the basis of boolean operations. *Mathematics and Computers in Simulation*, **28**(4), pp. 297–303.

CREMER, M. & PAPAGEORGIOU, M. (1981). Parameter identification for a traffic flow model. *Automatica*, **17**(6), pp. 837–843.

DAGANZO, C.F. (1994). The cell transmission model: A dynamic representation of highway traffic consistent with the hydrodynamic theory. *Transportation Research Part B: Methodological*, **28**(4), pp. 269–287.

DAGANZO, C.F. (1995a). Requiem for second-order fluid approximations of traffic flow. *Transportation Research Part B: Methodological*, **29**(4), pp. 277–286.

DAGANZO, C.F. (1995b). The cell transmission model, part II: Network traffic. *Transportation Research Part B: Methodological*, **29**(2), pp. 79–93.

DAGANZO, C.F., LIN, W.-H., & DEL CASTILLO, J.M. (1997). A simple physical principle for the simulation of freeways with special lanes and priority vehicles. *Transportation Research Part B: Methodological*, **31**(2), pp. 103–125.

DAVIS, L.C. (2004). Effect of adaptive cruise control systems on traffic flow. *Physical Review E: Statistical, Nonlinear, Biological and Soft Matter Physics*, **69**, 066110.

DAVIS, L.C. (2007). Effect of adaptive cruise control systems on mixed traffic flow near an on-ramp. *Physica A: Statistical Mechanics and its Applications*, **379**(1), pp. 274–290.

DEL CASTILLO, J., PINTADO, P., & BENITEZ, F. (1994). The reaction time of drivers and the stability of traffic flow. *Transportation Research Part B: Methodological*, **28**(1), pp. 35–60.

DELIS, A.I., NIKOLOS, I.K., & PAPAGEORGIOU, M. (2014). High-resolution numerical relaxation approximations to second-order macroscopic traffic flow models. *Transportation*

Research Part C: Emerging Technologies, **44**, pp. 318–349.

DELIS, A.I., NIKOLOS, I.K., & PAPAGEORGIOU, M. (2015a). Macroscopic traffic flow modeling with adaptive cruise control: Development and numerical solution. *Computers & Mathematics with Applications*, **70**(8), pp. 1921–1947.

DELIS, A.I., NIKOLOS, I.K., & PAPAGEORGIOU, M. (2015b). Macroscopic Modelling and Simulation of Multi-lane Traffic. *Proceedings of the 2015 IEEE 18th International Conference on Intelligent Transportation Systems*, pp. 2213–2218.

DEMIR, C. (2003). Modelling the Impact of ACC-Systems on the Traffic Flow at Macroscopic Modelling Level. *Traffic and Granular Flow'01*. Springer, Berlin, Heidelberg, pp. 305–317.

FORBES, T.W., ZAGORSKI, H.J., HOLSHOUSER, E.L., & DETERLINE, W.A. (1958). Measurement of Driver Reactions to Tunnel Conditions. *Highway Research Board Proceedings*, **37**, pp. 345-357.

FREJO, J.R.D., CAMACHO, E.F., & HOROWITZ, R. (2012). A parameter identification algorithm for the METANET model with a limited number of loop detectors. *Proceedings of the 2012 IEEE 51st IEEE Conference on Decision and Control (CDC)*, pp. 6983–6988.

GAZIS, D.C., HERMAN, R., & ROTHERY, R.W. (1961). Nonlinear Follow-The-Leader Models of Traffic Flow. *Operations Research*, **9**(4), pp. 545–567.

GERLOUGH, D.L. & HUBER, M.J. (1976). Traffic Flow Theory. *Transportation Research Board Special Report*.

GIPPS, P.G. (1981). A behavioural car-following model for computer simulation. *Transportation Research Part B: Methodological*, **15**(2), pp.105–111.

GUPTA, A.K. & DHIMAN, I. (2014). Analyses of a continuum traffic flow model for a nonlane-based system. *International Journal of Modern Physics. C*, **25**(10), 1450045.

GUPTA, A.K. & KATIYAR, V.K. (2005). Analyses of shock waves and jams in traffic flow. *Journal of Physics A: Mathematical and General*, **38**, 4069.

GUPTA, A.K. & KATIYAR, V.K. (2006). A new anisotropic continuum model for traffic flow. *Physica A: Statistical Mechanics and its Applications*, **368**(2), pp. 551–559.

HALKIAS, B., KOPELIAS, P., PAPANDREOU, K., POLITOU, A., PREVEDOUROS, P., & SKABARDONIS, A. (2007). Freeway Bottleneck Simulation, Implementation, and Evaluation. *Transportation Research Record: Journal of the Transportation Research Board*, **2012**(1), pp. 84–93.

HASEBE, K., NAKAYAMA, A., & SUGIYAMA, Y. (2003). Dynamical model of a cooperative driving system for freeway traffic. *Physical Review E: Statistical, Nonlinear, Biological and Soft Matter Physics*, **68**, 026102.

HEGYI, A., SCHUTTER, B.D., & HELLENDOORN, H. (2005a). Model predictive control for optimal coordination of ramp metering and variable speed limits. *Transportation Research Part C: Emerging Technologies*, **13**(3), pp. 185–209.

HEGYI, A., SCHUTTER, B.D., & HELLENDOORN, J. (2005b). Optimal coordination of variable speed limits to suppress shock waves. *IEEE Transactions on Intelligent Transportation Systems*, **6**(1), pp. 102–112.

HELBING, D. (1997a). *Verkehrsdynamik: Neue physikalische Modellierungskonzepte*. Berlin Heidelberg: Springer-Verlag.

HELBING, D. (1997b). Modeling multi-lane traffic flow with queuing effects. *Physica A: Statistical Mechanics and its Applications*, **242**(1-2), pp. 175–194.

HELBING, D., HENNECKE, A., SHVETSOV, V., & TREIBER, M. (2001). MASTER: macroscopic traffic simulation based on a gas-kinetic, non-local traffic model. *Transportation Research Part B: Methodological*, **35**(2), pp. 183–211.

HELBING, D. & JOHANSSON, A. (2009). On the Controversy around Daganzo's Requiem for and Aw-Rascle's Resurrection of Second-Order Traffic Flow Models. *The European Physical Journal B*, **69**(4), pp. 549–562.

HELBING, D. & TREIBER, M. (1998). Gas-Kinetic-Based Traffic Model Explaining Observed Hysteretic Phase Transition. *Physical Review Letters*, **81**(14), pp. 3042–3045.

HELLY, W. (1961). Simulation of bottlenecks in single-lane traffic flow. *Proceedings of the Symposium on Theory of Traffic Flow*, Research Laboratories, General Motors, pp. 207-238.

HENCLEWOOD, D., SUH, W., RODGERS, M.O., FUJIMOTO, R., & HUNTER, M.P. (2017). A calibration procedure for increasing the accuracy of microscopic traffic simulation models. *SIMULATION*, **93**(1), pp. 35–47.

HERMAN, R., MONTROLL, E.W., POTTS, R.B., & ROTHERY, R.W. (1959). Traffic Dynamics: Analysis of Stability in Car Following. *Operations Research*, **7**(1), pp. 86–106.

HIDAS, P. (2002). Modelling lane changing and merging in microscopic traffic simulation. *Transportation Research Part C: Emerging Technologies*, **10**(5-6), pp. 351–371.

HIGHWAY AGENCY (1996). Design manual for roads and bridges (No. 12). The Stationery Office, London.

HOLLANDER, Y. & LIU, R. (2008). The principles of calibrating traffic microsimulation models. *Transportation*, **35**(3), pp. 347–362.

HOOGENDOORN, S. & HOOGENDOORN, R. (2010). Calibration of microscopic traffic-flow models using multiple data sources. *Philosophical Transactions of the Royal Society A: Mathematical, Physica and Engineering Sciences*, **368**(1928), pp. 4497–4517.

HOOGENDOORN, S.P. (1999). Multiclass continuum modelling of multilane traffic flow (PhD Thesis).

HOOGENDOORN, S.P. & BOVY, P.H.L. (2000). Continuum modeling of multiclass traffic flow. *Transportation Research Part B: Methodological*, **34**(2), pp. 123–146.

HOOGENDOORN, S.P. & BOVY, P.H.L. (2001). Model assessment of dynamic speed limit control.

Proceedings of the World conference on transport research, Seoul, Korea.

HOOGENDOORN, S.P. & OSSEN, S. (2005). Parameter Estimation and Analysis of Car-Following Models. *Proceedings of the 16th International Symposium on Transportation and Traffic TheoryUniversity of Maryland*, College Park, pp. 245-265.

HU, J.J. & GOODMAN, E.D. (2002). The hierarchical fair competition (HFC) model for parallel evolutionary algorithms. *Proceedings of the 2002 Congress on Evolutionary Computation*, pp. 49–54.

HUEPER, J., DERVISOGLU, G., MURALIDHARAN, A., GOMES, G., HOROWITZ, R., & VARAIYA, P. (2009). Macroscopic Modeling and Simulation of Freeway Traffic Flow. *IFAC Proceedings Volumes*, **42**(5), pp. 112–116.

IOANNOU, P.A. & CHIEN, C.C. (1993). Autonomous intelligent cruise control. *IEEE Transactions on Vehicular Technology*, **42**(4), pp. 657–672.

JIANG, R., JIN, C.-J., ZHANG, H.M., HUANG, Y.-X., TIAN, J.-F., WANG, W., HU, M.-B., WANG, H., & JIA, B. (2017) Experimental and Empirical Investigations of Traffic Flow Instability. *Transportation Research Procedia*, **23**, pp. 157–173.

JIN, S. & XIN, Z. (1995). The relaxation schemes for systems of conservation laws in arbitrary space dimensions. *Communications on Pure and Applied Mathematics*, **48**(3), pp. 235–276.

JONG, E.D. de, THIERENS, D., & WATSON, R.A. (2004). Hierarchical Genetic Algorithms. *Proceedings of the International Conference on Parallel Problem Solving from Nature*, Springer, Berlin, Heidelberg, pp. 232–241.

KERNER, B.S., & KONHÄUSER, P. (1993). Cluster effect in initially homogeneous traffic flow. *Physical Review E: Statistical Physics, Plasmas, Fluids, and Related Interdisciplinary Topics*, **48**(4), pp. R2335–R2338.

KERNER, B.S., & KONHÄUSER, P. (1994). Structure and parameters of clusters in traffic flow. *Physical Review E: Statistical Physics, Plasmas, Fluids, and Related Interdisciplinary Topics*, **50**(1), pp. 54–83.

KESTING, A. & TREIBER, M. (2008). How Reaction Time, Update Time, and Adaptation Time Influence the Stability of Traffic Flow. *Computer-Aided Civil and Infrastructure Engineering*, **23**(2), pp. 125–137.

KESTING, A., TREIBER, M., & HELBING, D. (2010). Enhanced Intelligent Driver Model to Access the Impact of Driving Strategies on Traffic Capacity. *Philosophical Transactions of the Royal Society A: Mathematical, Physical and Engineering Sciences*, **368**(1928), pp. 4585–4605.

KESTING, A., TREIBER, M., SCHÖNHOF, M., & HELBING, D. (2008). Adaptive cruise control design for active congestion avoidance. *Transportation Research Part C: Emerging Technologies*, **16**(6), pp. 668–683.

KESTING, A., TREIBER, M., SCHÖNHOF, M., KRANKE, F., & HELBING, D. (2006). Jam-avoiding adaptive cruise control (ACC) and its impact on traffic dynamics. *Traffic and Granular Flow 2005*, pp. 633–643.

KOMETANI, E. & SASAKI, T. (1961). *Dynamic behavior of traffic with a nonlinear spacing: speed relationship.* Amsterdam: Elsevier Publishing Co.

KOTSIALOS, A. & PAPAGEORGIOU, M. (2001). The Importance of Traffic Flow Modeling for Motorway Traffic Control. *Networks and Spatial Economics*, **1**(1-2), pp. 179–203.

KOTSIALOS, A., PAPAGEORGIOU, M., DIAKAKI, C., PAVLIS, Y., & MIDDELHAM, F. (2002). Traffic flow modeling of large-scale motorway networks using the macroscopic modeling tool METANET. *IEEE Transactions on Intelligent Transportation Systems*, **3**, pp. 282–292.

KOTSIALOS, A., PAPAGEORGIOU, M., & MESSMER, A. (1999). Optimal Coordinated and Integrated Motorway Network Traffic Control. *Proceedings of the 14th International Symposium on Transportation and Traffic Theory Transportation Research Institute*, pp. 621-644

KOTSIALOS, A., PAVLIS, Y., MIDDELHAM, F., DIAKAKI, C., VARDAKA, G., & PAPAGEORGIOU, M. (1998). Modelling of the Large Scale Motorway Network Around Amsterdam. *IFAC Proceedings Volumes*, **31**(20), PP. 349–354.

KÜHNE, R. & MICHALOPOULOS, P. (1997). Continuum flow models (Traffic flow theory: A state-of-the-art report, chapter 5).

LAGARIAS, J., REEDS, J., WRIGHT, M., & WRIGHT, P. (1998). Convergence Properties of the Nelder--Mead Simplex Method in Low Dimensions. *SIAM Journal on Optimization*, **9**(1), pp. 112–147.

LEBACQUE, J.P. (1996). The Godunov Scheme and what it means for First Order Traffic Flow Models. *Proceedings of the 13th International Symposium on Transportation and Traffic Theory*, Lyon, France, pp. 647-677.

LEBACQUE, J.-P. (2002). A Two Phase Extension of the LWR Model Based on the Boundedness of Traffic Acceleration: *Proceedings of the 15 th International Symposium on Transportation and Traffic Theory*, Adelaide, Australia, pp. 697–718.

Leclercq, L. (2007). A New Numerical Scheme for Bounding Acceleration in the LWR Model. *Proceedings of the 4th IMA International Conference on Mathematics in Transport*, pp. 279-292.

LEE, J.-B. & OZBAY, K. (2009). New Calibration Methodology for Microscopic Traffic Simulation Using Enhanced Simultaneous Perturbation Stochastic Approximation Approach. *Transportation Research Record: Journal of the Transportation Research Board*, **2124**, pp. 233–240.

LENZ, H. (1999). Entwicklung nichtlinearer, diskreter Regler zum Abbau von Verkehrsflussinhomogenitaeten mithilfe makroskopischer Verhkehrsmodelle.

LEUTZBACH, W. (1988). *Introduction to the Theory of Traffic Flow*. Berlin Heidelberg: Springer-Verlag.

LI, P.Y. & SHRIVASTAVA, A. (2002). Traffic flow stability induced by constant time headway policy for adaptive cruise control vehicles. *Transportation Research Part C: Emerging Technologies*, **10**(4), pp. 275–301.

LI, X. & KIRLEY, M. (2002). The effects of varying population density in a fine-grained parallel genetic algorithm. *Proceedings of the 2002 Congress on Evolutionary Computation*, pp. 1709–1714.

LI, X., LI, Z., HAN, X., & DAI, S. (2009). Effect of the optimal velocity function on traffic phase transitions in lattice hydrodynamic models. *Communications in Nonlinear Science and Numerical Simulation*, **14**(5), pp. 2171–2177.

LI, Y., ZHU, H., CEN, M., LI, Y., LI, R., & SUN, D. (2013). On the stability analysis of microscopic traffic car-following model: a case study. *Nonlinear Dynamics*, **74**(1-2), pp. 335–343.

LIANG, C. & PENG, H. (2002). String Stability Analysis of Adaptive Cruise Controlled Vehicles. *JSME International Journal Series C*, **43**(3), pp. 671–677.

LIANG, C.-Y. & PENG, H. (1999). Optimal Adaptive Cruise Control with Guaranteed String Stability. *Vehicle System Dynamics*, **32**(4-5), pp. 313–330.

LIANG, C.-Y. & PENG, H. (2000). String Stability Analysis of Adaptive Cruise Controlled Vehicles. *JSME International Journal Series C Mechanical Systems, Machine Elements and Manufacturing*, **43**(3), pp. 671–677.

LIGHTHILL, M.J. & WHITHAM, G.B. (1955). On kinematic waves I. Flood movement in long rivers. *Proceedings of the Royal Society A: Mathematical, Physical and Engineering Sciences*, **229**(1178), pp. 281–316.

LIU, G., LYRINTZIS, A., & MICHALOPOULOS, P. (1998). Improved High-Order Model for Freeway Traffic Flow. *Transportation Research Record: Journal of the Transportation Research Board*, **1644**(1), pp. 37–46.

LLORÀ, X. & GARRELL, J.M. (2001). Knowledge-independent Data Mining with Fine-grained Parallel Evolutionary Algorithms. *Proceedings of the 3rd Annual Conference on Genetic and Evolutionary Computation*, pp. 461–468.

LU, X.Y., QIU, T.Z., VARAIYA, P., HOROWITZ, R., & SHLADOVER, S.E. (2010). Combining Variable Speed Limits with Ramp Metering for freeway traffic control. *Proceedings of the 2010 American Control Conference*, pp. 2266–2271.

LUQUE, G. & ALBA, E. (2011). *Parallel Genetic Algorithms: Theory and Real World Applications*, Studies in Computational Intelligence. Berlin Heidelberg: Springer-Verlag.

LUSPAY, T., KULCSÁR, B., VARGA, I., & BOKOR, J. (2010). Parameter-dependent modeling of freeway traffic flow. *Transportation Research Part C: Emerging Technologies*, **18**(4), pp. 471–488.

LYRINTZIS, A.S., LIU, G., & MICHALOPOULOS, P.G. (1994). Development and Comparative Evaluation of High-Order Traffic Flow Models. *Transportation Research Record*, **1457**, pp. 174-183

MARSDEN, G., MCDONALD, M., & BRACKSTONE, M. (2001). Towards an understanding of adaptive cruise control. *Transportation Research Part C: Emerging Technologies*, **9**(1), pp. 33–51.

MESSER, C. (1998). Simulation Studies of Traffic Operations at Oversaturated, Closely Spaced Signalized Intersections. *Transportation Research Record: Journal of the Transportation Research Board*, **1646**, pp. 115–123.

MESSMER, A. & PAPAGEORGIOU, M. (1990). METANET: A Macroscopic Simulation Program for Motorway Networks. *Traffic Engineering & Control*, **31**(8), pp. 466–470.

MILANÉS, V. & SHLADOVER, S.E. (2014). Modeling cooperative and autonomous adaptive cruise control dynamic responses using experimental data. *Transportation Research Part C: Emerging Technologies*, **48**, pp. 285–300.

MILANÉS, V., SHLADOVER, S.E., SPRING, J., NOWAKOWSKI, C., KAWAZOE, H., & NAKAMURA, M. (2014). Cooperative Adaptive Cruise Control in Real Traffic Situations. *IEEE Transactions on Intelligent Transportation Systems*, **15**(1), pp. 296–305.

MONAMY, T., HAJ-SALEM, H., & LEBACQUE, J.-P. (2012). A Macroscopic Node Model Related to Capacity Drop. *Procedia - Social and Behavioral Sciences*, **54**(4), pp. 1388–1396.

MUÑOZ, L., SUN, X., HOROWITZ, R., & ALVAREZ, L. (2006). Piecewise-Linearized Cell Transmission Model and Parameter Calibration Methodology. *Transportation Research Record: Journal of the Transportation Research Board*, **1965**(1), pp. 183–191.

MUÑOZ, L., SUN, X., SUN, D., GOMES, G., & HOROWITZ, R. (2004). Methodological calibration of the cell transmission model. *Proceedings of the 2004 American Control Conference*, pp. 798–803.

NAGEL, K. & SCHRECKENBERG, M. (1992). A cellular automaton model for freeway traffic. *Journal de Physique*, **2**(12), pp. 2221–2229.

NAUS, G.J.L., VUGTS, R.P.A., PLOEG, J., MOLENGRAFT, M.J.G. van de, & STEINBUCH, M. (2010). String-Stable CACC Design and Experimental Validation: A Frequency-Domain Approach. *IEEE Transactions on Vehicular Technology*, **59**(9), pp. 4268–4279.

NELDER, J.A. & MEAD, R. (1965). A Simplex Method for Function Minimization. *The Computer Journal*, **7**(4), pp. 308–313.

NEWELL, G.F. (1961). Nonlinear Effects in the Dynamics of Car Following. *Operations Research*, **9**(2), pp. 209–229.

NEWELL, G.F. (1965). Instability in Dense Highway Traffic: A Review, *Proceedings of the 2nd Symposium on the Theory of Road Traffic Flow*.

NEWELL, G.F. (2002). A simplified car-following theory: a lower order model. *Transportation Research Part B: Methodological*, **36**(3), pp. 195–205.

NGODUY, D. (2006). Derivation of Continuum Traffic Model for Weaving Sections on Freeways. *Transportmetrica*, **2**(3), pp. 199–222.

NGODUY, D. (2009). Macroscopic Effects of Multianticipative Driving Behavior on Traffic Flow Characteristics. *Transportation Research Record: Journal of the Transportation Research Board*, **2124**, pp. 103–112.

NGODUY, D. (2011). Kernel Smoothing Method Applicable to the Dynamic Calibration of Traffic Flow Models. *Computer-Aided Civil and Infrastructure Engineering*, **26**(6), pp. 420–432.

NGODUY, D. (2012a). Application of gas-kinetic theory to modelling mixed traffic of manual and ACC vehicles. *Transportmetrica*, **8**(1), pp. 43–60.

NGODUY, D. (2012b). Effect of driver behaviours on the formation and dissipation of traffic flow instabilities. *Nonlinear Dynamics*, **69**(3), pp. 969–975.

NGODUY, D. (2012c). Application of gas-kinetic theory to modelling mixed traffic of manual and ACC vehicles. *Transportmetrica*, **8**(1), pp. 43–60.

NGODUY, D. (2013a). Platoon-based macroscopic model for intelligent traffic flow. *Transportmetrica B: Transport Dynamics*, **1**(2), pp. 153–169.

NGODUY, D. (2013b). Instability of cooperative adaptive cruise control traffic flow: A macroscopic approach. *Communications in Nonlinear Science and Numerical Simulation*, **18**(10), pp. 2838–2851.

NGODUY, D. (2013c). Analytical studies on the instabilities of heterogeneous intelligent traffic flow. *Communications in Nonlinear Science and Numerical Simulation*, **18**(10), pp. 2699–2706.

NGODUY, D. (2014). Generalized macroscopic traffic model with time delay. *Nonlinear Dynamics*, **77**(1-2), pp. 289–296.

NGODUY, D., HOOGENDOORN, S., & VAN ZUYLEN, H. (2004). Comparison of Numerical Schemes for Macroscopic Traffic Flow Models. *Transportation Research Record: Journal of the Transportation Research Board*, **1876**(1), pp. 52–61.

NGODUY, D., HOOGENDOORN, S.P., & LIU, R. (2009). Continuum modeling of cooperative traffic flow dynamics. *Physica A: Statistical Mechanics and its Applications*, **388**(13), pp. 2705–2716.

NGODUY, D., HOOGENDOORN, S.P., & VAN LINT, J.W.C. (2005). Modeling Traffic Flow Operation in Multilane and Multiclass Urban Networks. *Transportation Research Record*, **1923**(1), pp. 73–81.

NGODUY, D. & MAHER, M.J. (2012). Calibration of second order traffic models using continuous cross entropy method. *Transportation Research Part C: Emerging Technologies*, **24**, pp. 102–121.

NGODUY, D. & TAMPERE, C. (2009). Macroscopic effects of reaction time on traffic flow characteristics. *Physica Scripta*, **80**, 025802.

NGODUY, D. & WILSON, R.E. (2014). Multianticipative Nonlocal Macroscopic Traffic Model. *Computer-Aided Civil and Infrastructure Engineering*, **29**(4), pp. 248–263.

NI, D., LEONARD II, J., GUIN, A., & WILLIAMS, B. (2004). Systematic Approach for Validating Traffic Simulation Models. *Transportation Research Record*, **1876**, pp. 20–31.

NIKOLOS, I. (2011). Surrogate modeling in evolutionary based engineering design optimization. *Soft Computing Methods for Civil and Structural Engineering*, pp. 173–203.

NIKOLOS, I.K. (2004). Inverse design of aerodynamic shapes using differential evolution coupled with artificial neural network. *Proceedings of the ERCOFTAC Conference in Design Optimization: Methods and Applications*. Athens, Greece.

NIKOLOS, I.K. (2013). On the use of multiple surrogates within a differential evolution procedure for high-lift airfoil design. *International Journal of Advanced Intelligence Paradigms*, **5**(4), pp. 319–341.

NIKOLOS, I.K., DELIS, A.I., & PAPAGEORGIOU, M. (2015). Macroscopic Modelling and Simulation of ACC and CACC Traffic. *Proceedings of the IEEE 18th International Conference on Intelligent Transportation Systems*, pp. 2129–2134.

NOWAKOWSKI, C., SHLADOVER, S.E., CODY, D., BU, F., O'CONNELL, J., SPRING, J., DICKEY, S., & NELSON, D. (2011). Cooperative Adaptive Cruise Control: Testing Drivers' Choices of Following Distances. *PATH Research Report*.

NTOUSAKIS, I.A., NIKOLOS, I.K., & PAPAGEORGIOU, M. (2015). On Microscopic Modelling of Adaptive Cruise Control Systems. *Transportation Research Procedia*, **6**, pp. 111–127.

OLIVEIRA, A., LORENA, L., STEPHANY, S., & JÔNATAS PRETO, A. (2004). A hierarchical fair competition genetic algorithm for numerical optimization.

PAPAGEORGIOU, M. (1998). Some remarks on macroscopic traffic flow modelling. *Transportation Research Part A: Policy and Practice*, **32**(5), pp. 323–329.

PAPAGEORGIOU, M., BLOSSEVILLE, J.-M., & HAJ-SALEM, H. (1990). Modelling and real-time control of traffic flow on the southern part of Boulevard Peripherique in Paris: Part II: Coordinated on-ramp metering. *Transportation Research Part A: General*, **24**(5), pp. 361–370.

PAPAGEORGIOU, M., DIAKAKI, C., DINOPOULOU, V., KOTSIALOS, A., & YIBING WANG (2003) Review of road traffic control strategies. *Proceedings of the IEEE*, **91**(12), pp. 2043–2067.

PAYNE, H.J. (1971). Models of Freeway Traffic and Control. *Mathematical Models of Public Systems. Simulation Council*, **1**, pp. 51–61.

PAYNE, H.J. (1979). FREFLO: A Macroscopic Simulation Model of Freeway Traffic. *Transportation Research Record*, **722**, pp. 68–77.

PENG, G., NIE, F., CAO, B., & LIU, C. (2012). A driver's memory lattice model of traffic flow and its numerical simulation. *Nonlinear Dynamics*, **67**(3), pp. 1811–1815.

PHILLIPS, W.F. (1979). A kinetic model for traffic flow with continuum implications. *Transportation Planning and Technology*, **5**(3), pp. 131–138.

PIPES, L.A. (1953). An Operational Analysis of Traffic Dynamics. *Journal of Applied Physics*, **24**(3), pp. 274–281.

POOLE, A. & KOTSIALOS, A. (2012). METANET Model Validation using a Genetic Algorithm.

IFAC Proceedings Volumes, **45**(24), pp. 7–12.

PRICE, K., STORN, R.M., & LAMPINEN, J.A. (2005). *Differential Evolution: A Practical Approach to Global Optimization*, Natural Computing Series. Berlin Heidelberg: Springer-Verlag.

PRIGOGINE, I. (1961). A Boltzmann-like approach to the statistical theory of traffic flow, pp. 158–164.

PRIGOGINE, I. & ANDREWS, F.C. (1960). A Boltzmann-Like Approach for Traffic Flow. *Operations Research*, **8**(6), pp. 789–797.

RAJAMANI, R., LEVINSON, D.M., MICHALOPOULOS, P., WANG, J., SANTHANAKRISHNAN, K., & ZHU, X.I. (2005). Adaptive Cruise Control System Design And Its Impact on Traffic Flow. *Research Report*.

REUSCHEL, A. (1950). Fahrzeugbewegungen in der Kolonne. *Oesterreichisches Ingenieur-Archir*, **4**, pp. 193–215.

RICHARDS, P.I. (1956). Shock Waves on the Highway. *Operations Research*, **4**(1), pp. 42–51.

SANWAL, K.K., PETTY, K., WALRAND, J., & FAWAZ, Y. (1996). An extended macroscopic model for traffic flow. *Transportation Research Part B: Methodological*, **30**(1), pp. 1–9.

SCOTT, E.O. & DE JONG, K.A. (2015a). Evaluation-Time Bias in Asynchronous Evolutionary Algorithms. *Proceedings of the Companion Publication of the 2015 Annual Conference on Genetic and Evolutionary Computation*, New York, pp. 1209–1212.

SCOTT, E.O. & DE JONG, K.A. (2015b). Understanding Simple Asynchronous Evolutionary Algorithms. *Proceedings of the 2015 ACM Conference on Foundations of Genetic Algorithms XIII*, New York, pp. 85–98.

SHLADOVER, S., SU, D., & LU, X.-Y. (2012). Impacts of Cooperative Adaptive Cruise Control on Freeway Traffic Flow. *Transportation Research Record: Journal of the Transportation Research Board*, **2324**(1), pp. 63–70.

SHVETSOV, V. & HELBING, D. (1999). Macroscopic dynamics of multilane traffic. *Physical Review E: Statistical Physics, Plasmas, Fluids, and Related Interdisciplinary Topics*, **59**(6), pp. 6328–6339.

SPILIOPOULOU, A., KONTORINAKI, M., PAPAGEORGIOU, M., & KOPELIAS, P. (2014). Macroscopic traffic flow model validation at congested freeway off-ramp areas. *Transportation Research Part C: Emerging Technologies*, **41**, pp. 18–29.

SPILIOPOULOU, A., PAPAMICHAIL, I., PAPAGEORGIOU, M., TYRINOPOULOS, I., & CHRYSOULAKIS, J. (2015). Macroscopic Traffic Flow Model Calibration Using Different Optimization Algorithms. *Transportation Research Procedia*, **6**, pp. 144–157.

STEWART, J., BAKER, M., & VAN AERDE, M. (1996). Evaluating Weaving Section Designs Using INTEGRATION. *Transportation Research Record: Journal of the Transportation Research Board*, **1555**, pp. 33–41.

STORN, R. & PRICE, K. (1995). Differential Evolution: A Simple and Efficient Adaptive Scheme

for Global Optimization over Continuous Spaces. *Journal of Global Optimization*, **23**(1).

STORN, R. & PRICE, K. (1997). Differential Evolution – A Simple and Efficient Heuristic for global Optimization over Continuous Spaces. *Journal of Global Optimization*, **11**(4), pp. 341–359.

STROFYLAS, G.A. & NIKOLOS, I.K. (2015). Reverse Engineering of a Wind Turbine Blade Surface using Differential Evolution. *Proceedings of the Fourth International Conference on Soft Computing Technology in Civil, Structural and Environmental Engineering.*

SWAROOP, D. & HEDRICK, J.K. (1996). String stability of interconnected systems. *IEEE Transactions on Automatic Control*, **41**(3), pp. 349–357.

SWAROOP, D., HEDRICK, J.K., CHIEN, C.C., & IANNOU, P. (1994). A Comparison of Spacing and Headway Control Laws for Automatically Controlled Vehicles. *Vehicle System Dynamics*, **23**(1), pp. 597–625.

SWAROOP, D. & RAJAGOPAL, K.R. (1999). Intelligent cruise control systems and traffic flow stability. *Transportation Research Part C: Emerging Technologies*, **7(6)**, pp. 329–352.

TAMPERE, C., HOOGENDOORN, S., & VAN AREM, B. (2005). A Behavioural Approach to Instability, Stop and Go Waves, Wide Jams and Capacity Drop. *Transportation and traffic theory*, **16**, pp. 205–228.

TANG, T., WANG, Y., YANG, X., & WU, Y. (2012). A new car-following model accounting for varying road condition. *Nonlinear Dynamics*, **70**(2), pp. 1397–1405.

TANG, T.Q., HUANG, H.J., & XU, G. (2008). A new macro model with consideration of the traffic interruption probability. *Physica A: Statistical Mechanics and its Applications*, **387**(27), pp. 6845–6856.

TANG, T.Q., LI, C.Y., WU, Y.H., & HUANG, H.J. (2011). Impact of the honk effect on the stability of traffic flow. *Physica A: Statistical Mechanics and its Applications*, **390**(20), pp. 3362–3368.

THEIL, H. (1961). *Economic forecasts and policy*. North-Holland Pub. Co.

TIAN, C., SUN, D., & ZHANG, M. (2011). Nonlinear analysis of lattice model with consideration of optimal current difference. *Communications in Nonlinear Science and Numerical Simulation*, **16**(11), pp. 4524–4529.

TOMASSINI, M. (2005). *Spatially Structured Evolutionary Algorithms: Artificial Evolution in Space and Time*, Natural Computing Series. Berlin Heidelberg: Springer-Verlag.

TREIBER, M. & HELBING, D. (1999). Macroscopic Simulation of Widely Scattered Synchronized Traffic States. *Journal of Physics A: Mathematical and General*, **32**(1), pp. L17–L23.

TREIBER, M. & HELBING, D. (2001). Microsimulations of Freeway Traffic Including Control Measures. *Automatisierungstechnik,* **49**(11).

TREIBER, M., HENNECKE, A., & HELBING, D. (1999). Derivation, properties, and simulation of a gas-kinetic-based, nonlocal traffic model. *Physical Review E*, **59**(1), pp. 239–253.

TREIBER, M., HENNECKE, A., & HELBING, D. (2000). Congested Traffic States in Empirical Observations and Microscopic Simulations. *Physical Review E*, **62**, pp. 1805–1824.

TREIBER, M. & KESTING, A. (2011). Evidence of convective instability in congested traffic flow: A systematic empirical and theoretical investigation. *Transportation Research Part B: Methodological*, **45**(9), pp. 1362–1377.

TREIBER, M. & KESTING, A. (2013). *Traffic Flow Dynamics: Data, Models and Simulation*. Berlin Heidelberg: Springer-Verlag.

TREIBER, M., KESTING, A., & HELBING, D. (2006). Delays, inaccuracies and anticipation in microscopic traffic models. *Physica A: Statistical Mechanics and its Applications*, **360**(1), pp. 71–88.

TREIBER, M., KESTING, A., & HELBING, D. (2010). Three-phase traffic theory and two-phase models with a fundamental diagram in the light of empirical stylized facts. *Transportation Research Part B: Methodological*, **44**(8-9), pp. 983–1000.

VAN AREM, B., VAN DRIEL, C.J.G., & VISSER, R. (2006). The Impact of Cooperative Adaptive Cruise Control on Traffic-Flow Characteristics. *IEEE Transactions on Intelligent Transportation Systems*, **7**(4), pp. 429–436.

VAN MAARSEVEEN, M.F.A.. (1982). The Theory of Martingales in Stochastic Systems Theory – Surveillance and Control of Freeway Traffic Flow.

VAN WAGENINGEN-KESSELS, F.L.M. (2013). Multi-class continuum traffic flow models: Analysis and simulation methods (PhD Thesis).

VANDERWERF, J., SHLADOVER, S., KOURJANSKAIA, N., MILLER, M., & KRISHNAN, H. (2001). Modeling Effects of Driver Control Assistance Systems on Traffic. *Transportation Research Record: Journal of the Transportation Research Board*, **1748**(1), pp. 167–174.

WAGNER, P. (2010). Fluid-dynamical and microscopic description of traffic flow: a data-driven comparison. *Philosophical Transactions of the Royal Society of London A: Mathematical, Physical and Engineering Sciences*, **368**(1928), pp. 4481–4495.

WANG, M., DAAMEN, W., HOOGENDOORN, S.P., & VAN AREM, B. (2014). Rolling horizon control framework for driver assistance systems. Part I: Mathematical formulation and non-cooperative systems. *Transportation Research Part C: Emerging Technologies*, **40**, pp. 271–289.

WANG, Y. & PAPAGEORGIOU, M. (2005). Real-time freeway traffic state estimation based on extended Kalman filter: a general approach. *Transportation Research Part B: Methodological*, **39**(2), pp. 141–167.

WANG, Y., PAPAGEORGIOU, M., & MESSMER, A. (2006). RENAISSANCE – A unified macroscopic model-based approach to real-time freeway network traffic surveillance. *Transportation Research Part C: Emerging Technologies*, **14**(3), pp. 190–212.

WHITHAM, G.B. (1974). *Linear and Nonlinear Waves*. John Wiley & Sons.

WIEDEMANN, R. (1974). Simulation des Straßenverkehrsflusses.

WILSON, R.E., BERG, P., HOOPER, S., & LUNT, G. (2004). Many-neighbour interaction and non-locality in traffic models. *The European Physical Journal B - Condensed Matter and Complex Systems*, **39**(3), pp. 397–408.

YI, J. & HOROWITZ, R. (2002). Macroscopic traffic flow stability for adaptive cruise controlled (ACC) vehicles. *Proceedings of the 41st IEEE Conference on Decision and Control,* pp. 893–899.

YI, J. & HOROWITZ, R. (2006). Macroscopic traffic flow propagation stability for adaptive cruise controlled vehicles. *Transportation Research Part C: Emerging Technologies*, **14**(2), pp. 81–95.

YI, J., LIN, H., ALVAREZ, L., & HOROWITZ, R. (2003). Stability of macroscopic traffic flow modeling through wavefront expansion. *Transportation Research Part B: Methodological*, **37**(7), pp. 661–679.

YU, L., SHI, Z., & ZHOU, B. (2008). Kink–antikink density wave of an extended car-following model in a cooperative driving system. *Communications in Nonlinear Science and Numerical Simulation*, **13**(10), pp. 2167–2176.

ZHANG, H.M. (1998). A theory of nonequilibrium traffic flow. *Transportation Research Part B: Methodological*, **32**(7), pp. 485–498.

ZHANG, H.M. (2002). A non-equilibrium traffic model devoid of gas-like behavior. *Transportation Research Part B: Methodological*, **36**(3), pp. 275–290.

ZHANG, P. & WONG, S.C. (2006). Essence of conservation forms in the traveling wave solutions of higher-order traffic flow models. *Physical Review E: Statistical, Nonlinear, Biological and Soft Matter Physics*, **74**, 026109.

ZHANG, P., WONG, S.C., & DAI, S.Q. (2009). A conserved higher-order anisotropic traffic flow model: Description of equilibrium and non-equilibrium flows. *Transportation Research Part B: Methodological*, **43**(5), pp. 562–574.

ZHENG, L.-J., TIAN, C., SUN, D.-H., & LIU, W.-N. (2012). A new car-following model with consideration of anticipation driving behavior. *Nonlinear Dynamics*, **70**(2), pp. 1205–1211.

ZHOU, J. & PENG, H. (2005). Range policy of adaptive cruise control vehicles for improved flow stability and string stability. *IEEE Transactions on Intelligent Transportation Systems*, **6**(2), pp. 229–237.